Optical and AFM Studies of ZnO: Excitonic Properties, Surface Morphology and Etching Effects

JAMES FRYAR (B.Sc., M.Sc.)

School of Physical Sciences
Dublin City University

A thesis submitted to

for the degree of
Philosophiae Doctor

Research Supervisor
Dr. Enda McGlynn

April 2005

Declaration

I hereby certify that this material, which I now submit for assessment on the programme of study leading to the award of Philosophiae Doctor, is entirely my own work and has not been taken from the work of others save and to the extent that such work has been cited and acknowledged within the text of my own work.

Signed: _____ *ID Number:* 94454311

Date: 10/8/2005

Acknowledgements

I would like to express my sincere thanks to my supervisor, Dr. E. McGlynn for his encouragement and enthusiasm in guiding me through the research presented here. Had it not been for his level of dedication, knowledge and experience, this thesis would not have been possible.

I am indebted to Prof. M. O. Henry for always finding the time for many valuable conversations, and whose continuous help with regard to the analysis of results obtained has enabled me to complete this research.

I would like to acknowledge Ms. C. J. Hanson and Dr. A. A. Cafolla for all their help and support with regard to the operation of the AFM and interpretation of the results presented here, and also Dr. J.-R. Duclère for his aid in obtaining and analysing the x-ray rocking curves.

To my parents and brothers for their support, and to Deirdre for her help, patience and love.

Abstract

Optical and AFM Studies of ZnO: Excitonic Properties, Surface Morphology and Etching Effects

The oxygen- and zinc-terminated polar surfaces of ZnO bulk crystals are examined using both optical spectroscopy and surface probe microscopy techniques. An initial study of as-received ZnO wafers purchased from three different companies reveals that there are large optical differences between each grower's material in terms of bound-exciton and green band luminescence, and free-exciton reflectance resonances. Topographic data obtained using atomic force microscopy (AFM) and x-ray diffraction results suggest that these optical variations are partly due to the different polishing methods applied to the surfaces.

The effects of etchant solutions on each polar face, both in terms of surface morphology and optical characteristics are examined. The O-terminated surface reacts strongly to hydrogen ions in acidic solutions and one observes high vertical-to-lateral etch ratios on such surfaces and dramatic increases in surface roughness, with corresponding decreases in bound-exciton luminescence and free-exciton reflectance resonances. The morphology of Zn-terminated surfaces is dominated by lateral etching which has a tendency to reduce roughness and improve luminescence and reflectance characteristics.

Differences in the efficacy of cleaning for each polar face is explored through the analysis of AFM force-displacement plots and lateral force microscopy. The data show that the O-terminated face is strongly hydrophilic (as also seen in the etching behaviour) and that fluid layers of significant thickness can form on this face in ambient conditions. In comparison, the fluid layers present on the hydrophobic Zn-terminated surfaces are approximately half as thick or less.

Finally the reflectance spectra of polycrystalline thin film and bulk ZnO wafers are modelled using a semi-classical model of the exciton-polariton interaction. A two-band dielectric response function is found to adequately describe the excitonic resonances, and the effects of Fabry-Perot oscillations in the thin film material are examined.

List of Acronyms

ABC	*Additional Boundary Condition*
ADC	*Analogue-to-Digital Converter*
AFM	*Atomic Force Microscopy*
BE	*Bound-Exciton*
FE	*Free-Exciton*
FT	*Fourier Transform*
HAc	*Acetic Acid* (CH_3COOH)
HT	*Hydrothermal*
ISA	*Ironed Surface Area*
LFM	*Lateral Force Microscopy*
PID	*Proportional/Integral/Differential*
PL	*Photoluminescence Spectroscopy*
PLD	*Pulsed Laser Deposition*
RC	*Rocking Curve*
RF	*Reflectance Spectroscopy*
RMS	*Root Mean Square*
SD	*Standard Deviation*
STM	*Scanning Tunnelling Microscopy*
SVPT	*Seeded Vapour Phase Transport*
XRD	*X-ray Diffraction*

Chapter 1

Introduction

1.1 Introduction

Zinc oxide is a group II-VI wide direct band-gap semiconductor (~ 3.4 eV at room temperature [1]) that has been extensively studied for many years. Although the main technical applications of this material were initially related to its high luminescent efficiency and uses in power electronics [2-4], ZnO has also found extensive use in the cosmetics industry and is a major component of antiseptic creams and UV-blocking lotions. More recently ZnO has re-emerged as a leading candidate semiconductor for UV and blue light emitting devices, primarily as a result of its strong exciton binding energy (~ 60 meV) [5]. Excitonic recombination in ZnO will persist to well beyond room temperature due to this large binding, and therefore the material offers an efficient means of producing short-wavelength light under low excitation intensity in practical devices. For the purposes of comparison, the exciton binding energy of GaN is ~ 25 meV [6]. ZnO is also a promising material for spintronics applications if doped with magnetic impurities [7,8].

Developments in ZnO have been relatively rapid over the last decade or so, partially as a result of the availability of high-quality, large-area substrates grown by hydrothermal [9] and vapour-phase transport [10] methods, and also because high quality ZnO thin films can be grown by various techniques such as MBE, PLD, MOCVD, etc. [11-18]. Much of the recent work has involved growth of such thin films and also nano-scale materials based on ZnO, such as nanotubes [19], nanowires [20], and nanobelts [21]. Optically pumped lasing has been reported in ZnO platelets [22], thin films [23], clusters consisting of nanocrystals [24], and nanowires [25], and a homo-structural ZnO p-n junction has been reported [26].

Perhaps the major impediment to the production of photonic devices using ZnO is the p-type doping issue. It has proved very difficult to reliably dope ZnO p-type to the high concentrations and carrier mobility required for devices. There are a number of

reasons for this. Nominally undoped ZnO is actually quite highly n-type (~10^{16} cm^{-3}), although the origin of this behaviour is still largely under debate. This n-type conductivity has been conventionally attributed to intrinsic defects such as Zn interstitials and O vacancies [27], but recent first-principles investigations have suggested that none of the native defects exhibits characteristics consistent with a high-concentration shallow donor [28]. Ubiquitous extrinsic defects, primarily hydrogen, have been subsequently suggested as the source of the n-type behaviour [29]. ZnO also has a low acceptor solid solubility and high acceptor activation energies (~ 200 meV), and therefore only a small fraction of the total are ionised to create free holes at room temperature.

A number of avenues have been tried in order to obtain high levels of p-type doping - annealing at temperatures above 600°C in suitable gaseous environments can remove H from the crystal [30], and the use of Group V elements on the O site which generally have smaller activation energies than Group I elements on the Zn site (for example, Li is a deep amphoteric defect). A number of authors have shown that doping with N acceptors results in higher resistivity ZnO thin films [31,32], and that these acceptors are compensated by donor defects [33]. N is a main p-type contender as its size is the best match for replacing O with minimal strain. Limited success at creating p-type ZnO has also been reported using a co-doping mechanism involving both Ga (a donor) and N [34,35], where the addition of the donor in conjunction with the acceptor helps to overcome the solubility limits of the material [36-40]. The most recent, and promising technique, is the growth of lattice-matched ZnO thin films on various substrates to reduce the concentration of intrinsic defects. Progress has been slow but recently, for the first time, reproducible p-type doping and homo-junction production has been reported using PLD growth on lattice-matched SCAM ($ScAlMgO_4$) substrates, with N acceptors and a varying temperature deposition technique [41]. It now appears that the p-type problem has reached the beginning of the end for ZnO.

Another important issue that remains a topic of considerable scientific interest, and is of central concern to this thesis, relates to the stability of the polar faces of bulk ZnO wafers. ZnO crystallises in the hexagonal wurtzite structure where each oxygen or zinc atom is respectively located at the centre of a zinc or oxygen distorted tetrahedron. One observes an O-Zn bi-layer stacked in a direction parallel to the *c*-axis of the crystal and, when sliced perpendicular to this axis, one obtains both (0001) Zn-terminated and $(000\bar{1})$ O-terminated polar surfaces on opposite sides of the wafer [27]. In bulk material the inter-planar distances are equal to 0.61 Å inside the bi-layer and 1.99 Å between bi-layers [42].

In 1979, *P. W. Tasker* published a seminal paper regarding the surface properties of ionic crystals [43] and (0001)-terminated ZnO is a 'type III' material in *Tasker*'s parlance [42] – the polar surfaces are charged, having a dipole moment in the repeat unit perpendicular to the surface and should therefore reconstruct to reduce the overall electrostatic energy. We shall consider that each layer in ZnO consists of either positive Zn or negative O ions, where the magnitude of the charge density of each layer is σ. To determine the total dipole moment density *M* arising as a result of the bulk crystal, one sums the individual dipole moments of each layer (*Figure 1.1*). The total dipole moment density is therefore;

$$M_{BULK} = N\sigma(R_1)$$

Eqn. 1.1

where *N* is the number of these double-layers through the crystal.

This dipole moment and associated electric field means that the electrostatic energy of unreconstructed, bulk-terminated crystals diverge with thickness. Most polar surface crystals (e.g. (111) GaAs) reconstruct their faces to eliminate this electric field and associated electrostatic energy. However, surface science studies tend to indicate a bulk-like surface termination for the (0001) ZnO polar faces, resulting in a hard-to-explain scenario of a stable, high-energy surface termination. Three possible explanations have been proposed; a charge transfer by carrier transport within the

sample [42,44,45], by selective atomic loss and gain at the O- and Zn-terminated faces [46], or through adsorption of charged impurities [44,47]. In order to cancel out the macroscopic dipole moment associated with the unreconstructed ZnO slab, one must transfer a charge σ' between the two faces, and the dipole associated with this charge must cancel that of the unreconstructed slab. Hence;

$$N\sigma'(R_1 + R_2) = N\sigma R_1$$

Eqn. 1.2

and this leads to the stability condition;

$$\sigma' = \frac{\sigma R_1}{R_1 + R_2}$$

Eqn. 1.3

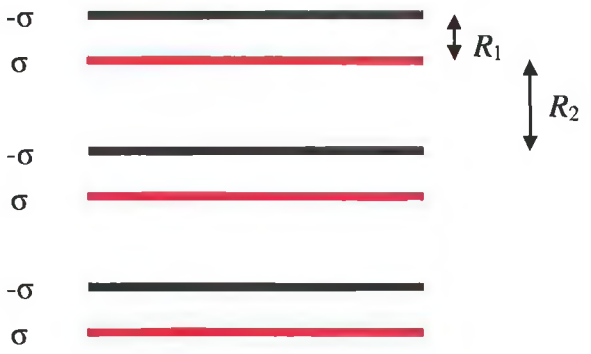

Figure 1.1: *Illustration of the bi-layer structure of ZnO. To determine the dipole moment density arising from the bulk material, one sums the contribution of the N bi-layers through the crystal, and the total dipole moment density is therefore given by Eqn. 1.1.*

Using the values for ZnO of 0.61 Å for R_1 and 1.99 Å for R_2, *Eqn. 1.3* predicts that the polar surfaces will be stable if $\sigma' \approx 0.25\sigma$ or in words, if the surface charge density after charge transfer is approximately three-quarters of the bulk reconstruction charge density. An understanding of this stabilisation mechanism in ZnO is essential as the O-terminated surface has potential for bio-sensing applications [48].

Of particular relevance to this dissertation is the third of the above proposed stabilisation mechanisms, involving charged impurity atoms. *Staemmler et al.* [47] have demonstrated that the O-terminated face shows a significant H coverage even in UHV conditions, and in Ref. [44] stabilisation involving H adsorption on the O-terminated face and OH adsorption on the Zn-terminated face is considered. In *Chapter 3* the efficacy of cleaning procedures is examined and it is found that O-terminated faces have a higher density of particulate material attached after cleaning than Zn-terminated faces. These differences are attributed to the trapping of such material by adsorbed fluid layers (*Chapter 4*), and analysis of force-displacement curves suggests that the fluid layers are approximately twice as thick for O-faces as for Zn-surfaces. Thus, there appears to be a correlation between proposed surface stabilisation mechanisms, experimental data obtained in UHV, and the experiments discussed herein which were conducted in ambient conditions. The presence of charged water layers, at pressures ranging from ambient atmospheric to UHV, could have important consequences for the processing of ZnO faces and may explain some of the inconsistencies in the literature as to which surface termination is optimal for epitaxial growth [17,49,50].

A substantial body of knowledge exists regarding the optical properties of ZnO from photoluminescence (PL), reflectance and other measurements. PL involves the optical excitation of electrons to the conduction band and subsequent observation of the emitted light as carriers recombine. There are various recombination paths, details of which are given by *Basu* [51], but only those that are radiative are of interest since the emitted photons can be detected. *Figure 1.2* is a summary of some of these paths.

ZnO exhibits a large number of bound-exciton (BE) emission lines that span a relatively narrow energy range (~ 3.35 to 3.37 eV) [52]. Each of these features is accompanied by transitions from excited 'rotator' states, analogous to rotational states of the H_2 molecule [53-55]. The so-called 'green band' (~ 2.0 – 2.8 eV), associated with transitions from deep levels, is also widely observed in both polycrystalline and bulk material [56-60]. The BE lines and green band shall be discussed in detail in *Chapter 3*,

where photoluminescence data for ZnO wafers grown by three separate companies is presented, along with the identification and correlation of observed features with the literature.

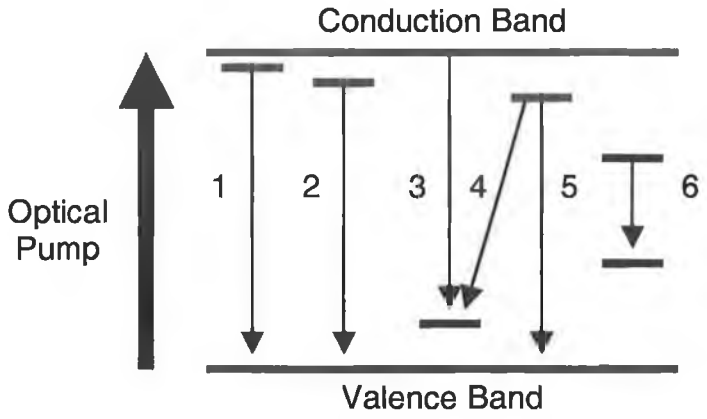

Figure 1.2: *Illustration of a number of recombination paths for carriers in semiconductors. 1 – free exciton (FE); 2 – bound exciton (BE); 3 – electron to acceptor (e,A); 4 – donor to acceptor (D,A); 5 – hole to donor (h,D); 6 – impurity or defect internal transition*

J. A. Sans et al. have shown that the absorption coefficient of a film of ZnO deposited on mica is approximately 2×10^5 cm^{-1} [61]. This value gives a penetration depth of ~ 50 nm for the 325 nm HeCd line used to excite carriers in the case of the PL results presented here, and the technique is therefore only sensitive to defects lying close to the surface layers of ZnO samples. One might consequently expect that different surface preparations could have an impact on obtained PL spectra. *Suscavage et al.* demonstrated that increases in the intensity of near band-edge luminescence at room temperature were the result of a reduction in sub-surface strain due to the application of a chemo-mechanical polishing technique to the polar faces of ZnO, as opposed to a purely mechanical polish [62]. In this thesis, PL techniques and reflectance spectroscopy are used in combination with AFM techniques to study ZnO wafers before and after etching (*Chapters 3* and *5*).

Since many of the etching treatments used in this work involve sample immersion in low pH, hydrogen-rich solutions, we have also been interested in the effects on optical properties of H incorporation in samples. There has been much recent interest in the properties of hydrogen in ZnO and related oxides, particularly in relation to the p-type doping issue described above. Theoretical predictions suggest that interstitial atomic hydrogen will introduce a shallow donor state in ZnO [5,29,63,64], and these assertions are supported by experimental data for its muonium counterpart [65]. The presence of hydrogen during the growth or subsequent processing of ZnO can significantly affect the electrical and optical properties [66-71]. In particular, hydrogen appears to passivate the surfaces of ZnO and increase the intensity of BE PL features.

To summarise briefly, there is experimental evidence that the photoluminescence of ZnO wafers is at least partially influenced by the 'quality' of the crystal surfaces and also by the incorporation of hydrogen into surface layers. That there is also experimental evidence for the stabilisation of the polar faces through adsorption of H or hydroxyl groups suggests that there may be a broader relationship between optical properties of as-received ZnO wafers, the surface preparation techniques that have been applied to the faces, and the resultant ability of the surfaces to stabilise as a result of contributions from adsorbed charged impurity atoms.

To my knowledge no such link has been previously proposed or investigated and, to this end, the effects of morphology changes, induced using wet chemical etchants and quantified by atomic force microscopy, on the optical properties of the polar surfaces are examined in *Chapter 5*. Since the O-terminated surfaces are found to be hydrophilic, they are vertically etched much more rapidly by acidic solutions (with high concentrations of H^+ cations) than the Zn-terminated faces [72], although lateral etching [73] occurs on both faces. This anisotropy allows the optical properties of Zn-terminated surfaces to be improved as the relatively low vertical-to-lateral etch ratio has a tendency to smooth topographic variations across this polar face. In some cases, O-faces showing extensive topographic damage after etching with low pH acids exhibit

unusually intense optical features when compared to the effects of weaker solutions. This behaviour is attributed to the incorporation of H into the surface layers.

A particularly useful optical technique, and one that is extensively discussed in this thesis, is reflectance spectroscopy (RF). RF simply involves the shining of white light onto a sample and the subsequent spectral analysis of the light reflected from its surface. In wavelength regions between ~ 360 - 370 nm the exciton-polariton interaction is observed for ZnO, where in-coming photons couple to free-excitons and resonance features are seen in the reflectance data. *Hopfield* and *Thomas* [74] have provided a semi-classical model for this interaction that assumes free-excitons behave as harmonic oscillators. At optical frequencies close to the natural frequency of these oscillators one finds that the coupling alters the dielectric constant of the material and hence the refractive index. Since the reflectance of the surface is related to the refractive index through the Fresnel equations, analysis and modelling of reflectance data can provide valuable information about the properties of free-excitons. In the late 1970s and early 80s, *Lagois* used the theory of *Hopfield* and *Thomas* to model the reflectance of single crystal ZnO [75,76]. However, there is little published data regarding the reflectance of polycrystalline ZnO material and in *Chapters 6* and *7* the semi-classical theory is described and used to model the reflectance spectra obtained from a reference bulk crystal and a polycrystalline ZnO thin film grown using the Pulsed Laser Deposition technique (PLD). ZnO has three valence bands derived from the three p-orbitals of Zn and O [77-79], referred to as Γ_7, Γ_9 and Γ_7 using group theoretical symmetry notations. One generally observes reflectance resonances corresponding to excitons with holes from the Γ_7, Γ_9 and Γ_7 valence bands, and these are called *A*, *B*, and *C* excitons respectively in order of increasing energy (*Figure 1.3*).

In order to model the exciton-polariton interaction, near-normal angles of incidence were used to obtain reflectance spectra. With this geometry only transverse modes propagate in the crystal, which reduces the analysis in *Chapter 7* to solving a system of simultaneous equations in one spatial dimension only. At non-normal

incidence both longitudinal and transverse modes can propagate, and the modelling would require a more complicated analysis that would need to account for the angle of incidence itself. Nevertheless, excitonic resonances are still apparent in reflectance spectra at non-normal incidence and reflectance with this geometry is also used to investigate free-exciton properties, in conjunction with PL, for etched and unetched bulk samples.

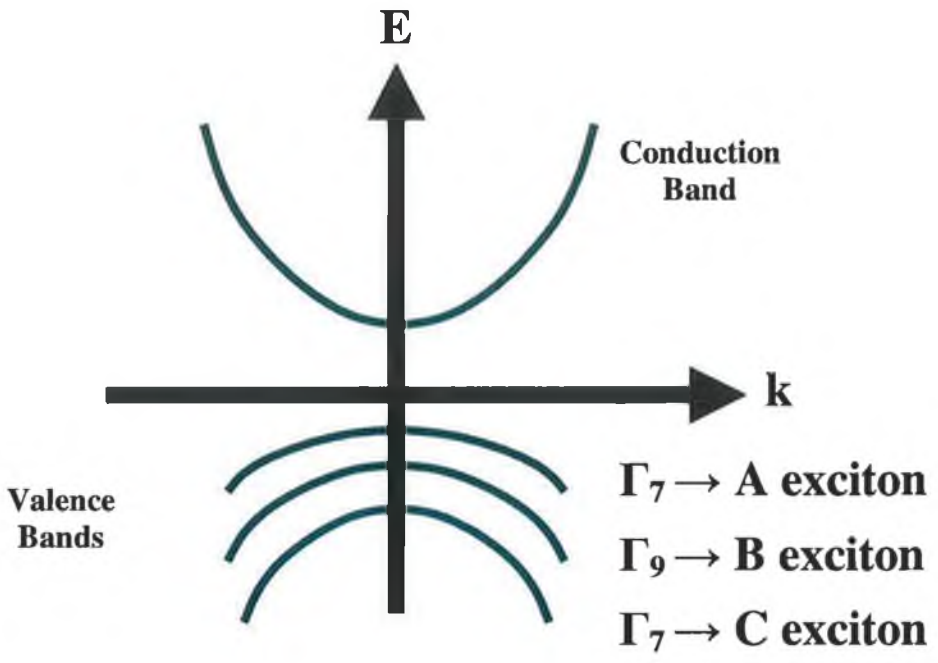

Figure 1.3: *Illustration of the valence band splitting observed in ZnO. In reflectance spectra, one generally observes excitonic resonances corresponding to each band for bulk material.*

In the next chapter the experimental apparatus shall be discussed. For the examination of the effects of adsorbed fluid layers and etchant solutions on the polar faces of ZnO it was necessary to use atomic force microscopy (AFM) techniques [80]. AFM provides high vertical resolutions, relatively rapid acquisition of data and does not require any significant preparation of surfaces. This latter point is particularly relevant since maintaining the integrity of faces is vital for a correlation between the surface morphology and optical characteristics of given ZnO wafers. The experimental apparatus used for optical photoluminescence and reflectance measurements is also

described in *Chapter 2*, along with a description of the operation of Fourier Transform (FT) spectrometers in short-wavelength regions. In the case of reflectance spectroscopy, the discussion in this chapter relates to a general 'all-purpose' arrangement of the apparatus used to examine excitonic resonances in etched material where the intensity of reflected light is poor due to the damaged surfaces.

1.2 References

[1] D. C. Look, *Mater. Sci. Eng. B* **80** (2001) 383

[2] P. R. Emtage, *J. Appl. Phys.* **48** (1977) 4372

[3] R. Einzinger, *Appl. Surf. Sci.* **3** (1979) 5372

[4] L. F. Lou, *J. Appl. Phys.* **50** (1979) 555

[5] C. G. Van der Walle, *Physica B* **308-310** (2001) 899

[6] B. Monemar, *Phys. Rev. B* **10** (1974) 676

[7] T. Fukumura, Z. Jin, A. Ohtomo, H. Koinuma, and M. Kawasaki, *Appl. Phys. Lett.* **75** (1999) 3366

[8] K. Sato and H. Katayama-Yoshida, *Physica E* **10** (2001) 251

[9] N. Sakagami and K. Shibayama, *Jpn. J. Appl. Phys.* **20** (1981) 201

[10] D. C. Look, D. C. Reynolds, J. R. Sizelove, R. L. Jones, C. W. Litton, G. Cantwell, and W. C. Harsch, *Solid State Commun.* **150** (1998) 399

[11] H. J. Ko, Y. F. Chen, Z. Zhu, T. Yao, I. Kobayashi, and H. Uchiki, *Appl. Phys. Lett.* **76** (2000) 1905

[12] H. Kato, M. Sano, K. Miyamoto, and T. Yao, *J. Crystal Growth* **237-239** (2002) 538

[13] E. McGlynn, J. Fryar, G. Tobin, C. Roy, M. O. Henry, J.-P. Mosnier, E. de Posada, and J. G. Lunney, *Thin Solid Films* **458** (2004) 330

[14] X. W. Sun and H. S. Kwok, *J. Appl. Phys.* **86** (1999) 408

[15] F. Vigué, P. Vennégues, S. Vézian, M. Laügt, and J.-P. Faurie, *Appl. Phys. Lett.* **79** (2001) 194

[16] T. Makino, G. Isoya, Y. Segawa, C. H. Chia, T. Yasuda, M. Kawasaki, A. Ohtomo, K. Tamura, and H. Koinuma, *J. Crystal Growth* **214/215** (2000) 289

[17] T. P. Smith, H. McLean, D. J. Smith, and R. F. Davis, *J. Crystal Growth* **265** (2004) 390

[18] K. Iwata, P. Fons, S. Niki, A. Yamada, K. Matsubara, K. Nakahara, and H. Takasu, *Phys. Stat. Sol. (a)* **180** (2000) 287

[19] Y. J. Xing, Z. H. Xi, Z. Q. Xue, X. D. Zhang, J. H. Song, R. M. Wang, J. Xu, Y. Song, S. L. Zhang, and D. P. Yu, *Appl. Phys. Lett.* **83** (2003) 1689

[20] M. H. Huang, Y. Wu, H. Feick, N. Tran, E. Weber, and P. Yang, *Adv. Mater.* **13** (2001) 113

[21] X. Y. Kong and Z. L. Wang, *Appl. Phys. Lett.* **84** (2004) 975

[22] D. C. Reynolds, D. C. Look, and B. Jogai, *Solid State Commun.* **99** (1996) 873

[23] D. M. Bagnall, Y. F. Chen, Z. Zhu, T. Yao, S. Koyama, M. Y. Shen, and T. Goto, *Appl. Phys. Lett.* **70** (1997) 2230

[24] H. Cao, J. Y. Xu, E. W. Seelig, and R. P. H. Chang, *Appl. Phys. Lett.* **76** (2000) 2997

[25] M. H. Huang, S. Mao, H. Feick, H. Yan, Y. Wu, H. Kind, E. Weber, R. Russo, and P. Yang, *Science* **292** (2001) 1897

[26] T. Aoki, Y. Hatanaka, and D. C. Look, *Appl. Phys. Lett.* **76** (2000) 3257

[27] For a review see G. Heiland, E. Mollwo, and F. Stöckmann in *Solid State Physics,* edited by F. Seitz and D. Turnbull (Academic, New York, 1959), vol. 8, p. 191.

[28] A. F. Kohan, G. Ceder, D. Morgan, and C. G. Van de Walle, *Phys. Rev. B* **61** (2000) 15019

[29] C. G. Van de Walle, *Phys. Rev. Lett.* **85** (2000) 1012

[30] K. Ip, M. E. Overberg, Y. W. Heo, D. P. Norton, S. J. Pearton, C. E. Stutz, S. O. Kucheyev, C. Jagadish, J. S. Williams, B. Luo, F. Ren, D. C. Look, and J. M. Zavada, *Sol. Stat. Elect.* **47** (2003) 2255

[31] K. Iwata, P. Fons, A. Yamada, K. Matsubara, and S. Niki, *J. Crystal Growth* **209** (2000) 526

[32] X. Wang, S. Yang, J. Wang, M. Li, X. Jiang, G. Du, X. Liu, and R. P. H Chang, *J. Crystal Growth* **226** (2001) 123

[33] E.-C. Lee, Y.-S. Kim, Y.-G. Jin, and K. J. Chang, *Physica B* **308-310** (2001) 912

[34] M. Joseph, H. Tabata, H. Saeki, K. Ueda, and T. Kawai, *Physica B* **302-303** (2001) 140

[35] K. Nakahara, H. Takasu, P. Fons, A. Yamada, K. Iwata, K. Matsubara, R. Hunger, and S. Niki, *J. Crystal Growth* **237-239** (2002) 503

[36] T. Yamamoto and H. Katayama-Yoshida, *J. Crystal Growth* **214/215** (2000) 552

[37] T. Yamamoto and H. Katayama-Yoshida, *Physica B* **302-303** (2001) 155

[38] T. Yamamoto, *Thin Solid Films* **420-421** (2002) 100

[39] S. B. Zhang, S.-H. Wei, and Y. Yan, *Physica B* **302-303** (2001) 135

[40] M. Komatsu, N. Ohashi, I. Sakaguchi, S. Hishita, and H. Haneda, *Appl. Surf. Sci.* **189** (2002) 349

[41] A. Tsukazaki, A. Ohtomo, T. Onuma, M. Ohtani, T. Makino, M. Sumiya, K. Ohtani, S. F. Chichibu, S. Fuke, Y. Segawa, H. Ohno, H. Koinuma, and M. Kawasaki, *Nature Materials* **4** (2005) 42

[42] C. Noguera, *J. Phys.: Condens. Matter* **12** (2000) R367

[43] P. W. Tasker, *J. Phys. C: Solid State Phys.* **12** (1979) 4977

[44] A. Wander and N. M. Harrison, *J. Chem. Phys.* **115** (2001) 2312

[45] A. Wander, F. Schedin, P. Steadman, A. Norris, R. McGrath, T. S. Turner, G. Thornton, and N. M. Harrison, *Phys. Rev. Lett.* **86** (2001) 3811

[46] N. Jedrecy, M. Sauvage-Simkin, and R. Pinchaux, *Appl. Surf. Sci.* **162-163** (2000) 69

[47] V. Staemmler, K. Fink, B. Meyer, D. Marx, M. Kunat, S. Gil Girol, U. Burghaus, and C. H. Wöll, *Phys. Rev. Lett.* **90** (2003) 106102

[48] K. Ogata, T. Komuro, K. Hama, K. Koike, S. Sasa, M. Inoue, and M. Yano, *Phys. Stat. Sol. (b)* **241** (2004) 617

[49] S. Zhu, C.-H. Su, S. L. Lehoczky, M. T. Harris, M. J. Callahan, P. McCarty, and M. A. George, *J. Cryst. Growth* **219** (2000) 361

[50] F. Hamdani, M. Yeadon, D. J. Smith, H. Tang, W. Kim, A. Salvador, A. E. Botchkarev, J. M. Gibson, A. Y. Polyakov, M. Skowronski, and H. Morkoç, *J. Appl. Phys.* **83** (1998) 983

[51] P. K. Basu in *Theory of Optical Processes in Semiconductors (Bulk and Microstructures)*, (Oxford Science Publications, 1997), chapter 10, p. 205

[52] D. C. Reynolds, C. W. Litton, and T. C. Collins, *Phys. Rev.* **140** (1965) 1726

[53] A. Schildknecht, R. Sauer, and K. Thonke, *Physica B* **340-342** (2003) 205

[54] K. Thonke, Th. Gruber, N. Teofilov, R. Schönfelder, A. Waag, and R. Sauer, *Physica B* **308-310** (2001) 945

[55] D. C. Reynolds, D. C. Look, B. Jogai, C. W. Litton, T. C. Collins, W. Harsch, and G. Cantwell, *Phys. Rev. B* **57** (1998) 12151

[56] R. Dingle, *Phys. Rev. Lett.* **23** (1969) 579

[57] H.-J. Egelhaaf and D. Oelkrug, *J. Crystal Growth* **161** (1996) 190

[58] X. L. Wu, G. G. Siu, C. L. Flu and H. C. Ong, *Appl. Phys. Lett.* **78** (2001) 2285

[59] S.-S. Chang, G. J. Choi, H. J. Park, M. E. Stora, and R. E. Hummel, *Mater. Sci. Eng. B* **83** (2001) 29

[60] K. Vanheusden, C. H. Seager, W. L. Warren, D. R. Tallant, and J. A. Voigt, *Appl. Phys. Lett.* **68** (1996) 403

[61] J. A. Sans, A. Segura, M. Mollar, and B. Marí, *Thin Solid Films* **453-454** (2004) 251

[62] M. Suscavage, M. Harris, D. Bliss, P. Yip, S.-Q. Wang, D. Schwall, L. Bouthillette, J. Bailey, M. Callahan, D. C. Look, D. C. Reynolds, R. L. Jones, and C. W. Litton, *MRS Internet J. Nitride Semicond. Res.* **4S1** (1999) G3.40

[63] C. Kilic and Z. Zunger, *Appl. Phys. Lett.* **81** (2002) 73

[64] D. M. Hofmann, A. Hofstaetter, F. Leiter, H. Zhou, F. Henecker, B. K. Meyer, S. B. Schmidt and P. G. Baranov, *Phys. Rev. Lett.* **88** (2002) 045504

[65] S. J. F. Cox, E. A. Davis, S. P. Cottrell, P. J. C. King, J. S. Lord, J. M. Gil, H. V. Alberto, R. C. Vilão, D. J. P. Duarte, N. A. de Campos, A. Weidinger, R. L. Lichti and S. J. C. Irving, *Phys. Rev. Lett.* **86** (2001) 2601

[66] B. Theys, V. Sallet, F. Jomard, A. Lusson, J.-F. Rommeluere, and Z. Teukam, *J. Appl. Phys.* **91** (2002) 3922

[67] S. O. Kucheyev, P. N. K. Deenapannay, C. Jagadish, J. S. Williams, M. Yano, K. Koike, S. Sasa, M. Inoue, and K. Ogata, *Appl. Phys. Lett.* **81** (2002) 3350

[68] N. Ohashi, T. Ishigaki, N. Okada, T. Sekiguchi, I. Sakaguchi and H. Haneda, Appl. Phys. Lett. **80** (2002) 2869

[69] C. S. Han, J. Jun and H. Kim, *Appl. Surf. Sci.* **175/176** (2001) 567

[70] Y. Natsume and H. Sakata, *J. Mater. Sci.: Materials in Electronics* **12** (2001) 87

[71] K. Ip, M. E. Overberg, Y. W. Heo, D. P. Norton, S. J. Pearton, S. O. Kucheyev, C. Jangadish, J. s. Williams, R. G. Wilson, and J. M. Zavada, *Appl. Phys. Lett.* **81** (2002) 3996

[72] A. N. Mariano and R. E. Hanneman, *J. Appl. Phys.* **34** (1963) 384

[73] H. Maki, T. Ikoma, I. Sakaguchi, N. Ohashi, H. Haneda, J. Tanaka, and N. Ichinose, *Thin Solid Films* **411** (2002) 91

[74] J. J. Hopfield and D. G. Thomas, *Phys. Rev.* **132** (1963) 563

[75] J. Lagois, *Phys. Rev. B* **16** (1977) 1699

[76] J. Lagois, *Phys. Rev. B* **23** (1981) 5511

[77] B. K. Meyer, H. Alves, D. M. Hofmann, W. Kriegseis, D. Forster, F. Bertram, J. Christen, A. Hoffmann, M. Straburg, M. Dworzak, U. Haboeck, and A. V. Rodina, *Phys. Stat. Sol. (b)* **241** (2004) 231

[78] D. C. Reynolds, D. C. Look, B. Jogai, C. W. Litton, G. Cantwell, and W. C. Harsch, *Phys. Rev. B* **60** (1999) 2340

[79] B. Gil, *Phys. Rev. B* **64** (2001) 201310

[80] G. Binnig, C. F. Quate, and C. Gerber, *Phys. Rev. Lett.* **56** (1986) 930

Chapter 2

Experimental Apparatus

2.1 *Constant-Force Contact Atomic Force Microscopy*

A Digital Instruments (now Veeco) Nanoscope IIIa AFM system with a Dimension 3100 controller was used to examine the polar faces. In contact-mode AFM a small tip, attached to the end of a cantilever, is brought into direct contact with a surface. Laser light is reflected from the back of the cantilever and a split photodiode monitors its vertical deflection as the tip is scanned across the sample. In constant-force operation the user defines a 'deflection set-point' that relates to the differential voltage output of the split photodiode, and hence the cantilever deflection and magnitude of force applied to the face [1]. An electronic feedback loop causes piezoelectric scanners to adjust the height of the cantilever assembly (Δz) in order to maintain this constant deflection. *Figure 2.1* is an illustration of the constant-force AFM system.

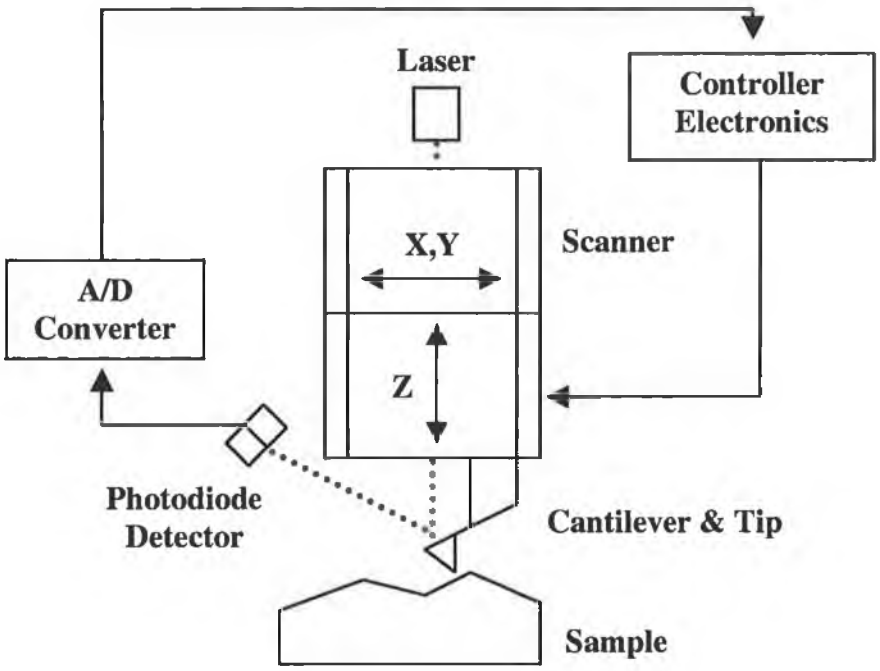

Figure 2.1: *Illustration of Contact Mode AFM system. A laser is reflected from the cantilever and a split photodiode detector monitors the cantilever deflection as the tip is scanned across the surface. In constant-force operation the controller electronics attempt to maintain a constant cantilever deflection and the distance moved by the piezoelectric scanner in order to achieve this is proportional to the topographic height at each surface location.*

Figure 2.2 is an illustration of the optical system used for determining the cantilever deflection. The change in angle of reflected laser light as the cantilever interacts with surface topography is monitored by the split photodiode, and the output from each segment is collected by a differential amplifier. If one refers to the output voltage from the lower diode as '*B*' and the upper as '*A*', changes in the deflection of the cantilever will alter the relative ratio of the intensity of light falling on each diode and hence their relative voltage output. It should be noted that in reality the diode has four segments, and though the significance of this shall be examined below with regard to Lateral Force Microscopy, it does not detract from the following discussion.

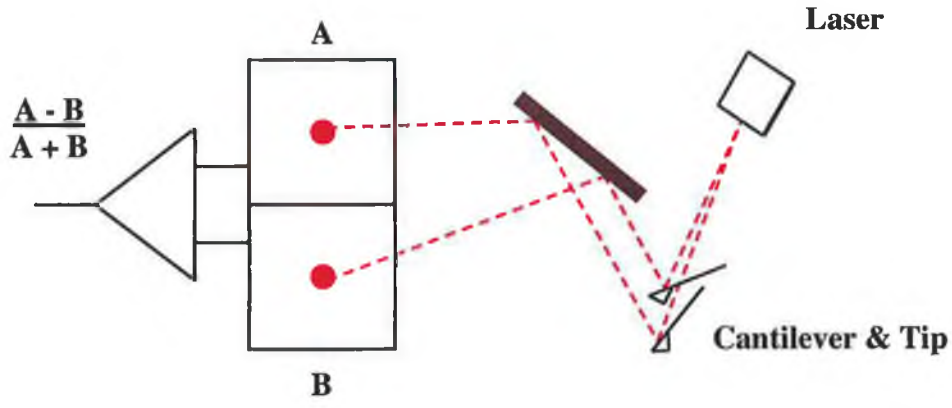

Figure 2.2: *Split photodiode and laser system used for determining AFM cantilever deflection. As the cantilever is deflected by topographic changes, the relative ratio of light falling on photodiode 'A' compared to diode 'B' is altered. The voltage from each is taken as an input into a differential amplifier, where the output is A-B / A+B.*

Figure 2.3 is a summary of the PID (Proportional, Integral, Differential) feedback control system for maintaining the constant cantilever deflection. Following the flow-diagram from the top-left in an anti-clockwise direction the user enters the deflection set-point, corresponding to the required ratio of photodiode voltages and hence the applied force. The differential amplifier attached to the split photodiode outputs an analogue signal;

$$Output_{Vertical} = \frac{A-B}{A+B}$$

Eqn. 2.1

from which this set-point is subtracted. The subtraction produces an error signal that is subsequently digitised by an analogue-to-digital converter. In the case of the integral section of the feedback loop, this digital error is multiplied by an integral gain value and added to an accumulator. In parallel with this process, the digital error is also simply multiplied by a proportional gain. Both the accumulated integral and proportional gain bits are summed and the result converted back to an analogue signal. This is sent to the piezoelectric scanner, altering the cantilever deflection, and completing the feedback loop. For a detailed description of the operation of PID controllers, see Ref. [2].

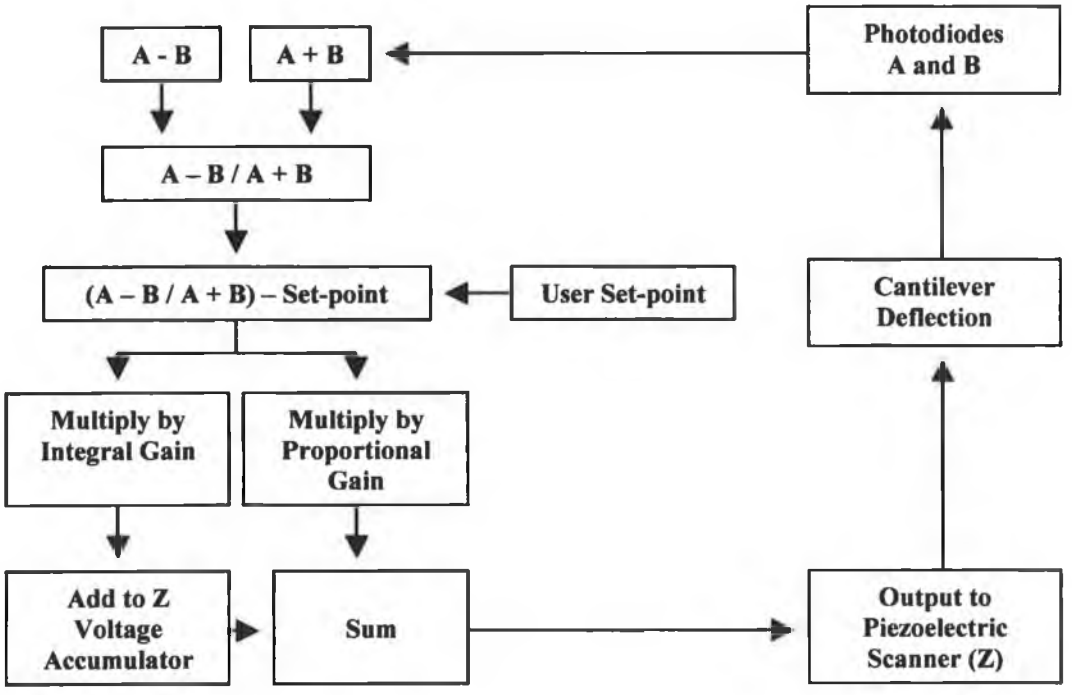

Figure 2.3: *PID feedback loop for maintaining constant deflection/force of AFM tip.*

The operation of constant-force AFM can be simply described using Hooke's Law. Given an ideally flat and hard surface the magnitude of the force F applied to the sample at any given (x,y) location, and correspondingly the magnitude of the reaction force acting on the cantilever itself, is given by;

$$|F| = kd$$

Eqn. 2.2

where k is the spring-constant of the cantilever and d is the initial height of the cantilever assembly above the surface required for the deflection to match the user-defined set-point. If one takes this hypothetical surface and adds or subtracts a topographic height of Δz, the total force applied to the sample or cantilever in this case will be;

$$|F| = k(d \pm \Delta z)$$

Eqn. 2.3

The addition or subtraction of surface height either increases or decreases the cantilever deflection and hence the applied force. Since the user defines the required force to be maintained by the PID controller, the piezoelectric scanners must move the tip a distance of $\mp \Delta z$, corresponding to the change in topography, towards or away from the sample surface to restore F to its original value. This sequence is illustrated in *Figure 2.4* for an increase in topographic height. The imaging of surface topography using constant-force contact AFM is therefore largely independent of the choice of spring-constant value for the cantilever or the choice of deflection set-point.

In the above description, the assumption was made that surfaces are hard. If surfaces elastically deform under the application of a force from the cantilever, the determination of topographic heights will be affected. In *Chapters 3, 4* and *5* images are presented of the etched and unetched surfaces of ZnO, but any errors in height determinations due to deformation of the surfaces are likely to be insignificant due to the hardness of the material [3] and relatively large scale of the features of interest.

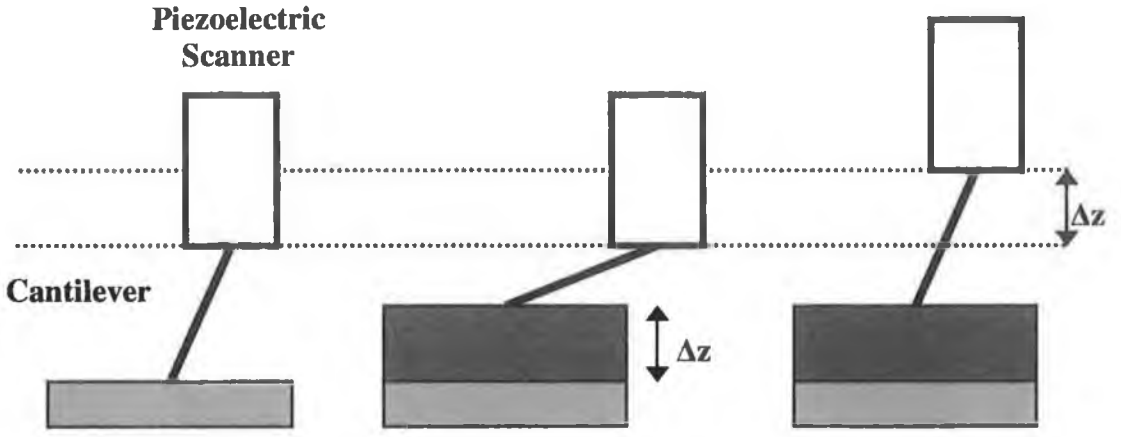

Figure. 2.4: *Illustration of the operation of constant-force contact AFM. In the first case (left) the cantilever applies a specific force to the sample. The reaction force causes a cantilever deflection and the piezoelectric scanners adjust the height until the deflection matches the user-defined deflection set-point. If a topographic feature of height Δz is now added (middle) the applied force and reaction force are increased, as is the cantilever deflection. To restore the original deflection the piezoelectric scanners must move a distance of Δz, equivalent to the change in topography (right).*

For the results presented in subsequent chapters, silicon nitride cantilevers with a gold reflective coating and tips of 20 – 60 nm radius of curvature were used. These were procured from the Veeco corporation [4]. Cantilevers are short in order to provide a high resonant frequency and thus lower their sensitivity to vibrational instabilities, but since they must also be deflected by very small forces, cantilevers are generally manufactured to be extremely thin. Each of the silicon nitride substrates used has four triangular cantilever probes with different spring-constants and sizes, as indicated in *Figure 2.5* and *Table 2.1* below [5].

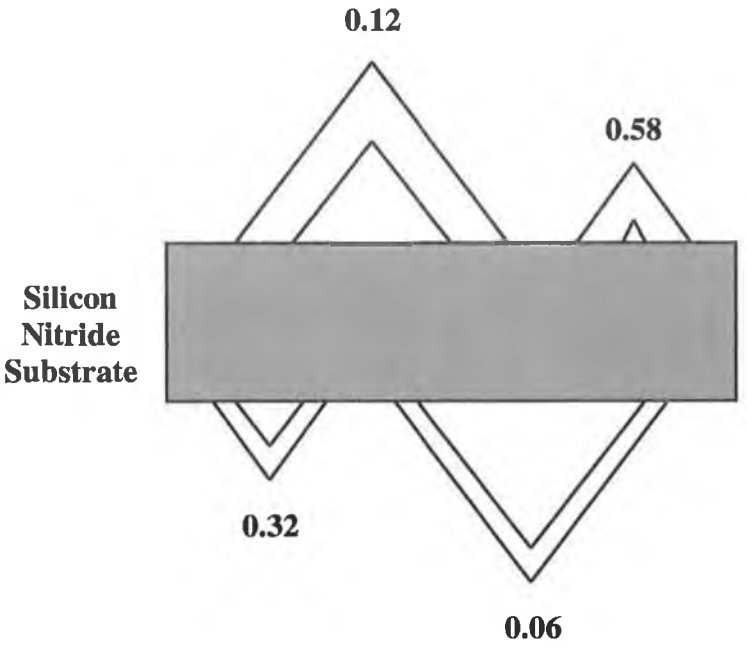

Figure 2.5: *Diagram of the four silicon nitride cantilevers per substrate showing spring-constants for each (units are N/m). Cantilevers are available in lengths of ~ 100 and ~ 200 μm, with either wide legs (top) or narrow legs (bottom).*

Table 2.1: *Cantilever data as supplied by Veeco* [5]. *The 'Cantilever Length' refers to the distance from the substrate to the apex of each triangular cantilever. For each cantilever length, there are two probes having different leg widths and hence different spring-constants.*

Cantilever Length (μm)	***Spring-Constant k (N/m) (narrow legs)***	***Nominal Resonant Frequency (kHz)***	***Spring-Constant k (N/m) (wide legs)***	***Nominal Resonant Frequency (kHz)***
115	0.32	56	0.58	57
196	0.06	18	0.12	20

It should be noted that the spring-constants in *Fig. 2.5* and *Table 2.1* are calculated by the manufacturer based on a cantilever thickness of 0.6 μm, although they state that the actual thickness ranges from 0.4 to 0.7 μm. Using this data one can calculate the possible deviation in spring-constants from this determined value. The spring-constant k is proportional to the cube of the cantilever thickness h [6];

$$k \propto h^3$$

Eqn. 2.4

Since the spring-constants shown in *Fig. 2.5* and *Table 2.1* are calculated on the basis of a 0.6 μm cantilever thickness, a proportionality constant A can be simply determined;

$$A = \frac{k}{\left(0.6 \times 10^{-6}\right)^3}$$

Eqn. 2.5

The values for this constant A are given in *Table 2.2*, along with the minimum and maximum calculated spring-constants taking the cantilever thickness h to be either 0.4 or 0.7 μm respectively. One finds that the actual value of spring-constant, compared to the value calculated by Veeco, could vary by as much as ± 66%.

Obtaining accurate spring-constants is a non-trivial exercise and the two most widely used techniques are the Cleveland and Sader methods. The Cleveland method involves monitoring the change in fundamental cantilever resonant frequency as known masses are added to the free end of the cantilever [7], whereas the Sader method involves measurement of the radial resonant frequency (and the quality factor of the resonant peak) for a cantilever immersed in fluid, usually air [8].

Table 2.2: *Determination of the range of possible values for spring-constants based on cantilever thickness values of 0.4 and 0.7 μm*

Calculated k (N/m) h = 0.6 μm	***Proportionality Constant A (N/m^4)***	***Calculated k (N/m) h = 0.4 μm***	***Calculated k (N/m) h = 0.7 μm***
0.06	2.77×10^{17}	0.02	0.10
0.12	5.56×10^{17}	0.04	0.19
0.38	1.76×10^{18}	0.11	0.60
0.58	2.68×10^{18}	0.17	0.92

However, a detailed calibration of the cantilevers is not necessary in the case of the AFM measurements on the polar oxygen- and zinc-terminated surfaces of ZnO, presented in *Chapters 3, 4* and *5*. The difference between the calculated and actual spring-constants will not dramatically affect topographic data, as discussed above in relation to constant-force contact mode, and although it has an impact on results obtained in relation to force-curve and friction determinations, results are directly comparable for each surface provided the same cantilever is used.

An important consideration, particularly with respect to the analysis of force curves, is the resonant frequency of each cantilever. Cantilevers with a nominal spring-constant of 0.06 and 0.12 N/m have resonant frequencies of 18 and 20 kHz respectively. In fact, due to the errors in determining the spring-constants, one might expect the resonant frequency of some cantilevers to be lower than these values. Observations have shown that such cantilevers are particularly sensitive to environmental disturbances such as audible noise in laboratories.

The Nanoscope IIIa AFM allows relatively large lateral scan sizes of up to ~ 60×60 μm with a maximum image resolution of 512×512 pixels. As with all AFM systems, although atomic resolution in certain operating modes can be achieved in terms of sensitivity to surface height (Δz), planar resolutions (x,y) are limited by the pixel field

size and tip radius. *Table 2.3* gives the typical scan sizes used along with the expected resolution based on this 512×512 matrix.

Table 2.3:

AFM Scan Width (μm)	*Number of Pixels*	*Expected Resolution (AFM scan width / no. of pixels) (μm / pixel)*
50	512	0.098
20	512	0.039
10	512	0.020
5	512	0.010

Given the resolution calculations in the above table, each pixel of image data will correspond to a region of almost 100 nm^2 if the scan size is set to 50×50 μm. An area of approximately 10 nm^2 is represented by each pixel for a 5×5 μm scan, although the actual resolution will depend on the tip radius (20 – 60 nm in the case of the measurements discussed below). Large scans will give a general indication of the surface topography but will not be capable of resolving changes over small regions. Reducing the scan area, on the other hand, will reveal these finer details but the images obtained may not necessarily be representative of the topography overall. This shall be discussed further in *Chapter 5*, where small-scale AFM images are used to investigate correlations between topographic features and large-scale optical properties.

Alternatively the 512×512 pixel field can be viewed as a rastered image of 512 lines, where the tip is scanned across each line in both directions (a 'trace' and 'retrace' line). The AFM images presented here were captured in either trace or retrace directions and in no case are the directions mixed for any given image. The typical scanning rates were set between 0.25 and 1 Hz, corresponding to a trace *and* retrace time per line of 4 seconds or 1 second respectively. While this rapidity of data acquisition is one of the

advantages of contact-mode AFM, high scan rates present a number of problems when considering the operation of the constant-force PID feedback.

At a scan rate of 1 Hz and a field size of 512×512 pixels, each pixel will take approximately 1 millisecond to image in either the trace or retrace directions. If a surface undergoing analysis is generally smooth the proportional and integral gains set by the user will enable the PID controller to make small adjustments to the piezoelectric scanner (Δz) to maintain the cantilever deflection at a constant value in times of less than the 1 millisecond required per pixel. If the tip encounters a sudden large change in topography relative to the flat surface these initial gain settings may no longer be sufficient and one may observe a subsequent increase in the time-constant required to settle at the set deflection. If the required deflection set-point is not achieved in less than 1 millisecond then adjoining pixels in the scanning direction (either trace or retrace) will appear at a false height.

This problem can be overcome by comparing both trace and retrace topographic data in real-time. In 'scope' mode, the piezoscanners are set to scan back and forth across a single line and a surface profile is displayed, as illustrated in *Figure 2.6*. The proportional and integral gain settings, as well as the deflection set-point and scanning rate, can be altered until the cantilever is following the topography in both trace and retrace line directions with minimal differences between each. If, as suggested above, the PID settings are not correctly set then data will appear at a false height on opposite sides of topographic features in the trace and retrace profiles.

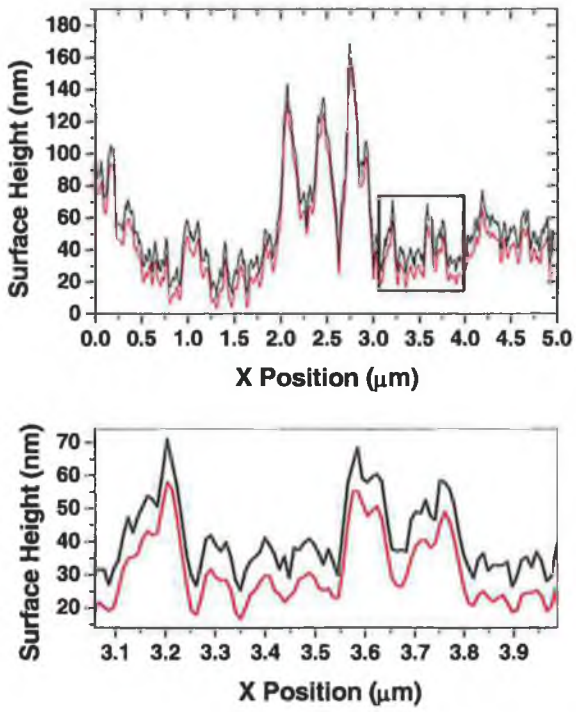

Figure 2.6: *The top figure shows profile data obtained in scope mode for a single line of a particular AFM image and is taken in real-time. The black profile represents the topographic height as a function of position on the surface in the trace direction, whereas the red profile is taken in the retrace direction. Optimisation of the PID gain settings, scan rate and deflection set-point can be achieved by ensuring that differences are minimal in each direction. The boxed region in the top figure is magnified below. Although the trace and retrace profiles are similar, there is a small vertical offset due to a slight hysteresis in the piezoelectric behaviour. This is largely inconsequential as it is the relative heights of features that are of interest in topographic scans.*

Generally, the piezoelectric (x,y) scanners do not maintain the cantilever assembly at a constant height above the sample during scanning, particularly when imaging large areas. *Figure 2.7* shows; *(a)* a 50×50 μm topographic image of the O-terminated surface of an Eagle-Picher ZnO wafer (to be discussed in *Chapter 3*); and *(b)* a horizontal profile scan across the centre of this image, illustrating piezoelectric 'bow' where lateral and vertical motions of the probe are coupled. The height of the cantilever above the surface changes as a second-order function of position and creates a false impression of the topographic height, but this can be removed by fitting a parabolic

function to each image line and subtracting this fit from the data. The 'flattened' image and profile are shown in *Figs. 2.7(c)* and *(d)* respectively.

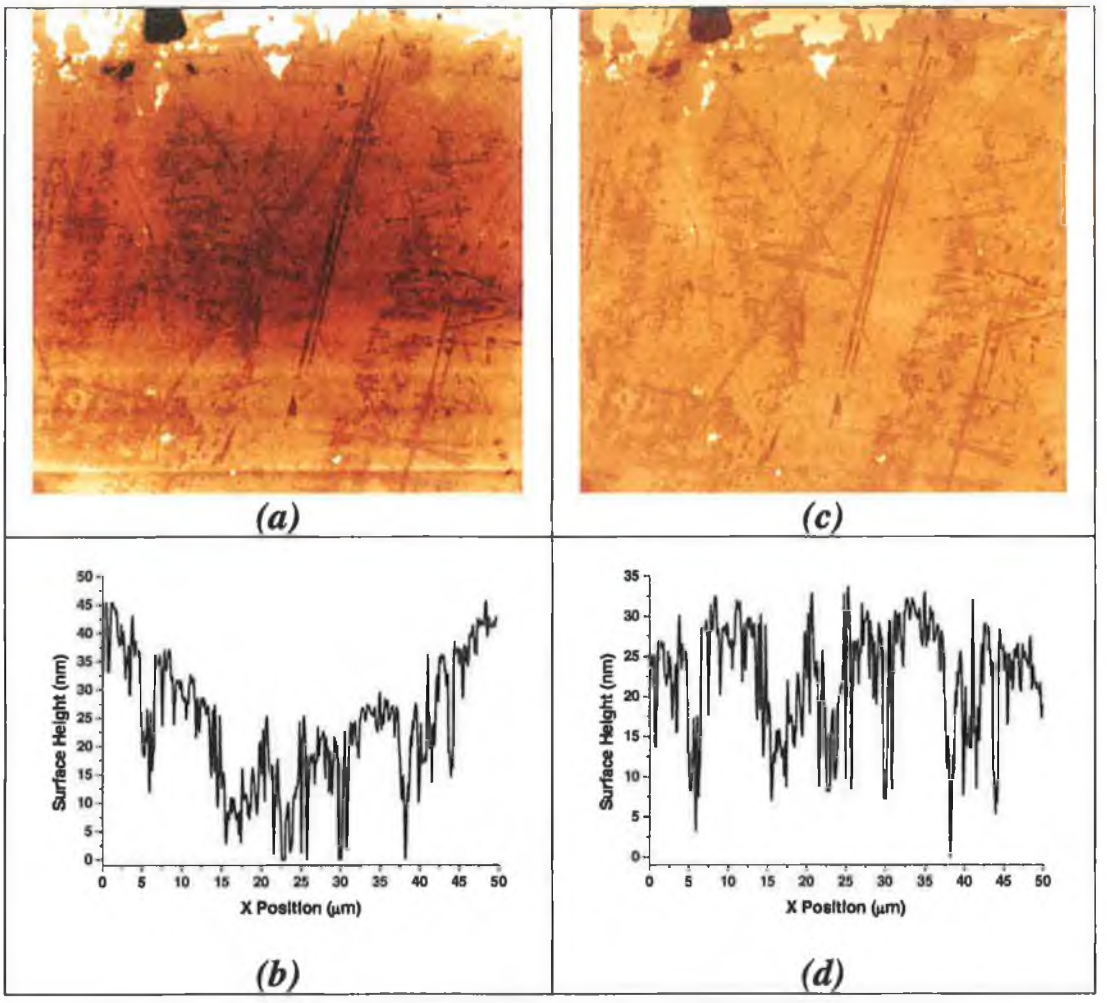

Figure 2.7: *Illustration of piezoelectric 'bow', where the height of the cantilever assembly above the surface changes as a second-order function of lateral position. In the first image (a) there is a distortion of surface heights caused by this effect, as shown by the profile in (b). Fitting a parabolic function to each line and subtracting this from the data 'flattens' the image, as shown in image (c) and profile (d).*

Over smaller scanning regions (< 5×5 μm) this bowing effect is not as significant. While each pixel on a given image line will have an associated height that is relative to the other pixels on that line, there may not be a direct relationship in height between one line and another. This can be caused, for example, by slight drifts of the laser position on the split photodiode during scanning, which effectively changes the determination of the zero cantilever deflection point. *Figure 2.8(a)* is a 5×5 μm image showing this effect. Fitting a straight line through the profile data of each image line and subsequently subtracting this linear fit from the height data flattens the image, as shown in *Figure 2.8(b)*.

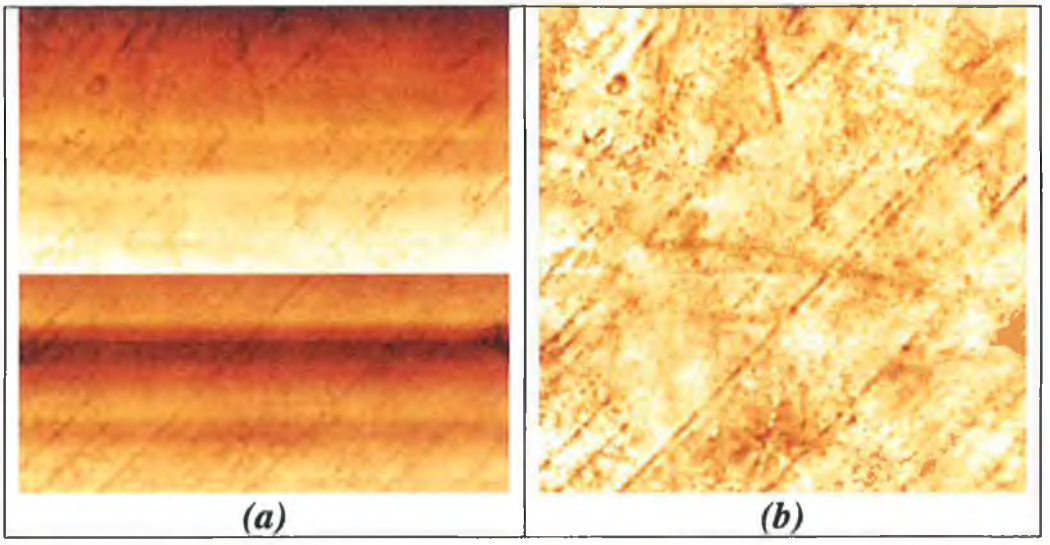

Figure 2.8: *Illustration of flattening using a first-order line fit. In image (a) each line contains pixels that have associated topographic heights relative to one another. However, a drifting of the laser spot on the split photodiode during scanning offsets the topographic height of each line with respect to the others. Taking each image line, fitting a linear function, and subtracting this from the data ensures that the heights of each line are normalised to one another (b).*

In terms of the AFM images presented in *Chapters 3*, *4* and *5*, the only manipulation of data performed was the application of a first-order line or second-order parabolic flattening as described above, or a cropping of images to highlight regions of interest. In these images the (*x,y*) position of each pixel relates to the location on the surface, with the topographic heights shown as changes in colour. However, in *Chapter 5*, concerning the effects of etchants on polar surfaces of ZnO, 3D data is also presented along with the flattened images. *Figure 2.9(a)* is a 4×4 μm image of an O-terminated ZnO surface after annealing and shows a thermal pit (discussed in *Chapter 5*). In this case the image has been linearly flattened. *Fig. 2.9(b)* is the same image but perspective and light-shading algorithms have been applied. While this representation clearly highlights topographic differences, the shading algorithm alters the colour map of the image and one cannot directly infer that regions of the same colour in *Figs. 2.9(a)* and *(b)* have equivalent topographic heights. *Fig. 2.9(c)* is a full 3D representation of a region of *Fig. 2.9(a)*. As with *(b)*, although plots of this type are useful visualization aids, the colour of each pixel is not representative of its actual topographic height. All AFM data presented was analysed and plotted using the freeware WSxM software, available for download at the referenced website [9].

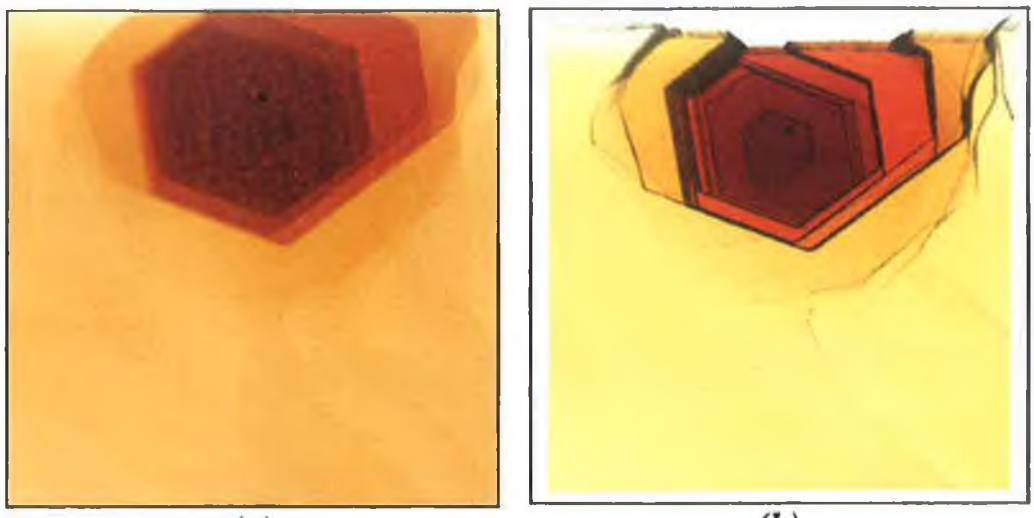

(a) (b)

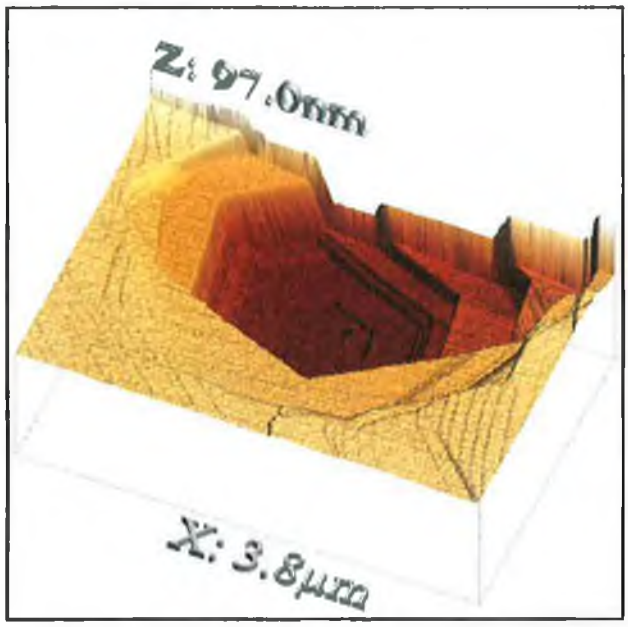

(c)

Figure 2.9: *2D and 3D representations of topographic images. In the first case (a) the image has been flattened using a first-order linear function. The second image (b) has been subjected to perspective and light-shading algorithms to highlight topographic differences. While useful as a visualization aid, the shading algorithm alters the colour map of the image and, therefore, surface features in (a) that appear the same colour as in (b) may not necessarily be at the same height. Note, for example, the relative brightness of the yellow planar region around the pit. This is also the case for (c) which is a full 3D representation of a cropped region of (a).*

2.2 *Force-Displacement Curves*

Once the AFM has been configured correctly and the tip is accurately tracking the topography of the sample, it is possible to obtain force-displacement graphs where the cantilever deflection is monitored as the tip is brought into contact with the face and subsequently removed. Generally one will observe repulsive and/or attractive forces as the tip approaches the surface, and the magnitude and nature of these can be related to the direction and magnitude of the cantilever deflection during this approach phase. In the case of the ZnO wafers examined in *Chapter 4*, adsorbed fluid layers are present on both the polar Zn-terminated and O-terminated faces in ambient environments. As the tip approaches this fluid layer, capillary forces attract the tip and bring it into contact with the surface [10]. During the retraction phase the meniscus that forms around the tip ensures that the magnitude of the force required to remove it from the fluid is greater than the attractive force that initially brought the tip into contact with the face. The presence of an adsorbed fluid layer is therefore seen as a discontinuity in the cantilever deflection during the approach and retraction phases, with significant hysteresis between the two [11]. Similar behaviour is also observed if the tip-surface interaction is due to van der Waal's or electrostatic forces, particularly if the force gradient during the approach phase is larger than the spring-constant of the cantilever. For the measurements discussed in *Chapter 4*, electrostatic and van der Waal's explanations for the nature of obtained force curves can be ruled out because of observed differences between curves obtained in air and water.

Figure 2.10 is an illustration of the cantilever deflections expected during the extension and retraction phases, whereas *Figure 2.11* is an actual force curve obtained from a ZnO surface. The labelling of relevant features has been kept the same in both figures for clarity.

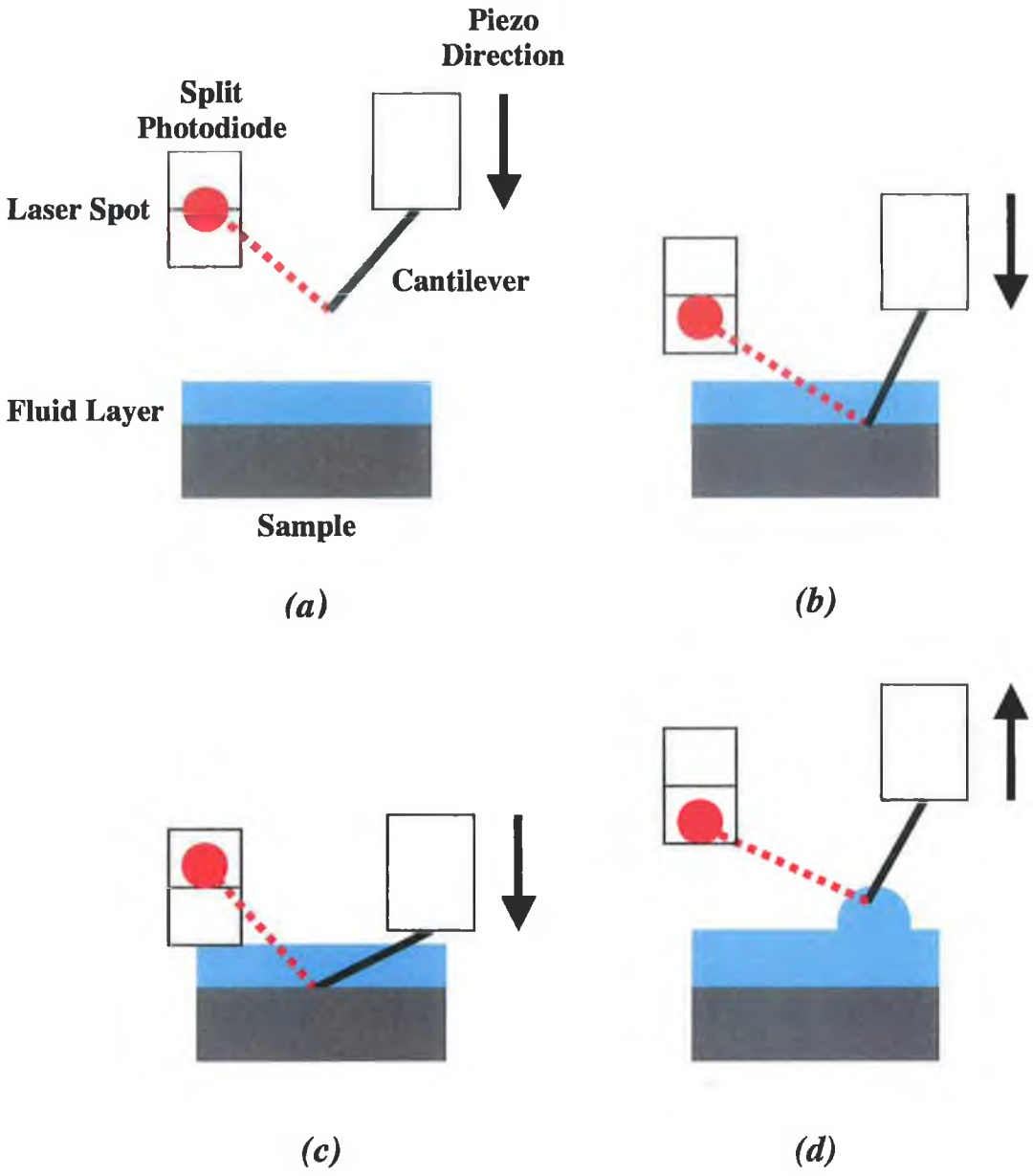

Figure 2.10: *Illustration of cantilever deflections during each phase of the piezoelectric movement. In (a) the cantilever deflection remains at an initial value as the scanners extend and bring the tip closer to the surface. Capillary forces cause the cantilever to deflect as the tip interacts with the fluid layer, as indicated by the change in position of the laser spot on the diode, and the tip 'jumps' into contact with the surface (b). As the scanners continue to move, the cantilever deflects in the opposite direction due to the reaction force from the surface itself (c). Finally, the piezoelectric scanners begin to retract but the fluid meniscus that forms around the tip prevents it from leaving the fluid layer until the cantilever deflection, and hence the piezo retraction distance, is sufficiently large to free it (d).*

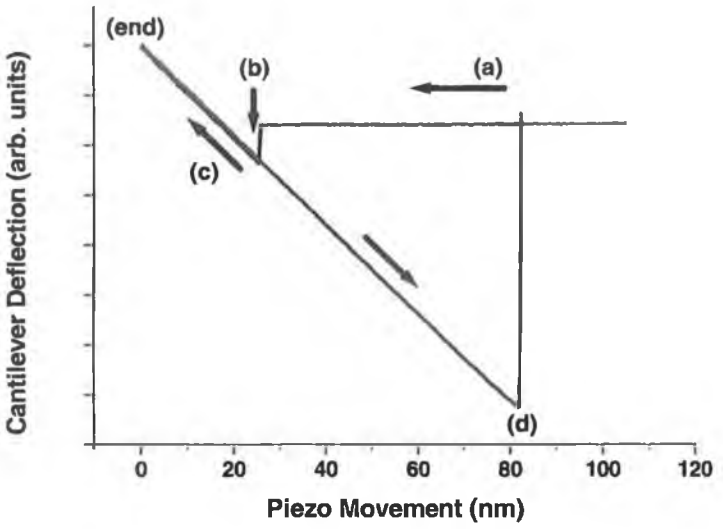

Figure 2.11: *Example of a force curve from the polar faces of ZnO. Section (a) represents the extension phase where the cantilever deflection remains at its initial value. The interaction of capillary forces as the tip approaches the fluid layer is observed as a sudden change in the cantilever deflection. This jump-to-contact point is shown at (b). As the piezoelectric scanners move closer to the surface the cantilever deflects due to the reaction force from the face (c) until the scanner reaches the end of its set movement limit (end). The scanner now retracts, but the meniscus that forms around the tip prevents it from leaving the fluid layer until (d). At this point the piezo retraction distance is sufficient for the cantilever to break free from the fluid and the deflection returns to its zero position.*

In *Figure 2.11*, it should be noted that the cantilever deflection is given in arbitrary units on the *y*-axis of the force-displacement plot. The reason for this is that the deflection is monitored by the split photodiode, and is measured in terms of voltage changes. It is therefore generally necessary to calibrate the force curve in order to relate this voltage to a more meaningful unit for deflection.

Figure 2.12 shows the 'loading portion' of *Fig. 2.11*, where the tip is in contact with the surface and the cantilever deflects as a result of the scanner movement towards the sample in the extension phase. In this case the cantilever deflection is given in its original units of voltage and a 'sensitivity' value, in units of V/nm, can be obtained by

determining the slope of the loading portion (-0.01823 V/nm in this case). Taking the reciprocal of this slope one calculates the value of the sensitivity to be -54.85 nm/V, and it is possible to relate the voltage deflection to a deflection in nanometers. For the example given, the cantilever deflection changes by 1 Volt for every 54.85 nm that the piezoscanners move towards the surface. Since the unit for spring-constant is N/m, multiplying the *y* co-ordinate of each point on the force curve (units of V) by both the absolute value of the sensitivity (units of m/V) and spring-constant (units of N/m) of the cantilever, the voltage deflection values can be converted to an applied force (*Figure 2.13*).

During the acquisition of force-curves, data is displayed in real-time by the Nanoscope software. The user plots a line along the loading portion of the curve from which the software calculates the sensitivity and multiplies this by the voltage of each point on the curve, converting from voltage to nanometer deflection. Data is saved in this format and the user, with an accurate determination of the spring-constant can subsequently convert to applied force. The above discussion, however, has been slightly simplified – in fact there is an additional 'detector sensitivity' value that relates directly to the response of the diode itself. This is also included in the multiplication to obtain the correct voltage deflection values, but is a factor (0.125) that relates to instrument calibration rather than any physical concept.

In *Figure 2.13* the calculated forces are negative as a result of an initial offset of the laser spot on the split photodiode (typically -2 Volts vertically in the case of the Nanoscope AFM in contact-mode). It is a trivial matter to re-normalise the curve by defining the *y*-axis origin to be located at the same vertical height as the extension/retraction regions of the curve where the tip is not interacting with the surface (*Figure 2.14*).

It is clear that an accurate determination of the forces requires an accurate calibration of the spring-constant of the cantilever. This was not performed, however,

for the data presented in *Chapter 4*. Since the fluid layer present on a surface is observed as a discontinuity in the approach and retraction phases of the force-displacement plots, the thickness of the adsorbed layer (as well as the thickness of the adsorbed layer on the tip) can be estimated by examining *only* the piezoelectric movement. The magnitude of the forces involved, in the case of the study presented below, is largely irrelevant and provided the same cantilever is used to examine Zn- and O-terminated faces, a comparison of adsorbed thickness on each polar face is possible. The adsorbed layer thickness on the sample surface may be estimated by the distance the piezoelectric scanner must move between the initial jump-to-contact point and the point at which the cantilever deflection returns to zero after contact with the sample [12], as shown in *Figure 2.15*.

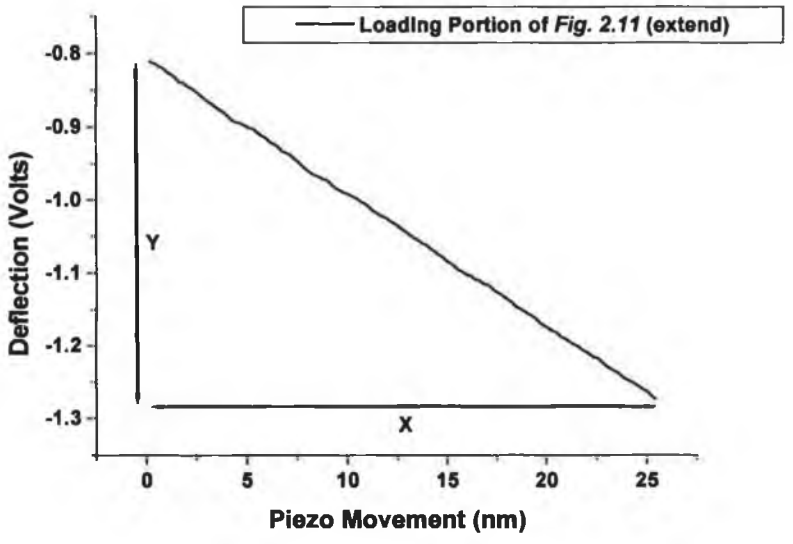

Figure 2.12: *Plot of the loading portion of the force-curve shown in Fig. 2.11, where the cantilever deflects as a result of the interaction with the surface in the extension phase. The x-axis corresponds to the piezo travel, whereas the y-axis is a determination of the cantilever deflection in units of voltage by the split photodiode. Taking the slope of this graph enables a 'sensitivity' factor to be determined in units of V/nm (-0.01823 V/nm in this case).*

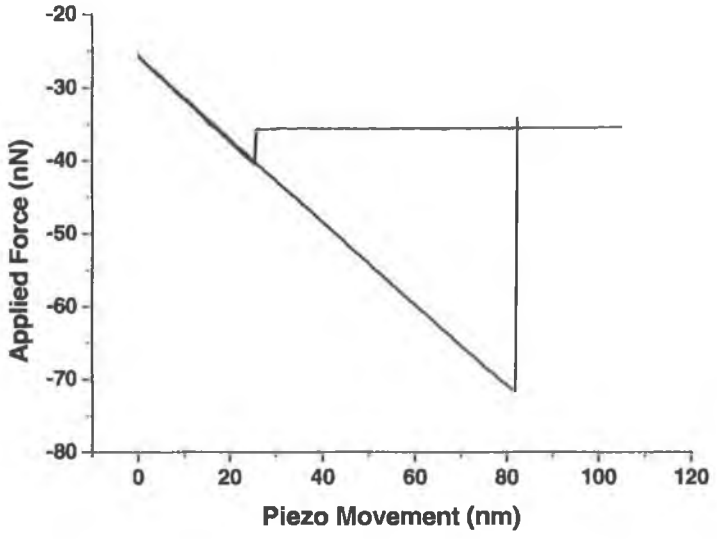

Figure 2.13: *Force-displacement plot after y-axis conversion to units of Newtons. Taking the reciprocal of the sensitivity calculated from the slope of the loading portion of the curve (Fig. 2.12), one obtains a sensitivity of -54.85 nm/V. Multiplying the y co-ordinate of each point on the plot by the absolute value of this sensitivity and the spring-constant converts the vertical axis from Volts to units of Newtons. The negative values of force are a direct consequence of the vertical offset of the laser spot on the photodiode (typically –2 Volts for the Nanoscope AFM in contact mode).*

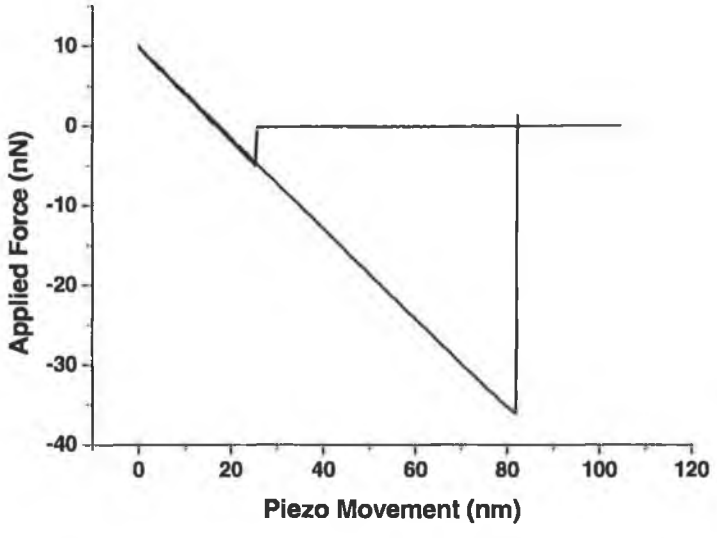

Figure 2.14: *Normalisation of force-displacement plot. Examining the cantilever deflection (y-axis) at piezo distances far removed from the effects of the fluid layer (25 – 110 nm on the x-axis) and determining this to be zero deflection (i.e. the deflection of the cantilever in the absence of any surface-related force), the y-axis can be simply re-normalised to show the magnitude and direction of forces acting on the cantilever.*

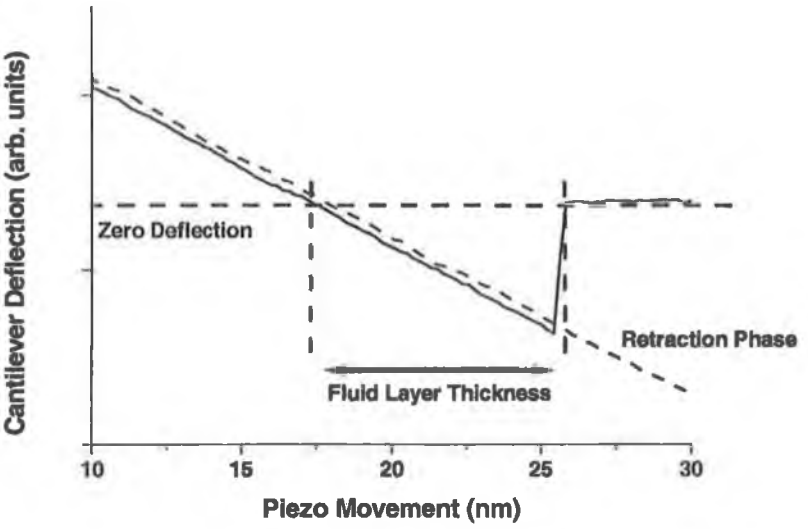

Figure 2.15: *Magnified portion of the force curve in Fig. 2.11, showing the jump-to-contact region in the approach phase. The adsorbed fluid layer thickness can be estimated by measuring the distance the piezoelectric scanner travels between the jump-to-contact point and the point at which the cantilever deflection reaches zero after contact with the sample surface.*

2.3 *Lateral Force Microscopy*

Lateral Force Microscopy (LFM) is a technique whereby the trace and retrace scanning directions are altered so that each imaged line is obtained perpendicular to the direction of the apex of a triangular cantilever, or at right angles to the major axis of a rectangular cantilever. The resultant frictional force acting on the tip as it is dragged across a sample surface causes the cantilever to deflect laterally, in addition to the vertical deflections as a result of topographic features [13]. By maintaining a constant applied force to the surface one can monitor the lateral cantilever deflection at each surface location and hence obtain a 'friction map' of the face, whereby an increase in frictional force at a given point is observed as an increase in the lateral deflection of the cantilever. This lateral deflection is monitored by the AFM laser system using a split photodiode, only in the case of LFM the differential voltage output is from diodes laid horizontally side-by-side rather than just vertically as in the case of topographic measurements. It is clear that in order to perform LFM a four-segment diode is required to monitor both vertical and lateral cantilever deflections simultaneously, as illustrated in *Figure 2.16*.

Since the frictional force is largely determined by the interaction between the tip and the surface, LFM in repulsive contact-mode has been shown to be sensitive to the chemical composition of the face [14,15]. However, this technique is generally used to image frictional or chemical changes across a single surface. For the measurements presented in *Chapter 4*, a comparative analysis of the frictional forces acting on the tip as a result of the interaction with each ZnO polar surface is needed.

Assuming an ideally flat and chemically uniform surface, and a constant scan rate, the lateral cantilever deflection will be related to the uniform frictional force acting on the tip. The friction will be equal in magnitude but opposite in direction depending on whether one examines the lateral deflection in a trace or retrace direction (*Figure 2.17*). Since the lateral deflection is determined by the split photodiode in terms of

output voltages, this effectively means that the deflections will give positive voltages in one line direction and negative voltages in the other. Taking half of the separation between the trace and retrace voltage gives a value that is directly related to the frictional force experienced by the tip. If the cantilever and the reflection point of the laser remain the same, this method of determining friction allows a comparison between different surfaces – as the frictional force changes from one surface to the next, it will be reflected in a change in the separation between trace and retrace voltages.

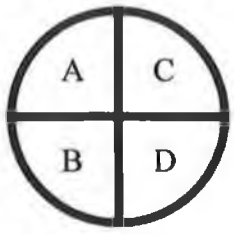

Figure 2.16: *Illustration of a four-segment photodiode as required for Lateral Force Microscopy. To obtain a 'friction map' of a surface, it is necessary that the applied normal force, and hence the reaction force, remain constant. This is achieved in the same manner as discussed above in relation to topographic imaging using constant-force contact AFM. With a four-segment diode, the differential output of the diodes for monitoring vertical deflections is given by;*

$$Output_{Vertical} = \frac{(A+C)-(B+D)}{(A+C)+(B+D)}$$

Eqn. 2.6

which simplifies to Eqn. 2.1 in the case where the lateral deflections are not monitored and the outputs of the upper and lower diodes are coupled. The lateral deflection is, analogously, given by

$$Output_{Lateral} = \frac{(A+B)-(C+D)}{(A+B)+(C+D)}$$

Eqn. 2.7

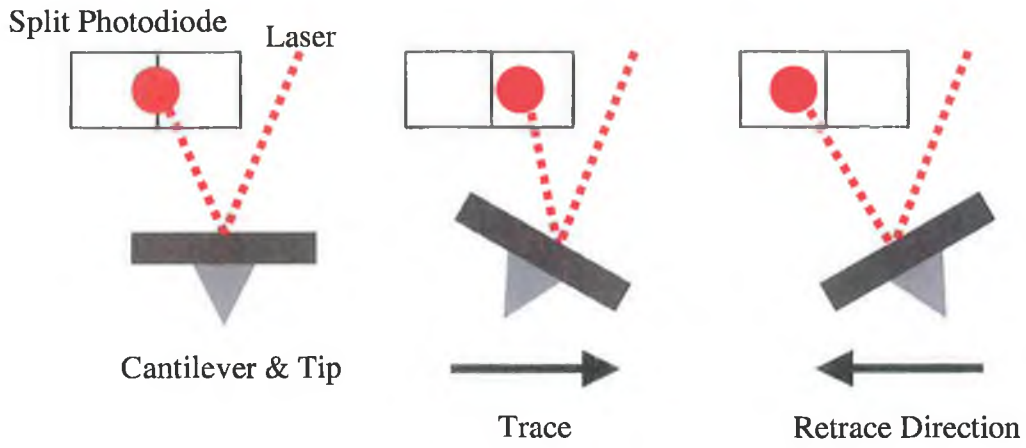

Figure 2.17: *Illustration of the relationship between diode voltage and line direction. In the case where the tip is not scanned across the surface (left), the laser spot is reflected to an initial point on the diode. As the tip is scanned in the trace direction the frictional force acting on it causes the cantilever to deflect laterally, thereby altering the position of the laser spot on the detector (middle). When the scanning direction is reversed, the direction of the frictional force and cantilever deflection is opposite to that in the trace direction and one observes a shift in the spot on the photodiode. Thus, the change in position of the laser spot (and hence the separation between positive and negative output voltages) between the trace and retrace directions gives a measure of the frictional force applied by the surface to the tip.*

Generally, a surface is not flat and topographic variations across the scanning region will affect the lateral deflection. This 'tripping' of the tip will cause deviations in the lateral deflection and hence the voltage values obtained, but one can estimate the frictional force that would be present if the surface was ideally flat by taking the mean of the trace and retrace values. The standard deviation about this mean is used as an indication of the topographical contribution to the lateral deflection results.

For *Chapter 4*, friction measurements were taken in both trace and retrace line directions and an example of the scans obtained is shown in *Figure 2.18*, where the (x,y) co-ordinate of each pixel relates to the position on the surface and the colour relates to the magnitude of lateral deflection at that location. With a 512×512 field size each trace and retrace image pair contains over half a million data points and these were saved in

an (*x,y,z*) format. Using the data shown in *Fig. 2.18*, *Figure 2.19* is a plot of the lateral deflection of each pixel in the trace and retrace images, where the voltages are positive for the trace and negative for the retrace data. The separation between the mean deflections of both datasets yields a value, in this case, of 0.585 Volts. Dividing by two, one obtains a deflection value of 0.293 Volts for the particular surface examined (an annealed O-terminated surface of a hydrothermally-grown ZnO wafer) which can be compared to subsequent samples using the same cantilever, scan rate and deflection set-point (applied normal force). The standard deviations are 0.041 Volts around the mean of the trace data in *Fig. 2.19* and the retrace standard deviation is 0.037 Volts. Taking the larger value therefore gives a rough indication of the topographical contribution to the lateral deflections.

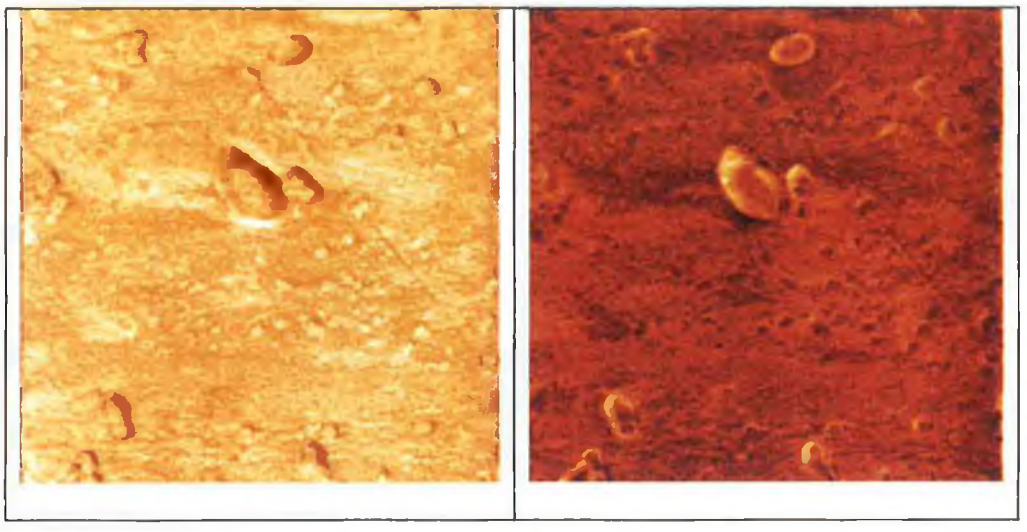

Figure 2.18: *5×5 μm friction plots of O-terminated surface after annealing for 24 hours in a 0.5 bar O_2 atmosphere at 1000°C. The image to the left was obtained in the trace direction and the image to the right was acquired in the retrace direction. The colour of each pixel is related to the magnitude of lateral deflection (brighter shades indicate higher lateral forces and hence larger frictional forces for the trace image, and opposite for the retrace). The voltage scales have been omitted as a more detailed analysis of the relative magnitudes of lateral deflections is given in Fig. 2.19. Each image is 512 × 512 pixels, corresponding to more than half a million data points for the trace-retrace pair in an (x,y,z) data format.*

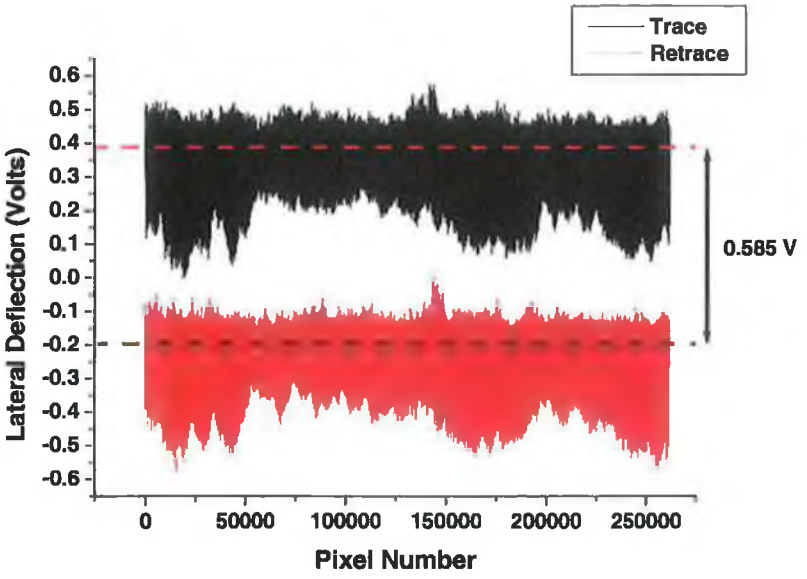

Figure 2.19: *Plot of lateral deflections for the trace and retrace images in Fig. 2.18. Taking each of the (x,y,z) data points, ignoring the (x,y) position, and graphing only the lateral deflection (z) for each pixel reveals that voltage values are positive for trace images and negative for retrace images. The dotted lines through both datasets are the calculated mean lateral deflections for each line direction. It should be noted that the plotted mean values appear somewhat biased to higher voltage and are not 'centered' within each data set. This is due to the limited print resolution, which cannot accurately reproduce the finer detail of the graph. Taking the separation between the means (0.585 V) and halving this figure (0.293 V) allows a friction value to be obtained for the images which can be compared to subsequently examined surfaces. The standard deviation in the trace and retrace data around these means provides a measure of the topographic contribution to lateral deflections.*

The validity of this simple analysis can be demonstrated by examination of the frequency of occurrence of each lateral deflection value in trace and retrace images. *Figure 2.20* is a frequency plot of the data presented in *Fig. 2.19*, where the bin size is 1 mV, showing maximum occurrences at approximately –0.2 V and 0.4 V for the retrace and trace data respectively. Thus, as one might expect, this separation is equivalent to the separation of the mean values in the linear plot above. However, the Gaussian shape of the frequency plots around these mean values is entirely consistent with the notion that the spread of values is due to topographic contributions.

In the above discussion, and for the measurements presented in *Chapter 4*, lateral deflections have been left in units of Volts. Although it is possible to convert this to metres by first performing the sensitivity measurements discussed in relation to force-curve analysis, conversions to force (i.e. to obtain a value for the frictional force in units of Newtons) requires knowledge of the lateral spring-constant of the cantilever. While in principle the lateral spring-constant can be calculated using the dimensions of the cantilever and the Poisson ratio for the material, this would involve measuring the thickness of the cantilever since the value quoted by the manufacturer (0.6 μm) is known to vary from one cantilever to the next. Recent studies have addressed this problem using variations of the Cleveland and Sader methods [16], but such calibration issues are largely irrelevant in the case of the measurements discussed herein. Provided the same cantilever is used to examine frictional forces on each surface, the voltage deflection values enable the simple comparison required.

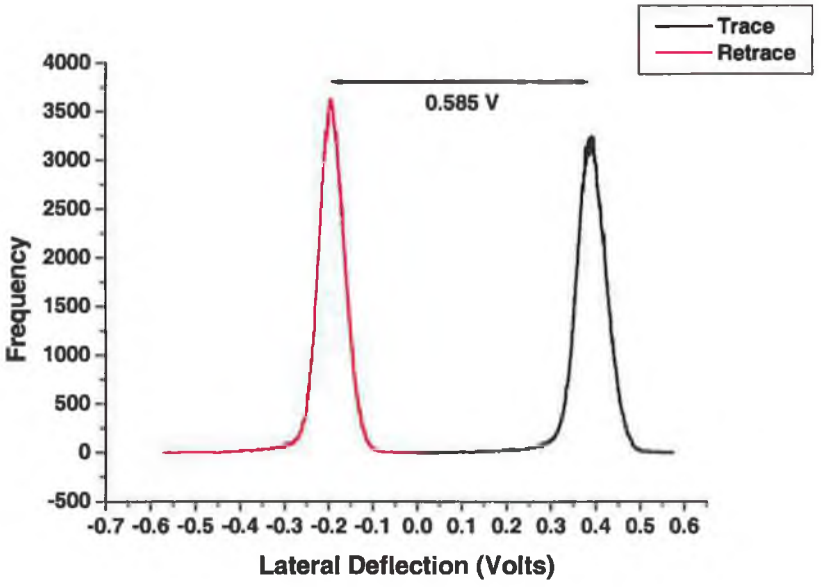

Figure 2.20: *Frequency plot of the occurrence of each lateral deflection voltage for the trace and retrace images shown in Fig. 2.18. The separation between the maxima of each curve matches the separation between the mean lateral deflections shown in Fig. 2.19. The distribution of values around the centres can be fit to a Gaussian curve, indicating a Normal distribution as a result of topographical contributions to the lateral deflection.*

2.4 *Fourier Transform Spectroscopy in UV and Visible Regions*

A Bomem DA8 spectrometer was used to obtain the optical spectra presented. This instrument is a Fourier Transform (FT) spectrometer based on a Michelson Interferometer, an illustration of which is shown in *Figure 2.21*. In this configuration light is collected through an entrance aperture and separated into two beams by a beamsplitter. A fixed mirror *B* reflects one beam, while the other is reflected by a moving mirror *A*, and the two recombine at the beamsplitter itself. Altering the position of mirror *A* introduces a phase difference between the beams and the resultant interference pattern is detected as a function of mirror position.

In the case of a monochromatic light source, after passing through the beamsplitter the electric field intensity of the two light waves can be described by;

$$E_1 = E_0 Sin(kx - \omega t)$$
$$E_2 = E_0 Sin(kx - \omega t + \phi)$$

Eqn. 2.8

where ϕ is the relative phase of the two waves, which depends on the position of mirror *A*. If one refers to the position of the moving mirror *A*, relative to the fixed mirror *B*, as *D/2* and define *D/2=0* when the path lengths are equal (known as the Zero Path Difference (ZPD) point), the number of additional wavelengths travelled by the light in path *A* as the mirror is moved is given by;

$$N = \frac{2D}{\lambda}$$

Eqn. 2.9

This can be converted into a phase angle ϕ in radians, yielding;

$$\phi = \frac{2\pi.D}{\lambda} = k.D$$

Eqn. 2.10

The electric field intensity of the resultant light wave at the beamsplitter (E_T) when both beams recombine is;

$$E_T = E_1 + E_2 = E_0[\sin(kx - \omega t) + \sin(kx - \omega t + \phi)]$$
$$= 2E_0 \sin\left(kx - \omega t + \frac{\phi}{2}\right).\cos\left(\frac{\phi}{2}\right)$$

Eqn. 2.11

To determine the light intensity I at the detector, the time average of the square of the electric field intensity must be examined;

$$I = \left\langle E_T^{\,2} \right\rangle = E_0^{\,2} + E_0^{\,2} \cos(k.D)$$

Eqn. 2.12

where the phase ϕ has been converted to $k.D$ (*Eqn. 2.10*). Thus one finds that the intensity at the detector varies in a cosinusoidal manner and is a function of mirror movement D and the wavelength of the source (related through k). *Figure 2.22* is an illustration of an interferogram (a plot of detector intensity against mirror position) for a monochromatic light source.

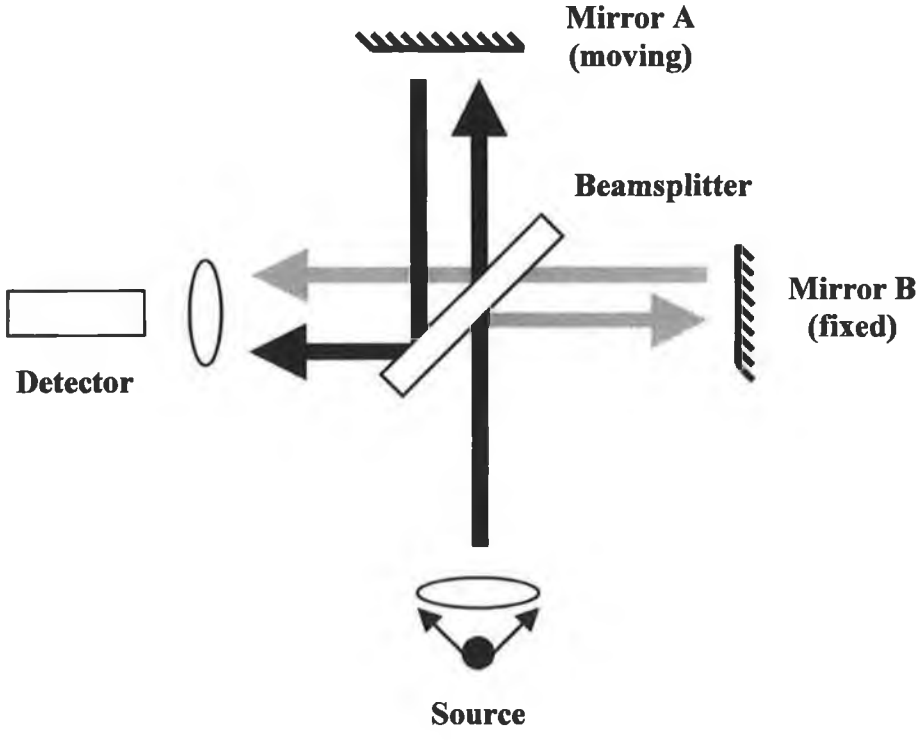

Figure 2.21: *Illustration of FT spectrometer using Michelson interferometer. Light from a source is passed through a beamsplitter and a phase difference between the two beams is introduced by the moving mirror A. The resulting interference pattern as a function of mirror position is captured by a detector.*

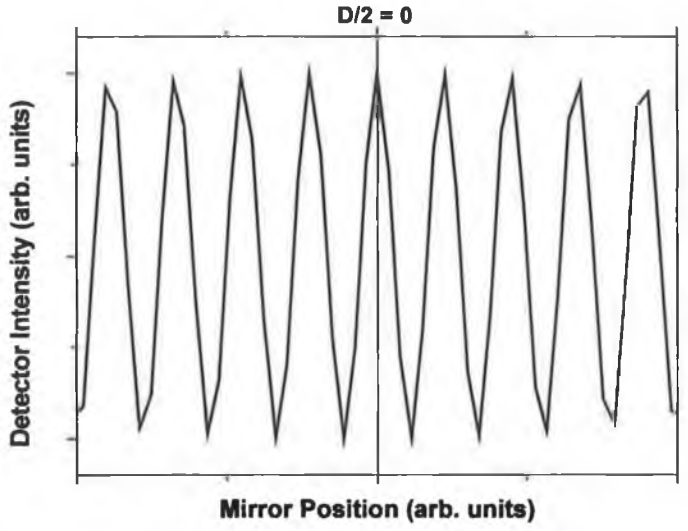

Figure 2.22: *Example of an interferogram for a monochromatic light source. The interferogram intensity varies as a cosinusoidal function of mirror position, according to Eqn. 2.12. At D/2=0 path lengths from mirror A and B are equal. Although in theory the interferogram is infinitely wide for a monochromatic source, it is experimentally impossible to achieve an infinite mirror movement and this has important consequences, as discussed below*

For an emission source with a complicated output spectrum consisting, for example, of adsorption lines, broad bands or emission lines, one can consider that the spectrum is actually composed of *n* monochromatic sources at each wavelength, where each monochromatic source has an intensity corresponding to the intensity of the spectrum at that wavelength (*Figure 2.23*). Every monochromatic source will contribute a cosinusoidal signal to the interferogram and each will have a characteristic period as the mirror moves. The amplitude of each cosinusoid is proportional to the spectral line intensity, and the intensity observed by the detector at each mirror position is;

$$I(D) = E_1^2 + E_1{}^2 \cos(k_1.D) + \ldots + E_n{}^2 + E_n{}^2 \cos(k_n.D)$$

Eqn. 2.13

For an infinite number of monochromatic sources representing an infinite number of wavelengths (related to k) across the spectrum;

$$I(D) = \int_{-\infty}^{+\infty} E^2(k) + E^2(k)\cos(k.D)\ dk$$

Eqn. 2.14

or, taking a constant of *I(k)* to represent the square of the electric field intensities;

$$I(D) = \int_{-\infty}^{+\infty} I(k)\left(1+\cos(k.D)\right)\ dk$$

Eqn. 2.15

The detailed interferogram shape contains all the information about the spectral content of the light source that generated it. Each optical frequency (k) in the source generates a cosinusoidal contribution to the interferogram with spatial frequency proportional to $1/k$. Considering only the varying part of *Eqn. 2.15* and performing an FT we get;

$$I(k) = \int_{-\infty}^{+\infty} I(D)\cos(2\pi k.D)\ dD$$

Eqn. 2.16

Which decomposes the interferogram into its constituent cosinusoids, and hence one obtains the original spectrum.

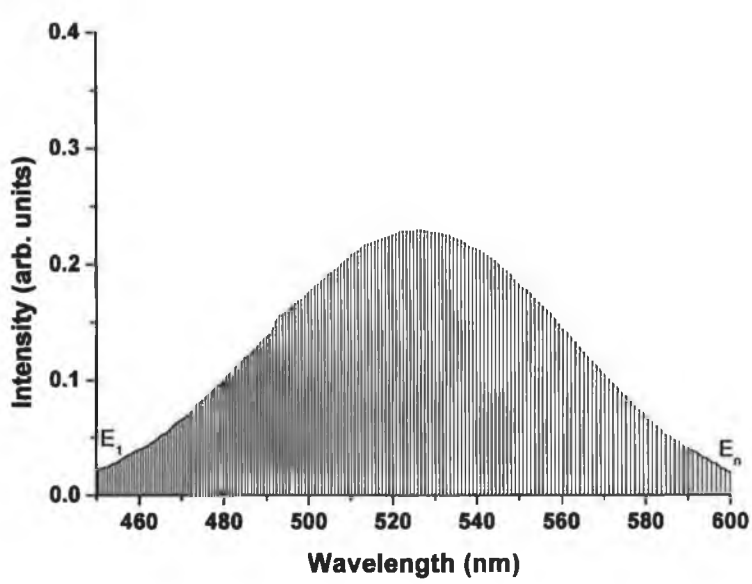

Figure 2.23: *Spectrum of the green band of ZnO at 25 K. Although the band is broad, one can consider that it is the result of n monochromatic light sources, each source having an intensity E_n corresponding to the intensity of the band at that wavelength.*

In the above description it was assumed that the limits of the FT integral extend from $-\infty$ to $+\infty$, i.e. that mirror A has an infinite travel. Of course, no practical instrument can accomplish such a movement and so the integral must be confined and is performed over the distance that the mirror can travel ($-a$ to $+a$);

$$I(k) = \int_{-a}^{+a} I(D)\cos(2\pi.kD)\ dD$$

Eqn. 2.17

This has the effect of truncating the interferogram, which affects the FT and hence the obtained spectrum. *Figure 2.24* shows the effect of taking a Fourier Transform of a finite monochromatic interferogram, such as that shown in *Fig. 2.22.* Although it is clear that the spectrum is of a single, monochromatic source, one observes a series of side-lobes around the emission line (known as Gibb's phenomenon [17]) as a result of the 'box-car' truncation, where values in the FT integral outside of the mirror movement limit are set to zero. Although the line-width of the major peak in the obtained spectrum is narrow, the relative intensity of these side-lobes could mask other weak spectroscopic emission lines. By applying a function to the interferogram that smoothly reduces the intensity to zero at the mirror movement limit, known as *apodization*, one can decrease the magnitude of these side-lobes at the expense of resolution.

The apodization function $A(D)$ is included in the Fourier Transform integral;

$$I(k) = \int_{-a}^{a} I(D)\cos(2\pi.kD)\ A(D)\ dD$$

Eqn. 2.18

and in the case of the spectra obtained herein, the 'Hamming' apodization function was used;

$$A(D) = 0.54 + 0.46\cos\left(\frac{\pi D}{a}\right)$$

Eqn. 2.19

A plot of this function is shown in *Figure 2.25.*

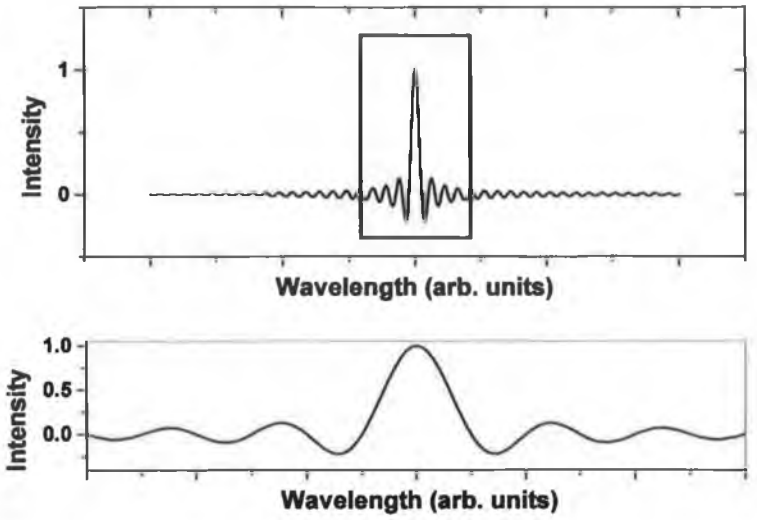

Figure 2.24: *Fourier Transform of a finite monochromatic cosinusoidal interferogram (Fig. 2.22). Although the single wavelength of the source is clearly visible as an intense peak, performing the FT on the truncated interferogram results in the observed 'ringing' of the spectrum. This extends far from the monochromatic wavelength peak in both directions in real-space, as shown in the upper plot. The lower plot is a magnified portion showing the 'side-lobes' that result. These can mask weaker signals in a spectrum.*

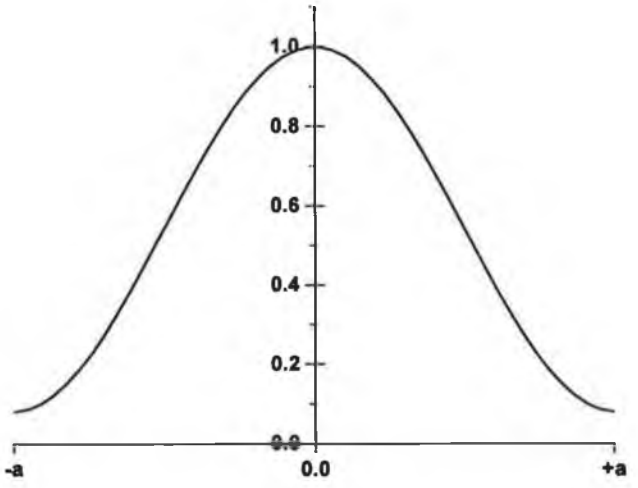

Figure 2.25: *Plot of the Hamming apodization function between the mirror movement limits of +a and -a. Multiplying an interferogram by this function gently brings the intensity to almost zero (~ 0.08) at these limits. Performing an FT on the apodized interferogram reduces the 'ringing' and strength of the side-lobes, as in Fig. 2.24, but at the expense of resolution (Fig. 2.26, below)*

If one applies the Hamming apodization function to the finite sinusoidal interferogram and obtains the FT, the line-width of the monochromatic peak in real-space increases (FWHM after the Hamming function is approximately 1.8 times the FWHM obtained after box-car truncation). However, although there is a loss in resolution, the side-lobes are substantially reduced in intensity (*Figure 2.26*).

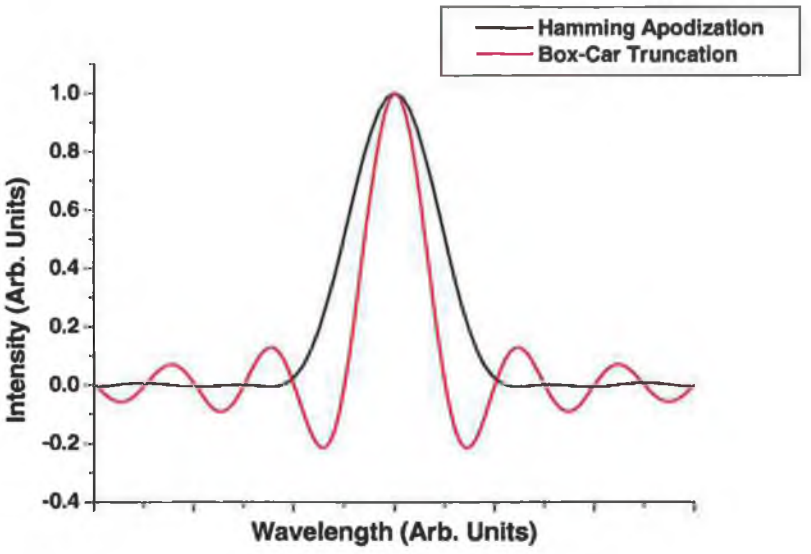

Figure 2.26: *Illustration of the effect of applying a Hamming apodization function to a finite monochromatic interferogram. The red spectrum shows the monochromatic emission line, after performing the FT, and the side-lobes that result from the box-car truncation. The black spectrum shows the result of applying the Hamming function. Although the line width increases, signifying a loss of resolution, the side-lobes are significantly reduced. Apodization is tolerated as it improves the line-shape of the resultant spectrum.*

From the above discussion it can be seen that the act of truncating an interferogram has a direct influence on the obtained spectral line-widths. More generally, the resolution of an obtained spectrum after performing a Fourier Transform operation is ultimately dependent on the limits $-a$ to $+a$ in the FT integral, and hence the total distance that the travelling mirror can move. It should be noted that high-resolution information regarding the real-spectrum is obtained from regions of the

interferogram that are far from the ZPD. Suppose one was to use an FT spectrometer to examine two emission lines that are extremely close in wavelength. Although each line will contribute a cosinusoidal pattern to the interferogram, these patterns will have similar periods as a function of mirror movement. If the mirror is moved only a short distance from the ZPD, it may not be sufficient for the FT spectrometer to detect each cosinusoidal function – the slight difference in wavelength only becomes apparent the further the mirror moves.

Obviously, any practical FT spectrometer must have an entrance aperture of finite dimensions in order to allow light to pass through the beamsplitter. *Figure 2.28* is an illustration of light entering an FT spectrometer through different points on an open entrance aperture. In general, light going into the spectrometer at a point near the edge of the aperture (blue rays) has a slightly longer path to the detector than light at the centre of the aperture (red rays). If we suppose that the source is monochromatic, then the electric field intensity at the detector as a result of the recombination of on-axis (red) rays after passing through each arm of the interferometer is;

$$E_1 = E_0 + E_0 \sin(kx - \omega t + kD)$$

Eqn. 2.20

where D is the mirror movement. Analogously, for the slightly off-axis rays the total E-field at the detector will be;

$$E_2 = E_0 + E \sin(kx - \omega t + kD')$$

Eqn. 2.21

where D' is the effective optical path as a result of the extra distance the light must travel to the detector, and the assumption is made that the electric field intensity is the same for both on and off-axis rays (i.e. that the aperture is uniformly illuminated). At the ZPD point the optical path difference for all rays will be zero and in this case both E_1 and E_2 will have maximum values due to constructive interference of their two components.

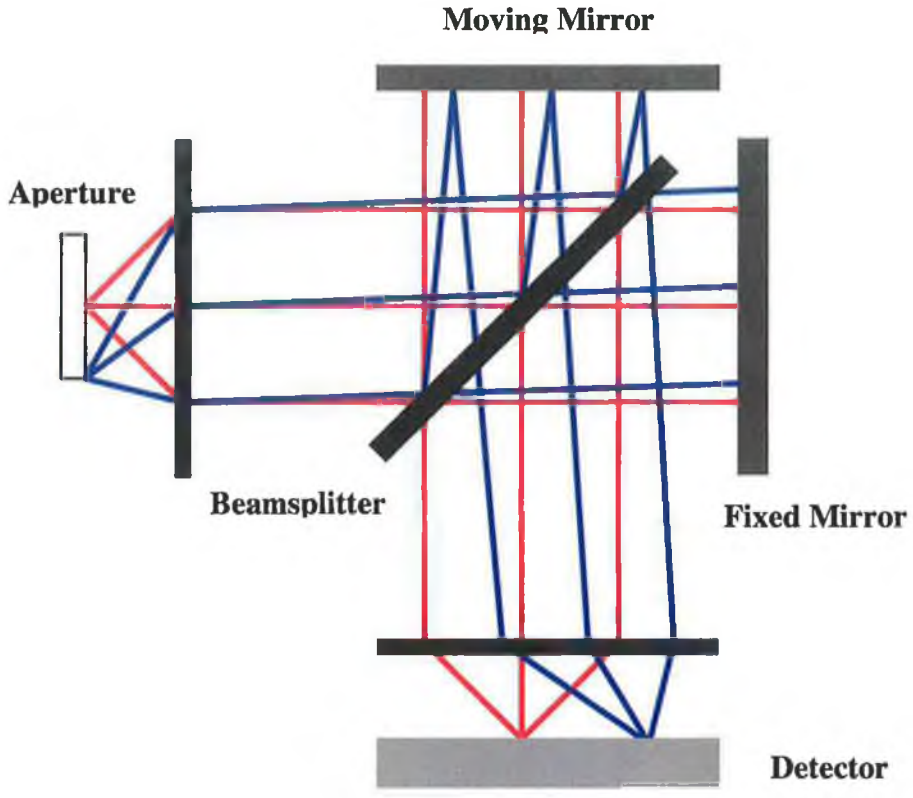

Figure 2.28: *Illustration of light entering the Michelson interferometer through two different points of the entrance aperture. The red rays are on-axis, and have a normal angle of incidence at both mirrors. The blue rays enter slightly off-axis, and thus have an additional phase due to the increased path length to the detector. However, the angle of incidence is not normal to the two mirrors and the subsequent movement of the mirror from the ZPD point introduces a phase shift in the off-axis light that is not equivalent to the phase shift of the on-axis light. The detector therefore detects two fringes, each with a different period as the mirror moves.*

As the mirror moves away from the ZPD, however, the situation becomes more complicated. The phase introduced by the mirror after a small movement ΔD in the case of the on-axis light (*Eqn. 2.10*) is simply;

$$\phi = k.\Delta D$$

where again, the distance $D/2=0$ corresponds to the ZPD point. Light entering off-axis will have an incident angle of θ to the moving mirror, and the phase shift as a result of a small mirror displacement is;

$$\phi = k.\Delta D\cos\theta$$

Eqn. 2.22

Therefore the mirror displacement required to bring on-axis rays from a condition of constructive interference at the ZPD to destructive interference will be different to the movement required for off-axis rays because of the dependence of their phase on incident angle. In the above case, where light enters the spectrometer through two different points in the aperture, the interferogram will consist of the superposition of two cosinusoidal patterns each with a different period with respect to mirror movement.

If one now considers monochromatic light passing through every point of a circular aperture, each ray will have a phase difference that depends on its angular distance from the centre of the aperture. This angular distance ultimately determines the incident angle of the rays at the travelling mirror, and hence will be different for rays entering the spectrometer through different points of the aperture. The interferogram obtained as a result of a finite aperture therefore consists of a superposition of cosinusoidal patterns with different periods. At a given mirror position one would observe a series of circular fringes at the detector due to the constructive and destructive interference of these off-axis rays and, as the mirror moved, each fringe would not necessarily alternate from bright to dark in phase with the others.

The detector is not capable of examining every fringe individually but measures the total light intensity falling on it. For a narrow aperture, most of the rays entering the spectrometer are close to being directly on-axis (i.e. the angle of incidence on the

moving mirror is close to zero) and the interferogram more closely resembles that of a theoretical infinitely-small aperture. Narrowing the aperture therefore provides high resolution but drastically lowers the intensity of light falling on the detector. Conversely, widening the aperture allows rays that are off-axis to reach the detector and results in a series of fringes which do not alternate from bright to dark in phase. The detector observes the constructive and destructive interference of on-axis rays as a function of mirror position, but superimposed on this is also the effect of the off-axis rays. In other words, the interferogram has an additional modulation due to these off-axis rays. A detailed analysis of this phenomena shows that this modulation has a tendency to reduce the intensity of the interferogram as the mirror moves away from the ZPD [18], as illustrated in *Figure 2.29*. Therefore, although a wider entrance aperture increases the amount of light reaching the detector, the apodization of the interferogram reduces the resolution. A wider aperture also produces a slight, systematic shift to lower wave-number of the line centre due to the contribution of off-axis rays.

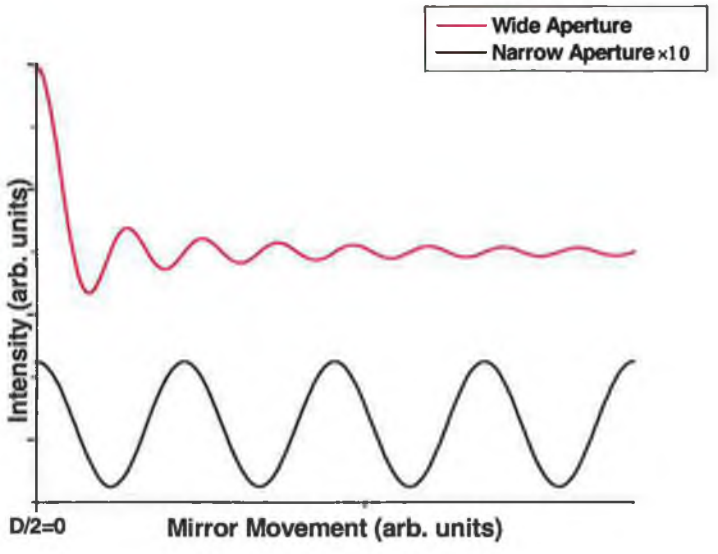

Figure 2.29: *For a narrow aperture (black) the interferogram of a monochromatic light source is simply a cosinusoidal function of mirror position. For a wide aperture, the additional off-axis light creates fringes at the detector that alternate from bright to dark out of phase with the on-axis rays. This has a tendency to modulate the interferogram and one observes an apodization of the signal, leading to a decrease in resolution.*

The resolving power R of a Michelson interferometer due to the aperture is;

$$R = \frac{2\pi}{\Omega}$$

Eqn. 2.23

where Ω is;

$$\Omega = \pi\left(\frac{\theta}{2}\right)^2$$

Eqn. 2.24

and represents the solid angle of admittance subtended by the source at the aperture, as illustrated in *Figure 2.30*.

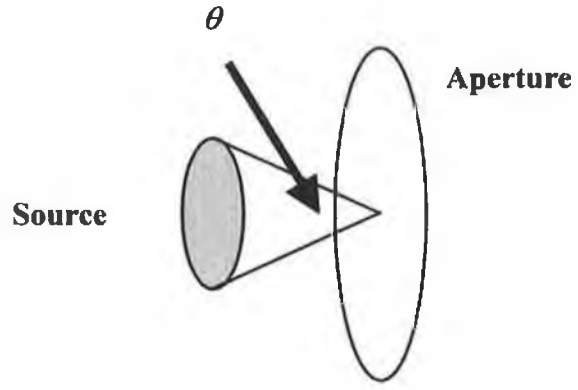

Figure 2.30: *Diagram showing the definition of the angle of admittance.*

It can be seen from *Eqns. 2.23* and *2.24* that if the solid angle decreases (as the result of a narrowing of the aperture), the resolving power increases. Narrowing the aperture, however, reduces the amount of light entering the spectrometer. Thus, Fourier Transform spectrometers behave in a similar fashion to dispersive spectrometers where there is a trade off between resolution and signal strength. Nevertheless, FT spectrometers have a distinct advantage, in terms of total throughput of light, over dispersive instruments. The product of the solid angle of admittance and the resolving power is;

$$R\Omega = 2\pi$$

which one generally finds is at least an order of magnitude greater than for grating spectrometers. This is known as the Jacquinot or throughput advantage [19] and effectively means that an FT system can operate, relative to dispersive instruments of similar dimensions, at both high resolving powers and high signal levels simultaneously. This advantage is present regardless of the wavelength region one is examining or the detector being used.

Suppose that one wishes to obtain a spectrum over a wavelength region $\lambda_2 - \lambda_1$ at a resolution of $d\lambda$ in a total time of T using a grating spectrometer. The total number of measurements required will be;

$$M = \frac{\lambda_2 - \lambda_1}{d\lambda}$$

Eqn. 2.25

and the time (dT) taken to acquire data at each interval $d\lambda$ will be;

$$dT = \frac{T}{M}$$

Eqn. 2.26

Therefore the integrated signal intensity for each spectral element examined will be proportional to T/M.

For a grating spectrometer, if the noise in the dispersive instrument is detector-noise limited, then the noise for each spectral element examined will be proportional to the square-root of the signal intensity and hence the signal-to-noise ratio is;

$$SNR_{Grating} \propto \sqrt{\frac{T}{M}}$$

Eqn. 2.27

Since a Fourier Transform spectrometer obtains an interferogram which is the result of the constructive and destructive interference of all spectral elements, it effectively examines all wavelength regions simultaneously. The integrated signal over the wavelength region $\lambda_2 - \lambda_1$ is proportional to the time T. The signal-to-noise ratio of an FT spectrometer, for a detector that is detector-noise limited, is;

$$SNR_{FT} \propto \sqrt{T}$$

Eqn. 2.28

and hence, the ratio of signal to noise for an FT spectrometer compared to a grating spectrometer is;

$$\frac{SNR_{FT}}{SNR_{Grating}} = \sqrt{M}$$

Eqn. 2.29

This is known as the Fellgett or multiplex advantage [20]. In summary, an FT operating with a detector that is detector-noise limited has significant advantages over grating spectrometers and one can obtain high-resolution spectra, with a higher throughput of light, in a reasonable time. FT spectrometers are therefore generally used in infra-red regions of the spectrum where the detectors satisfy this condition.

However, for the photoluminescence and reflectance studies of ZnO presented in later chapters, the bound- and free-exciton regions of interest lie in the near-UV (around 360 to 400 nm) and the green band lies in the visible region (between about 450 nm to 600 nm). We shall now examine the effects of operating an FT in these wavelength regions.

The position of the moving mirror must be accurately tracked to obtain a useful interferogram. In most FT systems this is accomplished by an internal single-mode stabilized HeNe laser (~ 633 nm) which is introduced along the same optical path as the external light. Since the interferogram of a monochromatic source is simply a cosinusoidal pattern as a function of mirror movement, and the wavelength of the HeNe line is accurately known, fringe counting electronics can determine the relative distance from the ZPD that the mirror has moved. If the electronics only examined the maxima (constructive) and minima (destructive) points of the HeNe interferogram, corresponding to a mirror movement of ~312 nm (180° out of phase), the shortest resolvable wavelength of the spectrometer would also be ~312 nm. However, by examining other points on the interferogram (say, at 90°) the mirror tracking can be

performed much more accurately thus decreasing the wavelengths to which the instrument can resolve the individual cosinusoidal contributions.

In the case of the studies discussed here, this intense laser line presents a number of problems. Since the FT spectrometer is a multiplexing instrument, examining all wavelength regions simultaneously, the HeNe line is generally much more intense than the light collected from a sample. The amplitude of each cosinusoidal component of the interferogram is directly related to the intensity of the emission line at each wavelength, and therefore the interferogram is dominated by the contribution of the HeNe line. Ultimately the spectrometer electronics must digitally sample the interferogram before performing the FT. The actual signal as a result of incoming light from the sample, compared to the HeNe line, would therefore account for only a small percentage of the bit-space.

In order to maximise the sample signal, in terms of the digital signal obtained by the A/D converter, it is therefore necessary to optically filter out the HeNe line. A band-pass Schott glass filter (BG25), with a transmittance of over 90% between ~ 350 and 450 nm, and ~ 10^{-3}% at 633 nm was used for examination of the bound- and free-exciton PL and reflectance spectra. For studies of the green band, a filter (C3C21) with a band-pass of > 90% between 400 and 510 nm, and transmittance of ~ 10% at 633 nm was used, where either filter was placed in front of the detector. The transmittance of both filters is shown in *Appendix I.*

Although the Jacquinot advantage remains even at short wavelengths, as the wavelength of light decreases one must proportionately narrow the entrance aperture to the FT spectrometer in order to obtain the same resolution of spectra, and overall light intensity through the beamsplitter for short wavelength light is substantially reduced. A photomultiplier tube was used with the FT to examine the visible and near-UV regions. For a photomultiplier tube, the shot-noise level increases with the signal level;

$$Noise \propto \sqrt{Signal}$$

Eqn. 2.30

and thus, the Fellgett advantage is completely lost.

In short, one must increase the number of scans in order to obtain a good signal-to-noise ratio for the interferogram when examining UV and visible spectral regions and there is little advantage in terms of the time of acquisition or resolution over a grating spectrometer. Light throughput is theoretically greater for an FT spectrometer, although this is not particularly significantly when compared to a blazed-grating spectrometer with a low-noise, cooled PM tube. However, the internal HeNe tracking laser provides a wavelength calibration of an FT instrument that is difficult to replicate with a grating spectrometer, and one can generally be more confident about absolute emission line energies (wavelengths) with an FT spectrometer.

In the above discussion we have ignored the problem of aligning the mirror as it travels, and the location of the ZPD point. Mirror alignment is continuously adjusted to ensure that both the moving mirror and fixed mirror are at right angles to one another. In the case of the DA8, this is achieved by reflecting the HeNe laser line from three points on the moving mirror and monitoring the intensity of each reflected beam with a photodiode. The 'fixed' mirror, in reality, is adjusted by tilt controls in response to the diode outputs to ensure that it remains at right angles to the moving mirror.

Although mirror tracking is performed with a HeNe laser, the instrument must also determine the physical location of the ZPD point. A broad band 'white' light source is used, and introduced along a similar optical path as the external light, though it is detected separately. This broad source will theoretically introduce a virtually infinite number of cosinusoidal patterns to the interferogram, each with a different period due to the different wavelengths entering the spectrometer, but at the ZPD point *all* wavelengths will constructively interfere since the path length from each arm of the

interferometer will be the same. The detector will observe a 'burst' of signal when the mirror passes through the ZPD point enabling its position to be located accurately.

To obtain reflectance spectra, one shines a bright white light source onto the sample and collects the reflected light into the spectrometer. Since the spectral characteristics of the external white light are similar to the internal source, and some cross-talk is inevitable, the FT spectrometer can have difficulty in locating the ZPD. This problem is overcome by filtering out wavelengths in the external source that are not required for the reflectance spectra. In other words, one can only examine reflectance over a relatively narrow spectral region.

One final dilemma involves the beamsplitter itself, which will introduce a phase shift to incoming rays as a result of their different wavelengths. It is necessary to account for this additional phase by first performing a 'phase scan' of the external light source (whether reflected light or luminescence). This is a low resolution symmetric scan (i.e. the interferogram is only captured for a small distance either side of the ZPD) and the complex FT spectrum is obtained;

$$I(k) = A(k)e^{i\phi(k)}$$

Eqn. 2.31

where the phase factor $\phi(k)$ is the correction which can be used on subsequently obtained spectra to take account of the phase shifts as a result of the beamsplitter and symmetrise the interferogram. A particularly useful consequence is that, having obtained a low resolution symmetric scan, a high resolution scan can be performed on only one side of the interferogram (i.e. starting at the ZPD and moving the mirror in only one direction away from it). Rather than use the total available mirror movement to scan the interferogram from $-a$ to $+a$, examining only one half of the interferogram over that movement increases the resolution since the FT integral limits are effectively changed from $-2a$ to $+2a$ as the region 0 to $+2a$ can be flipped in the origin (as it has been symmetrised).

Ideally, to obtain a phase spectrum one would use a broadband light source so that $\phi(k)$ can be determined and interpolated for each wavelength. Phase scans were performed when examining the reflectance of ZnO wafers, since this is spectrally broad. However when examining the bound-exciton photoluminescence emission lines, the phase factors used had a tendency to distort line shapes after high-resolution scans.

The reason for this is that the bound-exciton emission of ZnO consists of a number of very narrow, and closely separated short-wavelength lines which dominate the spectrum in the near band-edge region. Even a slight movement of the sample will slightly alter the path length to the spectrometer, and hence any phase factor obtained will not reflect the new position of the sample. To compensate for this the spectrometer used the acquired high-resolution spectrum as its own phase.

In the case of the green band of ZnO, its close proximity in wavelength to the internal HeNe laser line posed significant problems, even with the use of a filter. High-resolution scans of the band were difficult to perform because as one narrows the aperture to accommodate this, the external light intensity reduces in proportion to the intensity of the internal HeNe line. The green band was therefore examined by performing a low-resolution symmetric phase scan with a wide aperture. For comparison, the resolution of the bound-exciton spectra presented is typically ~ 0.1 meV, whereas the resolution of the free-exciton reflectance spectra is ~ 0.5 meV. The green band phase scans have a resolution of ~ 20 meV.

2.5 *Experimental Set-up for Optical Measurements*

For the photoluminescence (PL) examination of the bound-exciton and green band emission of ZnO wafers, samples were cooled in Janis CCS-500 closed-cycle cryostat between 20 and 300 K. The temperature was controlled and monitored with an Oxford Instruments ITC-4 controller, resistive heater, and a 27Ω rhodium-iron resistance sensor located on the sample holder. The 325 nm (c.w.) HeCd line of a Kimmon IK Series laser was used for excitation, with a power of ~ 40 mW unfocused on the sample. The Bomem DA8 FT spectrometer was fitted with a Hamamatsu R1913 photomultiplier tube and the PM output was matched to the spectrometer with a Bomem variable gain preamplifier (#IEH5700L). *Figure 2.31* is an illustration of the experimental set-up. Laser light is brought onto the sample and the luminescence collected by a collimating lens. A parabolic mirror then brings the light into focus at the spectrometer entrance aperture. For an examination of bound-exciton luminescence the BG25 Schott glass filter was placed before the detector, whereas the C3C21 filter was used for acquisition of green band data (*Appendix I*).

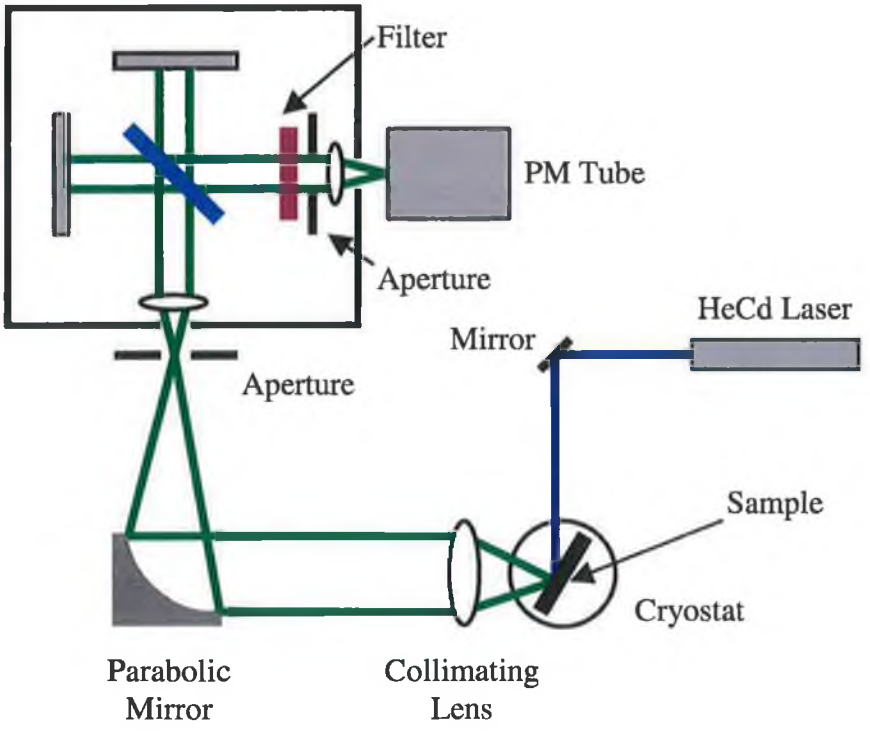

Figure 2.31: *Illustration of the experimental arrangement for PL spectroscopy.*

The set-up for reflectance (RF) spectroscopy described in this section is a 'general purpose' arrangement of the apparatus. The 45° incident angle allows the propagation of both longitudinal and transverse electric fields through the sample, and this complicates the analysis of the exciton-polariton behaviour (discussed in detail in *Chapters 6* and *7*). Nonetheless, excitonic resonances using this arrangement are readily apparent. The use of focusing optics increases the signal-to-noise ratio, which is particularly poor for samples after etching (*Chapter 5*).

Reflectance spectroscopy in this configuration is similar to that for PL. An Ealing 150W Xe lamp is used for illumination of the samples, and the beam is passed through a variable aperture and short-focal length lens, which brings the white light to a small, intense spot on the sample. The reflected light is directed through a long focal-length lens and its distance from the cryostat is adjusted so that the parabolic mirror brings the light into focus at the entrance aperture of the spectrometer. It is necessary to use two filters for reflectance spectroscopy. The first is the BG25 Schott glass filter, as used for PL studies of the bound-exciton region, which is placed before the detector and effectively filters out the internal HeNe tracking line but passes the near-UV.

Since an intense external white light source is used for reflectance, its spectral characteristics are similar to that of the internal white light source used by the spectrometer to locate the ZPD. One also finds that the PM tube is saturated by the large intensity of light falling on the detector from the Xe lamp and it is therefore necessary to use a band-pass filter that allows only the near-UV wavelengths to enter the spectrometer (i.e. another BG25 Schott glass filter). This second filter is placed at the entrance aperture itself. Even with these two filters in place, the intensity of light can be sufficient to saturate the detector. The variable aperture placed before the cryostat therefore allows an attenuation of the source to prevent this. *Figure 2.32* is an illustration of the experimental arrangement.

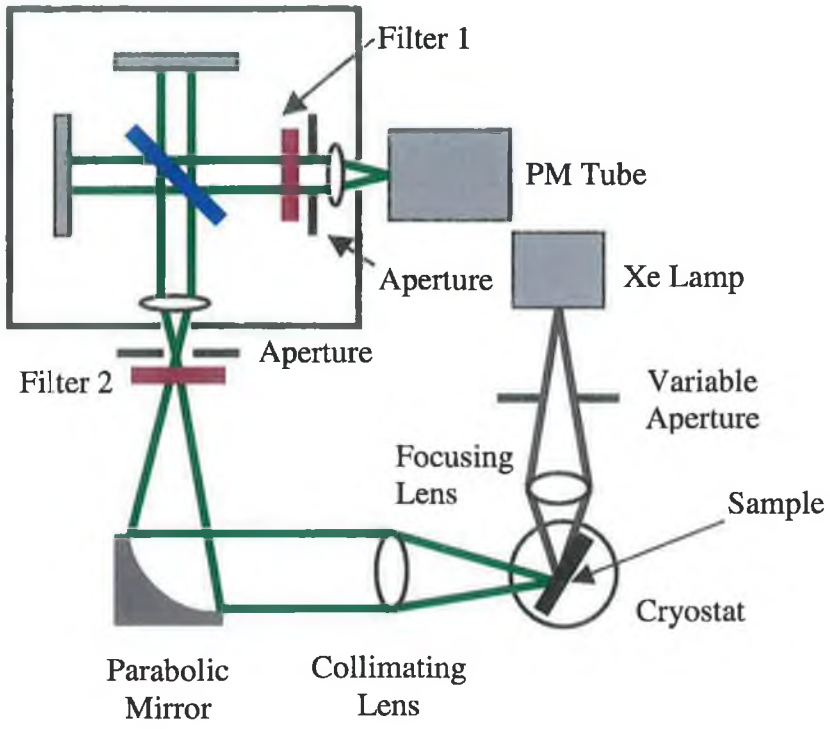

Figure 2.32: *Illustration of the experimental arrangement for reflectance spectroscopy with a non-normal incident angle.*

In order to normalise the reflectance spectra obtained from samples, and hence convert from arbitrary intensity values to a percentage reflectivity, a small piece of silicon coated with a thick aluminium layer was used as a reference. This was assumed to have 100% reflectivity over the wavelength region of interest, and all ZnO spectra were obtained in conjunction with a reference spectrum in order to take account of any variation in the experimental set-up. The cryostat sample holder can accommodate three samples at once, one of which will be the reference sample, and each is brought into the beam path by rotation of the holder. However, since the holder is not perfectly centred in the cryostat there will be a slight misalignment and the reflected light may not line up perfectly with the entrance aperture of the spectrometer. Provided the variable aperture between the Xe lamp and sample is not changed, and the relative distances of the focusing and collimating lens remain the same, the reflected light can be steered by making small adjustments to the lateral and vertical position of each lens until a maximum signal is reached.

2.6 References

[1] C. A. J. Putman, B. G. De Grooth, N. F. Van Hulst, and J. Greve, *J. App. Phys.* **72** (1992) 6

[2] C. Johnson in *Process Control Instrumentation Technology*, 4th edn. (Prentice Hall International, 1993), chapter 9, p. 386 and chapter 10, p. 412

[3] S. O. Kucheyev, J. E. Bradby, J. S. Williams, C. Jagadish, and M. V. Swain, *Appl. Phys. Lett.* **80** (2002) 956

[4] Veeco Instruments Ltd., Nanotech House, Anderson Road, Swavesey, Cambridge CB4 5UQ, England
website: www.veeco.com

[5] Veeco Corporation (see [4]), SPM probe model DNP
website: https://www.veecoprobes.com/product_detail.asp?NQPN=DNP

[6] C. T. Gibson, G. S. Watson, and S. Myhra, *Nanotechnology* 7 (1996) 259

[7] J. P. Cleveland, S. Manne, D. Bocek, and P. K. Hansma, *Rev. Sci. Instrum.* **64** (1993) 403

[8] J. E. Sader, *J. Appl. Phys.* **84** (1998) 64

[9] Nanotec Electronica, Centro Empresarial Euronova 3, Ronda de Poniente, 2 Edificio 2 - 1ª Planta - Oficina A, 28760 Tres Cantos, Madrid, Spain

WSxM software (V. 4.0, D. 7.4) downloadable from:
www.nanotec.es/download.htm

[10] A. L. Weisenhorn, P. K. Hansma, T. R. Albrecht, and C. F. Quate, *Appl. Phys. Lett.* **54** (1989) 2651

[11] R. Wiesendanger in *Scanning Probe Microscopy and Spectroscopy*, 1st edn. (Cambridge: Cambridge University Press, 1994), chapter 2, p. 235

[12] C. M. Mate and V. J. Novotny, *J. Chem. Phys.* **94** (1991) 8420

[13] G. Meyer and N. M. Amer, *Appl. Phys. Lett.* **57** (1990) 2089

[14] C. D. Frisbie, L. F. Rozsnyai, A. Noy, M. S. Wrighton, and C.M. Lieber, *Science* **265** (1994) 2071

[15] R. M. Overney, E. Meyer, J. Frommer, D. Brodbeck, R. Luthi, L. Howard, H.-J. Guntherodt, M. Fujihara, H. Tankano, and Y. Gotoh, *Nature* **359** (1992) 133

[16] C. P. Green, H. Lioe, J. P. Cleveland, R. Proksch, P. Mulvaney, and J. E. Sader, *Rev. Sci. Instrum.* **75** (2004) 1988

[17] J. W. Gibbs, *Nature* **59** (1899) 200 and 606

[18] J. Chamberlain in *The Principles of Interferometric Spectroscopy*, edited by G. W. Chantry and N. W. B. Stone (Wiley-Interscience Publication, 1979), chapter 8., p. 227

[19] P. Jacquinot, *Rep. Prog. Phys.* **23** (1960) 267
P. Jacquinot, *J. Opt. Soc. Amer.* **44** (1954) 761

[20] P. Fellgett, *J. Phys. Radium* **19** (1958) 187

Chapter 3

Optical and Surface Characterisation of As-Received Wafers

3.1 Introduction

The ZnO wafers studied herein were purchased from three different growers; the Eagle-Picher, Rubicon, and Crystal companies (references given below). All wafers were (0001)-oriented and 10×10×0.5 mm in dimension. The Crystal and Rubicon wafers were subsequently sliced into smaller samples with dimensions of ~ 5×4 mm by the Crystal GmbH corporation.

In this chapter the photoluminescence, reflectance and surface topography of the as-received ZnO samples are examined and compared. Although the measurements presented in *Chapter 5* largely concentrate on the Rubicon wafers, a comparison is nonetheless useful and references to the other wafers are made throughout the discussion. In *Chapter 4*, concerning the adsorbed fluid layer present on each polar face, all wafers are examined. It is therefore necessary to characterise each material before any experiments are conducted so that these results may be used as a reference for the subsequent interpretation of experimental data.

3.2 *Eagle-Picher Material – Optical Characteristics*

The (0001)-oriented Eagle-Picher [1] wafer was grown by the Seeded Vapour Phase Transport method (SVPT). Both the $(000\bar{1})$ O- and (0001) Zn-terminated faces were polished in-house by Eagle-Picher using a chemo-mechanical technique, the exact nature of which has not been publicly released. The donor concentration is expected to be in the 1×10^{17} cm^{-3} range [2], due to H and probably Al and Ga donors, while the acceptor concentration is about 2×10^{15} cm^{-3}, composed of Zn vacancies [3]. Based on preliminary measurements by the Eagle-Picher company, the dislocation density is estimated to be in the ~ 10^4 to 10^5 cm^{-2} range [4].

Figure 3.1 shows bound-exciton (BE) luminescence from the O- and Zn-surfaces of the Eagle-Picher material at 25 K. Both polar surfaces show intense BE emission features (labelled *A* to *H*) with narrow line-widths (~ 0.5 meV FWHM), although the peak intensity of each emission line observed from the Zn-terminated face is approximately half that of the corresponding line from the O-face. It should be noted that while the BE emission lines appear to be identical for both polar faces under excitation with a 325 nm HeCd line at ~ 40 mW power unfocused on the sample, some authors have reported significant differences between the $(000\bar{1})$ and (0001) faces on excitation with higher energy densities [5].

Figure 3.2 is a reproduction of a PL spectrum taken by *Schildknecht et al.* of Eagle-Picher material at 4.5 K [6]. In terms of the overall structure of this emission spectrum, the peaks assigned (D_{1b}^{0},X), (D_{1a}^{0},X), (D_{2a}^{0},X) and (D_{3a}^{0},X) by these authors are similar to the *A*, *B*, *G* and *H* lines assigned in *Fig. 3.1*. The separation between the (D_{1b}^{0},X) and (D_{1a}^{0},X) lines observed by *Schildknecht* is 1.1 meV, as is the separation between the *A* and *B* lines in *Fig. 3.1*. Furthermore, the separation in *Fig. 3.2* between the (D_{1b}^{0},X) and (D_{2a}^{0},X) lines, and also between the (D_{2a}^{0},X) and (D_{3a}^{0},X) lines, is 3.1 meV. This matches the separation of 3.1 meV observed between the *B* and *G* lines, and the separation of the *G* and *H* lines.

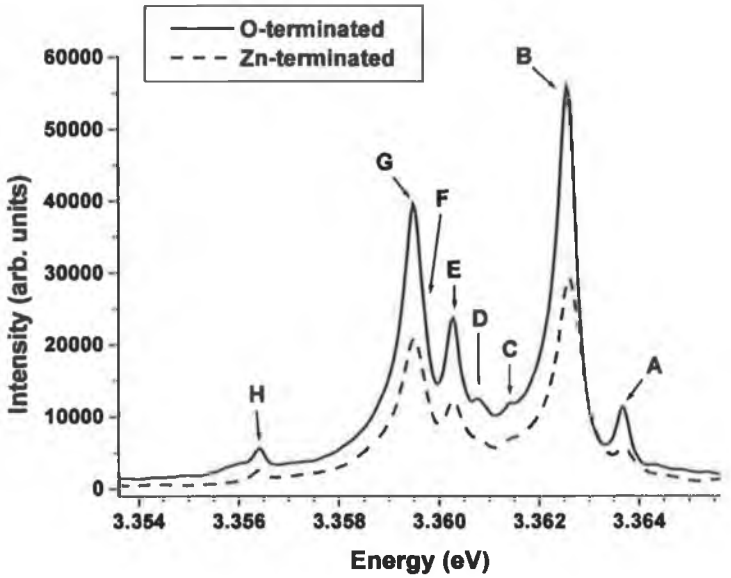

Figure 3.1: *PL of Eagle-Picher SVPT material at 25 K (resolution of ~ 0.1 meV). A number of closely-spaced BE peaks are observed with line widths ~ 0.5 meV (FWHM). The line marked 'F' is not well resolved and appears as a slight kink on the high energy side of line G.*

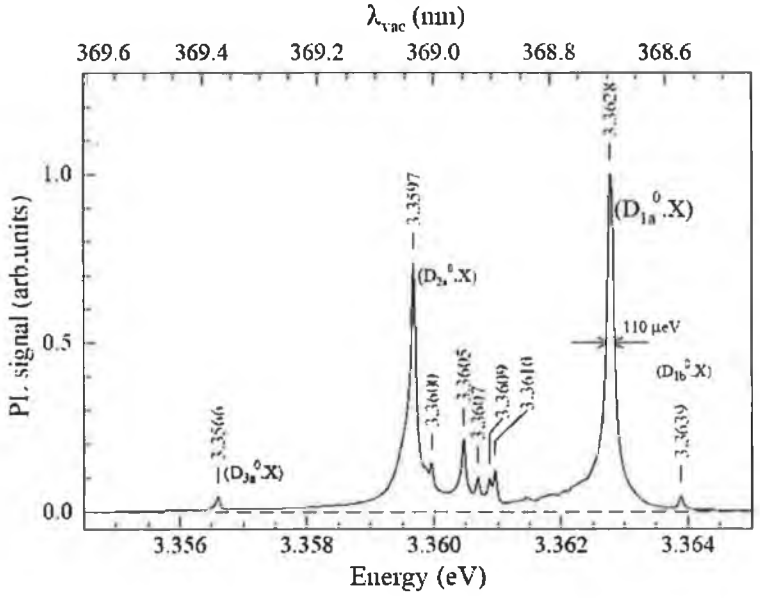

Figure 3.2: *PL spectrum of Eagle-Picher SVPT material at 4.5 K (Schildknecht et al.). The general structure of the spectrum is similar to that of Fig. 3.1.*

One would expect the lines shown in *Fig. 3.1* at 25 K to be offset to lower energy due to band-gap shrinkage compared to the data in *Fig. 3.2* which was obtained at 4.5 K. By shifting *Schildknecht's* spectrum to lower energy by 0.2 meV a strong correlation with the 25 K data presented here is observed (*Table 3.1*). The 0.2 meV shift is consistent with Varshni fits of temperature dependence data, but since these plots will also include free-exciton reflectance features we shall defer this discussion for the moment.

Table 3.1: *Comparison of observed emission line energies at 25 K with literature values at 4.5 K*

Energy @ 4.5 K[a] (eV)	***BE Line Assignment[b]***	***Energy @ 4.5 K – 0.2 meV[c]***	***BE Line Assignment[d]***	***Energy @ 25 K[e] (eV)***
3.3639	(D_{1b}^{0},X)	3.3637	*A*	3.3637
3.3628	(D_{1a}^{0},X)	3.3626	*B*	3.3626
			C	3.3614
3.3610		3.3608	*D*	3.3608
3.3609		3.3607		
3.3607		3.3605		
3.3605		3.3603	*E*	3.3603
3.3600		3.3598	*F*	3.3597 – 3.3599*
3.3597	(D_{2a}^{0},X)	3.3595	*G*	3.3595
3.3566	(D_{3a}^{0},X)	3.3564	*H*	3.3564

a *BE energy at 4.5 K as given in Fig. 3.2 by Schildknecht et al.* [6]
b *BE line assignment as given in Fig. 3.2*
c *BE energy as given in Fig. 3.2 shifted to lower energy by 0.2 meV to account for band-gap shrinkage at 25 K. The value of 0.2 meV is chosen simply because this provides the best correlation between the literature values and the experimental data presented here*
d *BE line assignment as given in Fig. 3.1*
e *BE energy at 25 K determined from Fig. 3.1 (± 0.1 meV)*
* *Peak F (Fig. 3.1) appears on the high energy side of peak G and is difficult to resolve. However the energy lies within the range quoted*

An identification of BE lines in ZnO has been found to be very difficult since they span a relatively narrow energy range and tend to vary in their position depending on the growth technique, strain conditions and impurity/vacancy content. In 1965 *Reynolds et al.* [7] assigned emission lines in ZnO platelets the designation I_1 to I_{10} and this naming convention is still largely used to this day. However, this has also been the source of much confusion due to the close separation of BE lines and authors tend now to give line energies rather than attempt to identify features with the *I* notation. *Table 3.2* shows the peak emission energies corresponding to each line, as observed by *Reynolds et al.* at 1.2 K.

Table 3.2: *Reynolds' et al. notation for BE emission lines in ZnO*

BE Line Assignment (*Reynolds et al.* [7])	***Energy @ 1.2 K (eV)***
I_1	3.3720
I_2	3.3680
I_3	3.3671
I_4	3.3621
I_5	3.3617
I_6	3.3609
I_7	3.3604
I_8	3.3601
I_9	3.3571
I_{10}	3.3536

Having correlated the lines observed in *Fig. 3.1* at 25 K with those of *Schildknecht* at 4.5 K, it is now necessary to identify them in terms of this I_n notation to facilitate a comparison with the literature. The line referred to as (D_{1a}^0,X) above is referred to as the I_4 line by *Thonke et al.* [8] based on *Reynolds*' notation. *Thonke* and *Schildknecht* observe this peak in Eagle-Picher material at 3.3628 eV at 4.2 and 4.5 K respectively, while *Reynolds* positions the I_4 line at 3.3621 eV at 1.2 K (*Table 3.2*). The discrepancy between the authors is 0.7 meV. Considering that the separation of the (D_{1a}^0,X) and (D_{1b}^0,X) lines is 1.1 meV, and *Schildknecht* observes lines with an energy

separation of just 0.1 – 0.2 meV (*Table 3.1*), the difficulty in identifying and correlating emission lines from different samples based on energy alone is apparent.

There is general consensus regarding the identity of the dominant I_4 line. Theoretical analysis suggests that hydrogen is a shallow donor in ZnO [2,9,10], and annealing studies have shown that the intensity of the I_4 line diminishes on annealing [11] with temperatures above 600°C, the temperature at which H leaves the lattice [12]. The line can be re-introduced on exposure of the samples to a H plasma [13]. The I_4 line has been attributed to neutral donor bound-excitons (D^0,X) [6,8,14,15], and investigation in high magnetic fields demonstrate that it is accompanied by a transition from an excited initial state [6]. Hence, in the above discussion, *Schildknecht* has assigned the I_4 line to a neutral donor bound-exciton (D_{1a}^0,X), and the line associated with a transition from its excited state as (D_{1b}^0,X). Line *B* in *Fig. 3.1* is therefore this I_4 hydrogen-related BE emission line, and *A* its excited state transition.

The line assigned as (D_{2a}^0,X) in Eagle-Picher material by *Schildknecht* (3.3597 eV) to neutral donor bound-excitons, corresponding to line *G* in *Fig. 3.1*, was previously designated as the I_8 line by *Thonke* [8]. The donor responsible is likely to be Ga [16-18]. Recently *Johnston et al.* have implanted radioactive ^{72}Zn into bulk ZnO crystals, which decays through ^{72}Ga to stable ^{72}Ge, and have shown that the intensity of the I_8 line follows the decay of Zn to Ga and subsequently from Ga to Ge [19].

The separation between the (D_{2a}^0,X) peak observed by *Schildknecht* and the slightly less intense line at higher energy (3.3605 eV) is 0.8 meV (*Fig. 3.2*), which corresponds to the separation between the I_8 and I_6 lines observed by *Reynolds* (*Table 3.2*) and between lines *G* and *E* in *Fig. 3.1* and *Table 3.2*. Thus the line referred to as *E* in *Fig. 3.1* is likely to be I_6. The I_6 line has been attributed to donor bound-excitons by a number of authors [8,20,21] and studies have suggested it is related to Al [22]. Based on this assignment of I_6 and I_8 lines, the (D_{3a}^0,X) line (line *H* in *Fig. 3.1*) is likely to be the I_9 line. Although *Schildknecht* has attributed this to donor bound-excitons, *Gutowski et*

al. attribute this line (as well as the I_6 and I_8 lines discussed above) to acceptor bound-excitons [23]. There is some evidence that the I_9 line is related to Na [24,25] which is expected to be an acceptor in ZnO. However, more recent investigations have shown that In, which is likely to be a donor, may be involved in the defect transition [26].

Figure 3.3 shows the same BE luminescence spectrum as *Fig. 3.1* from the O-terminated face of the Eagle-Picher material at 25 K, but with the line assignments changed from the initial *A-H* notation based on the above discussion. The Eagle-Picher material shows the most intense luminescence in the BE region and shall therefore be used as a reference in the identification of features in the hydrothermal ZnO samples discussed below. The dominant BE lines (I_4, I_6 and I_8) are each accompanied by lines relating to a thermalising transition from their respective excited states.

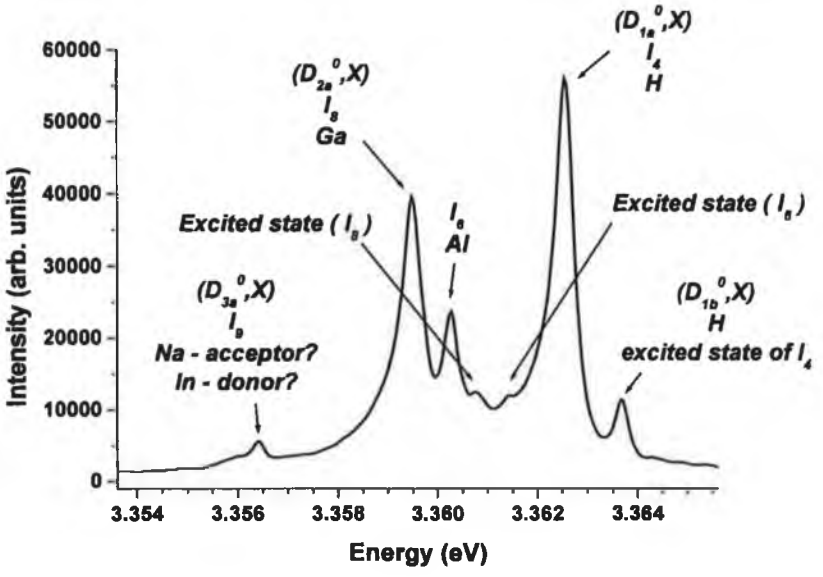

Figure 3.3: *PL spectrum of Eagle-Picher O-terminated surface at 25 K. The (D_n^0,X) notation is that of Schildknecht et al., while the I_n notation is that of Reynolds et al.. The donor (or acceptor in the case of I_9) species thought to be responsible for each BE line is also given.*

Figure 3.4 is a low resolution (~ 2 meV) PL spectrum, taken at 25 K, encompassing a broad emission energy region for both the O- and Zn-terminated Eagle-Picher surfaces. There is little evidence of green band emission from either polar face. A discussion of the green band itself shall be deferred to *Section 3.3*, as hydrothermal Rubicon material shows significant luminescence in this region.

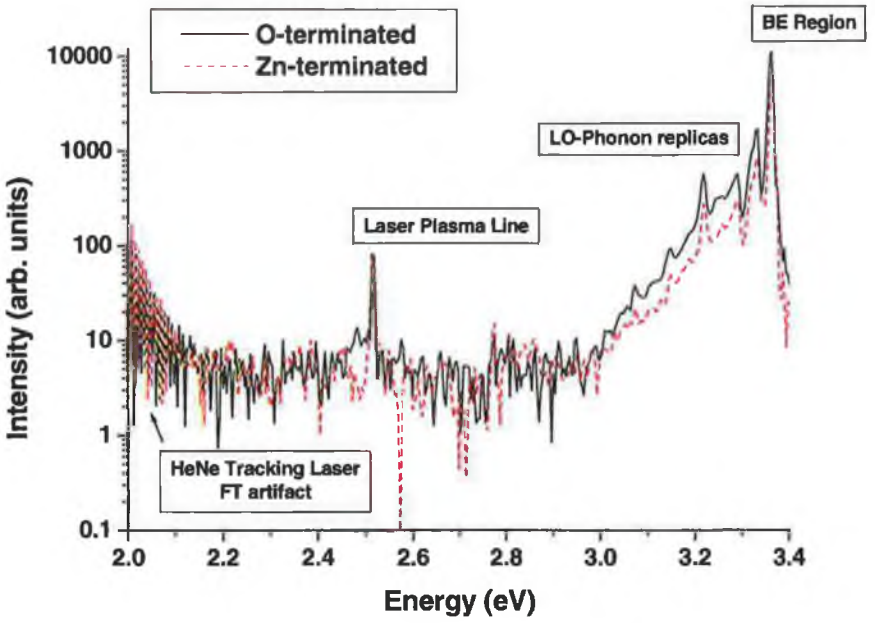

Figure 3.4: *Low resolution (~ 2 meV) PL spectrum of the O- and Zn-terminated polar faces of Eagle-Picher material at 25 K. Although the BE region and related LO-phonon replicas are clearly visible, there is no evidence of the green band between 2.8 and 2.2 eV.*

Reflectance spectra of the O- and Zn-terminated surfaces of the Eagle-Picher material show strong free-exciton (FE) resonances at 25 K corresponding to excitons (X) where the electron has been excited from either the A (X_A) or B (X_B) valence bands (*Figure 3.5*). The excited states of the free-excitons are also visible in the reflectance spectra, although they are not well resolved, appearing to have a slight sinusoidal structure. The energy of the excitonic transition is assumed to be located at the inflection point of the resonance [21]. However, in the case of the X_A free-exciton, where the resonance feature is relatively narrow there is a separation of 2 meV from the high energy maximum of the resonance to its low energy minimum representing the

longitudinal-transverse (LT) splitting (*Chapter 6*), whereas the separation for the X_B exciton is 10 meV. These figures compare well to the literature values of 1.8 and 10.2 meV for the X_A and X_B LT splitting respectively [27], considering that the resolution of the reflectance spectra is ~ 0.5 meV. The X_A and X_B energies are ~ 3.376 and ~ 3.384 eV respectively for the O-terminated surface, where the energy is taken from the maximum of the corresponding resonance peak which is close to the transverse exciton energy (see *Chapter 6*). The energies of the free-excitons on the Zn-terminated face are shifted to lower energy by ~ 1 meV for X_A and ~ 0.5 meV for X_B. As with the PL spectra above, there is a clear difference in the intensity of Zn-terminated features compared to those of the O-terminated surface. In energy regions far from the excitonic resonances (3.8 – 3.5 eV), the reflectivity is approximately 30% for the O-face and 10% for the Zn-face.

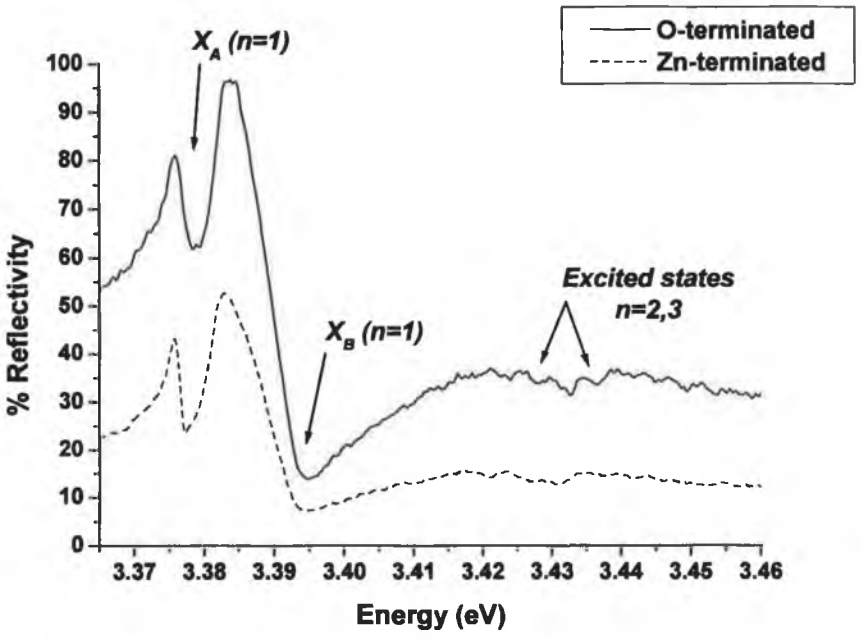

Figure 3.5: *Reflectance spectra of the O- and Zn-terminated faces of Eagle-Picher material at 25 K. Both faces exhibit strong exciton resonances corresponding to the A (X_A) and B (X_B) free-excitons, with evidence of excited states.*

Figure 3.6 shows the above reflectance spectrum (25 K) from the O-terminated face (*Fig. 3.5*) superimposed on a PL spectrum of the same face at 50 K. A number of broad PL features are observed at energies below 3.34 eV. The broad peak between ~ 3.22 – 3.24 eV is ~ 72 meV from the feature between ~ 3.30 – 3.32 eV. Projecting to higher energy by a further 72 meV places one close to the transverse energy of the X_A free-exciton observed in reflectance spectra. Similarly if one takes the transverse energy of the X_B free-exciton resonance and projects to lower energy by 72 meV, one arrives at the higher energy side of the same broad features. The data therefore compares well with the longitudinal optic (LO) phonon energy of 72 meV [28]. The exact location of the *A* and *B* LO phonon replicas are difficult to resolve due to the broad nature of the replicas, and at a 45° angle of incidence the reflectance maxima do not correspond directly to the transverse energy of the excitons. Nevertheless there is a good correlation between reflectance and PL features and the non-normal reflectance set-up provides a reasonable and useful measure of the free-exciton energies.

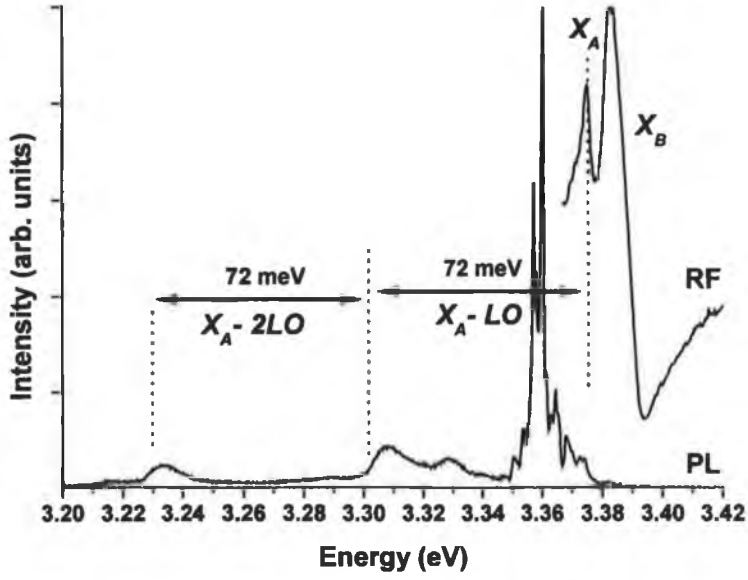

Figure 3.6: *Reflectance (RF) at 25 K and photoluminescence (PL) at 50 K of the O-terminated face of Eagle-Picher material. Broad PL features are observed at lower energy than the BE lines, the separation of which relates well to the LO phonon energy of 72 meV reported in the literature* [28]. *Projection to higher energies by the values indicated show a correlation to the position of the X_A and X_B free exciton resonances observed in RF spectra.*

In the above discussion it was necessary to shift the PL data obtained by *Schildknecht et al.* [6] (*Fig. 3.2*) by 0.2 meV to lower energy in order to compare BE line positions with the 25 K data presented here (*Fig. 3.1* and *Table 3.1*). It is possible to estimate the shift in BE line position and FE energies with increasing/decreasing temperature using the semi-empirical Varshni equation [29]:

$$E(T) = E(0) - \frac{\alpha T^2}{\beta + T}$$

Eqn. 3.1

where $E(T)$ is the band-gap energy at temperature T, $E(0)$ is the band-gap energy at 0 K, and α and β are fitting parameters. *Ko et al.* examined the properties of ZnO epilayers on CaF_2 substrates and, based on curve fits of the change in energy as a function of temperature of a line corresponding to the (D_{1a}^0,X) or I_4 discussed above, obtained values of -7.2×10^{-4} eV/K and −1077 K for α and β respectively [30], where the assumption made is that the change in band-gap energy is mirrored in the change of both free-exciton and bound-exciton energy. Using reflectance and photoluminescence spectra to determine the position of the X_A exciton as a function of temperature in a bulk ZnO crystal, *Boemare et al.* [21] have similarly obtained values of -6.7×10^{-4} eV/K and -672 K for α and β respectively.

Figures 3.7(a) and *(b)* are graphs of the observed change in energy of the I_4 and I_8 PL BE lines, and the *A* and *B* FE reflectance resonances, as a function of temperature between 20 and 100 K. Missing data points at higher temperatures are due to difficulties in assigning an energy due to the broad nature of features. In *Fig. 3.7(a)* the Varshni equation is used to fit the temperature data with the values given for α and β by *Ko et al.*. The extrapolated energies for the I_4 and I_8 lines at 4.5 K are 3.3631 and 3.3599 eV respectively based on these parameters, representing a shift to higher energy by ~ 0.5 meV compared to the 25 K data presented in *Table 3.1*. Similarly, the FE resonances are determined to occur at 3.376 and 3.383 eV for the *A* and *B* excitons respectively at 4.5 K, where the energy quoted was taken from the maximum of the resonance which roughly corresponds to the transverse energy. Given that the resolution of the

reflectance data is ~ 0.5 meV, these figures suggest a shift to higher energy of the resonances at 4.5 K by less than 1 meV compared to the 25 K data presented in *Fig. 3.5* and are therefore consistent with the 0.5 meV shift extrapolated for the BE PL lines.

In *Fig. 3.7(b)* the energies at lower temperatures are obtained using the Varshni equation with the values of α and β obtained by *Boemare et al.*, but the fit is clearly not as good as that of *Fig. 3.7(a)*. Finally, *Fig. 3.7(c)* is a fit taking an α value of -6.7×10^{-4} eV/K (*Boemare et al.*) and a β value of –1077 K (*Ko et al.*) and is found to match the temperature dependence data of the BE PL lines more closely. From this plot the extrapolated energies at 4.5 K are 3.3628 and 3.3597 eV for the I_4 and I_8 lines respectively, which match the experimental energy determination of these lines reported by *Schildknecht et al.* at 4.5 K. The FE resonances occur at 3.376 eV for the *A* exciton and 3.383 for the *B* exciton.

To summarise the analysis, a comparison has been made between the PL spectrum of BE emission lines observed here at 25 K with that of *Schildknecht et al.* at 4.5 K. One finds that despite the difference in temperature, the dominant lines remain observable at 25 K. The energy shift required for the 4.5 K line positions to match those at 25 K is only ~ 0.2 meV, which we find to be consistent with a Varshni fit using literature parameters. The BE lines have been identified in terms of the *Reynolds'* notation and hence in terms of the donor or acceptor thought to be responsible based on the literature. One also finds that the Eagle-Picher wafers have virtually no green band luminescence. The estimates of the *A* and *B* free-exciton LT splitting, through examination of the energy difference between the reflectance maxima and minima, are found to be close to the literature values. Using the reflectance spectra as a reference, photoluminescence features corresponding to the LO phonon replicas of the *A* and *B* free-excitons have been identified. Finally, one notes the differences in the overall intensity of reflected light, and the shift in energy of resonances between the O- and Zn-faces which may be related to the surface preparation technique.

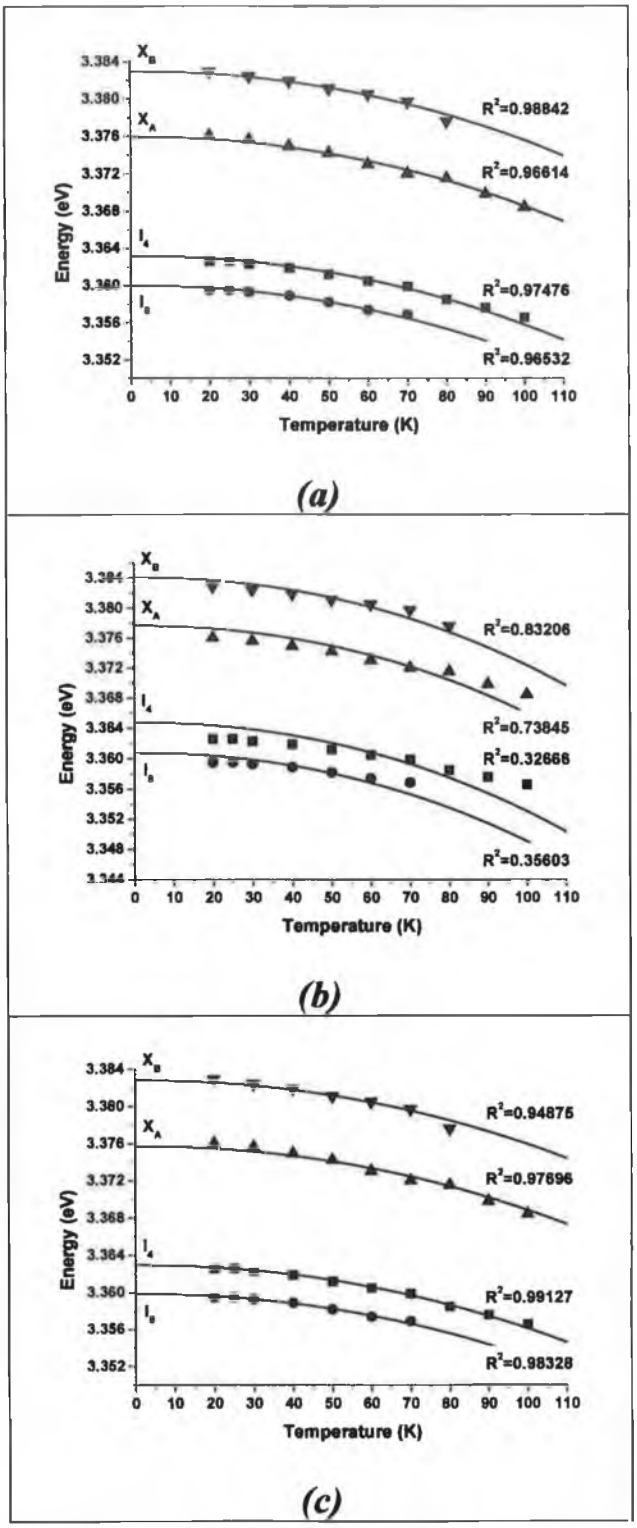

Figure 3.7: *In (a) the energy change of the I_4 and I_8 lines, and the A and B FEs, as a function of temperature have been fit to a Varshni plot using parameters given by Ko et al.. Plot (b) is a fit using the values of Boemare et al.. Combining the α value given by Boemare et al. and the β value given by Ko et al., one finds that the Varshni fit more closely matches the experimental data for the BE lines (c). The predicted energies of both BE lines in plot (c) at 4.5 K match the experimental values given by Schildknecht et al..*

3.3 Rubicon Material – Optical Characteristics

Hydrothermally-grown (HT) (0001)-oriented wafers were purchased from Rubicon Technology [31], and were mechanically epi-polished on either the $(000\bar{1})$ O- or (0001) Zn-terminated faces. In the discussion that follows, when referring to O- or Zn-terminated samples, it should be noted that it is the polished face that is under examination. The wafers originally had dimensions of 10×10 mm and a thickness of 0.5 mm, but were subsequently sliced by the Crystal corporation [32] into 4×5 mm samples using a saw blade of 150 μm width. Photoluminescence and reflectance measurements taken before and after indicate that the optical properties of the wafers were not adversely affected by the dicing process or the methanol rinse employed by Crystal to clean samples. The dislocation density of the Rubicon wafers is approximately 10^2 per cm^2 and the two major impurities are Ni and Fe at about 10^{-4} % for each. All other impurities are in concentrations less than 10^{-4} % [33].

Figure 3.8 is a PL spectrum of the polished O- and Zn-terminated surfaces of Rubicon material at 25 K. It is immediately obvious that there are substantial differences in the BE luminescence of these HT samples compared to the SVPT Eagle-Picher wafer discussed above. The O-terminated face exhibits relatively strong luminescence (although the intensity of the dominant peak in *Fig. 3.8* is just 5% that of the I_4 line in the Eagle-Picher sample), while the Zn-terminated face shows no BE emission whatsoever at this temperature. There are six significant O-terminated BE lines, labelled *I* to *N* in *Fig. 3.8*. The dominant peak *J* lies at 3.3605 eV, which is close in energy to the 3.3603 eV I_6 Al-related line observed in Eagle-Picher ZnO at 25 K, and has a FWHM line-width of ~ 0.4 meV. *Reynolds* and *Schildknecht* observe a separation of 0.8 meV between the I_6 and I_8 lines and, assuming that line *J* is indeed the I_6 BE peak, the I_8 line would lie at the low energy side of I_6. One observes a slight kink on the low energy side of peak *J*, indicated by *K*, with roughly the right energy separation to be consistent with the I_6 and I_8 assignment.

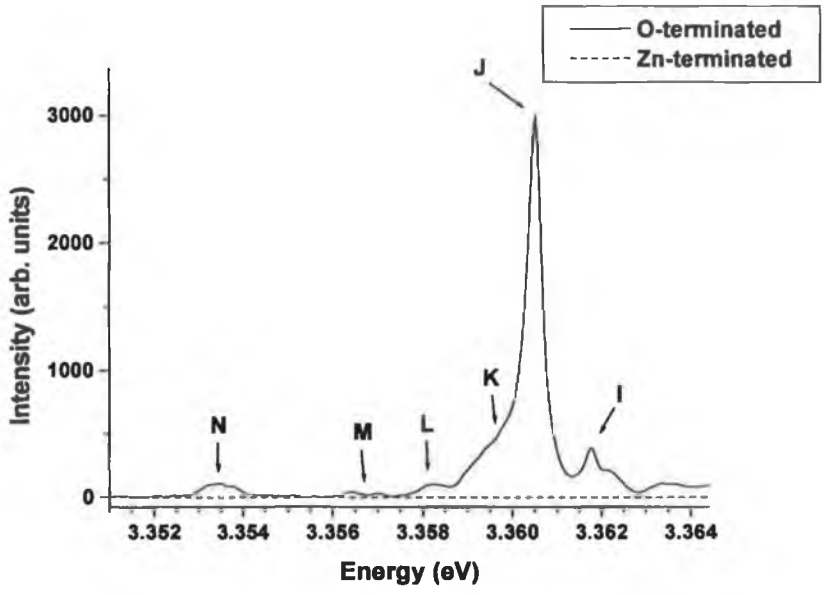

Figure 3.8: *PL of Rubicon HT material at 25 K (resolution of ~ 0.1 meV). A number of BE peaks are observed, and have been designated I-N. The line marked 'K' is not well resolved and appears as a slight kink on the low energy side of line J.*

The broad feature *N* at ~ 3.3535 eV is ~ 7 meV from line *J*, which compares well to the separation of 7.3 meV for the I_6 and I_{10} lines given in *Table 3.2*. The I_{10} line has been previously assigned to acceptor bound-excitons, with some evidence that the acceptor is Li [25]. This line is not observed in the Eagle-Picher SVPT material, suggesting that the defect responsible may be incorporated during the HT growth process. Although the exact growth details are not available for the Rubicon wafers, LiOH can be used as a solvent in this technique [34].

The separation between the *N* and *M* features is ~ 3.2 meV, which is close to the 3.5 meV observed by *Reynolds* between the I_{10} and I_9 lines. Therefore, line *M* is probably the I_9 line. In *Fig. 3.8* there appears to be two small peaks near the marked location of *M*, but these could be different aspects of a single broad feature where the decrease in intensity in the mid-region is due to a slight variation in the phase acquisition of the FT spectrometer. In any case, if one takes this centre point as the energy of peak *M*, the energy is determined to be 3.3567 eV which is close to the 3.3564 eV observed for the I_9 line in Eagle-Picher material at 25 K.

Line *I* at 3.3618 eV is 1.3 meV higher in energy than line *J* (I_6) and is likely to be due to a transition from an excited state of I_6. Its energy corresponds closely to the energy of the peak labelled '*C*' in relation to the Eagle-Picher material (3.3614 eV), above. Line *L* (3.3582 eV) does not correlate with any line observed by *Schildknecht* or *Reynolds*, although it lies at an energy of approximately 1.5 meV higher than line *M* and may be the excited state transition of the I_9 line (*M*). *Figure 3.9* shows *Fig. 3.8* again, with the line assignments altered from the *I-N* notation based on the above discussion. In every case, BE features observed in the O-terminated Rubicon samples are shifted to higher energy by 0.2 – 0.4 meV compared to the same lines observed in Eagle-Picher material at equivalent temperatures. This shift may indicate slightly different strain conditions in the Rubicon, compared to the Eagle-Picher, surfaces due to the epi-polishing procedure.

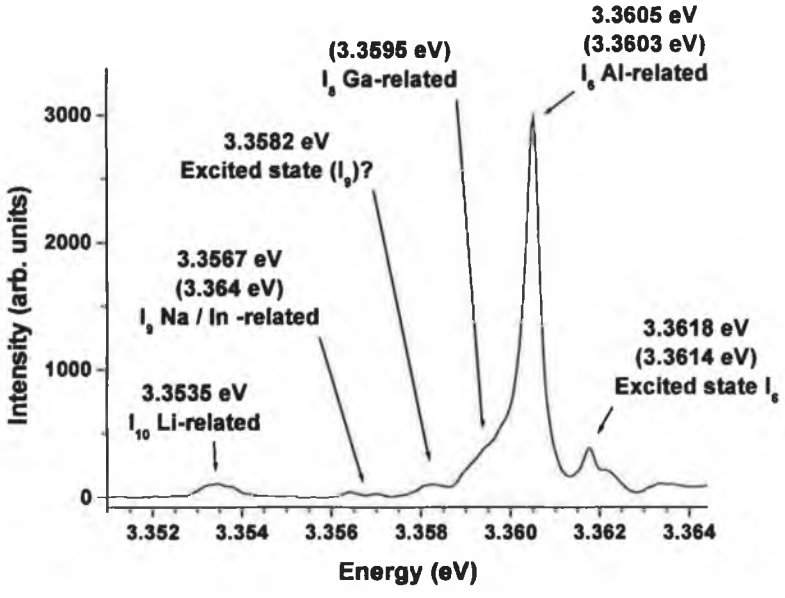

Figure 3.9: *BE emission line assignments for the O-terminated surface of the Rubicon wafers (25 K), based on the Eagle-Picher material discussed above. The energy of each line is shown along with the energy of the corresponding feature from the Eagle-Picher wafer at 25 K (values in parentheses) and the I_n notation introduced by Reynolds. The Rubicon I_8 line appears on the low energy side of the I_6 peak, and although an exact energy determination is difficult, it lies close to the expected energy based on the Eagle-Picher material.*

Figure 3.10 shows the reflectance spectra from each polar face of the Rubicon wafer at a temperature of 25 K. Unlike the Eagle-Picher material, Rubicon samples only exhibit strong excitonic resonances for the O-terminated surface. The maxima of the *A* and *B* resonances (transverse energy) are at ~ 3.376 and ~ 3.383 eV respectively, with an LT splitting of ~ 1 meV for X_A and ~ 11 meV for X_B. These values are, within the ~ 0.5 meV resolution limit, virtually identical to those of the Eagle-Picher wafer discussed above.

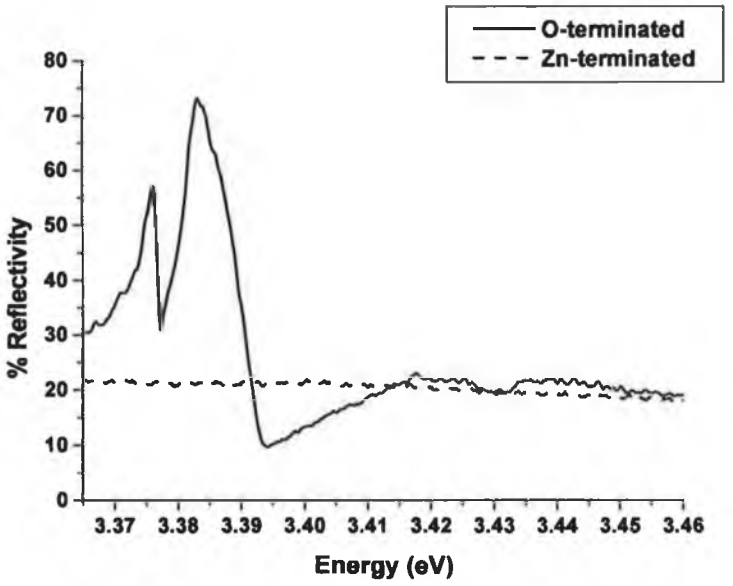

Figure 3.10: *Reflectance spectra of O- and Zn-terminated surfaces of Rubicon ZnO material at 25 K. Optically the excitonic resonances of the A and B FEs are similar to that of the Eagle-Picher material in the case of the O-face, with LT splitting values and transverse exciton energy almost equivalent. The overall reflectivity of each polar face is also similar to the Eagle-Picher wafers in regions far from the resonances. The Zn-face of the Rubicon wafers demonstrates only slight evidence of the B FE.*

Figure 3.11 is a PL spectrum of the O- and Zn-terminated Rubicon surfaces, showing the green band that extends from ~ 2.0 – 2.8 eV. The green band is associated with transitions from deep levels and, in 1969, isotope substitution experiments by *R. Dingle* suggested the involvement of Cu [35]. This Cu-related emission band exhibits a pronounced LO-phonon structure, although it should be noted that a band emission is more frequently observed without such structure. This implies that there are at least two

different species of green band. The unstructured green band has been historically attributed to intrinsic defects such as interstitial O [36], O vacancies [37], interstitial Zn or Zn vacancies [38], However, *Leiter et al.* have demonstrated by optically detected magnetic resonance spectroscopy (ODMR) that the unstructured green band is a spin triplet recombination with properties similar to that of anion vacancies in ionic crystals, and conclude that it originates from O-vacancies [39].

Recent experimentation involving the implantation of radioactive isotopes has demonstrated that the structured green band intensity increases over a time that roughly correlates with the half-life decay of the implanted species. This behaviour has been attributed to the creation of vacancies as a consequence of the large recoil energy of the radioactive isotopes used. A comparison of this recoil energy and the theoretical binding energy of Zn and O atoms in the ZnO lattice suggest that it is Zn-vacancies, rather than Cu, that are responsible for the structured green band [40].

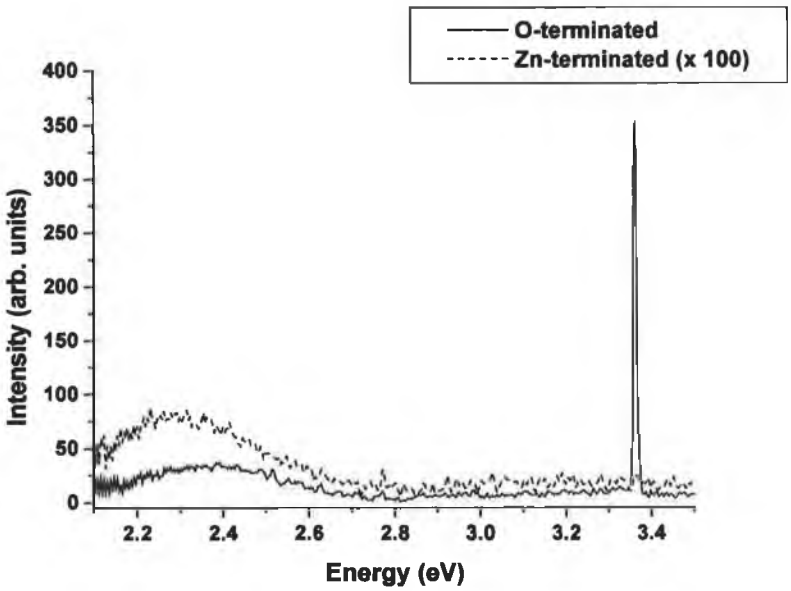

Figure 3.11: *PL spectrum of green band emission at 25 K of the O- and Zn-terminated surfaces of the Rubicon material. The green band is relatively weak, approximately 10% of the BE peak intensity for the O-terminated face, while the intensity for the Zn-face is just 2% of that from the O-terminated surface.*

3.4 Crystal Material – Optical Characteristics

As with the Rubicon wafers discussed above, the Crystal ZnO wafers [32] were grown by a hydrothermal technique, although both O- and Zn-terminated surfaces of all wafers were mechanically polished. The Crystal corporation was not able to supply any information regarding defect concentrations or dislocation densities. The wafers originally had dimensions of 10×10 mm, but were sliced into 4×5 mm samples.

Figure 3.12 shows the PL spectra of the BE region of both Crystal polar faces at a temperature of 25 K. Only a single, weak and broad (FWHM of ~ 16 meV) BE line is observed for the O-terminated surface, with a peak energy at 3.3608 eV. For comparison, the intensity of this line is just ~ 0.2% and ~ 0.1% of the intensity of the dominant line in the Eagle-Picher or Rubicon material respectively. Since there are no other BE lines present, and because the line is extremely broad and weak, it is difficult to identify in terms of the literature assignments. The Zn-terminated surface demonstrates only slight BE luminescence at this temperature, with a peak roughly matching the energy of that for the O-face.

The reflectance spectra at 25 K (*Figure 3.13*) reveal a substantial reduction in the oscillator strengths of the FEs, in the case of the O-terminated surfaces, compared to the other ZnO material. Although the *B* free-exciton is clearly visible there is only slight evidence of the *A* free-exciton. The transverse energies for the O-face are ~ 3.362 eV and 3.369 eV for the *A* and *B* FEs respectively, although it is clear that there are obvious difficulties in determining the maximum of each resonance feature. These values represent a shift of approximately 14 meV to lower energy of the transverse energy when compared to both Eagle-Picher and Rubicon wafers, suggesting a substantial difference in the strain conditions. The LT splitting is ~ 5 meV for the *A* and ~ 17 meV for the *B* free-exciton, compared to values of ~ 1 and ~ 10 meV respectively for the other ZnO wafers, though the grossly distorted line shape makes such estimates very

unreliable. For the Zn-terminated surface, only the *B* FE resonance is observed. The transverse energy is roughly 3.368 eV, and the LT splitting is ~ 19 meV.

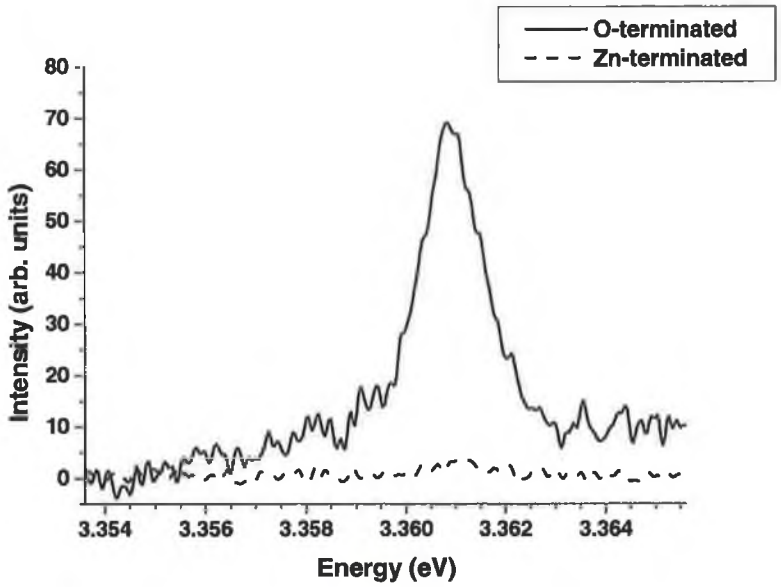

Figure 3.12: *PL spectra of the Crystal polar faces at 25 K. Only a single BE peak is observed, with a peak energy at 3.3608 eV and FWHM of ~ 16 meV.*

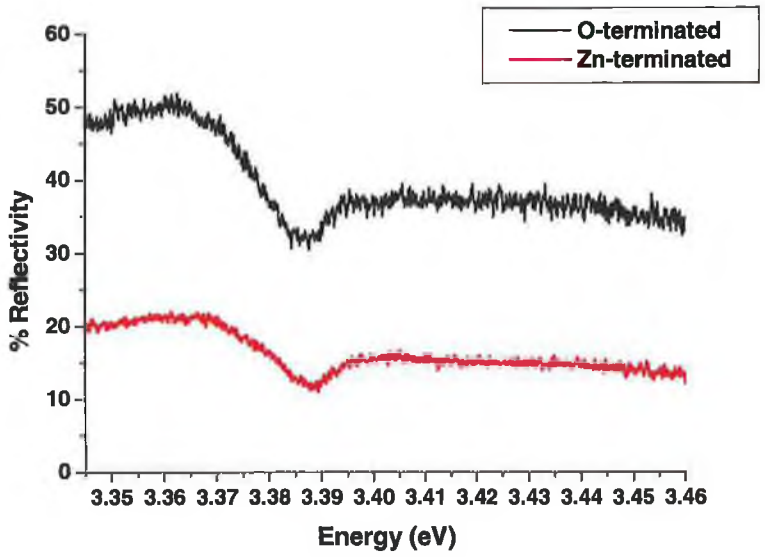

Figure 3.13: *Reflectance spectra of the Crystal polar faces at 25 K. One observes a substantial reduction in the strength of the A FE, and a severely damped B exciton oscillation. The transverse energy of both FEs is shifted to lower energy by ~ 15 meV and the LT splitting also increases although such estimates are clearly rough indications due to the distorted line shapes.*

Figure 3.14 shows the PL spectra over a large energy region from each polar surface at 25 K. As with the Eagle-Picher wafer, there is little evidence of the green band.

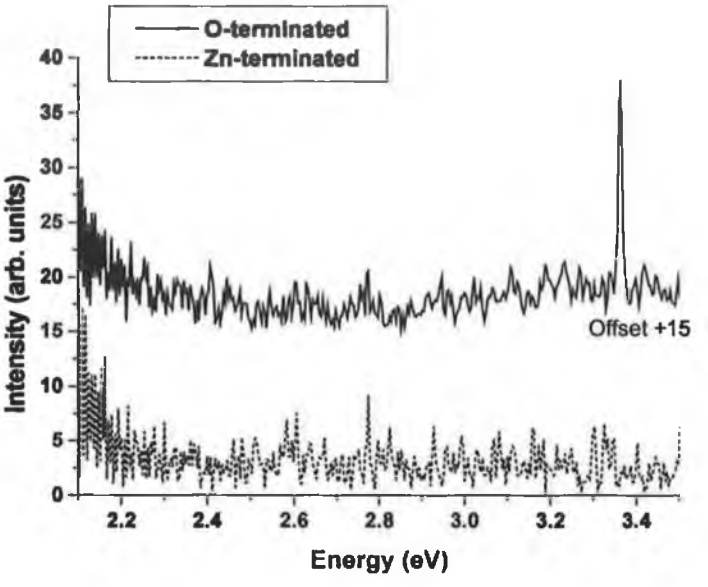

Figure 3.14: *PL spectrum at 25 K of both Crystal polar surfaces. There is no evidence of green band emission from either surface.*

3.5 Comparison of Surface Topography

It is clear from the above discussion that the ZnO wafers differ considerably in terms of the optical properties of the polar faces when compared to one another. Although this can be explained in terms of defect concentrations, growth methods and general 'quality' of the crystal, in this section the effect of the polishing technique applied to each face is examined.

All of the ZnO crystals were cleaned in an ultrasonic bath for five minutes using acetone, then for five minutes in toluene, followed by a further five minutes in acetone [41]. Both solvents were of ≥ 99% purity and purchased from Merck [42]. Although the majority of samples were subsequently dried using flowing nitrogen gas for a period of approximately two minutes, a number of wafers were rinsed with de-ionised water before drying. *Figure 3.15(a)* is a 50×50 μm AFM topographical image of the O-terminated surface of a Rubicon hydrothermally-grown crystal having been left in de-ionised water for approximately ten minutes. To the right of the image is a region that was masked using PTFE tape and, to the left, the region exposed to water. The ridge that runs from top to bottom is simply dirt that has collected under the edge of the PTFE mask and should be ignored. One observes that prolonged exposure to water etches the O-terminated face and it should be noted that this etching is not observed for Zn-terminated surfaces (for equivalent exposure times to water) or for material cleaned without the water rinse.

Figure 3.15(b) is a similar 50×50 μm scan of an O-terminated surface of a different Rubicon wafer exposed to de-ionised water, confirming that the observed etch pits are not sample specific. The largest pits have widths of ~ 1 μm and depths of ~ 50 nm, which are similar in dimension to the etch pits observed on exposure of the O-terminated surfaces to dilute acids for periods of two minutes or less. It is therefore believed that the same etch mechanism operates for acids and water and shall be discussed below in *Chapter 5*.

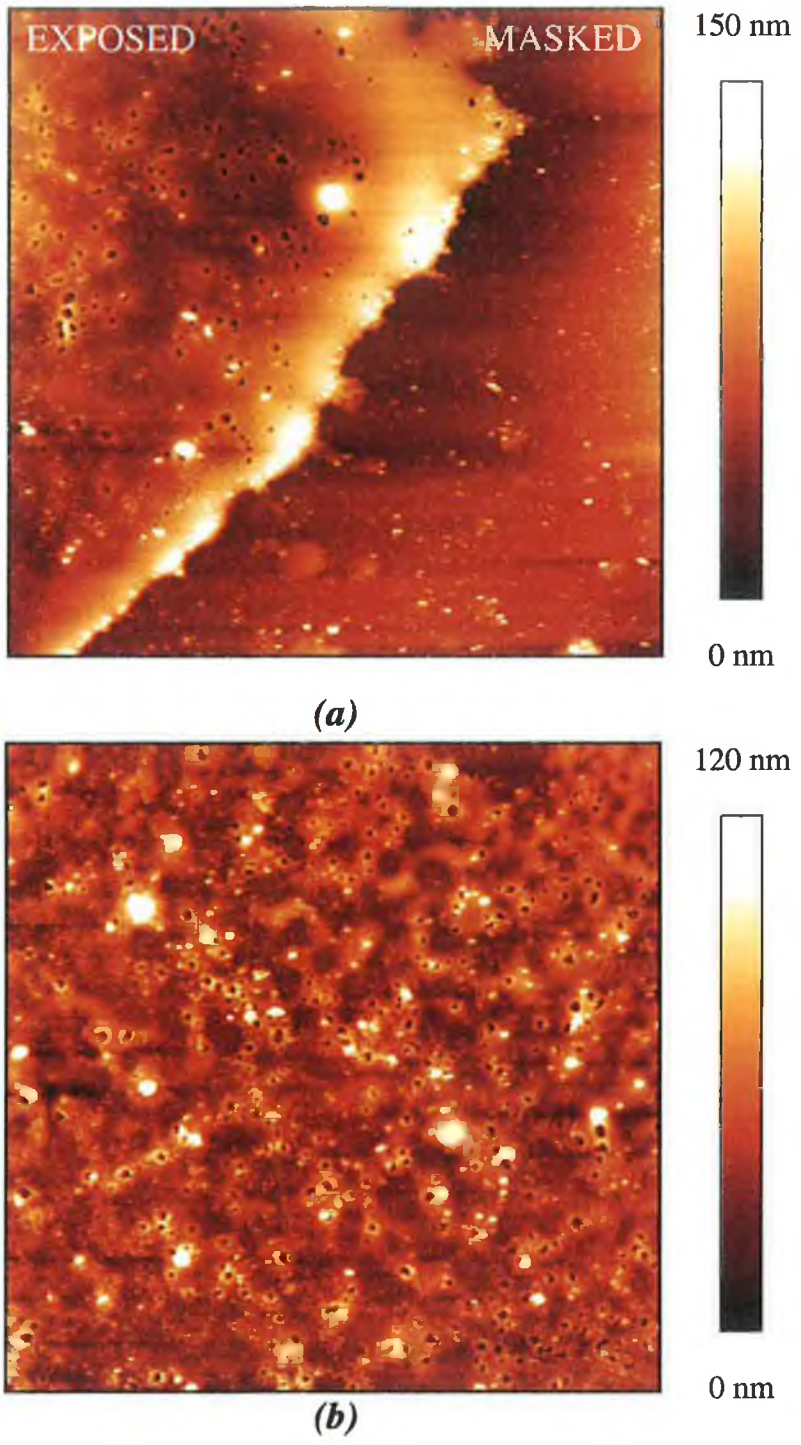

Figure 3.15: *50×50 μm AFM topographic scans of O-terminated Rubicon wafers after exposure to de-ionised water for a period of ~ 10 minutes. The top image (a) shows a region that has been exposed to and etched by the water (left) and a masked region that remains relatively untouched (right). The ridge running diagonally from top to bottom is dirt that was attached to the edge of the PTFE mask. The bottom image (b) is a scan from a different sample that was completely immersed in water without masking.*

The damage caused to O-terminated faces as a result of water exposure is believed to be cumulative and the results presented suggest that, where possible, water rinses of (0001)-oriented wafers should be avoided. Also, as shall be demonstrated in *Chapter 4*, fluid layers of significant thickness are found on the O-terminated surface in ambient conditions, indicating that ZnO crystals should be stored with desiccant to avoid surface damage due to exposure to water vapour.

Figure 3.16 shows 50×50 μm AFM topographic scans of the O- and Zn-terminated surfaces of each wafer and it can be seen that the O-faces (*Figs. 3.16(a)*, *(c)*, and *(e)*) have a higher concentration of residual particulates after cleaning compared to the Zn-faces (*Figs. 3.15(b)*, *(d)*, and *(f)*). This shall be discussed further in *Chapter 4*, where capillary forces as a result of adsorbed fluid layers are examined. *Table 3.3* gives the RMS surface roughness values as determined for the images shown in *Fig. 3.16*, and are deemed to be typical of the surfaces as a whole. The RMS roughness figures for the Eagle-Picher sample are ~ 7.0 nm for both the O- and Zn-terminated surfaces and it is difficult to distinguish between the surfaces on the basis of topography alone. Nevertheless, the fact that particulate material is preferentially attached to the O-terminated surfaces suggests that the determined roughness for this face is somewhat misleading. One generally finds, using smaller AFM scan sizes, that the O-terminated surface has a slightly lower RMS value than the Zn-face. The Rubicon wafer has an RMS roughness of 1.2 nm and 5.2 nm for the epi-polished O- and Zn-faces, respectively. Although the O-terminated surface is relatively smooth and uniform, the Zn-terminated face is crossed with a high concentration of, presumably, polish-induced scratch marks. Both surfaces of the Crystal samples are scratched as a result of the mechanical polish although the surface RMS figures (~ 3 nm) for the O- and Zn-terminated faces are similar.

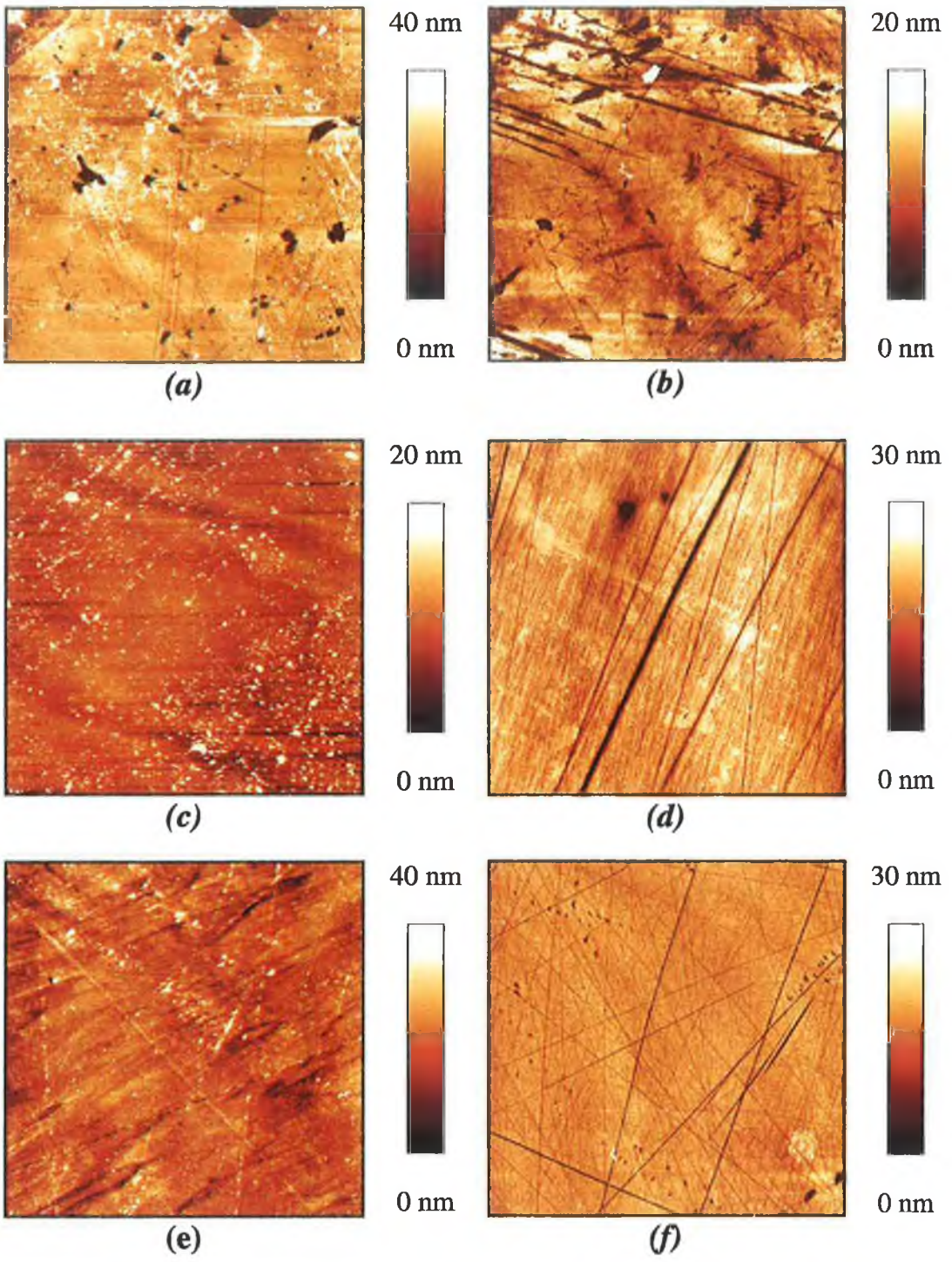

Figure 3.16: *50×50 μm images of the O-terminated (a, c, e) and Zn-terminated (b, d, f) faces of Eagle-Picher (top), Rubicon (middle) and Crystal (bottom) samples respectively after ultrasonic cleaning. In each case one observes a higher concentration of residual particulates, shown as white specks in the above images, on the O-terminated surfaces compared to the Zn-faces.*

Table 3.3: *Comparison of surface roughness of each wafer and associated reflectivities*

Sample	***O-surface RMS roughness (nm)***	***Zn-surface RMS roughness (nm)***	***% Reflectivity (O-surface)***	***% Reflectivity (Zn-surface)***
Eagle-Picher	7.0	6.8	~ 30	~ 10
Rubicon	1.1	5.2	~ 20	~ 20
Crystal	2.9	2.7	~ 35	~ 15

In general, one finds on the basis of *Table 3.3* and the AFM images in *Fig. 3.16* that there is no correlation between the overall reflectance or PL data and the RMS surface roughness values for each wafer. Certainly the overall reflectivity of the samples should not be affected by surface topography to any great extent since the topographic variations across the face are much smaller than the examined wavelengths of reflected light. The PL data is not expected to be dependent on the surface topography for this reason (i.e. that the topographic variations do not appreciably scatter the light) and is more likely to depend on surface recombination velocities and defect concentrations within the ~50 nm probe depth of the 325 nm HeCd laser line.

However, in *Chapter 5* where the surfaces of Rubicon wafers are etched, one does observe such a correlation between topography and reflected light intensity. This is because the scattering is appreciable due to relatively large scale of topographic features induced by etching, compared to the wavelengths of light examined.

3.6 X-ray Rocking Curves

In the case of the Eagle-Picher wafer the luminescence and reflectance resonances are strong for both polar surfaces. This behaviour is somewhat anomalous when compared to the Rubicon and Crystal samples, which both exhibit substantially reduced intensities/resonances for the Zn-terminated faces, in particular, despite the smoother polish finish compared to the Eagle-Picher material. One possible explanation could be that the chemo-mechanical polish applied by Eagle-Picher reduces the sub-surface strain, leading to improved optical characteristics.

Suscavage et al. have previously grown hydrothermal ZnO crystals and examined the effects of both a purely mechanical and Eagle-Picher's chemo-mechanical polishing on the optical properties of their samples' Zn- and O-terminated surfaces [43]. By examining x-ray rocking curves and attributing their FWHM widths to sub-surface strain, the authors reported both a reduction in the strain and subsequent improvement in luminescence after the chemo-mechanical polish compared to the purely mechanical polish.

Table 3.4, below, shows the rocking curve widths for each polar surface of the Eagle-Picher, Rubicon and Crystal wafers examined here. It is immediately apparent that, in fact, the Eagle-Picher surfaces have the widest rocking curves of all the samples and consequently, according to *Suscavage et al.*, the largest sub-surface strain! Although a reduction in strain may result if the same material is polished by the chemo-mechanical technique as opposed to a purely mechanical technique, this does not appear to hold true for different materials grown by different methods. It should be noted that the dislocation density of the SVPT Eagle-Picher wafer is estimated to be in the 10^4 – 10^5 cm^{-2} range, and ~10^2 cm^{-2} for the hydrothermal Rubicon material.

The Rubicon wafer exhibits a marked difference in the surface RMS roughness values obtained for the O-terminated faces (1.5 nm) and Zn-faces (5.2 nm). This is mirrored in the rocking curve widths of 0.040° and 0.052° for the O- and Zn-faces respectively. The Crystal polar surfaces have RMS values of ~ 2.9 and 2.7 nm for the O- and Zn-terminated faces respectively, and consequently similar rocking curve widths of ~ 0.028° for each surface. The Eagle-Picher polar surfaces, despite having similar topographic polish finishes, have remarkably different rocking curve widths which may be the result of some type of additional processing of the Zn-terminated surface, hence leading to improved optical characteristics.

Table 3.3: *Rocking curve widths (FWHM) of each polar surface of the ZnO wafers*

Sample	***Polar Surface***	***Rocking curve width (FWHM) (degrees)***
Eagle-Picher	**O**	0.066
	Zn	0.125
Rubicon	**O**	0.040
	Zn	0.052
Crystal	**O**	0.028
	Zn	0.029

3.7 Discussion of Results and Conclusions

Of the three different ZnO wafers examined herein, the Eagle-Picher sample has the most intense BE luminescence. The BE line-widths are relatively narrow (~ 0.5 meV FWHM) and the spectrum from each polar face is dominated by the hydrogen-related I_4 line. One observes somewhat anomalous behaviour when compared to the other samples in that both O- and Zn-terminated surfaces exhibit similar luminescence properties. The reflectance spectra show strong resonances of the *A* and *B* free-excitons for each polar face and evidence of their excited states. As with the PL, these results are somewhat contrary to the other wafers, where substantial reductions in the oscillator strengths are observed either for the Zn-terminated face in the case of the Rubicon wafers, or for both polar faces in the case of the Crystal wafers.

The optical properties of the Eagle-Picher material do not appear to be directly related to the mechanical aspects of the polish applied. Not only are both polar faces rougher than the other ZnO samples, but the sub-surface strain is also higher than for the other wafers, particularly for the Zn-terminated surface. This leads to the conclusion that it is intrinsic defects, or their absence, that are partly responsible for the enhanced optical properties, but one cannot discount the chemical aspect of the chemo-mechanical polish that may result in a passivation of the Zn-terminated surface in particular. The dominance of the hydrogen-related I_4 line is likely to be due to the fact that hydrogen is used as a transport gas in the SVPT growth technique. In *Chapter 5*, where the effects of etchants on optical properties are examined, it will be shown that some of the surfaces exposed to low pH acids (i.e. having a high concentration of H cations) exhibit unusually intense luminescence features near the position of the I_4 line despite highly damaged surfaces.

In the case of the Crystal sample, BE luminescence is weak from both polar faces and line-widths are broad (~ 16 meV FWHM). Reflectance spectra show distorted *B* free-exciton resonances and have virtually no *A* resonances. Since both the surface

roughness and rocking curve widths are low, one can conclude that the poor optical characteristics are largely due to intrinsic defects rather than the quality of the polish applied to the faces.

Finally, the Rubicon samples exhibit intense BE luminescence with narrow line-widths (~ 0.4 meV) and strong free-exciton resonances for the O-terminated surfaces only. The Zn-terminated faces reveal no BE features and only slight evidence of the *B* free-exciton in reflectance spectra. However, unlike the other hydrothermally grown wafers examined here, one observes substantial differences in both the surface RMS roughness values and rocking curve widths between each polar face. This suggests that the surface finish is, at least partially responsible for the diminished reflectance features from Zn-terminated surfaces since, in *Chapter 5*, a more detailed examination of the Zn-terminated surface of Rubicon wafers reveals that the polish-induced scratches have widths of the order of 200 nm. This hypothesis is tested by applying chemical etchants to the surfaces and one observes an improvement in free-exciton oscillator strengths on Zn-terminated surfaces as a result of a 'smoothing' of the faces when acids are applied with high lateral-to-vertical etch ratios.

3.8 References

[1] Eagle-Picher Technologies, L.L.C., 200 B.J. Tunnell Blvd., Miami, OK 74354, USA

[2] D. M. Hofmann, A. Hofstaetter, F. Leiter, H. Zhou, F. Henecker, B. K. Meyer, S. B. Orlinskii, J. Schmidt, and P. G. Barnov, *Phys. Rev. Lett.* **88** (2002) 45504

[3] F. Tuomisto, V. Ranki, K. Saarinen, and D. C. Look, *Phys. Rev Lett.* **91** (2003) 205502

[4] D. C. Look, Private Communication

[5] R. E. Sherriff, D. C. Reynolds, D. C. Look, B. Jogai, J. E. Hoelscher, T. C. Collins, G. Cantwell, and W. C. Harsch, *J. Appl. Phys.* **88** (2000) 3454

[6] A. Schildknecht, R. Sauer, and K. Thonke, *Physica B* **340-342** (2003) 205

[7] D. C. Reynolds, C. W. Litton, and T. C. Collins, *Phys. Rev.* **140** (1965) 1726

[8] K. Thonke, Th. Gruber, N. Teofilov, R. Schönfelder, A. Waag, and R. Sauer, *Physica B* **308-310** (2001) 945

[9] C. G. Van de Walle, *Physica B* **308-310** (2001) 899

[10] C. G. Van de Walle, *Phys. Rev. Lett.* **85** (2000) 1012

[11] D. C. Look, C. Coşkun, B. Clafin, and G. C. Farlow, *Physica B* **340-342** (2003) 32

[12] K. Ip, M. E. Overberg, Y. W. Heo, D. P. Norton, S. J. Pearton, C. E. Stutz, S. O. Kucheyev, C. Jagadish, J. S. Williams, B. Luo, F. Ren, D. C. Look, and J. M. Zavada, *Sol. Stat. Elect.* **47** (2003) 2255

[13] Y. M. Strzhemechny, J. Nemergut, J. Bae, D. C. Look, and L. J. Brillson, *Mater. Res. Soc. Symp. Proc.* **744** (2003) M3.9.1

[14] D. C. Reynolds, D. C. Look, B. Jogai, C. W. Litton, T. C. Collins, W. Harsch, and G. Cantwell, *Phys. Rev. B* **57** (1998) 12151

[15] K. Thonke, N. Kerwien, A. Wysmolek, M. Potemski, A. Waag, and R. Sauer in Physics of Semiconductors 2002, Institute of Physics Conference Series Number 171, edited by A.R. Long and J.H. Davies (IOPP, Bristol, 2002), paper number P22

[16] H. J. Ko, Y. F. Chen, S. K. Hong, H. Wenisch, T. Yao, and D. C. Look, *Appl. Phys. Lett.* **77** (2000) 3761

[17] H. Kato, M. Sano, K. Miyamoto, and T. Yao, *J. Crystal Growth* **237-239** (2002) 538

[18] F. Reuss, C. Kirchner, Th. Gruber, R. Kling, S. Maschek, W. Limmer, A. Waag, and P. Ziemann, *J. Appl. Phys.* **95** (2004) 3385

[19] K. Johnston, D. McCabe, M. O. Henry and the ISOLDE collaboration (CERN), submitted for publication

[20] D. C. Reynolds and T. C. Collins, *Phys. Rev.* **185** (1969) 1099

[21] C. Boemare, T. Monteiro, M. J. Soares, J. G. Guilherme, and E. Alves, *Physica B* **308-310** (2001) 985

[22] M. Schilling, R. Helbig, and G. Pensl, *J. Lumin.* **33** (1985) 201

[23] J. Gutowski, N. Presser, and I. Broser, *Phys. Rev. B* **38** (1988) 9746

[24] O. Schirmir and D. Zwingel, *Solid State Commun.* **8** (1970) 1559

[25] E. Tomzig and R. Helbig, *J. Lumin.* **14** (1976) 403

[26] B. K. Meyer, H. Alves, D. M. Hofmann, W. Kriegseis, D. Forster, F. Bertram, J. Christen, A. Hoffmann, M. Straβburg, M. Dworzak, U. Haboeck, and A. V. Rodina, *Phys. Stat. Sol. (b)* **241** (2004) 231

[27] J. Lagois, *Phys. Rev. B* **23** (1981) 5511;
J. Lagois, *Phys. Rev. B* **16** (1977) 1699

[28] R. L. Weiherr, W. C. Tait, *Phys. Rev.* **166** (1968) 791

[29] Y. P. Varshni, *Physica (Amsterdam)* **34** (1967) 149

[30] H. J. Ko, Y. F. Chen, Z. Zhu, T. Yao, I. Kobayashi, and H. Uchiki, *Appl. Phys. Lett.* **76** (2000) 1905

[31] Rubicon Technology, Inc., 3000 Lakeside Drive, Suite 105N, Bannockburn, IL 60015, USA

[32] Crystal GmbH, Ostendstraβe 2-14, Berlin D-12459, Germany

[33] Mark A. Campo, Materials Science Engineer, Rubicon Technology, Inc., Private communication

[34] T. Sekiguchi, S. Miyashita, K. Obara, T. Shishido, and N. Sakagami, *J. Crystal Growth* **214/215** (2000) 72

[35] R. Dingle, *Phys. Rev. Lett.* **23** (1969) 579

[36] M. Liu, A. H. Kitai, and P. Mascher, *J. Lumin.* **54** (1992) 35

[37] K. Vanheusden, W. L. Warren, C. H. Seager, D. R. Tallant, J. A. Voight, and B. E. Gnade, *J. Appl. Phys.* **79** (1996) 7983

[38] E. G. Bylander, *J. Appl. Phys.* **49** (1978) 1188

[39] F. Leiter, H. Alves, D. Pfisterer, N. G. Romanov, D. M. Hofmann, and B. K. Meyer, *Physica B* **340-342** (2003) 201

[40] T. Agne, K. Johnston, D. McCabe and the ISOLDE collaboration (CERN), submitted for publication

[41] M. J. Vellekoop, C. C. G. Visser, P. M. Sarro, and A. Venema, *Sensors Actuators A (Phys)* **A21-A23** (1990) 1027

[42] Merck chemicals supplied by: Gerard Laboratories Ltd., 35/36 Baldoyle Ind. Estate, Grange Road, Dublin 13, Ireland
Tel.: +353 1 8393 788
Fax : +353 1 8395 62

[43] M. Suscavage, M. Harris, D. Bliss, P. Yip, S.-Q. Wang, D. Schwall, L. Bouthillette, J. Bailey, M. Callahan, D. C. Look, D. C. Reynolds, R. L. Jones, and C. W. Litton, *MRS Internet J. Nitride Semicond. Res.* **4S1** (1999) G3.40

Chapter 4

The Dominant Role of Adsorbed Fluid Layers in Ambient Conditions

4.1 Introduction

During the acquisition of AFM topographic images presented in *Chapters 3* and *5* it was observed that deflection set-points, or the normal forces applied by the tip to the surface, generally need to be higher for O-terminated surfaces compared to Zn-terminated surfaces in order to acquire images. Although this behaviour could be explained in terms of slight variations in the experimental set-up, such as changes in the position on the cantilever from which the AFM laser was reflected, the relatively large number of cantilevers used, the number of topographic images obtained, and the frequency with which this behaviour was observed suggested that some other factor specific to the polar faces was responsible.

Large 50×50 μm topographic images of O- and Zn-terminated surfaces, as shown in the previous chapter, revealed differences in the efficacy of the cleaning procedure for each polar face and it was decided to investigate whether the increased concentration of residual particulate material on O-terminated surfaces was somehow linked to the requirement for larger deflection set-points for this face. A clue to the possible connection was observed on a particularly humid day when the application of the AFM tip appeared to create a square 'imprint', visible through the high-magnification of the AFM optical camera system, on an O-terminated surface. The imprinting was initially believed to be due to damage caused to the surface by the tip applying too high a force but the mark disappeared completely later in the day. It was concluded that a thin film of water had collected on the O-terminated surface and the scanning of the AFM tip had displaced this fluid, altering the appearance of the sample locally.

Previous studies of molecular adsorption onto Zn- and O-terminated faces suggest that it is the Zn-face that more strongly adsorbs a variety of species, such as CO [1]. The observed preferential adhesion of particulates to the O-terminated face is therefore somewhat contrary to these molecular adsorption studies. However, surface

adsorption experiments are generally conducted in ultra-high vacuum (UHV) conditions. The AFM images presented in this thesis were obtained in ambient environments and it is therefore suggested that the presence of adsorbed fluid layers on the polar surfaces may provide an explanation for the differences in particulate concentrations [2]. The O-terminated face is known to be strongly hydrophilic and this is seen in the etching behaviour of ZnO. Dangling bonds on the O-terminated face react strongly with the H^+ ions in conventional etchants, such as HCl [3], compared to low reactivity with the Zn-terminated face (*Chapter 5*). It is proposed that the thickness of the adsorbed fluid layer on the O-terminated surface is significantly larger than that on the Zn-terminated face in ambient due to this hydrophilic nature, and that small particulates are more effectively trapped in this fluid layer on the O-terminated face. Since the AFM images in the previous chapter demonstrate the strong reaction of the O-terminated surface to de-ionised water, it would be reasonable to assume that the adsorbed fluid present in ambient is also predominantly water.

In order to check the veracity of this hypothesis, lateral force microscopy and force curve analysis were used to investigate both the relative magnitude of tip-surface interaction and the adsorbed fluid layer thickness of the Zn- and O-terminated surfaces [4].

4.2 Lateral Force Microscopy Results

Interactions between a surface and an AFM tip in contact mode are due to similar van der Waal's effects affecting molecular adsorption on the surface. Lateral force microscopy (LFM) in repulsive contact mode is known to be sensitive to chemical composition in ambient conditions, indicating that direct tip-surface interactions are dominant for this mode of operation [5,6]. However, LFM is generally used to determine chemical or frictional changes across the scanning region of a *single* surface. In contrast, the measurements described within this section attempt to distinguish frictional differences, or differences in the tip-surface interaction, between O- and Zn-terminated polar surfaces using the method described in *Chapter 2*.

Friction images were obtained for the O- and Zn-terminated surfaces of the seeded vapour phase transport (SVPT) and hydrothermal (HT) materials in both trace and retrace directions, where the lateral cantilever deflection is examined for each (x,y) data point on the surface. Half of the difference between the mean lateral deflections in both line directions is taken as a measure of the average frictional force. The standard deviation in the lateral cantilever deflection around this mean for a rough surface will be related to the topography of the face. This technique is not ideal but it does allow a comparative analysis of both polar faces. The triangular cantilever used for LFM measurements is a semi-rigid body and the application of a lateral force to the tip will cause it to twist in a non-uniform fashion along its length. Since the lateral spring-constant is unknown, the units of deflection have therefore been left in units of voltage in the following discussion. In any case, even if the lateral spring-constant could be determined accurately, the non-linear twisting of a triangular cantilever implies that this value would vary depending on the position on the cantilever from which the laser is reflected. Provided that the same cantilever is used to image both O- and Zn-terminated surfaces of a given ZnO wafer, and that the laser alignment on the cantilever is not altered between examinations of each polar face, results from each face should be directly comparable.

Figure 4.1 shows the average lateral deflection of the cantilever for the O- and Zn-terminated surfaces of the *(a)* Eagle-Picher SVPT, *(b)* Rubicon HT, and *(c)* Crystal HT wafers respectively as a function of applied normal force. The same cantilever was used for all measurements and has a stated vertical spring-constant of 0.58 N/m, although the actual figure can deviate by ± 66% (*Chapter 2*). The applied normal force is determined using a value of 0.58 N/m for the spring-constant. This calculated applied force has an associated error equivalent to the possible error in the spring-constant, but all samples were subjected to the same normal forces since the same cantilever and deflection set-points (1 – 7 Volts) were used. The examined area was kept to a 5×5 μm size in order to minimise topographic variations and avoid particulates on the surfaces, and the scanning rate was 0.5 Hz in each case.

For each sample examined, the average lateral cantilever deflection is larger for the Zn-terminated faces than for the corresponding O-terminated surfaces by a factor of at least 1.5 times. One would not necessarily expect the relationship between the lateral cantilever deflection and applied normal force to be linear, due to the complex dynamics of a triangular cantilever attached to a tip interacting with the surface, but there is clear evidence that the cantilever deflection does indeed increase approximately linearly for each surface with increasing normal force, as indicated by the line fits in *Fig. 4.1*.

It can be seen that the linear fits in *Fig. 4.1* do not pass through the origin – the average lateral deflection or friction force does not appear to reach zero under zero applied normal force! As the cantilever is brought towards the surface, however, it will eventually reach a jump-to-contact point (*Section 4.3*). At this distance capillary forces as a result of adsorbed fluid layers or some native tip-surface interaction pull the tip into contact with the surface. The reaction force acting on the cantilever will be equal in magnitude to this force and scanning the tip across the surface will induce a small lateral deflection since this reaction force is present. Although the above discussion has referred to an 'applied normal force', this is in reality an additional applied force beyond the original normal force present as the tip comes into contact with the surface.

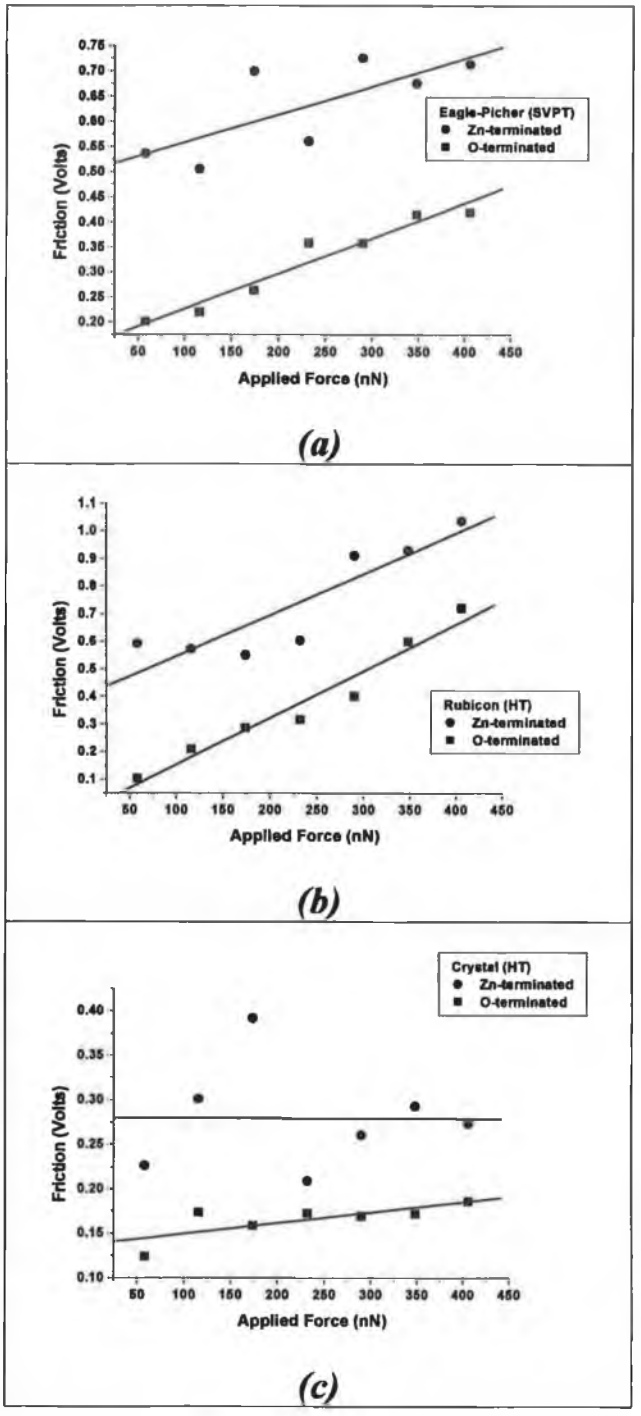

Figure 4.1: *Average lateral deflection (friction) as a function of applied normal force for (a) Eagle-Picher, (b) Rubicon, and (c) Crystal polar surfaces. The cantilever used has a stated vertical spring-constant of 0.58 N/m.*

Figure 4.2 shows the standard deviation in lateral cantilever deflection around the mean values plotted in *Fig. 4.1*. It is observed that the standard deviation values are only approximately 10% of the mean values. Therefore, even if one acknowledges that there is an error in determining the average lateral deflection as a result of topographic contributions, the error in the mean values plotted in *Fig. 4.1* is expected to be about ± 10% based on the standard deviation data. The average lateral deflection for Zn-terminated faces is at least 1.5 times that of the corresponding O-terminated surfaces and therefore this difference in frictional forces can not be accounted for by the ± 10% topographic contribution alone, particularly since AFM scans of the faces show that, in the case of Eagle-Picher and Crystal wafers, the surface roughness is approximately equivalent for each polar face (*Chapter 3*). Although capillary forces as a result of adsorbed fluid layers could be responsible for additional adhesion of the tip or an additional drag force, and hence a subsequent increase in the lateral deflection, the next section will show that it is the O-terminated surface that possesses a thicker fluid layer in ambient conditions. A simple calculation using Stokes' Law, taking the tip to be spherical and having a radius of 50 nm, indicates that the magnitude of the drag force as a result of a water layer would only be of the order of 10^{-15} N and is therefore not considered to be significant.

Since the Zn-terminated faces produce a larger lateral force on the AFM tip, one might conclude that a greater adhesive force between the tip and Zn-faces (but not related to the fluid layers) is responsible for this behaviour, particularly given the nature of the molecular adsorption studies using CO referenced above. However, it is doubtful whether these phenomena are connected due to the chemical specificity of adsorption processes and the fact that examination of the tip-surface interaction using force curve analysis of samples immersed in water (*Section 4.4*) will show that the magnitude and nature of the tip-surface interaction is roughly equivalent for both polar faces. The exact cause of the increased frictional force on Zn-terminated surfaces, compared to O-surfaces, remains unclear. However, the results are in contrast to the topographic observations on ultrasonically cleaned samples where higher trapped particulate

densities are seen on the O-terminated surface, not the Zn-face. This suggests that the role of fluid layers with respect to this phenomenon may be dominant in ambient conditions.

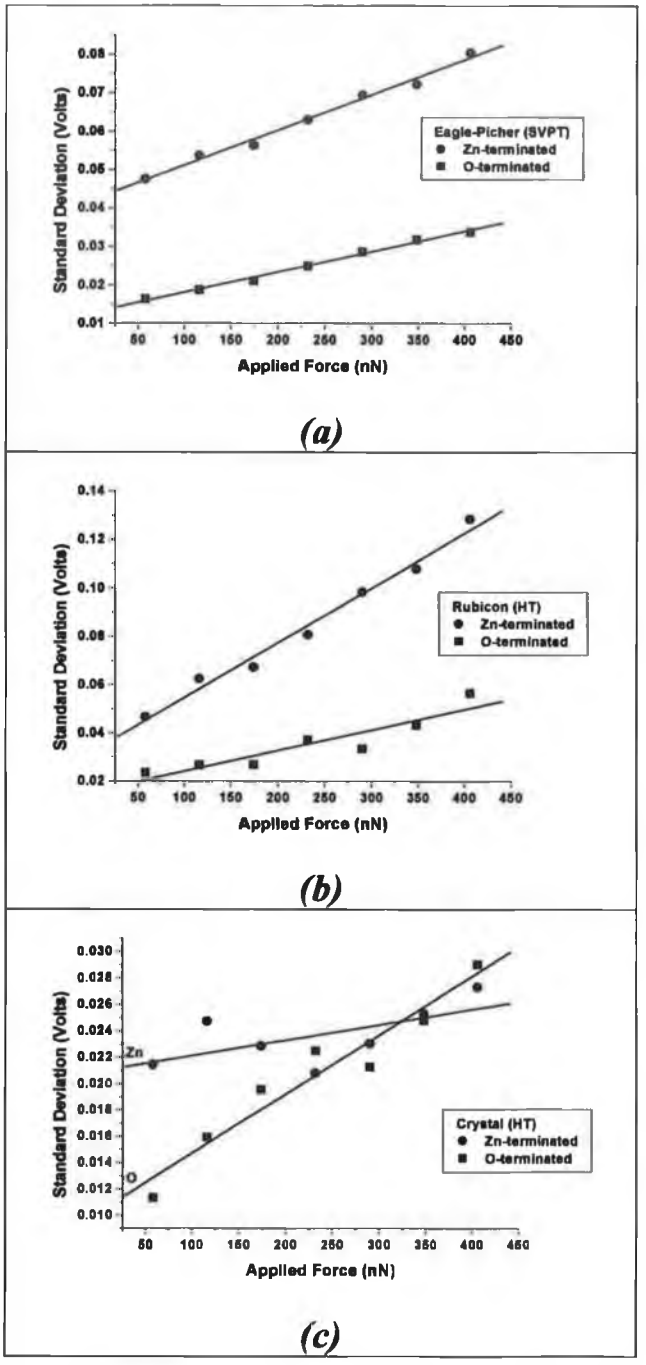

Figure 4.2: *Standard deviation of lateral deflection around the mean values plotted in Fig. 4.3 for (a) Eagle-Picher, (b) Rubicon, and (c) Crystal samples.*

Before examining the presence of water layers on the polar surfaces of samples, it is necessary to demonstrate the reproducibility of data presented in *Figs. 4.1* and *4.2*. *Figure 4.3(a)* shows the average lateral cantilever deflection for the Eagle-Picher polar faces as a function of applied normal force. In this case the area examined was 5×5 μm and the vertical spring-constant of the cantilever was 0.06 N/m, compared to 0.58 N/m in *Fig. 4.1*. Assuming that a reduction in the vertical spring-constant is mirrored by a similar change in the lateral spring-constant, this cantilever is far more susceptible to environmental disturbances, hence the rather large scatter of data. *Figures 4.3(b)* and *(c)* show similar data for the Rubicon and Crystal samples. In both cases the scanning area was also 5×5 μm and the vertical spring-constant was 0.12 N/m, although different tips were used for each sample. *Figure 4.4* is the complimentary standard deviation data for each of the mean value plots discussed above. The average lateral deflection is higher for the Zn-terminated faces than for the O-terminated surfaces and, as above, the corresponding standard deviation values are approximately 10% of the average lateral deflection values.

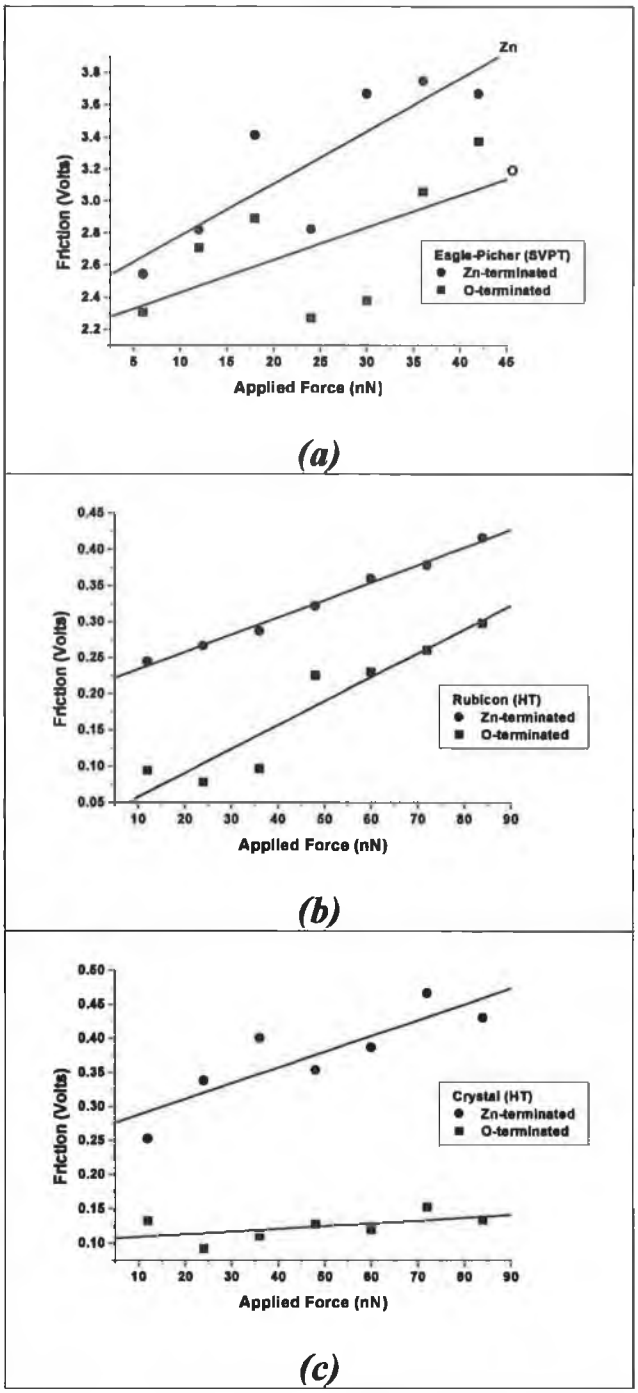

Figure 4.3: *Average lateral deflection (friction) as a function of applied normal force for (a) Eagle-Picher (k_z=0.06 N/m), (b) Rubicon (k_z=0.12 N/m), and (c) Crystal (k_z=0.12 N/m) polar surfaces.*

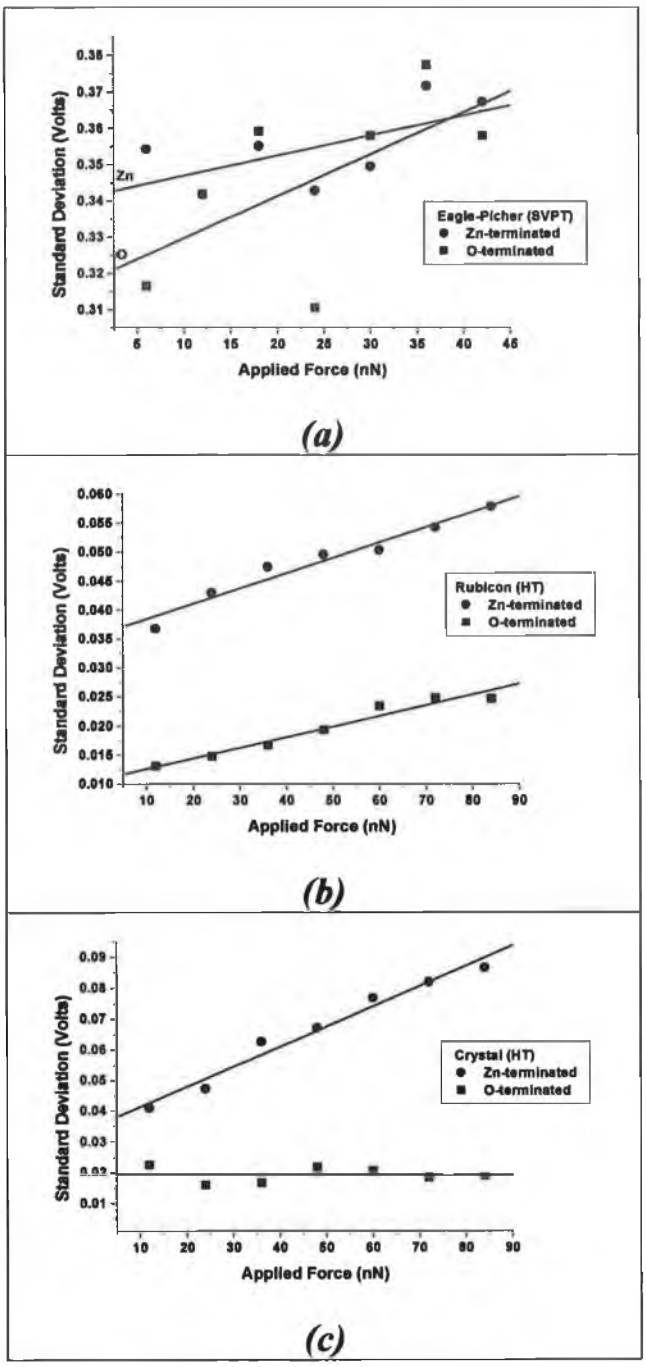

Figure 4.4: *Standard deviation of lateral deflection around the mean values plotted in Fig. 4.6 for (a) Eagle-Picher, (b) Rubicon, and (c) Crystal samples.*

4.3 *Force-Displacement Results in Ambient*

To study the adsorbed fluid layer, force curve measurements were performed in air, and also in water (*Section 4.4*). The presence of an adsorbed fluid layer is seen as a discontinuity in the cantilever deflection during the approach and retraction phases in air, with significant hysteresis between the two [7]. The adsorbed layer thickness on the sample surface (plus the thickness of adsorbed fluid on the tip) may be estimated by the distance the piezoelectric scanner must move between the initial jump-to-contact point and the point at which the cantilever deflection returns to zero after contact with the sample [8], as shown in *Chapter 2* and reproduced below for clarity (*Figure 4.5*).

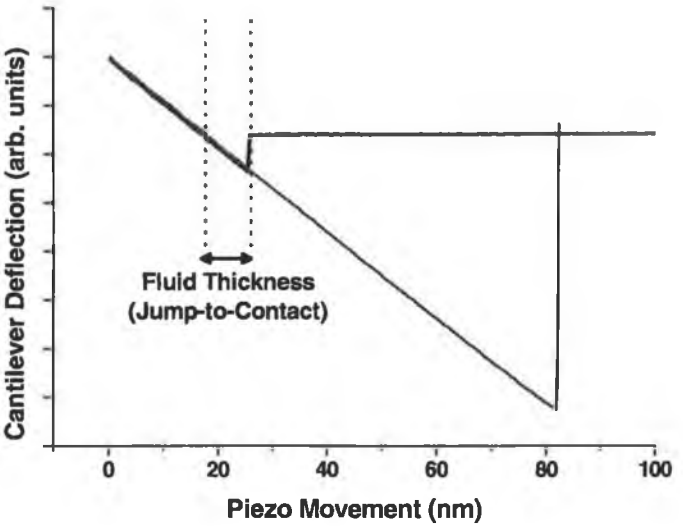

Figure 4.5: *Example of a force-displacement graph, obtained from the polar surfaces of ZnO. The thickness of the fluid layer is estimated by determining the distance the piezo moves between the initial jump-to-contact point and the point at which the cantilever deflection returns to zero after contact with the sample.*

Figure 4.6 shows the determined fluid layer thickness, obtained in the same manner as described in *Chapter 2* and in *Fig. 4.5*, for both polar faces of *(a)* Eagle-Picher, *(b)* Rubicon and *(c)* Crystal samples. Each pair of polar faces was examined with the same tip and cantilever (0.58 N/m). The wafers were not probed on the same day and one observes substantial variations in fluid thickness from sample to sample as a result of the differences in ambient humidity. However, both polar faces of a given wafer were studied within an hour. In order to obtain a reasonable measure of the relative fluid thickness on each polar surface it was decided to search for topographically smooth regions that were also free from debris, and obtain a series of curves from these specific locations. *Fig. 4.6*, therefore, shows the fluid layer thickness determined from each of twenty force curves at a single position on each polar face of each wafer. Since these twenty force curves were obtained at the same location, one would expect the layer thickness to remain constant. A straight line was fit to the data from each polar face, where the slope of this line was set to zero and the y-axis intercept was used as the fitting parameter. This intercept is taken as the average thickness of the fluid layer on each polar face, with the error determined from the fitting. *Table 4.1* gives the average fluid thickness present on each face, along with the ratio of thicknesses between O-terminated and Zn-terminated surfaces using data from *Fig. 4.6*.

In each case the fluid layer is indeed thicker for the O-terminated surfaces than for the corresponding Zn-terminated faces. The ratio values are sufficiently large, and the errors in determining the y-axis intercept of the line fits sufficiently small (less than 2.3% taking the 8.8 ± 0.2 nm value for the Zn-face of the Crystal sample) to be certain that these differences are not simply due to experimental errors. This experiment was conducted at two other locations on each polar face for the Eagle-Picher, Rubicon, and Crystal wafers. Although one observes differences in the fluid thickness due to changes in ambient humidity from day to day, in every case the O-terminated surfaces have thicker fluid layers than the Zn-terminated faces. Taking representative force curves from each set of twenty, *Table 4.2* gives a rough indication of fluid thickness at the other examined locations.

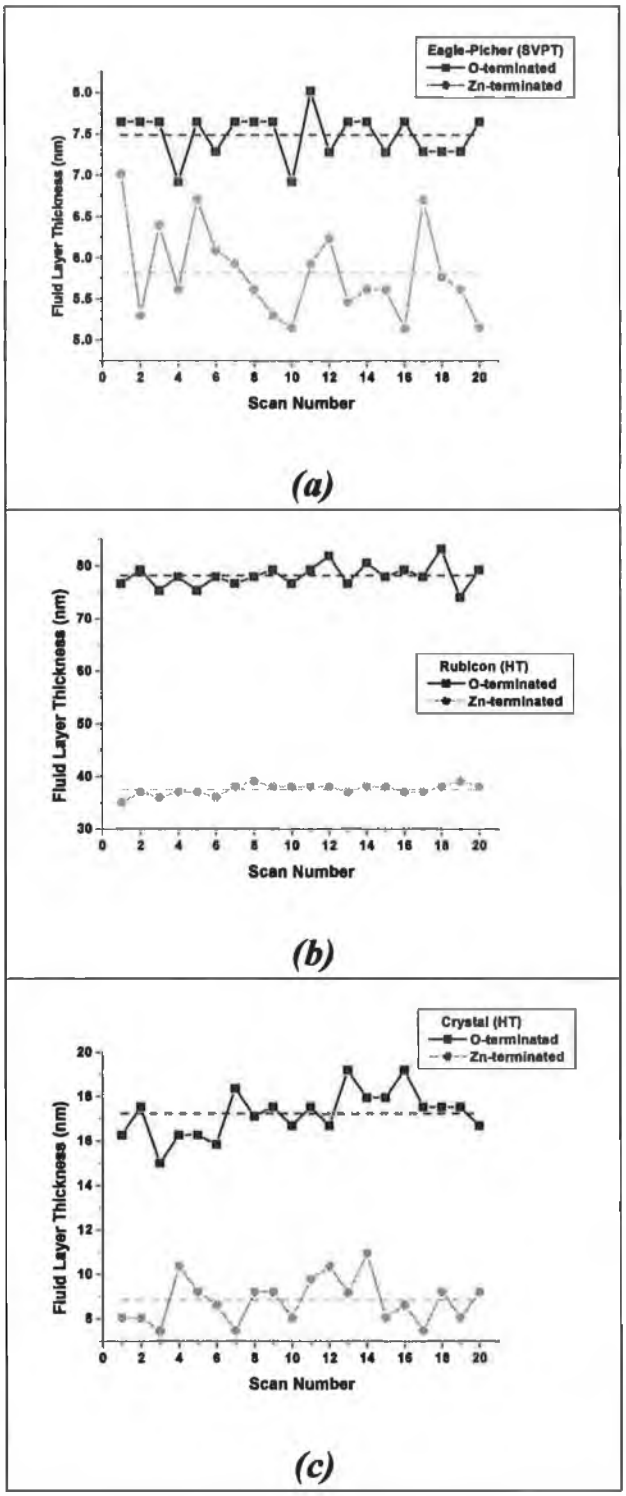

Figure 4.6: *Fluid layer thickness for both polar faces of (a) Eagle-Picher, (b) Rubicon, and (c) Crystal ZnO wafers. In all cases the determined thickness is larger for the O-terminated surface than for the corresponding Zn-terminated face.*

Table 4.1: *Determination of adsorbed fluid layer thickness (Fig. 4.6)*

Sample	*Polar Face*	*Adsorbed Fluid Thickness (nm)*	*Fluid Thickness Ratio (Oxygen / Zinc)*
Eagle-Picher	**O**	7.5 ± 0.1	
	Zn	5.8 ± 0.1	1.3
Rubicon	**O**	78.2 ± 0.5	
	Zn	37.5 ± 0.2	2.1
Crystal	**O**	17.2 ± 0.2	
	Zn	8.8 ± 0.2	2.0

Table 4.2: *Typical fluid thickness at other sample locations based on representative force curves.*

Sample	*Polar Face*	*Adsorbed Fluid Thickness (nm)*	*Fluid Thickness Ratio (Oxygen / Zinc)*
Eagle-Picher	**O**	75.8	
	Zn	28.4	2.7
	O	84.4	
	Zn	64.8	1.3
Rubicon	**O**	214.6	
	Zn	68.6	3.1
	O	90.9	
	Zn	71.2	1.3
Crystal	**O**	122.9	
	Zn	47.0	2.6
	O	37.4	
	Zn	23.2	1.6

It is clear from the ratios in *Tables 4.1* and *4.2* that the fluid thickness depends on the location of the tip on the surface. Thus, if ratio values are high (as with the 3.1 value for the Rubicon surfaces in *Table 4.2*) it is likely that either the fluid on the O-terminated face was thicker than average at this location, or the fluid on the Zn-terminated surface was thinner than average at the location examined. Similarly, if ratio values are low then the fluid would be expected to be thinner than average or thicker than average for the O- and Zn-terminated locations respectively. It is speculated that differences in topography between each examined region are responsible and there are a number of possible explanations within this hypothesis depending on the nature of the interaction between the surface and fluid layer. However, the measurements presented herein are incapable of proving or eliminating any of these possibilities, although the dominant role of the topography in each case is clear. *Figure 4.7* is an illustration of the three suggested reasons for the observed variations in retraction distances depending on surface location. Nevertheless, *Figure 4.8* is a plot of the ratios given in *Tables 4.1* and *4.2* showing that, on average, the fluid layer is 2.0 times as thick on the O-terminated surfaces compared to the Zn-terminated surfaces. The spread of possible ratios should also be noted, with a minimum ratio of 1.3 and maximum of 3.1.

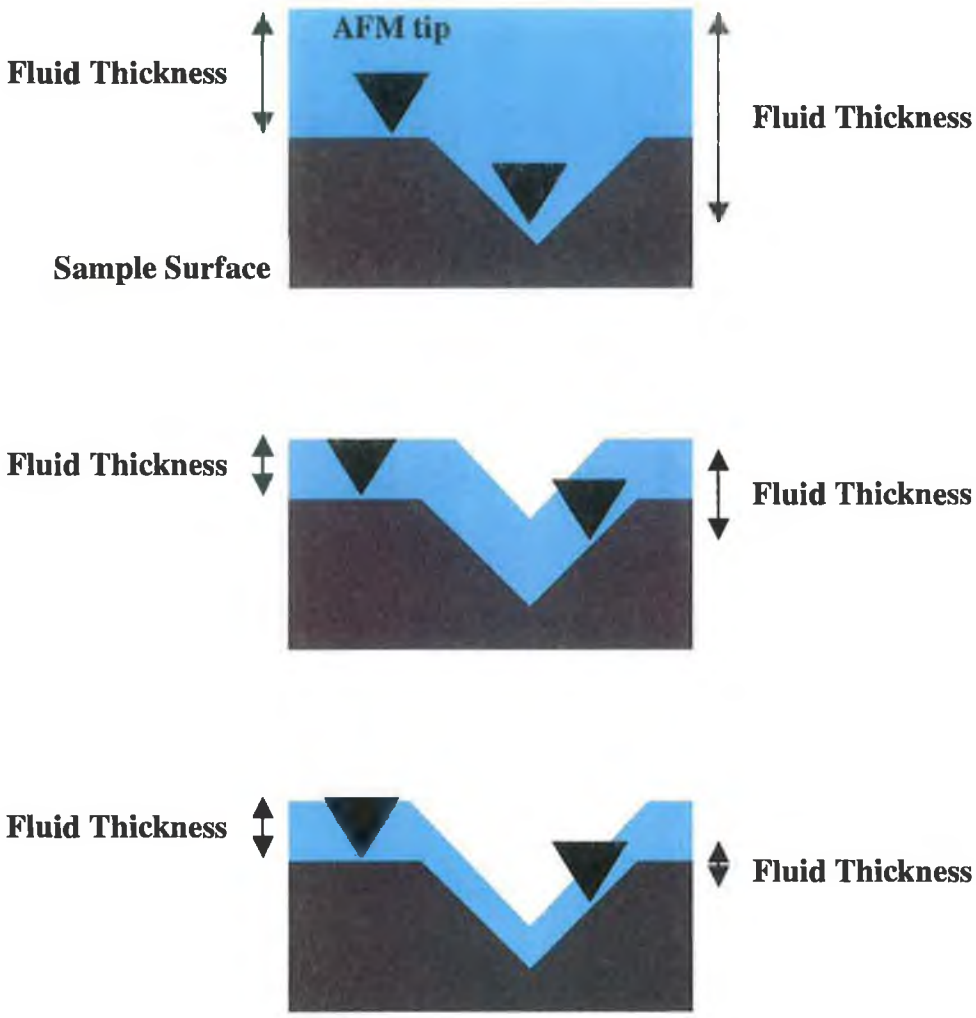

Figure 4.7: *Three possible variations in the nature of the interaction between surface and fluid layer. In the first case (top), the fluid layer has a particular thickness above the planar surface but fills all topographic regions lower than the plane. The fluid thickness therefore depends on the position of the tip and is directly related to the topography of the face.*

In the second case (middle) the fluid layer follows the topography of the surface but is equally thick at all locations perpendicular to the face. The AFM tip, which is brought into contact vertically, will therefore interact with greater or lesser thicknesses of fluid depending on the slope of the topography.

In the third and final case (bottom) the fluid follows the topography but is not equally thick perpendicular to the face. In ZnO, although the polar surfaces terminate with either O or Zn atoms, step edges will have a mixed nature. The fluid thickness could therefore vary depending on the nature of the termination, which in turn depends on the location of the tip.

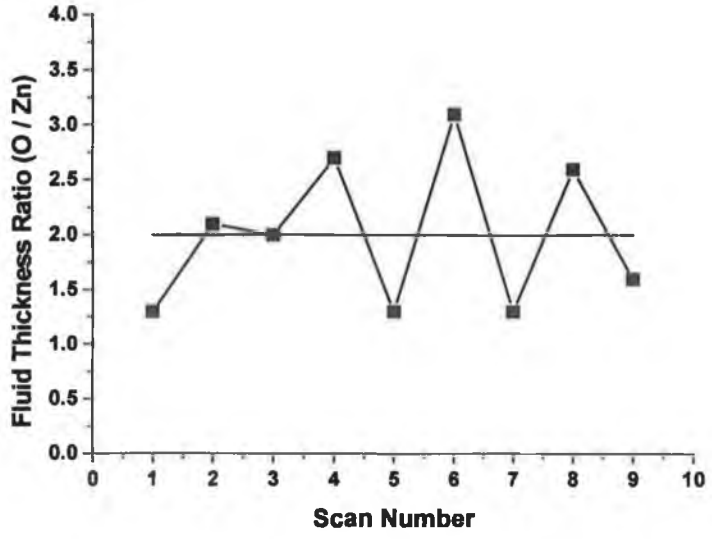

Figure 4.8: *Plot of the ratio of fluid thickness on O- terminated surfaces compared to Zn-terminated faces, where the data was taken from Tables 4.1 and 4.2. The average ratio is 2.0, implying that the fluid layers on O-terminated surfaces are about twice as thick as for Zn-faces.*

Rather than examine the fluid layer thickness in the jump-to-contact region, one can also use the retraction distance required for the piezoscanners to free the tip from the fluid (as illustrated in *Figure 4.9*, below) as an indirect method of comparing the thickness present on each polar face. *Figure 4.10* shows retraction distances for *(a)* Eagle-Picher, *(b)* Rubicon and *(c)* Crystal samples. The force curves for each ZnO wafer were captured within an hour to minimise the effects of humidity changes during the experiment and the cantilever used has a stated spring-constant of 0.12 N/m. Ten individual curves were obtained at five locations on each polar face of all three ZnO wafers. In *Fig. 4.10* the (y) values of the data points gives the retraction distance determined from each individual force curve, hence the fifty data points. Data points with horizontal (x) values of 1 to 10 were taken from the same location on the sample surface, as were data points with (x) values between 11 and 20, and so forth.

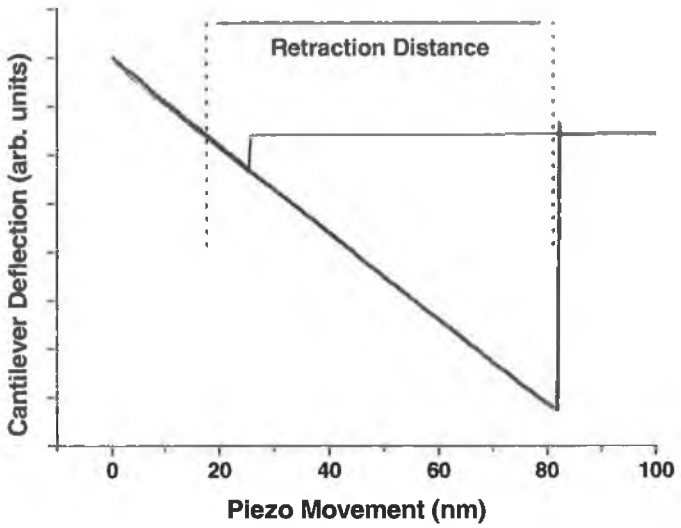

Figure 4.9: *Rather than determine the fluid thickness by directly measuring piezo movement in the jump-to-contact region, the retraction distances (i.e. the distance the piezo must move to free the tip from the fluid layer) can also be compared.*

These locations on each polar face were not chosen at random. Quick topographic scans were performed at a resolution of 128 rather than 512 lines per image in order to identify surface regions that were relatively flat and free of attached debris. The retraction distances required are significantly larger for the O-terminated surfaces than for the Zn-faces of the Eagle-Picher (*Fig. 4.10(a)*) and Rubicon (*Fig. 4.10(b)*) samples. The Crystal sample (*Fig. 4.10(c)*) does not exhibit such a marked difference between each of the polar faces, although there is a bias in the data presented suggesting that the retractions are generally larger for the O-terminated surface.

While it is possible that the examined surface regions and obtained force curves are not representative of the polar faces as a whole, it is certainly not probable that this is the case. The Eagle-Picher and Rubicon wafers show similar behaviour, with retraction distances spanning between 60 – 160 nm for both Zn-terminated surfaces and 200 – 360 nm for both O-terminated faces. In every case, with a total of two hundred force curves obtained for the polar faces of the Rubicon and Eagle-Picher wafers, the retractions for the O-terminated surfaces are larger than for the Zn-terminated faces.

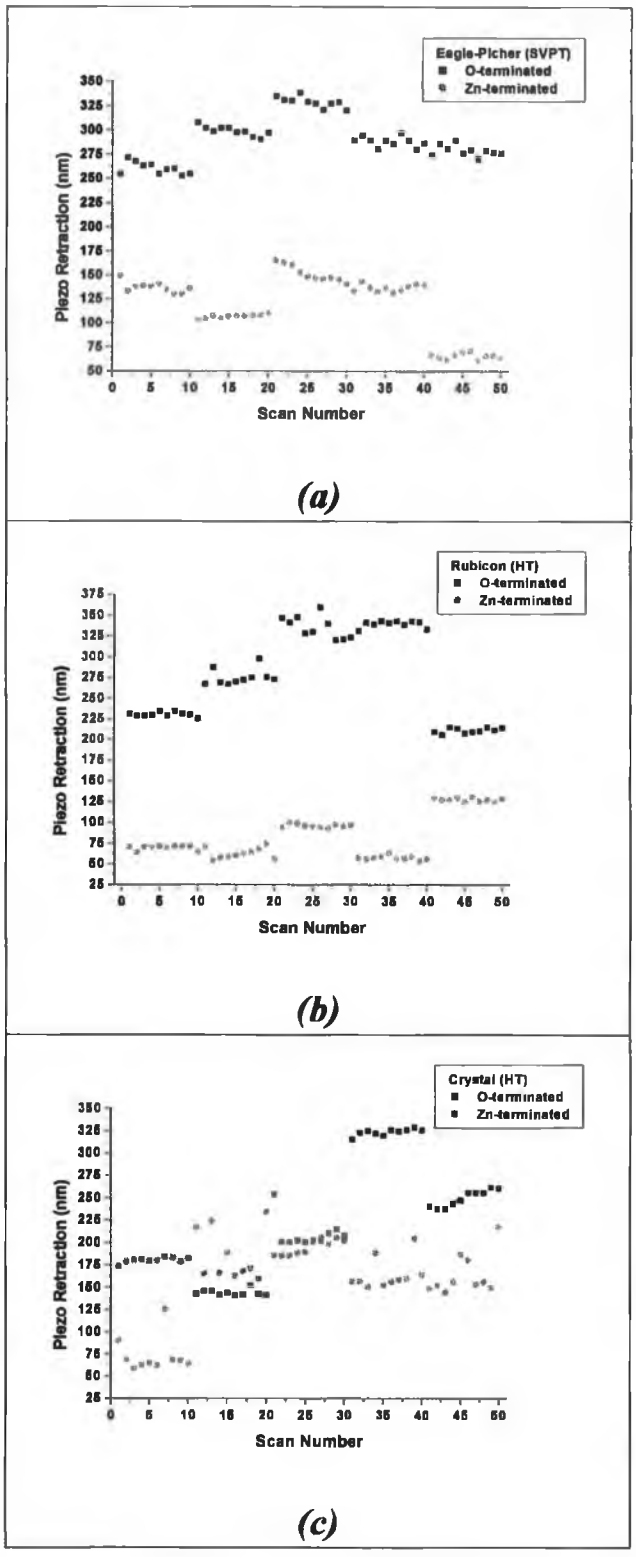

Figure 4.10: *Piezoelectric scanner retraction distances required to free the AFM tip from the adsorbed fluid layer. Ten force curves were obtained at five locations on each polar face. Therefore, data points with (x) values 1 – 10 were obtained at the same surface location, as were points with (x) values 11 – 20, etc.. In the case of (a) Eagle-Picher and (b) Rubicon samples, the retraction distances are larger for the O-terminated surfaces than for the Zn-terminated faces. For the Crystal sample (c) the difference is not as pronounced.*

The Crystal sample appears to be slightly at odds with the other ZnO wafers. To verify if this is the case, *Figure 4.11* shows retraction distances for the Crystal polar faces using a different wafer and cantilever (0.12 N/m). The data is not directly comparable with the previously presented graphs due to possible humidity changes and the errors associated with the determination of the spring-constant. Force curves were obtained at five locations on each polar face and twenty curves were acquired at each position. As above, there is a general trend in the data similar to that of the Rubicon and Eagle-Picher wafers, where the retractions are larger for the O-terminated surface than for the Zn-terminated face although, as with *Fig. 4.10(c),* the difference is not as dramatic for this Crystal sample. It is not immediately clear why this should be the case, although it could be due to the different surface preparations and polishing methods employed.

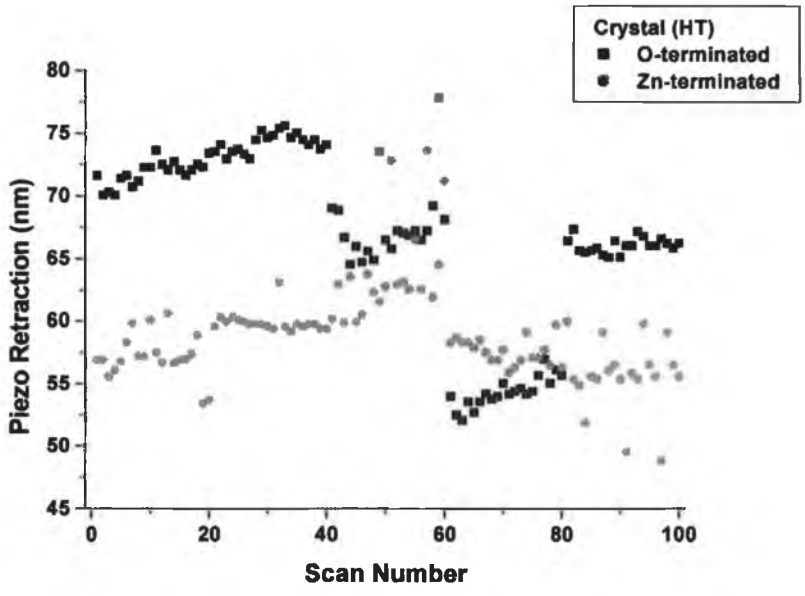

Figure 4.11: *Piezoelectric scanner retraction distances for the polar faces of Crystal sample. As with Fig. 4.10, there appears to be a general trend in the data, with retraction distances generally larger for the O-terminated surface than for the Zn-terminated face. The difference in retraction distances between each polar face is not as dramatic for the Crystal sample as for the Eagle-Picher and Rubicon wafers, and the overall appearance of the plot is similar to that of Fig. 4.10(c).*

In order to estimate the ratio of retraction distances required for O-terminated surfaces compared to Zn-terminated faces, it is necessary to average the data of *Fig. 4.10* in some meaningful way. Each set of ten consecutive data points represents the retractions required at a single location on a particular surface. The average was determined from these ten points (i.e. the average retraction distance at a single location) and since five different locations were examined, a total of five average retraction distances for the O- and five for the Zn-terminated surfaces of each wafer were obtained.

There is no reason to favour one set of results from the O-terminated surface and from the corresponding Zn-terminated data when determining the ratio. Simply taking the average retraction of points 1-10 on the O-terminated surface and dividing this by the average retraction of points 1-10 on the Zn-terminated surface may give a false indication of the ratio since, at these locations, the O-terminated fluid thickness may have been higher or lower than average and similarly may have been higher or lower than average for the Zn-terminated fluid thickness. In order to obtain the full spread of possible values, the ratio of retraction distances was calculated by taking each of the five average values for the O-terminated surface and dividing it by each of the five averages for the Zn-terminated surfaces, leading to twenty-five ratio values per wafer, or a total of seventy-five ratio values for all three wafers.

Figure 4.12 is a frequency plot of the occurrence of each ratio value, where a 0.4 bin size was used. Of the seventy-five ratios taken, half of the values lie in the relatively narrow range of 1.6 to 2.8. The mean ratio value of the full data set is 2.6 with a standard deviation of 1.3. Thus the ratio values determined by examination of the retraction distances roughly equate to those measured through examination of the jump-to-contact region (*Tables 4.1* and *4.2*). Although this analysis technique is crude, as a rough rule one can consider the retraction distances are about twice as large for the O-terminated surfaces as for the Zn-terminated surfaces.

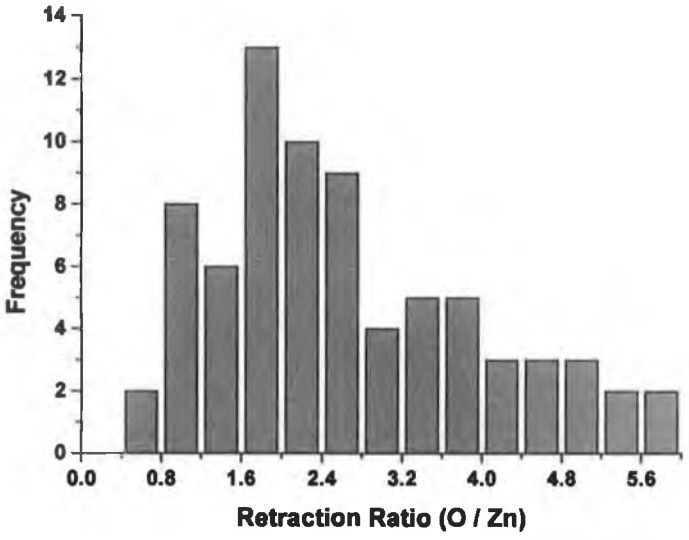

Figure 4.12: *Frequency of ratio values from the data presented in Fig. 4.10. Taking the average retraction distances from the O-terminated surfaces and dividing them by each of the average retraction distances from the corresponding Zn-terminated surfaces yields a total of 75 ratio values for the three ZnO wafers. Half of these ratios lie within the range 1.6 – 2.8 suggesting that the retraction distances are, generally, about twice as large for the O-terminated faces as for the Zn-terminated faces.*

Observation of the piezoelectric retraction distances allows a comparative analysis of the fluid layer thickness on each polar surface, and is less prone to errors than direct measurement of the thickness in the tip approach phase, due to the much larger distances involved. Obtaining force curves that are based on an average of many extension and retraction phases was not found to be a useful technique, and one finds that curves of this nature are distorted due to changes in the surface topography during the acquisition as a result of environmental disturbances or creeping of the position of the tip.

4.4 Force-Displacement Results in Water

It must now be demonstrated that the force curve characteristics discussed in the last section are actually due to adsorbed fluid layers and not some native tip-surface interaction. *Figure 4.13* shows initial determinations of the fluid layer thickness through examination of the jump-to-contact region in ambient conditions. These results were taken at a single location on the O- or Zn-terminated surfaces of each wafer, where the same cantilever with a spring-constant of 0.58 N/m was used for each sample and twenty force curves were acquired for each polar face. As with the results above, the fluid layer is thicker on the O-terminated surface than on the Zn-face. *Figure 4.14* is a plot of once-off force curves, indicating that the retraction lengths range from seventy to several hundred nanometers depending on the wafer and polar face. It should be noted that the distances are not comparable between samples as each wafer was examined on a different day and humidity was not controlled. However, the distances are comparable between complementary polar faces.

After obtaining twenty force curves from a particular face in ambient, water was syringed onto the surface. Acquiring force-displacement plots in water is complicated by the surface tension of the liquid, which resists the motion of the tip vertically downwards onto the sample. In fact one generally finds that the tip will simply sit on the surface of the liquid and a subsequent penetration into the fluid requires applied forces of such magnitude that the cantilever is either broken or damaged. A small amount of wetting agent, in this case Kodak 'Photo-Flo' (ethylene glycol), was therefore mixed with the de-ionised water in order to reduce the surface tension, allowing the tip to enter the fluid and a further twenty force curves were captured from water covered surfaces.

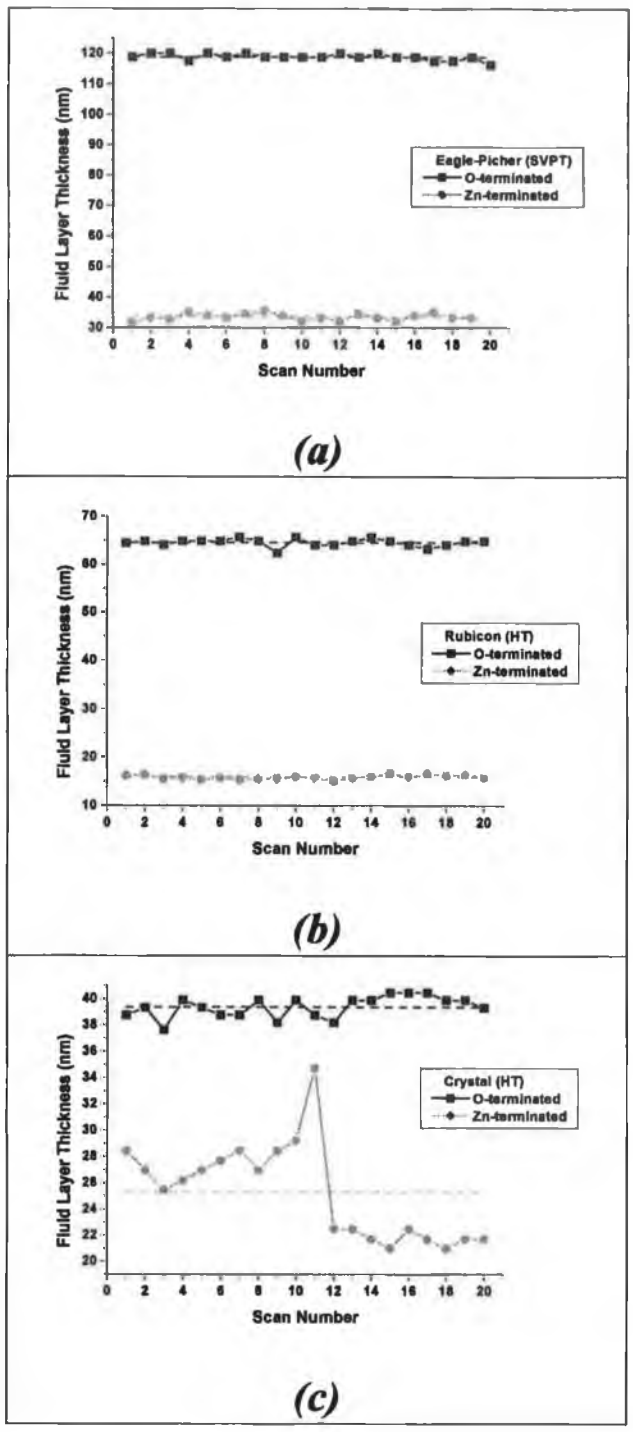

Figure 4.13: *Fluid layer thickness in ambient at one location on each of the O- and Zn-terminated surfaces of (a) Eagle-Picher, (b) Rubicon, and (c) Crystal wafers respectively.*

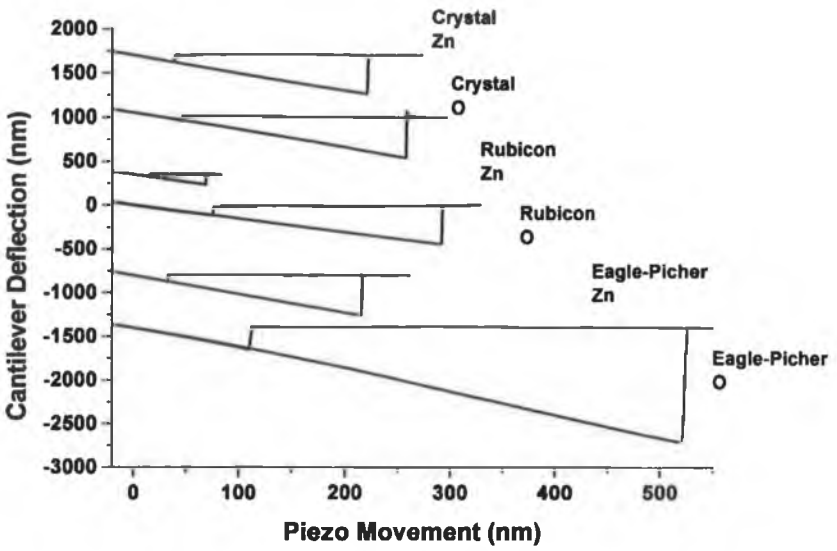

Figure 4.14: *Typical force curves obtained for Fig. 4.13 above. The retraction distances in ambient range from seventy to several hundred nanometers, depending on the polar face and sample examined. The hysteresis observed between approach and retraction phases is eliminated when sample surfaces are immersed in water (Fig. 4.15), indicating that it is fluid layers that are responsible for the data in ambient. The contact point for each curve has been set at the origin, and each curve has been shifted vertically for clarity.*

Figure 4.15 shows once-off curves for both polar faces of all three wafers after immersion in water. These force curves in water are directly comparable to the curves in *Fig. 4.14* (taken in ambient) as the same cantilever was used and the measurements in ambient and in water for any given polar face took place in a time scale of less than an hour. The hysteresis observed in ambient is eliminated in all cases and the force levels dramatically reduce, confirming that adsorbed fluid layers are responsible for the presented data in ambient. The curves are substantially different to those measured in air, with no jump-to-contact feature and strong evidence for tip repulsion during the approach phase for all polar faces.

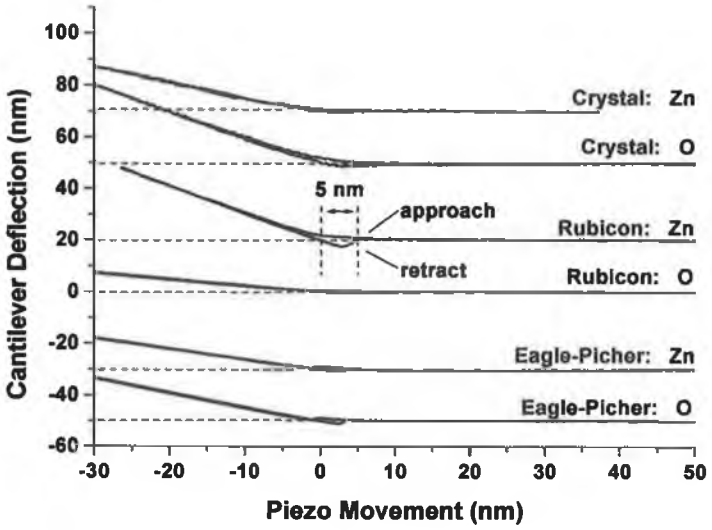

Figure 4.15: *Typical force curves obtained in water for both polar faces of each wafer. The contact point is set as the origin, and each curve has been shifted vertically for clarity. The method of calculating the retraction distance is shown for the Zn-terminated face of the Rubicon wafer. The hysteresis observed in air is eliminated in water, indicating that the data in ambient is due to adsorbed fluid layers. There is evidence of tip repulsion during the approach phase for all samples. The loading portion of the curves (i.e. where the tip is in contact with the surface, to the left of the origin) appears to have different slopes for each sample. This is due to the refractive index change from ambient to water, which alters the position on the cantilever from which the AFM laser is reflected. However, since the measurements of interest are all based on piezo retraction distances, this does not affect the results.*

In order to estimate the strength of the tip-surface interaction the retraction distances have been determined for each of the twenty force curves obtained in water for both polar faces of each wafer, and are plotted in *Fig. 4.16*. These retraction distances are taken as a measure of the native tip-surface interaction in the absence of capillary forces. However, the rather small forces involved for measurements in water means that these retractions have quite large errors associated with them (of ~ 50% from one measurement to the next) and are particularly prone to any slight environmental disturbances. There is evidence, however, that the retraction distances required for the

O-terminated surfaces are larger than for the Zn-terminated faces implying that adhesion force is stronger for the O-terminated face.

When the samples were removed from the water and dried with flowing nitrogen, the force curves were re-measured and returned to a form similar to that of *Fig. 4.14*, though some evidence of etching due to immersion in water was seen in topographic scans. The changes in the slope of the loading portion of the curves (where the tip contacts the surface and the cantilever begins to deflect) between samples in *Fig. 4.15* is due to the refraction of the AFM laser at the air-water interface. This causes the beam to reflect from a different part of the cantilever, thus effectively changing the spring-constant. As the syringed water-layer thickness was not controlled during the measurements in water, the *y*-axes of all the curves in *Fig. 4.15* are not comparable to one another.

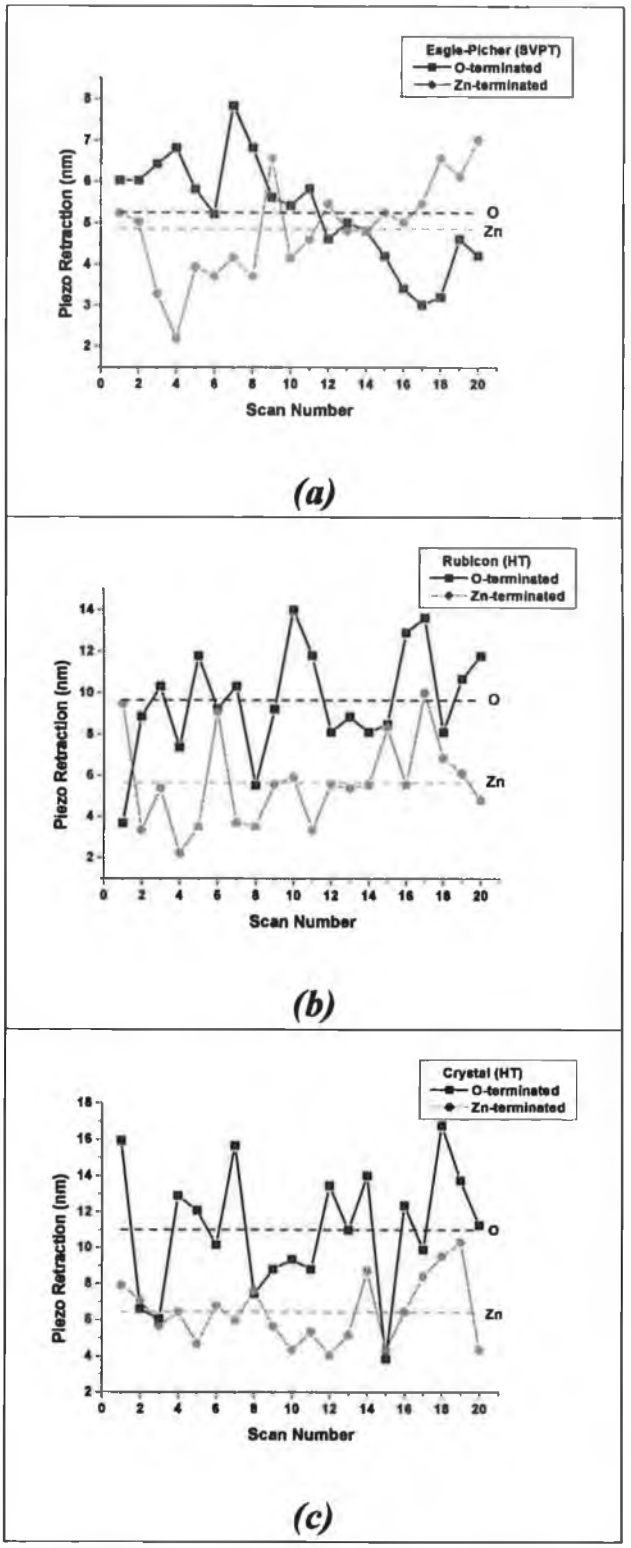

Figure 4.16: *Retraction distances for each polar face of (a) Eagle-Picher, (b) Rubicon, and (c) Crystal wafers in water. The distances are of the order of a few nanometers and there are substantial errors of ± 50% from one measurement to the next, where all measurements were made at the same location on each surface.*

4.5 Discussion of Results and Conclusions

AFM topographic scans in ambient conditions of ultrasonically cleaned (0001)-oriented ZnO samples indicate that the O-terminated surface has a considerably higher density of residual particulates after cleaning. Lateral force and force-curve results show that the origin of this effect is a significantly larger adhesion force due to the greater capillary effects of an adsorbed water layer on the O-face compared to the Zn-face. The thickness of fluid present on the hydrophilic O-terminated surface is approximately twice that on the Zn-terminated face, and the adhesion forces are expected to have the same ratio [7]. One can conclude that the adhesion energy for the O-terminated surface is about four times that of the Zn-terminated face.

There appears to be an inconsistency between the lateral force results, which suggest that the tip-surface interaction is stronger for the Zn-terminated surface, and the force-curve measurements performed in water which imply the exact opposite. However, the friction forces experienced by the tip are similar in magnitude for both polar surfaces and the simple analysis of friction plots performed probably does not allow a total decoupling of frictional from topographic effects.

The data presented does not allow a detailed analysis of why the surface termination should affect the adsorption of multi-layer water films of such large thickness, or of the microscopic origin of this effect. Recent theoretical studies, however, suggest that the dominant stabilization mechanism of the ZnO polar faces involves a transfer of electronic charge between the faces [9, 10] and *Staemmler et al.* have demonstrated that the O-terminated face shows a significant H-coverage even in UHV conditions [11]. In [10] an alternative stabilization mechanism is considered, involving H-adsorption on the O-terminated face and OH-adsorption on the Zn-terminated face. While this was shown to be less effective than the charge transfer at low temperatures, the authors comment that such a water-terminated slab will be stable

at higher temperatures and pressures, such as the ambient environment used in the case of the data presented here.

The authors also propose that the effects of H-adsorption on the O-terminated surface and OH-adsorption on the Zn-terminated face lead to metallization of the O-surface, but not of the Zn-surface which reverts to the bulk charge state [10]. Metallization of the O-surface by an initial H-coverage may result in substantially different adsorption for subsequent layers due to, for example, an increase in surface forces such as image charge forces, compared to the non-metallic Zn-surface with an OH-coverage. The high dielectric constant of ZnO (~ 6.2) [12] means that the image forces will only be of the order of 30% greater on the O-terminated surface compared to the Zn-terminated face [13] and such a simple mechanism cannot explain the relative scale of the fluid thicknesses observed on each polar face. However, the fact that theoretical predictions point to significant differences between the O- and Zn-surfaces in their interaction with water molecules indicates that further computational studies of the water/ZnO polar interface in ambient conditions may explain the data presented.

The presence of fluid layers, and the topographic images of samples cleaned ultrasonically, suggests that the cleaning and other preparation procedures necessary for the two polar surfaces before their use in applications, such as lattice-matched epitaxial growth, may be quite different. With regard to the optimal surface termination for epitaxial growth on ZnO, one finds that diametrically opposite conclusions are reached by different researchers [14-16] and the presence of adsorbed fluid layers of different thicknesses may explain some of the inconsistencies reported in the literature. These substantially different adsorbed layers may also be influential in the growth and subsequent stability in ambient conditions of certain nano-structured ZnO systems [17, 18]. In such systems the electrostatic energies of the polar surfaces are considered to be dominating effects on the morphology, and the reactivity is also known to depend on surface termination. Given that these systems are grown in environments far from UHV and that the adsorbed layers may become charged or develop dipole moments, it is

possible that these layers significantly alter the electrostatic energy considerations and also the surface reactivity vis-à-vis the growth of such nanostructures.

4.6 References

[1] M. Kunat and U. Burghaus, *J. Vac. Sci. Technol. A* **21** (2003) 1322

[2] S. Rozhok, P. Sun, R. Piner, M. Lieberman, and C. A. Mirkin, *J. Phys. Chem. B* **108** (2004) 7814

[3] A. N. Mariano and R. E. Hanneman, *J. Appl. Phys.* **34** (1963) 384

[4] G. Meyer and N. M. Amer, *Appl. Phys. Lett.* **57** (1990) 2089

[5] C. D. Frisbie, L. F. Rozsnyai, A. Noy, M. S. Wrighton, and C.M. Lieber, *Science* **265** (1994) 2071

[6] R. M. Overney, E. Meyer, J. Frommer, D. Brodbeck, R. Luthi, L. Howard, H.-J. Guntherodt, M. Fujihara, H. Tankano, and Y. Gotoh, *Nature* **359** (1992) 133

[7] R. Wiesendanger in *Scanning Probe Microscopy and Spectroscopy*, 1st edn. (Cambridge: Cambridge University Press, 1994), chapter 1, p. 235-239

[8] C. M. Mate and V. J. Novotny, *J. Chem. Phys.* **94** (1991) 8420

[9] A. Wander, F. Schedin, P. Steadman, A. Norris, R. McGrath, T. S. Turner, G. Thornton, and N. M. Harrison, *Phys. Rev. Lett.* **86** (2001) 3811

[10] A. Wander and N. M. Harrison, *J. Chem. Phys.* **115** (2001) 2312

[11] V. Staemmler, K. Fink, B. Meyer, D. Marx, M. Kunat, S. Gil Girol, U. Burghaus, and C. H. Wöll, *Phys. Rev. Lett.* **90** (2003) 106102

[12] J. Lagois, *Phys. Rev. B* **16** (1977) 1699

[13] D. J. Griffiths in *Introduction to Electrodynamics*, 1st edn. (Eaglewood Cliffs, NJ: Prentice-Hall, 1981), chapter 2, p. 106-109 and chapter 3, p. 163-164

[14] T. P. Smith, H. McLean, D. J. Smith and R. F. Davis, *J. Cryst. Growth* **265** (2004) 390

[15] S. Zhu, C.-H. Su, S. L. Lehoczky, M. T. Harris, M. J. Callahan, P. McCarty, and M. A. George, *J. Cryst. Growth* **219** (2000) 361

[16] F. Hamdani, M. Yeadon, D. J. Smith, H. Tang, W. Kim, A. Salvador, A. E. Botchkarev, J. M. Gibson, A. Y. Polyakov, M. Skowronski, and H. Morkoç, *J. Appl. Phys.* **83** (1998) 983

[17] X. Y. Kong and Z. L. Wang, *Appl. Phys. Lett.* **84** (2004) 975

[18] Z. L. Wang, X. Y. Kong, and J. M Zuo, *Phys. Rev. Lett.* **91** (2003) 185502

Chapter 5

Optical Properties of Polar Faces after Wet Chemical Etching

5.1 Introduction

One of the simplest methods of creating patterned microstructures on semiconductor surfaces is to preferentially remove material through careful application of wet chemical etchants. Even when patterning is not required, surfaces are often prepared or conditioned by chemical etching. There has been much interest in polycrystalline ZnO material due to the potential applications of thin film layers. In particular, crystal grains formed during growth can act as cavities for random lasing action and grain size can be controlled through careful annealing of the material. Chemical etching of bulk semiconductors, as opposed to growing polycrystalline material, may produce topographically comparable surfaces and, by varying concentrations, etch times or solution, surface morphology could potentially be controlled to a reasonable degree. An understanding of the impact of etchant solutions on surface topography may be useful for a wide range of processing steps for ZnO substrates.

In the case of the ZnO wafers examined here, the luminescence and reflectance differences observed between the chemo-mechanically polished polar surfaces of Eagle-Picher (SVPT) and the epi-polished Rubicon (HT) material (*Chapter 3*) suggests that the surface preparation technique is a contributing factor to the optical quality. The different terminating atoms on each of the polar faces leads to dramatic differences in the interaction of etchants and the surface, and the binary nature of ZnO could allow a greater degree of control over the resulting surface topography than is possible for elemental semiconductors. A detailed examination of the effects of surface topography on bound- and free-exciton characteristics of bulk ZnO has yet to be reported.

5.2 *Experimental Details*

In this study hydrothermally-grown (0001)-oriented Rubicon ZnO wafers [1] were etched using a number of different solutions and the bound-exciton luminescence and free-exciton resonance properties were examined and correlated to the changes in surface topography. Although each ZnO sample has both (0001) Zn-terminated and $(000\bar{1})$ O-terminated surfaces, the wafers as received were polished on one side only. Throughout this chapter, when referring to O-terminated [O] or Zn-terminated [Zn] surfaces, the discussion relates only to the polished polar face.

Vellekoop et al. have previously demonstrated a compatibility between ZnO and etchants traditionally used for silicon IC processing [2]. Using these investigations as a starting point, the effect of hydrochloric acid solutions, phosphoric and acetic acid solutions, and ammonium hydroxide and ammonium chloride solutions on the surface topography of each polar face was evaluated using constant-force contact-mode AFM. The bound-exciton and green band luminescence properties were studied using photoluminescence spectroscopy (PL), and free-exciton resonances by reflectance spectroscopy (RF) (see *Chapters 2* and *3*). *Table 5.1* is a summary of the etchants used, concentrations/volumes, and etch rates as given by *Vellekoop et al.*. Although the etching durations used for this study were based on the reported etch rates in the published data, these rates do not seem to take each polarity face into account or variations/differences in lateral and vertical etching. It was found that the etching characteristics differed substantially for each solution compared to the previously reported data.

With a study of this nature, involving chemical interactions between etchants and surfaces, the reproducibility of results must be demonstrated. Since four [O] and four [Zn] unannealed surfaces were etched with each solution, giving a total of 40 samples, the results presented herein are for each solution rather than each sample and are deemed to be representative of the overall effects. In cases where there are obvious

differences in topographic or optical data between wafers etched similarly, this data is also presented. It will be demonstrated, however, that the etching behaviour of the polar surfaces follows definite trends regardless of the solution used. Each sample was held with tweezers for the requisite time in the etchant solution followed by a rapid wash in de-ionised water to stop further etching. Samples were subsequently dried with flowing nitrogen gas. In all cases the solutions were mechanically agitated and the etching occurred at room temperature. The pH value for each solution used here, shown in *Table 5.1*, was also measured at room temperature before the ZnO samples were immersed. It is immediately apparent that the times reported by *Vellekoop et al.* for each solution to etch a depth of 1 μm do not correlate with the pH values of the solutions used here. For example, according to the published data, the 1% HCl solution should etch surfaces to a 1 μm depth in 6 seconds while the 1:1:10 ml phosphoric acid: acetic acid: water solution should etch to a similar depth in 40 seconds. However, the measured pH of the phosphoric solution is lower than that of the HCl solution, and it is therefore difficult to reconcile the reported etch rates with the determined pH values.

Given that the measured pH values of each acidic solution used herein do not appear to bear relation to the reported etch rates, and that the published etch rates do not take differences in the polar faces or differences in the vertical-to-lateral etch ratios into account, the reader might realistically ask what one intends to achieve with a study containing so many unknown variables. The aim, however, is not to accurately determine etching parameters for different solutions (which, as shall be discussed, is difficult on as-received wafers), but to investigate the impact of surface topography on optical properties. In this regard the actual details of the solutions or their etch rates are less important, provided that the resultant surface topography varies from one solution to the next, and that one can quantify the topographical changes that result after etching and compare the corresponding optical characteristics.

Table 5.1:

	Etchant[1]	*Volumes*[2]	*pH*[3] *(room temp.)*	*Etch Rate*[4] *(μm/min)*	*Etch Time*[5] *(1 μm)*
a.	HCl (37%) H_2O	1 ml 36 ml	0.9	10[?]	6 secs
b.	HCl (37%) H_2O	1 ml 99 ml	1.2	10[?]	6 secs
c.	H_3PO_4 (85%) HAc (96%) H_2O	1 ml 1 ml 10 ml	0.8	1.5	40 secs
d.	H_3PO_4 (85%) HAc (96%) H_2O	1 ml 100 ml 100 ml	1.4	0.8	75 secs
e.	NH_4Cl NH_4OH (25%) H_2O	6 g 4 ml 30 ml	9.7	0.5	120 secs

Note:

[1] *The etchants chosen for this study are based on those used by Vellekoop et al. [2]. However, this published report does not indicate the concentration of the constituents of the solution before mixing. The percentages shown in brackets represent the concentrations used here.*

[2] *The volumes used for each solution are identical to those used by Vellekoop et al..*

[3] *The pH of each solution was measured at room temperature, and it is immediately clear that the pHs do not correlate well with the reported etch rates. For example, note the 6 second etch time for the HCl solution (pH of 0.9) and the 40 second time for the phosphoric/acetic acid solution (pH of 0.8).*

[4] *The etch rate is that reported by Vellekoop et al., but this is not believed to take the different polarity faces into account or variations in lateral or vertical etch rates.*

[5] *The etch time is simply the estimated length of time required to etch to a 1 μm depth based on the reported etch rate.*

[?] *Vellekoop et al. do not specify whether the concentration of the HCl solution is 1% by volume or concentration. Since they simply report the HCl etch rate at 10 μm per minute, it is unclear as to which solution this rate refers.*

Although it is common practice to anneal material to improve surface topography before scanning-probe microscopy measurements, this inevitably leads to changes in excitonic properties and green band emission. Annealing single-crystal ZnO in O_2 atmospheres causes bound-exciton PL lines to merge into a single broad peak [3], while anneals in N_2 have been shown to increase the intensity of certain bound-exciton lines whilst decreasing others [4]. For the initial measurements discussed here, concerning the effects of surface topography on excitonic features, samples were not annealed in order to facilitate a meaningful comparison of bound-exciton, free-exciton, green band and surface characteristics before and after the etching process. The impact of etchants on annealed surfaces will also be examined below, though to a lesser extent.

To obtain the reflectance spectra, samples were illuminated by a 150 W Xe lamp focused on the crystal at an incident angle of ~ 45° (focal axis). It should be noted that although focusing increases the detector signal-to-noise ratio, which is particularly poor for surfaces damaged after etching, the varying incident angles of light into the spectrometer can introduce various anomalous 'dips' in the reflectance spectra which are pronounced for samples showing strong reflectance characteristics. While the non-normal incidence angle and subsequent focusing of light does not allow a detailed examination of exciton-polariton behaviour, as discussed in *Chapters 6* and *7*, the general strength of the excitonic resonances is readily apparent. The typical resolution of the reflectance data presented is ~ 0.5 meV over the wavelength region of interest. For PL measurements the 325 nm line of a HeCd laser was used for excitation, with typical powers of 40 mW unfocused on the samples. The resolution of PL data is ~ 0.1 meV. Further details on the apparatus used to obtain optical spectra are given in *Chapter 2*.

5.3 *Sample Characteristics Before Etching*

5.3.1 *Unannealed Wafers*

Figure 5.1 is a 4×4 μm AFM topographic image of the $(000\bar{1})$ O-terminated surface of a Rubicon hydrothermally-grown, epi-polished crystal and is typical of all samples with this polar orientation. Since a height scale of 4 nm is sufficient to encompass most of the surface features, excluding obvious particulate dirt, one can conclude that the O-terminated surfaces are relatively smooth and uniform after the polishing procedure. However, small pits are observed on this polar face in particular and the highlighted rectangular section of *Fig. 5.1* surrounds a region in which the concentration of these pits is noticeably high. This area is magnified in *Figure 5.2* and the enlarged image reveals not only these pits but a relatively high density of steps with heights of less than 1 nm and terraces with widths of the order of the tip radius (~ 50 nm). The distance between O-Zn bi-layers parallel to the *c*-axis of the crystal near the surface is approximately 0.5 – 0.6 nm. AFM profile data across the enlarged section of *Fig. 5.2* is shown in *Figure 5.3* and demonstrates that the pits/steps have depths corresponding to single or double atomic terraces formed during growth [5].

Figure 5.4 is a 5×5 μm AFM topographic scan of a (0001) Zn-terminated face. In comparison to the $(000\bar{1})$ surfaces, the Zn-terminated faces have a high concentration of scratches that are believed to be introduced by the epi-polishing process itself. Profile data, taken across the diagonal of *Fig. 5.4*, is shown in *Figure 5.5*. Although the scratches vary in dimension, the largest have widths of ~ 200 nm and depths of ~ 40 nm. However, since the AFM tip radius is approximately 50 nm (*Chapter 2*), the determination of the depths may not be accurate for scratches with lateral widths of this order.

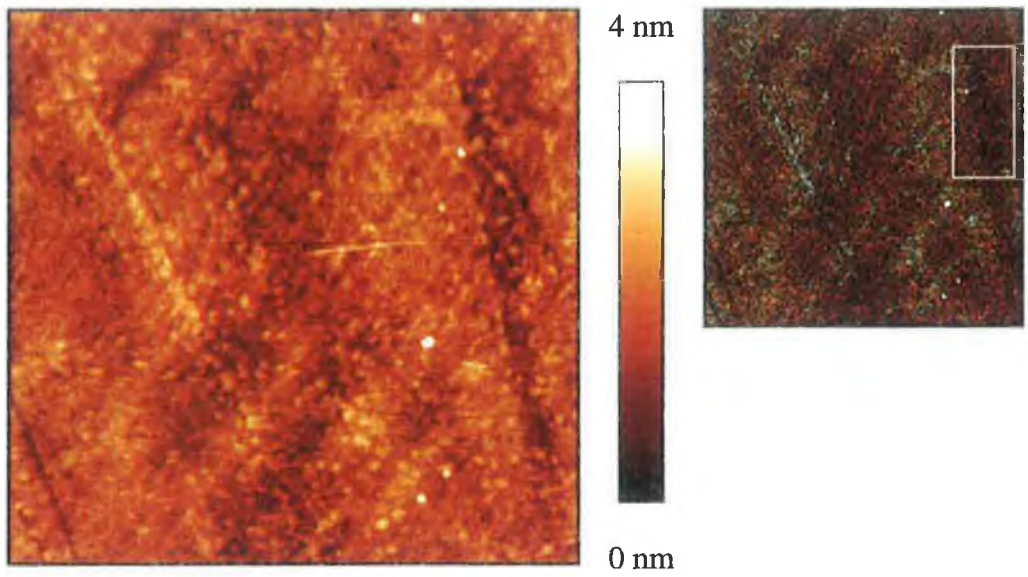

Figure 5.1: *4×4 μm AFM image of the polished O-terminated surface of a Rubicon wafer. This face has a large number of small pits (black regions) and relatively minor variations in surface height overall. The image to the right is a false colour version (due to application of lighting and perspective algorithm) of the original (left) to exaggerate the relative heights. The highlighted region has been magnified in Fig. 5.2.*

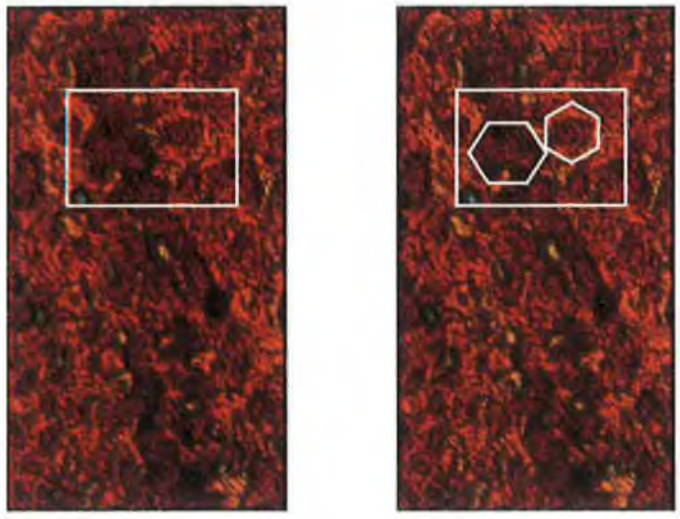

Figure 5.2: *0.9×1.7 μm enlargements of the indicated region of Fig. 5.1. The images shown have an additional perspective and lighting algorithm applied in order to show surface heights more effectively (< 2 nm over the image). The surface contains a high concentration of steps with heights typically less than 1 nm. The boxed area in the left image encompasses two hexagonal pits. The right image is identical, but with these hexagonal features highlighted for clarity.*

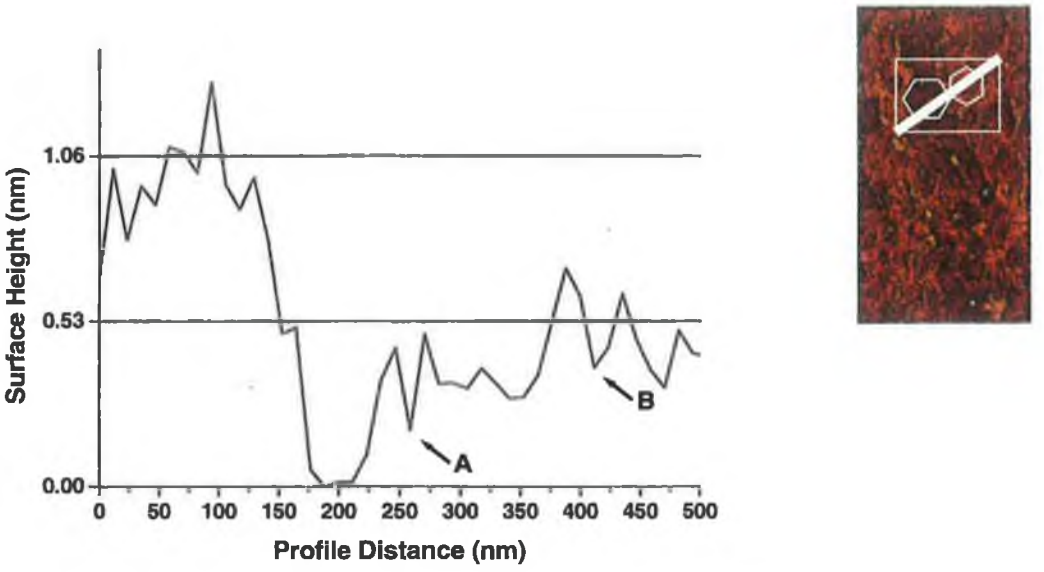

Figure 5.3: *AFM profile across a 500 nm section of the indicated region of Fig. 5.2 (shown right), encompassing the hexagonal pits. The data suggests that the larger pit has a width of approximately 100 nm, which is typical for other pits observed on the surface (50 – 100 nm). The height scale is set at increments of 0.53 nm, approximately equal to the bi-layer spacing determined from the literature. Although there appears to be steps that do not correlate in height with the measured separation, these features are likely to be small pits with sloped edges (examples are labelled A and B) that narrow to widths below the AFM tip radius. One can conclude that the O-terminated surface is generally polished to a height tolerance of a few bi-layers, explaining the standard deviation and RMS roughness values of typically less than 1 nm for small scanning regions.*

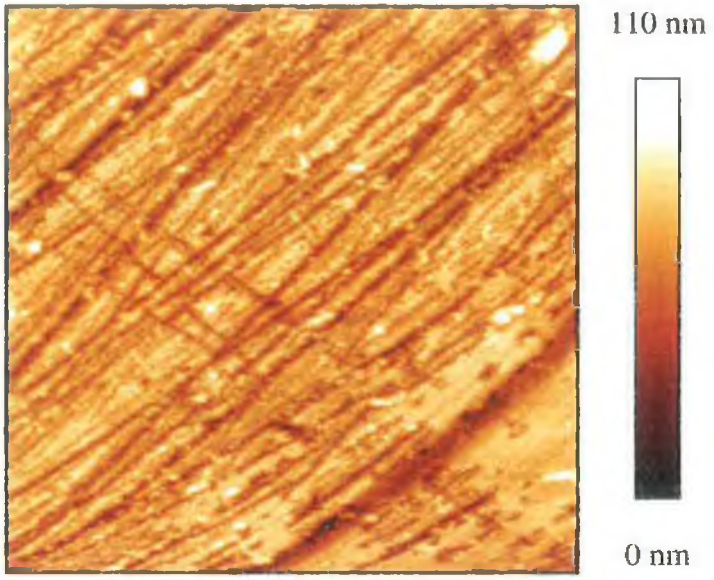

Figure 5.4: *5×5 μm AFM image of the polished Zn-terminated surface. This face has a high concentration of scratches, presumably introduced by the epi-polish process itself and thus, an increased surface roughness (standard deviation and RMS values of 5 – 10 nm) compared to polished O-terminated surfaces.*

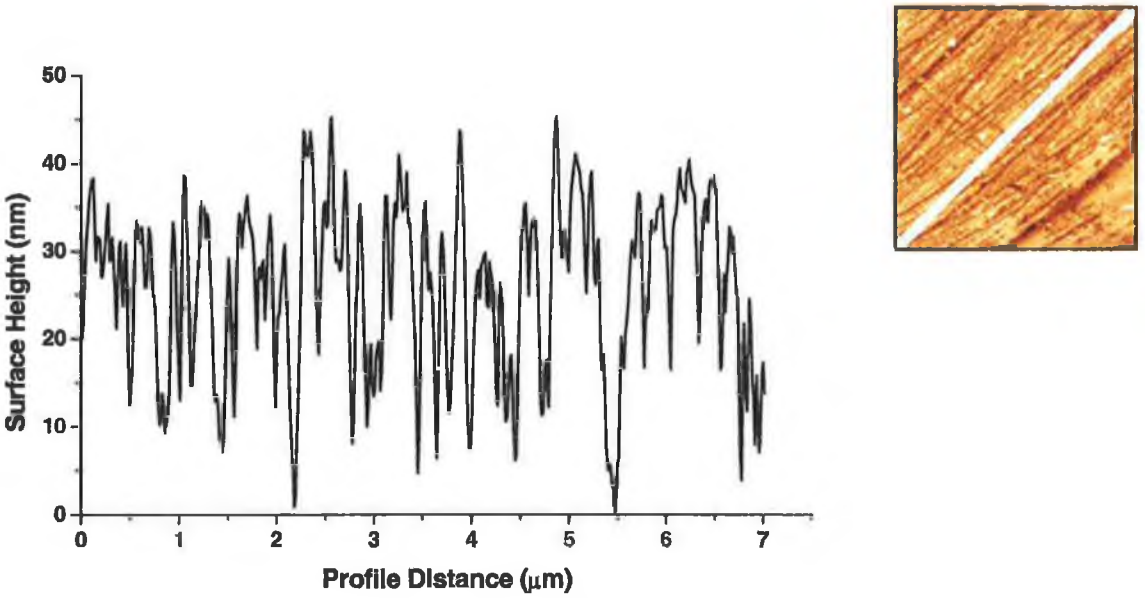

Figure 5.5: *AFM profile across the diagonal of Fig. 5.4 (shown right). The largest polish-induced scratches have widths of approximately 200 nm and depths of 40 nm.*

In order to quantify the roughness of surfaces, three different techniques are employed. The first, and simplest, is an RMS height analysis of data obtained by the AFM. An examination of six different as-received [O] Rubicon wafers, with AFM scan sizes ranging from 5 to 50 μm^2 for each, produces RMS surface roughness figures that vary from ~ 0.4 nm to ~ 18 nm. The wide range of values is a direct consequence of the difficulty in cleaning particulate material from this polar surface, as described in previous chapters. To minimise the impact of dirt on roughness analysis, AFM scans presented in this chapter were generally restricted to a 5×5 μm size. The RMS roughness for these small area scans are typically < 1 nm for [O] surfaces and between 5 and 9 nm for [Zn] faces.

The second method of determining surface roughness involves examining profile data across the diagonals, horizontal and vertical mid-sections of the AFM scans. The standard deviation (SD) in surface height for each direction was calculated relative to a line-fit representing an ideally flat surface profile. These SD figures were then averaged to obtain a quantitative value for the particular AFM image. Although this method does not take the entire imaged surface into account, the advantage is that profiles can be manually selected in order to avoid obvious surface contamination. The mean SD in surface height is 9.24 nm for the Zn-terminated image shown in *Fig. 5.4*, and 0.35 nm for the O-terminated face in *Fig. 5.1*. More generally, the mean standard deviations observed for Rubicon polar faces closely match the RMS roughness values, with SDs of less than 1 nm for [O] faces and between 5 and 10 nm for [Zn] faces.

Both RMS and standard deviation analysis suffer a similar problem – a theoretically infinite number of different surface topographies could result in the same determined roughness value. To augment these techniques, the 'ironed surface area' (ISA) of a given image was also obtained and compared to the planar surface area. The ISA is calculated by the WSxM software [6] by fitting a polygonal shape, such as a triangle, to adjacent pixels in an AFM image taking into account not only the (x,y) separation of the pixels, but the vertical (z) height also. In effect, the polygon will be a

three-dimensional structure and its area can be calculated. Mapping this polygon across the entire image, taking every pixel into account, and summing the area of each will give the total surface area of the AFM image [7]. This can then be compared to the expected planar/basal surface area. For example, a 5×5 μm region has a planar area of 25 μm^2 but, due to topographic variations, the total surface area will be slightly larger, say 25.025 μm^2. The roughness of the face can be expressed as a ratio;

$$\frac{Ironed\ Surface\ Area - Planar\ Surface\ Area}{Planar\ Surface\ Area} \times 100$$

which, in the case of the example, gives;

$$\frac{25.025 - 25}{25} \times 100 = 0.1\%$$

indicating that the surface area increases by 0.1% as a result of topographic features. One finds that for [O] surfaces, the ISA is between 0.2 and 0.7% greater than the planar surface area of 25 μm^2, whereas the area is 2.5 to 7% greater for [Zn] surfaces.

The optical properties of the Rubicon sample surfaces have been previously shown in *Chapter 3*. To summarise briefly, the O-terminated surfaces show both strong luminescence and free-exciton reflectance resonances, whereas the Zn-terminated surfaces demonstrate no bound-exciton emission features and severely damped free-exciton oscillations. One may readily imagine on the basis of the AFM images discussed above, that the poorer topographic quality of the Zn-terminated faces, compared to O-terminated material, is the cause of the poorer optical characteristics. It was initially concluded, on the basis of a less extensive analysis of surface roughness, that scattering of light by the polish-induced scratches was the origin of the reduced reflectance characteristics for Zn-terminated faces, with the intensity of PL lines being affected by surface defects [8]. This original conclusion still largely stands – the polish scratches on the [Zn]-face can have widths of 200 nm or greater which is not insignificant compared to the wavelength of light examined in reflectance spectra.

5.3.2 Annealed Wafers

Figure 5.6 is a 50×50 μm AFM scan of an O-terminated Rubicon surface after annealing for 24 hours at 1000°C in a 0.5 bar O_2 atmosphere, and reveals the presence of a high concentration of hexagonal pits. A number of authors have previously reported such structures on the O-terminated polar face after annealing [5,9], and these are believed to be thermal pits formed as a result of surface relaxation. While there is no indication from the literature that others observe a similarly high concentration of thermal pits, one may speculate that the initial presence of small hexagonal pits in the as-received wafers (*Fig. 5.2*) and the long duration of the anneal are the reasons for the large numbers observed after annealing. The surface roughness of *Fig. 5.6* is ~ 20 nm (SD) and ~ 19 nm (RMS), compared to figures of < 1 nm for unannealed material. The ISA is ~ 0.2% greater than the 50×50 μm planar area, which is similar to values calculated for 5×5 μm unannealed surface regions. Therefore, although one observes an increase in the RMS and SD figures, the ISA value demonstrates that the overall surface area is not increased dramatically.

Figure 5.7 shows profile data across the diagonal of *Fig. 5.6*, and *Figure 5.8* is a 4×2.5 μm enlargement of a typical thermal pit. Profile data for this thermal pit is shown in *Figure 5.9*. Generally one finds that the thermal pits have widths of the order of 2 to 5 μm (*Figs. 5.6* and *5.9*) and depths ranging from 20 to 80 nm. It should be noted that the profile data indicates relatively steep pit walls, hence explaining the fact that the total surface area is not greatly increased by their presence.

Although thermal pits are observed on all annealed [O] wafers, with roughness values and pit dimensions comparable for each, steps and plateaus are also seen in surface regions between the pits (*Figure 5.10*). *Figure 5.11* shows profile data across the diagonal of *Fig. 5.10*. The roughness of this image is 1.7 nm (RMS) and 1.3 nm (SD), and the ISA is just 0.1% larger than the planar surface area.

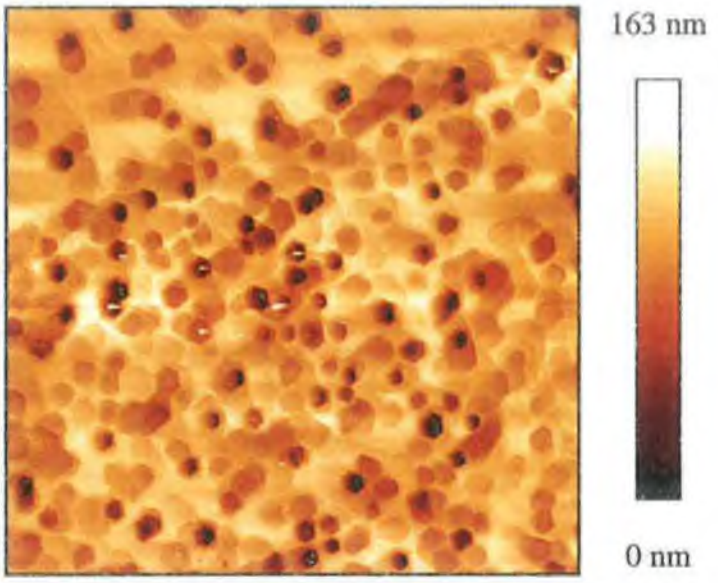

Figure 5.6: *50×50 μm AFM scan of O-terminated wafer after annealing for 24 hours at 1000°C in a 0.5 bar atmosphere of O_2. A high concentration of small pits is observed, having depths of the order of 60 nm and widths of about 3 μm. These 'thermal pits' are believed to be formed after surface relaxation during annealing. Although somewhat speculative, the high density of pits in the annealed material may be related to the initial concentration of pits (Fig. 5.2) observed for as-received surfaces.*

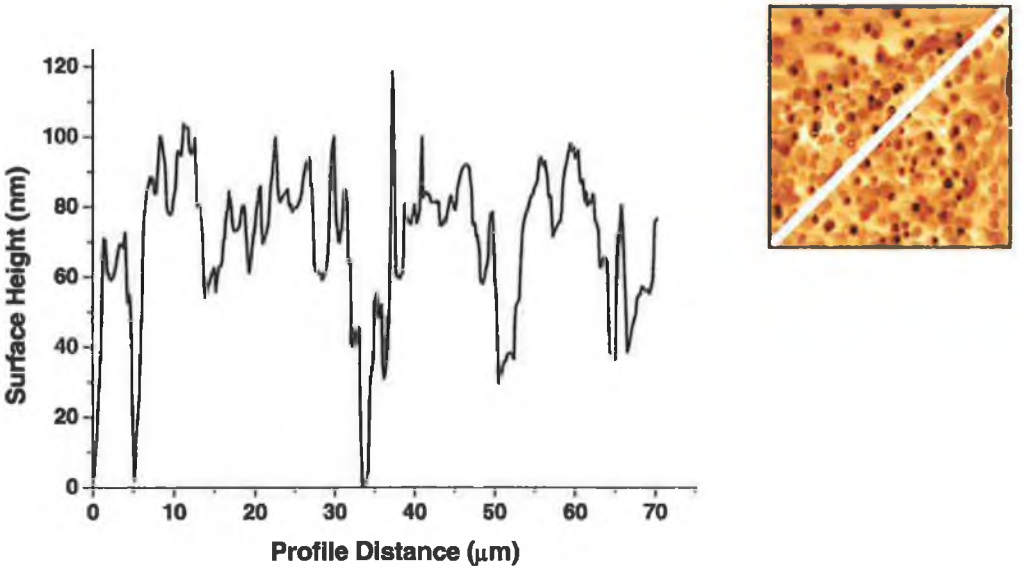

Figure 5.7: *Profile data across the diagonal of Fig. 5.6 (shown right), indicating that pits have typical depths of 20 – 80 nm and widths of 2 to 5 μm.*

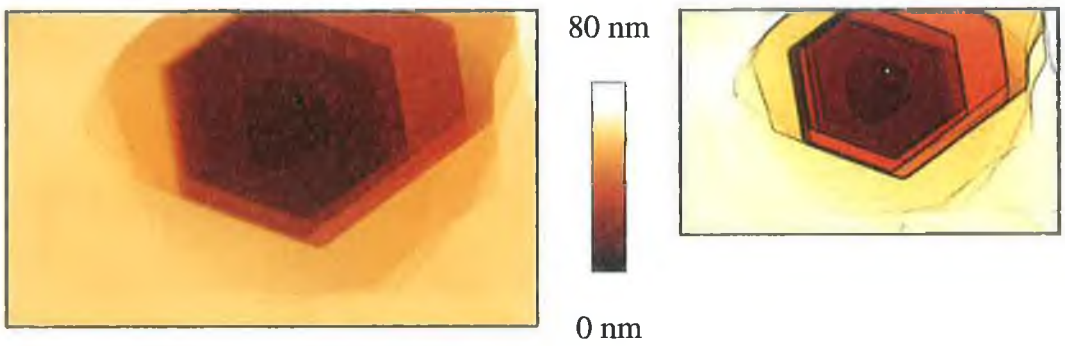

Figure 5.8: *4×2.5 μm enlargement of a typical thermal pit. The image to the left is the flattened AFM scan and demonstrates the hexagonal structure and stepped nature of the edges. The image to the right has been subjected to a perspective and lighting algorithm in order to highlight these steps.*

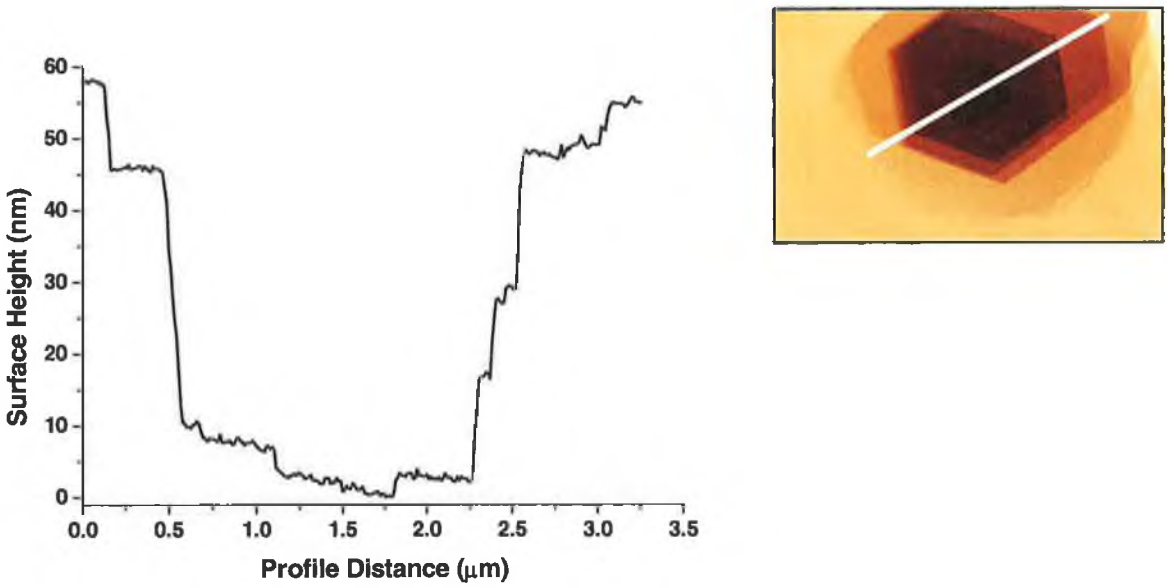

Figure 5.9: *Profile across the diagonal of the thermal pit in Fig. 5.8 (shown right). Note the steep walls of the pit which, based on the ISA analysis of the image, increase the overall surface area by only a small amount.*

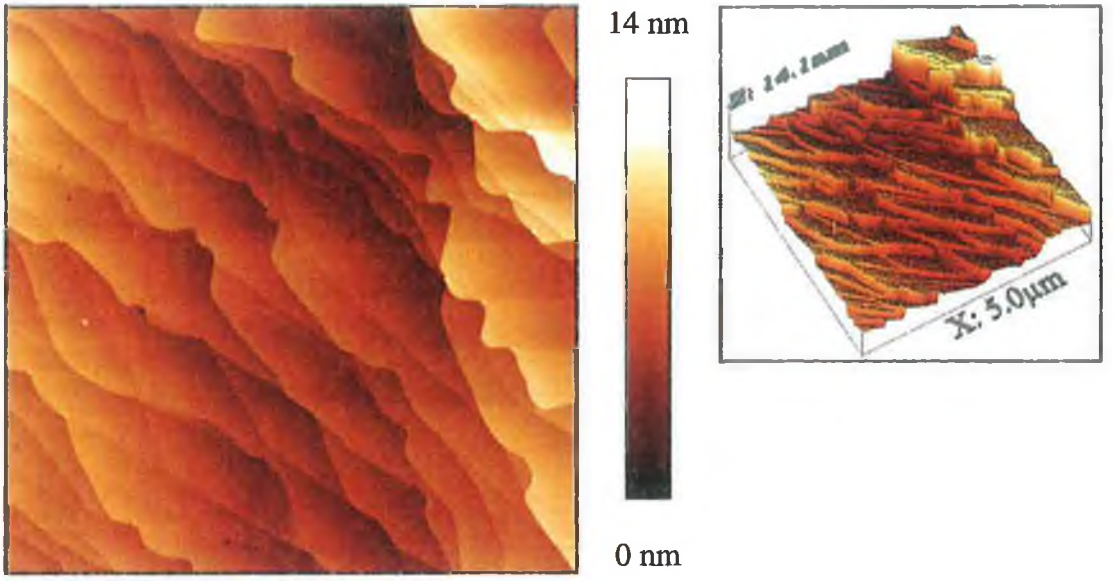

Figure 5.10: *5×5 µm AFM image of steps on annealed O-terminated surface. The figure to the left is the flattened scan. However, due to the presence of such a large number of steps across the image, the flattening is not effective and relative heights are somewhat distorted giving the impression of ridges rather than steps. The figure to the right is a 3D orthogonal plot of the same data, and shows the height differences in the image more clearly.*

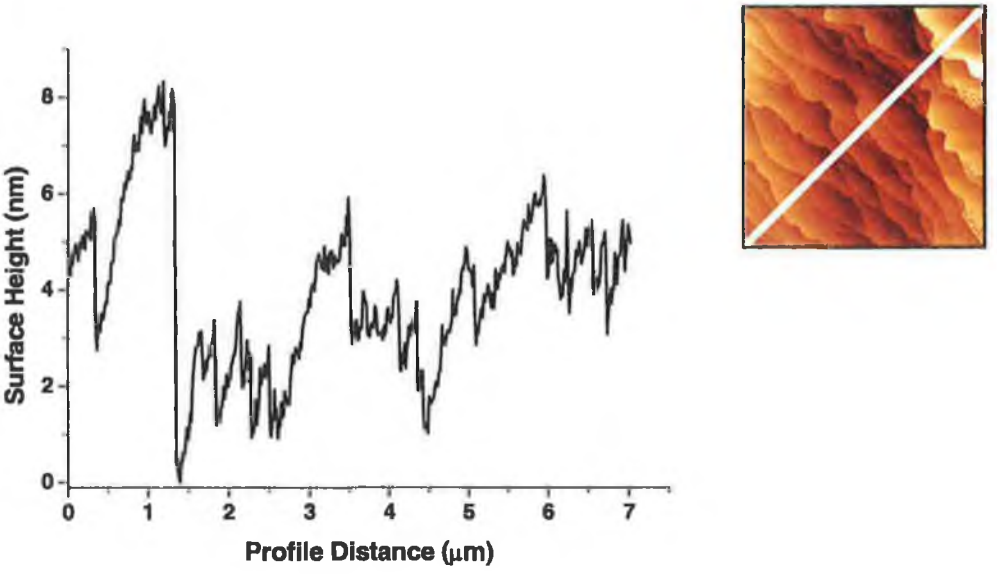

Figure 5.11: *Profile data across the diagonal of Fig. 5.10 (shown right).*

Having examined the surface morphology of annealed O-terminated surfaces, *Figure 5.12* shows an AFM topographic scan of a Zn-terminated surface after annealing with identical conditions to those discussed above. The image shown to the right of *Fig. 5.12* is a 50×50 μm scan of an unannealed, as-received [Zn] surface, whereas the image to the left is a equally sized scan of an annealed surface. Although both faces exhibit polish-induced scratch marks, the finer scratches appear less defined for the annealed face and one observes irregular-shaped plateaus across the surface as a whole. The roughness of this annealed face is 5.5 nm (RMS) and 4.8 nm (SD) and, considering the 50×50 μm scale of the image, these figures represent a slight reduction in topographic roughness (5 – 10 nm SD and RMS for 5×5 μm unannealed faces). For comparative purposes, the RMS roughness of the 50×50 μm unannealed face also shown in *Fig. 5.12* is 7.5 nm. The ISA of the annealed [Zn] face is just 0.07% larger than the 2500 μm^2 planar area, compared to a 3% increase for the unannealed face shown. *Figure 5.13* shows profile data for a diagonal cross-section of the annealed Zn-terminated face in *Fig. 5.12*. Although this data spans a length of some 70 μm, compared to 7 μm for the profile across an unannealed Zn-terminated face shown in *Fig. 5.5*, there appears to be a general reduction in the depth of scratches.

Figure 5.14 is a 5×5 μm enlargement of the irregular-shaped plateaus found across the annealed Zn-terminated faces. The RMS and SD roughness values for this image are 1.7 nm in both cases (compared to 5 - 10 nm for unannealed surfaces using similar scan sizes), with a total surface area increase of 0.05% over the expected planar area (compared to 2.5 – 7% for unannealed surfaces). Profile data for *Fig. 5.14* is given in *Figure 5.15*.

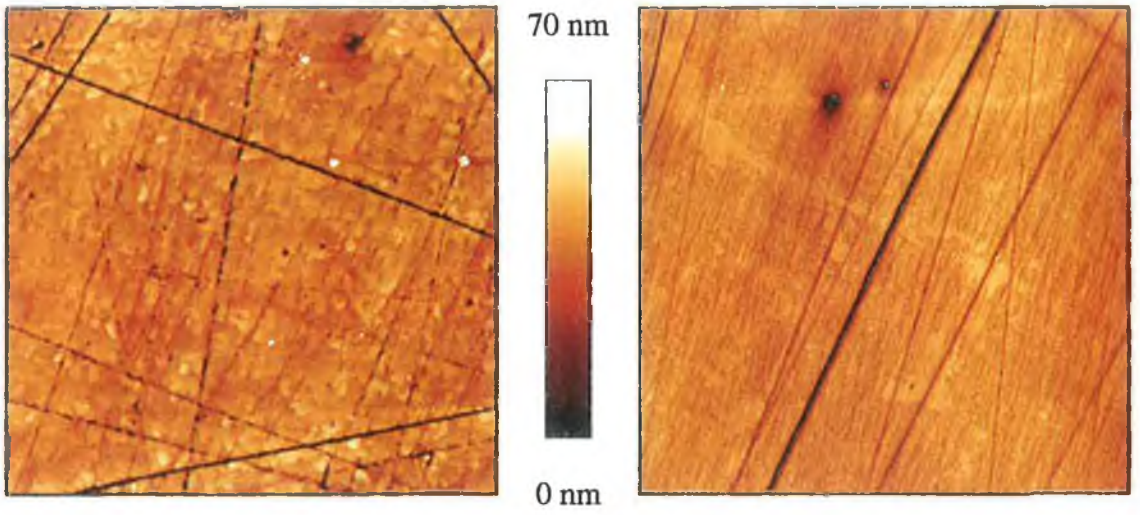

Figure 5.12: *50×50 μm AFM images of Zn-terminated surface after annealing for 24 hours at 1000°C in a 0.5 bar atmosphere of O_2 (left), and as-received (right). Although the images are of two different wafers, it is immediately apparent that the definition of the polish-induced scratches is reduced after the anneal and the surface appears to contain a high concentration of irregular-shaped features (magnified in Figure 5.14).*

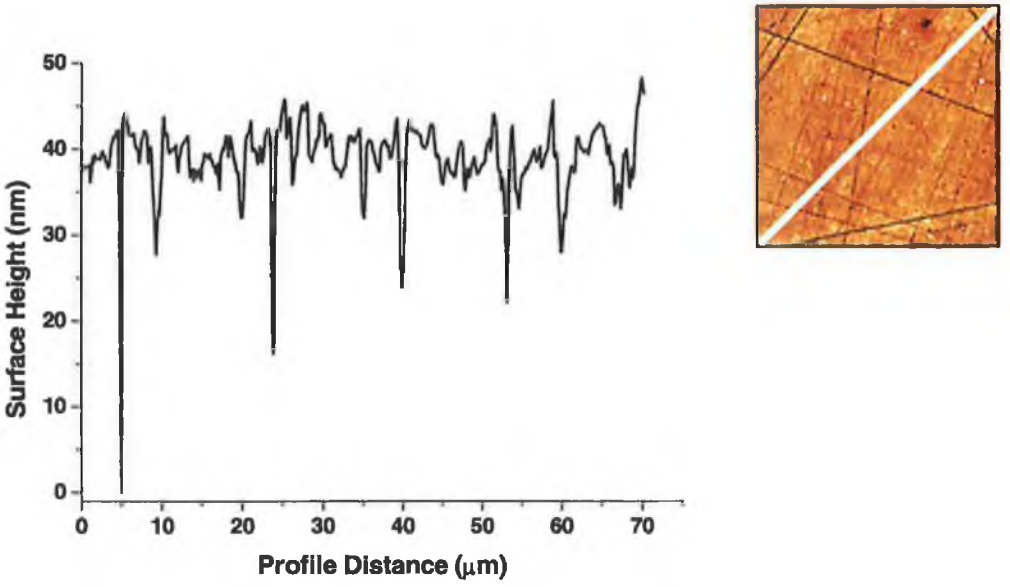

Figure 5.13: *Profile data taken across the diagonal of Fig. 5.12 (annealed surface), shown right, revealing a reduction in the scratch depths compared to Fig. 5.5.*

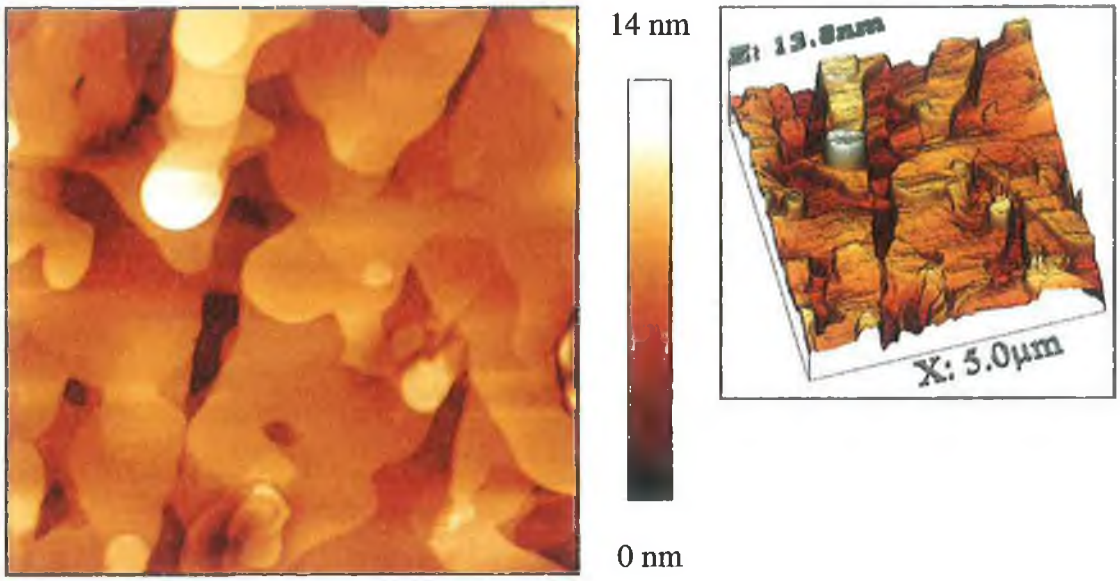

Figure 5.14: *5×5 µm AFM scan of annealed Zn-terminated surface showing irregular-shaped plateaus and steps. As with Fig. 5.10, flattening the image is complicated by the large number of steps. The image to the right is a 3D orthogonal projection of the data to highlight the relative heights between features.*

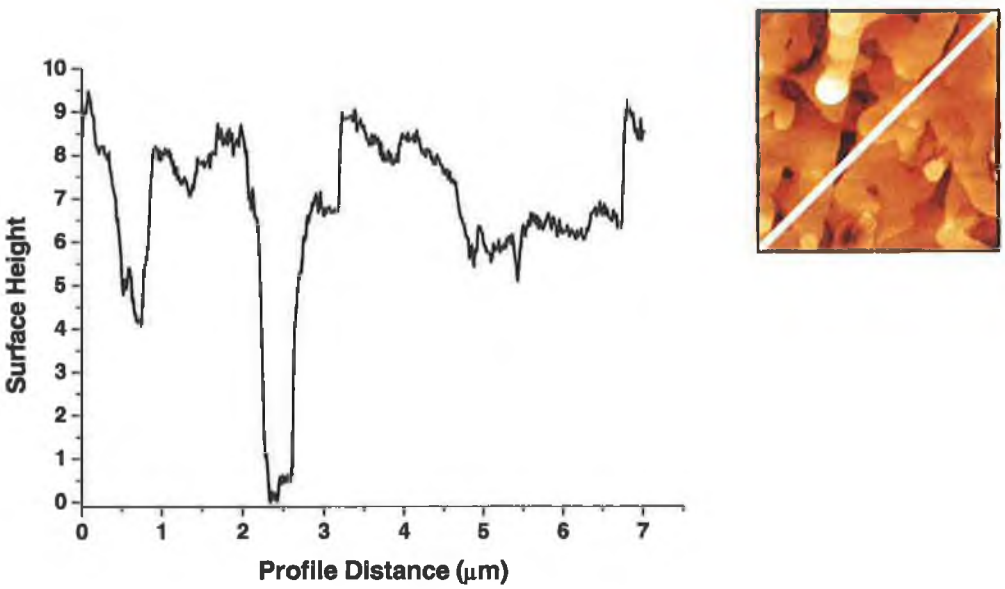

Figure 5.15: *Profile data taken across the diagonal of Fig. 5.14, shown right.*

To summarise, annealing of the polar surfaces causes the formation of plateaux and steps as a result of surface relaxation. In the case of O-terminated surfaces the morphology also creates thermal pits and generally increases surface roughness, as determined by RMS and Standard Deviation examinations of the height. However, the overall surface area does not substantially change compared to unannealed surfaces. This data indicates that the topography induced on annealing involves flat plateaus separated by steep steps, and pits with steep walls (and flat bases) rather than gradual inclines, which would increase the surface area more dramatically. One might expect that, on the basis of this AFM data, the intensity of light reflected from annealed O-terminated surfaces will be almost equivalent to unannealed surfaces since little additional scattering will occur. *Figure 5.16* shows reflectance spectra of both annealed and unannealed O-terminated surfaces at a temperature of 25 K. In energy regions away from the excitonic resonances (*inset*), the intensity of reflected light is ~ 5% lower for the annealed surface than for the unannealed surface. The excitonic resonances (*main figure*) are substantially reduced due to increased damping and are shifted to slightly lower energy for the annealed face ($A \approx 3.370$ eV, $B \approx 3.377$ eV), compared to the unannealed face ($A \approx 3.375$ eV, $B \approx 3.382$ eV), suggesting a change in the surface strain conditions and a reduction in face quality.

In contrast, although the [Zn] face also exhibits stepped surfaces after annealing, this generally has the effect of decreasing surface roughness. Polish scratches tend to reduce in dimension (as evidenced by the reduction in ISA percentage) and, as shown in the inset of *Figure 5.17*, overall intensity of reflected light increases by ~ 7% in regions far from the excitonic features due to the reduction in scattering from the surface. The resonances themselves (*main figure*) are substantially improved, with both *A* and *B* excitons visible and evidence of their excited states.

Thus, there is a strong correlation between small-scale AFM images (~ μm^2) of the surface topography and the overall intensity of reflectance spectra from large-scale areas (~ mm^2) on each of the polar faces. While there are many factors that affect the

strength of exciton resonances, such as strain, electric field intensity at step edges, etc., the quenching of these features is accompanied by increases in surface roughness, and their emergence by decreases in roughness.

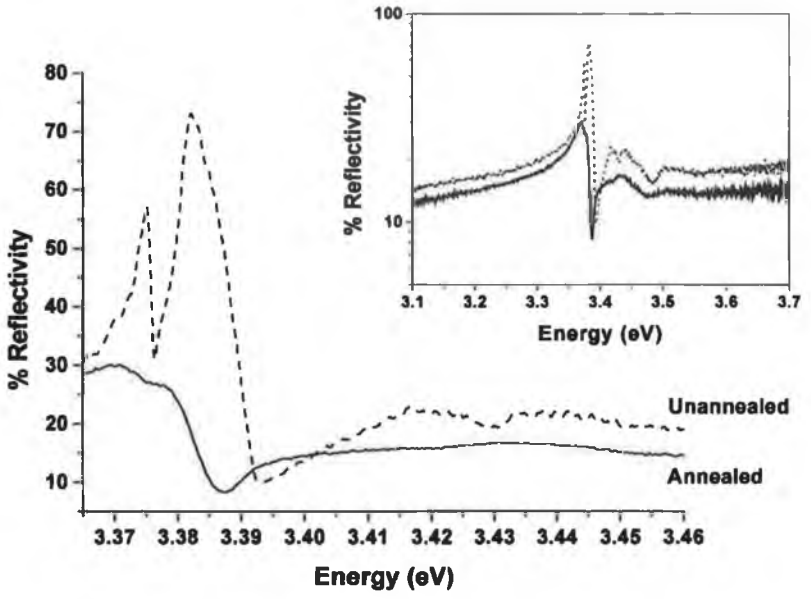

Figure 5.16: *Reflectance spectra (25 K) of annealed and unannealed O-terminated surfaces. The anneal increases the surface roughness and the intensity of light reduces as a result of scattering (inset). The excitonic resonances (main figure) are reduced in strength and shifted to slightly lower energy.*

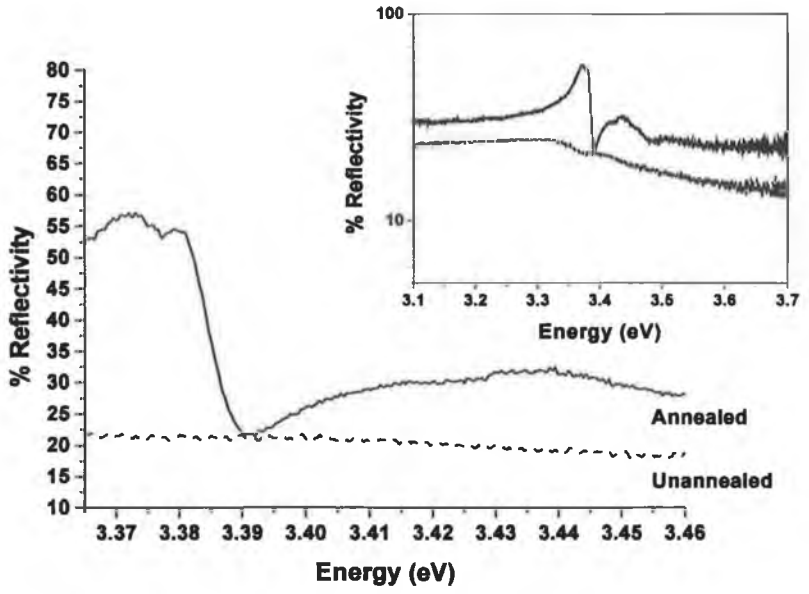

Figure 5.17: *Reflectance spectra (25 K) of annealed and unannealed Zn-terminated faces. The reduction in surface roughness after annealing reduces scattering and increases the intensity of reflected light (inset). One also observes dramatic improvements in the strengths of the exciton resonance features.*

Figure 5.18 shows PL spectra of the annealed and unannealed [O] faces at 25 K. Although the O-terminated surfaces are characterised by strong luminescence, it can be seen that bound-exciton features are completely quenched by the anneal. *J. A. Sans et al.* have shown that the absorption coefficient of a film of ZnO deposited on mica is approximately 2×10^5 cm^{-1}, giving a penetration depth of approximately 50 nm for light of wavelength 325 nm [10]. Although the samples examined in this study are bulk ZnO wafers, one might expect that the penetration depth of the HeCd laser used for PL measurements is certainly of this order. The quenching of BE luminescence is in agreement with the FE quenching observed earlier. This is likely to be due to the microscopic effects of surface roughness (e.g. point defect generation and alteration of surface recombination velocities) rather than scattering, since one would not expect PL

to be so markedly affected by scattering. The Zn-terminated surface, in comparison, exhibits no bound-exciton features before the anneal and no detectable change afterwards (not shown).

Although band-edge luminescence is entirely destroyed by the anneal in the case of the O-terminated faces, the intensity of the green band luminescence remains relatively unchanged and appears more structured than for unannealed samples (*Figure 5.19*). This structured nature of the band (seen as a series of 'undulations') is the result of phonon replicas (~ 72 meV separation between each) of a no-phonon line which is not apparent in the spectrum due to the limited resolution in this energy region (see *Chapter 2*), and has previously been attributed to Cu (*Chapter 3*). *Figure 5.20* shows the green band luminescence from the annealed Zn-terminated face, and it can be seen that the green band is not only structured, but increases substantially in intensity.

Thus, the effect of annealing in broad terms is to quench BE and FE signals, and it appears that deep level defects are introduced into the system. While the quenching of FE and BE features shows a correlation with surface roughness in both PL and reflectance studies of annealed O-terminated surfaces, in fact, this quenching is most likely due to microscopic deep defect generation. It is believed a similar process also occurs for Zn-terminated faces but in that case the quenching of FE resonances is partially offset by the observed reductions in surface roughness. One must consider the possibility that the anneal causes a considerable departure from stoichiometry in the surface region, creating deep level defects and quenching band-edge features. This explains the increase in green band signal and, although the structured green band is often associated with Cu, recent observations have suggested that it is related to Zn vacancies [11]. Hence, annealing in O_2 atmospheres may lead to the creation of Zn

vacancies, quenching of reflectance and band-edge PL features, and the growth of the structured green band – all in agreement with observations.

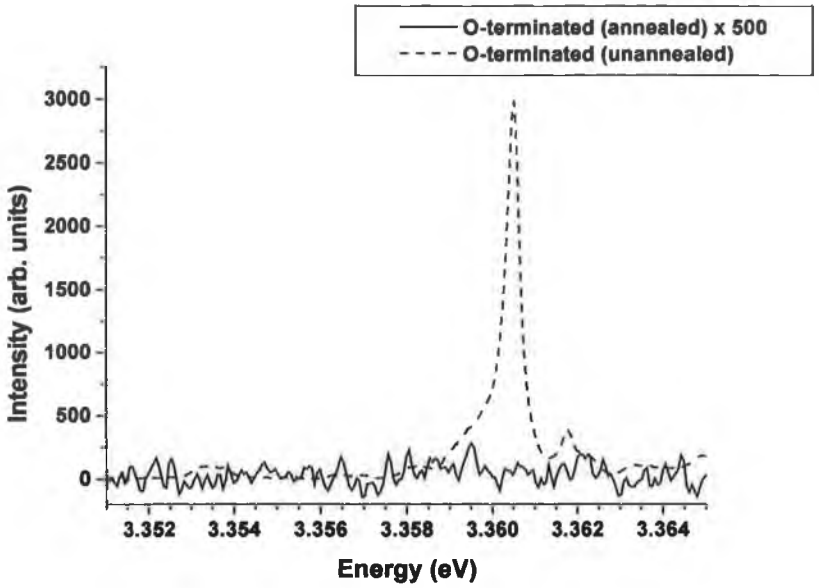

Figure 5.18: *PL spectra (25 K) showing the quenching of bound-exciton luminescence as a result of annealing O-terminated surfaces.*

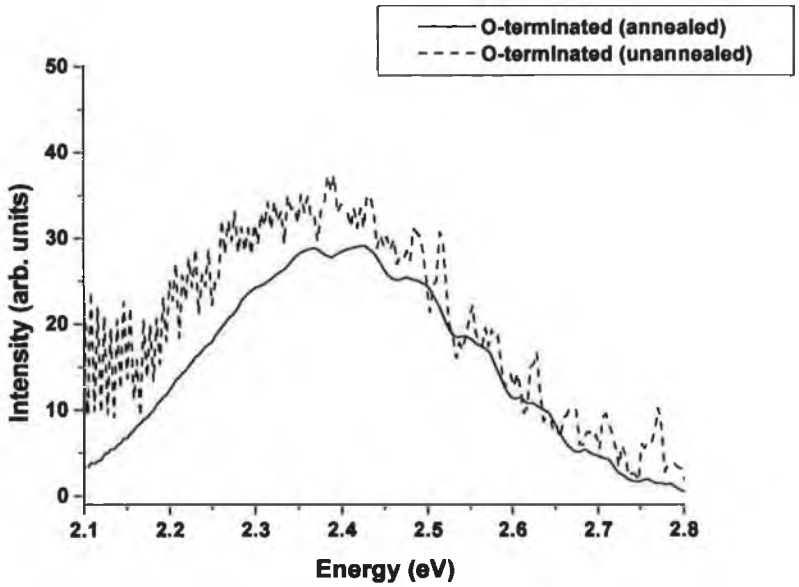

Figure 5.19: *Green band luminescence of O-terminated surfaces (25 K) before and after the anneal. Although BE luminescence is quenched, green band intensity remains relatively unchanged and the band itself appears structured.*

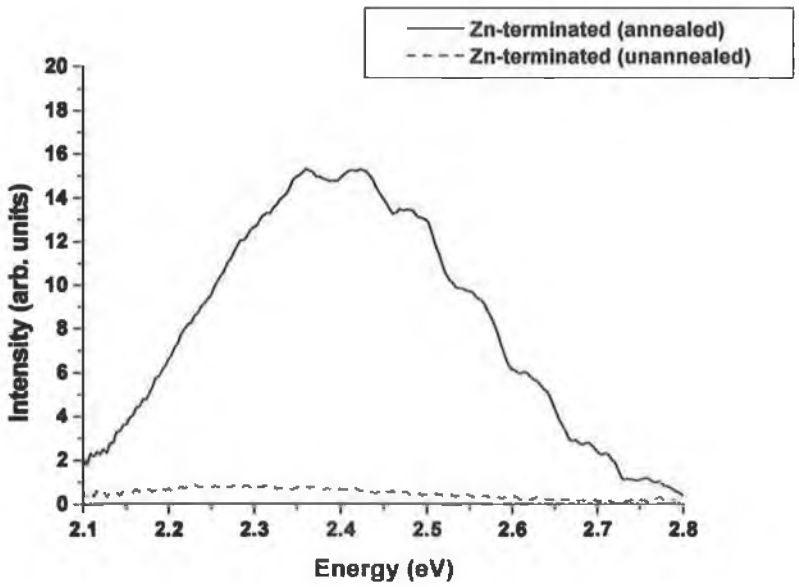

Figure 5.20: *Green band luminescence of Zn-terminated surfaces (25 K) before and after the anneal. As with the O-terminated face, the green band appears structured although one observes a substantial increase in intensity as a result of annealing.*

5.4 *Hydrochloric Acid Etching*

Since *Vellekoop et al.* do not specify in their report if the HCl solution used was 1% by volume or concentration, both solutions (*Table 5.1*) were used for the measurements discussed here. 1 ml of fuming HCl acid (37%) was mixed either with 99 ml or 36 ml of de-ionised water and samples were etched for ~ 6 seconds. The 1:36 ml solution (pH of 0.9) etches the O-terminated plane rapidly and the intensity of bound-exciton PL lines reduces to a level below the detectable limit of the apparatus. Since free-exciton resonances in reflectance spectra are also similarly quenched, this strong solution was only used to evaluate the effects of HCl on surface topography. The more dilute 1:99 ml HCl solution (pH of 1.2) was therefore used to determine the intermediate PL and reflectance characteristics.

Mariano et al. studied the interaction of HCl with the polar surfaces of ZnO and noted an anisotropy in etching behaviour [12]. In particular the O-terminated face, compared to the Zn-terminated face, was much more susceptible to attack from the acid. They attributed the difference in etch rates to the large difference in electronegativity between Zn and O, which leads to the O-terminated plane having two dangling electrons per O atom while the Zn-terminated surface has none. Etching of samples is therefore largely due to the bonding between hydrogen cations present in the acid and O from the material;

$$ZnO + 2HCl \rightarrow Zn^{2+} + 2Cl^{-} + H_2O$$

Figure 5.21 is a 4×4 μm AFM topographic image of the O-terminated surface and shows a high concentration of pits, separated by pronounced ridges, after etching with the stronger 1:36 ml HCl solution. The largest pits have depths of approximately 150 nm and widths of the order of 1 μm. The presence of such features dramatically changes the SD in height from < 1 nm to ~ 21 nm, with similar figures determined by RMS analysis. The ISA is 1.5% greater than the planar area of 16 μm^2, compared to < 0.7% for unetched surfaces. This suggests that the pits in this case have sloping edges

which contribute significantly to the overall topographic area, as shown in *Figure 5.22*. Optically, the [O] face exhibits no detectable luminescence in the near-band edge region after etching and reflectance spectra reveal only slight evidence of the *B* free-exciton resonance. Overall reflectivity reduces to less than 2% due to the high degree of scattering from the damaged surfaces, with damage on the order of the wavelength of light. The O-terminated face becomes visibly roughened as a result of the interaction with HCl compared to the [Zn] face which, as shall be seen, does not react to the same extent and this difference can be used as a simple means of identifying the termination of (0001) -oriented ZnO wafers.

As discussed above, a number of researchers have reported hexagonal thermal pits on the O-terminated polar face after annealing. *Maki et al.* [9] also etched these annealed faces and subsequently observed the formation of hexagonal ridges. The anneal creates flat terraces, interspersed with thermal pits with flat bases (terminating in O ions), that are preferentially etched by HCl with respect to the edges of the thermal pits (terminating in both Zn and O ions), leading to the appearance of hexagonal ridges or 'rings' (*Figure 5.23*). Since the samples discussed so far in this section were not annealed, and the O-terminated surface before etching already contains a relatively high concentration of small pits and steps, as shown previously, it is suggested that these observed features act as 'centres' for the etching in unannealed material in much the same manner as thermal pits behave for the mechanism proposed by *Maki et al.* in annealed material. In short, the high density of steps and pits in the unetched, unannealed surfaces examined herein is believed to account for the subsequent high density of ridges and pits observed in *Fig. 5.21*.

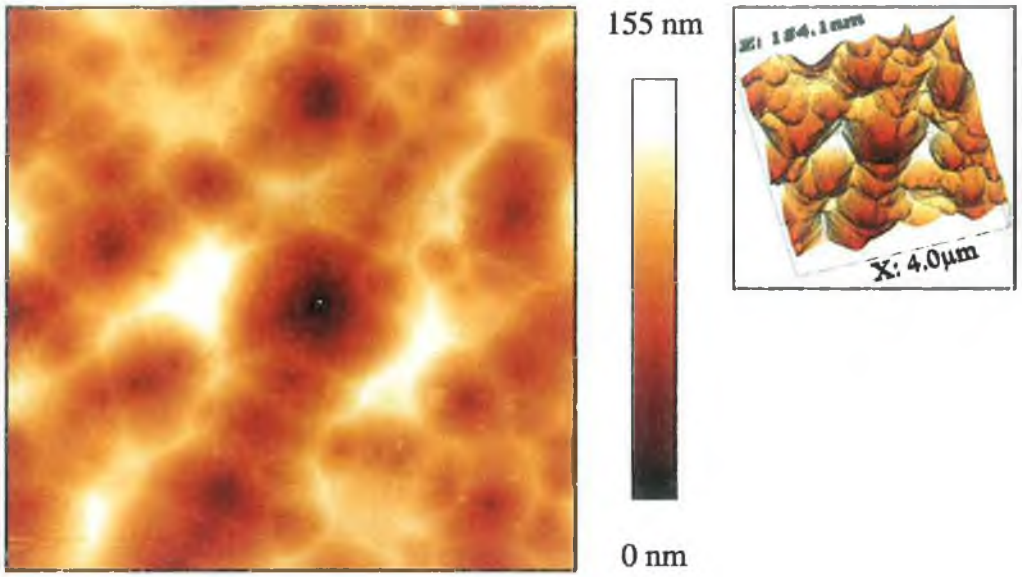

Figure 5.21: *4×4 µm AFM image of the O-terminated surface after a 6 second etch with the 1:36 ml HCl: H_2O solution showing hexagonal etch pits. The image to the right is a 3D orthogonal projection of the data to illustrate height differences across the scan.*

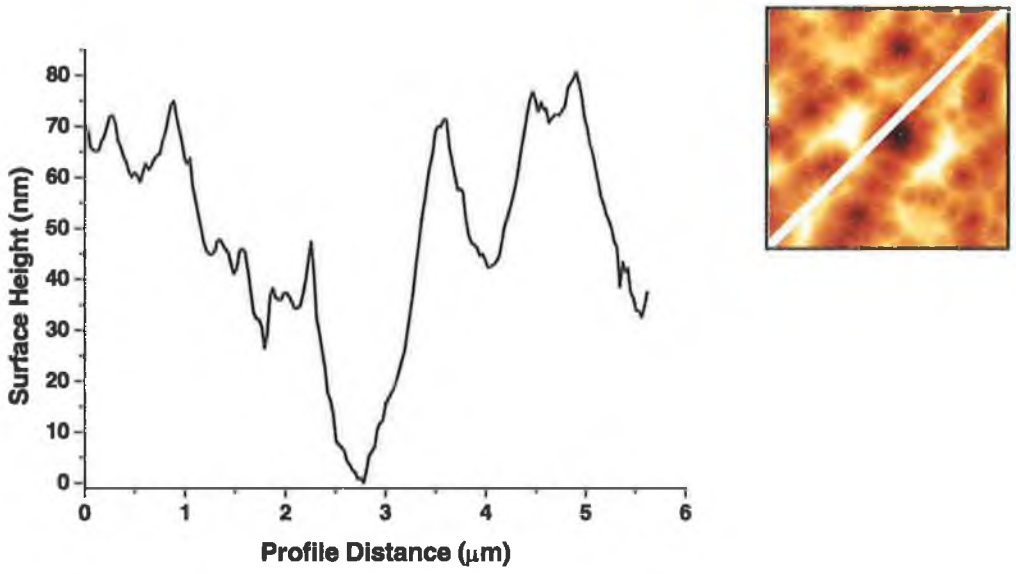

Figure 5.22: *Profile across diagonal of Fig. 5.21 (shown right). The data indicates that the pits have sloping edges (as compared to the thermal pits in Fig. 5.9) hence increasing the topographic area and increasing the amount of light scattered from the surface. The overall reflectivity drops to under 2%.*

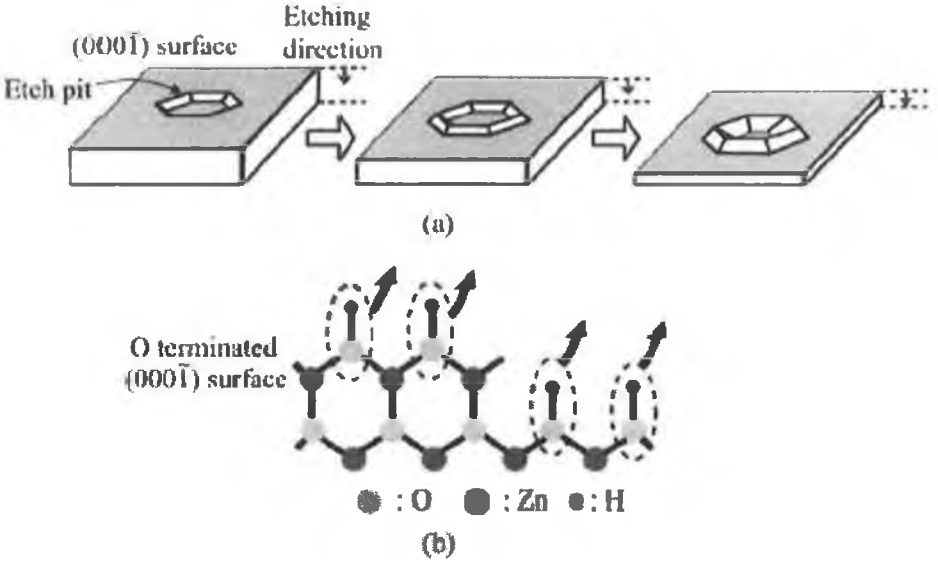

Figure 5.23: *Illustration, taken from Ref. [9], of the proposed mechanism for the creation of hexagonal 'rings' on O-terminated ZnO surfaces after annealing and etching with HCl. Thermal 'etch' pits are created after annealing, surrounded by relatively flat terraces. Since the pit edges terminate in both Zn and O atoms, one observes an anisotropy in the etching behaviour and the steps are etched to a lesser extent than the surrounding O-terminated terrace, leading to the eventual appearance of hexagonal 'rings' (a). The nature of the etch is shown in (b), where H cations from the acid bind to the O^{2-} ions in the material. Although the etched surfaces examined thus far in this dissertation were not previously annealed, one can readily imagine that the small pits and steps (having depths equivalent to the bi-layer spacing) observed in the as-received material act in much the same way as the thermal pits. The relatively high concentration of these features before etching accounts for the large number of pits observed after etching, as in Fig. 5.21.*

Intrinsic to the proposed mechanism by *Maki et al.* is the anisotropy of the etching, where the vertical etch rate (in a direction parallel to the *c*-axis of the crystal) is greater than the lateral etch rate (perpendicular to the *c*-axis) (*Figure 5.24*). One is therefore faced with a dilemma – the largest etch pits shown in *Fig. 5.21* have widths of 1 μm and depths of only 150 nm, suggesting that the etch rate is actually higher laterally than vertically by a ratio of approximately 10:1. *Figure 5.25* shows profile data taken across nine etch pits observed in *Fig. 5.21*. Using this data, line-fits to the two sides of each pit were obtained in order to determine the slope of the pit edges, from which the vertical (*z*)-to-lateral (*x,y*) etch rate may be estimated. The diameter and depth of each pit was also estimated from this profile data. If one imagines acid etching laterally from the centre of each pit (a distance of approximately half its width), dividing the depth by this 'radius' also determines the vertical-to-lateral rate. From the averages of both the slopes of pit edges and the relationship between pit radius and depth, the vertical-to-lateral etch ratio *appears* to be approximately 1:10 (*Table 5.2*).

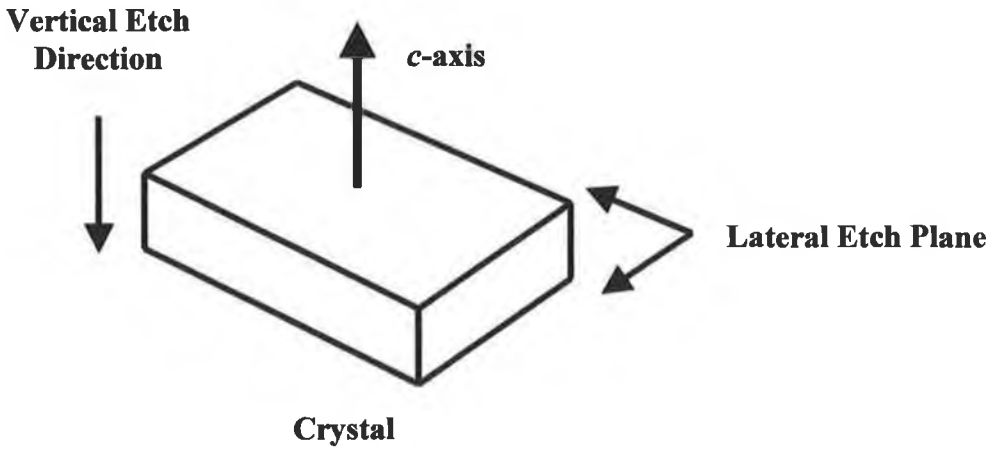

Figure 5.24: *Illustration of lateral and vertical etching directions. The lateral etch direction is perpendicular to the c-axis of the crystal (i.e. across the polar face) whereas the vertical etch direction is parallel to the c-axis (i.e. into the polar face)*

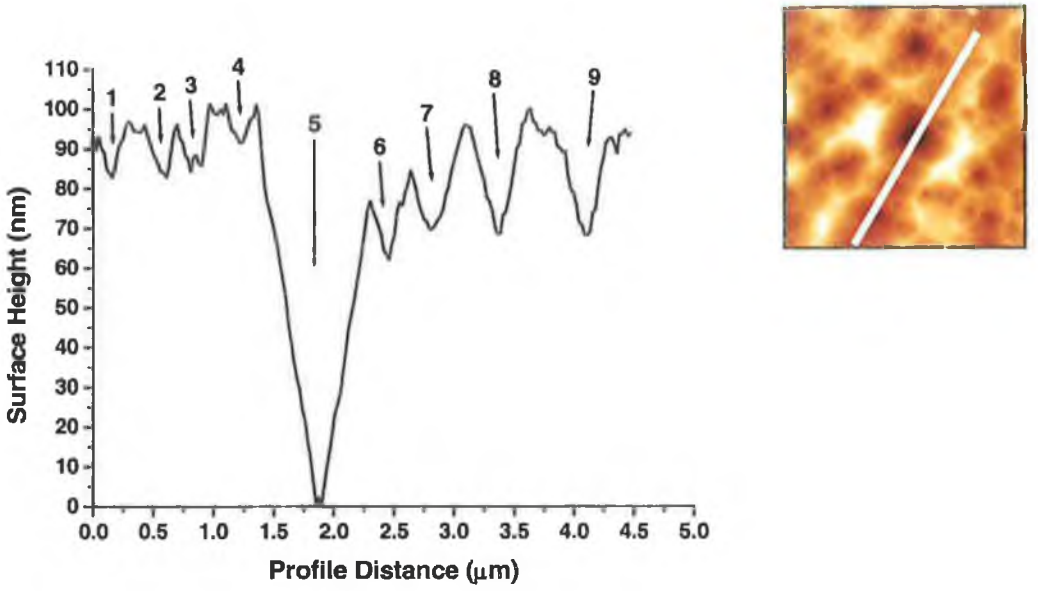

Figure 5.25: *Profile data taken across a section of Figure 5.21 (shown right), encompassing a total of nine etch pits. Using this data, lines were fit to the edges of each pit and the slope used as an estimate of the vertical-to-lateral etch rate. Similarly, the ratio was determined taking the depth of each pit and comparing it to the radius (Table 5.2).*

Table 5.2:

Pit Designation	***|Slope| (Left) (nm/μm)***	***|Slope| (Right) (nm/μm)***	***Diameter (μm)***	***Radius (μm)***	***Depth (nm)***	***Depth / Radius (nm / μm)***
Pit 1	92.8 ± 9.6	105.1 ± 7.7	0.260	0.130	12.5	96.2
Pit 2	85.0 ± 3.4	182.9 ± 16.8	0.265	0.133	13.8	103.8
Pit 3	99.0 ± 7.2	236.3 ± 20.7	0.270	0.135	13.7	101.5
Pit 4	81.4 ± 11.0	77.6 ± 7.0	0.254	0.127	23.8	187.4
Pit 5	193.3 ± 2.8	188.9 ± 1.7	0.949	0.475	87.2	183.6
Pit 6	97.0 ± 4.7	167.1 ± 22.4	0.344	0.172	18.1	105.8
Pit 7	95.9 ± 6.6	99.9 ± 4.9	0.452	0.226	21.2	93.8
Pit 8	119.5 ± 2.2	141.3 ± 5.4	0.503	0.252	28.1	111.5
Pit 9	127.3 ± 10	154.5 ± 8.4	0.373	0.187	24.3	129.9
Average:	**110.1 *(nm/μm)***	**150.4 *(nm/μm)***				**123.7 *(nm/μm)***

However, one can reconcile the reported anisotropy of the etching with the data obtained through examination of the slopes of pit edges by considering the original topography of the O-terminated polar face. The following sequence of graphs are illustrations of the proposed etch mechanism and are presented as a number of sequential steps (a vertical etch followed by a greatly magnified lateral etch).

Step 1: Taking the profile data from *Fig. 5.3*, shown as a *black line* below, the *red line* is a somewhat contrived fit, for illustrative purposes only, to the terrace heights of the steps observed on the unetched O-terminated surface (*Fig 5.2*). The bi-layer spacing is indicated to the right of the figure, representing a depth of 0.53 nm and all terraces are terminated with O ions.

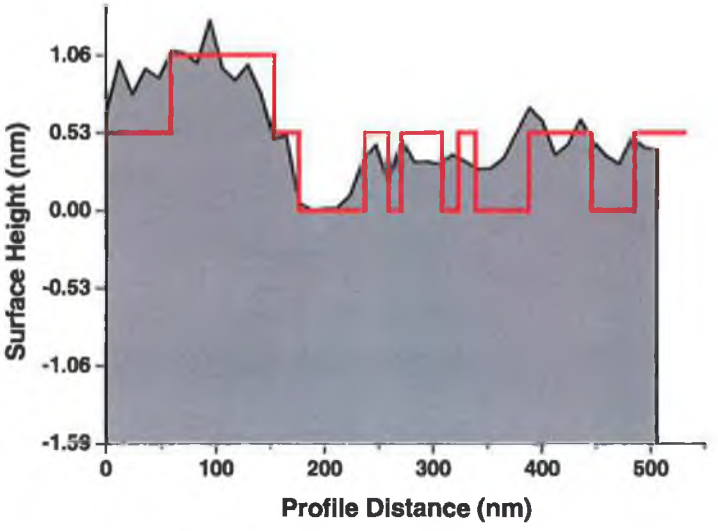

Step 2: The O-terminated terraces will be etched downwards (*blue arrows*) until the bi-layer beneath is exposed. Therefore, all terraces within the region will be etched downwards by 0.53 nm as in the illustration.

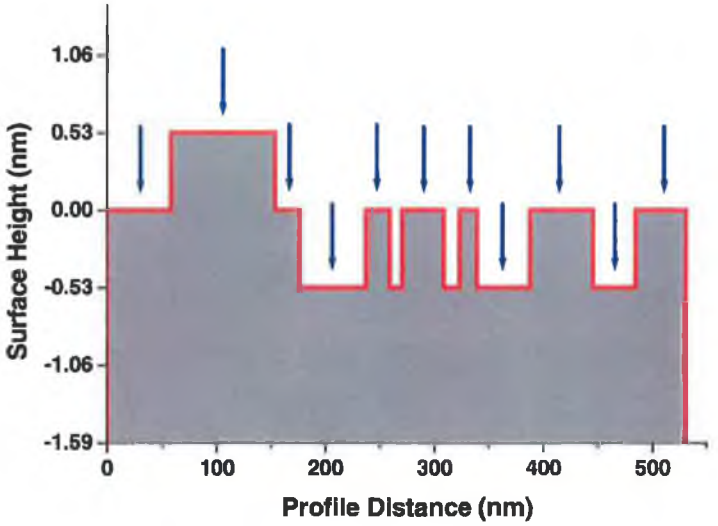

Step 3: The acid can remove O atoms along the step-edges and the etching will occur laterally, widening the small pits observed on this polar face and reducing the width of the material separating one pit from another, though the lateral etch rate is actually much lower than the vertical rate.

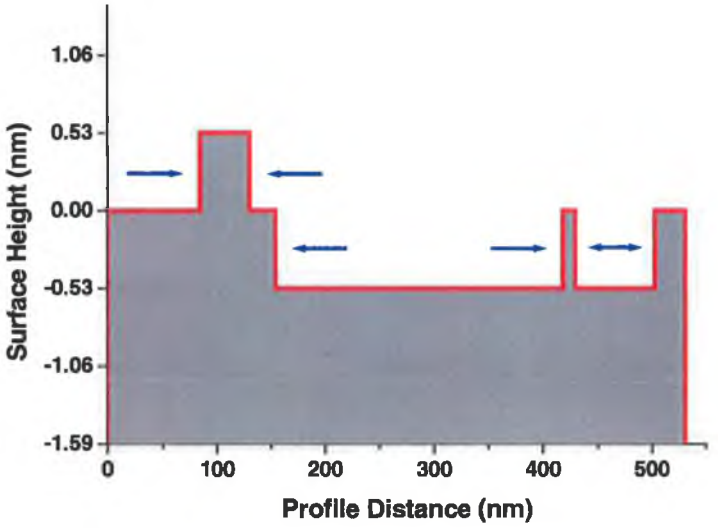

Step 4: The acid continues to etch vertically, and the assumption is made that the vertical etch strips away each O-Zn bi-layer, rather than simply removing O from the surface. As with the etch mechanism proposed by *Maki et al.*, the entire face is etched downwards but steps remain due to the mixed termination of their edges.

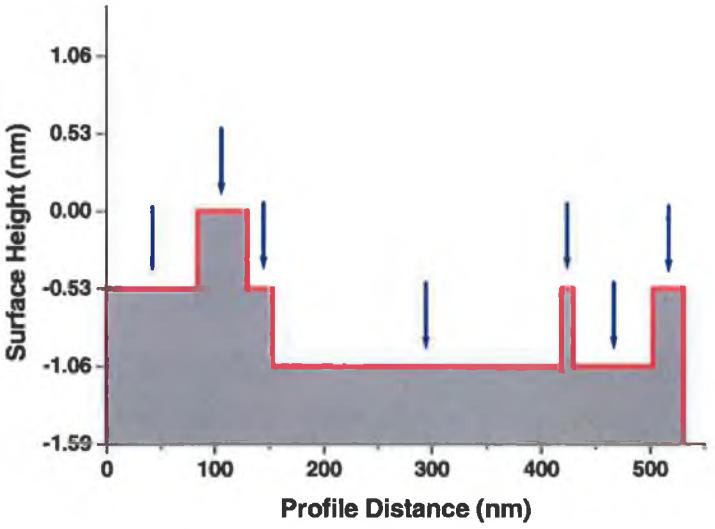

Step 5: As in *Step 3* above, the acid laterally etches the step-edges. This removes the separation between the original small pits and it can be seen that even a modest lateral etching could produce pits that appear very broad in nature.

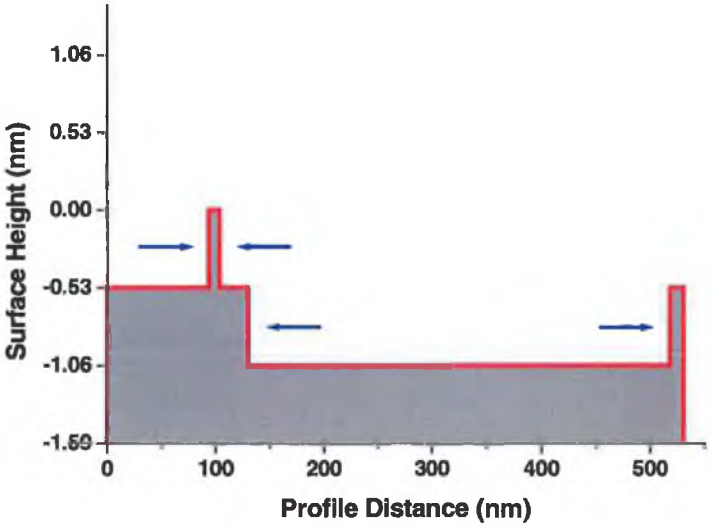

From the above discussion it is clear that the large width of the etch pits and seeming discrepancy in lateral-to-vertical etch rates can be explained in terms of the original surface topography. The small pits observed on as-received O-terminated wafers are approximately 50 nm in diameter and one would expect the terraces separating each to be roughly equivalent dimensions (see profile data in *Step 1* and *Fig. 5.3*). The pits formed after etching with the 1:36 ml HCl solution, shown in *Fig. 5.21*, have maximum depths of approximately 150 nm. This suggests that the observed large etch pits could form if the lateral etch rate is only one-sixth of the vertical rate (based on the estimated distance of ~ 50 nm of material separating one pit from another, and the fact that the lateral etching reduces this material in *both* directions simultaneously), rather than ten times the rate.

Figure 5.26 is a 5×5 μm AFM image of the O-terminated surface after etching with the weaker 1:99 ml HCl solution (pH of 1.2) for 6 seconds. Unlike the surfaces etched with the 1:36 ml solution, large pits are not observed. Since one would expect wide pits to form as a result of the merging of the original features observed in unetched surfaces, *Fig. 5.26* allows a glimpse of the intermediate topographic changes and reveals a large number of small, but defined pits (seen as black 'spots' in the image) that are generally close to one another. It can also be seen that the polish-induced 'scratches', originally having heights corresponding to a few bi-layers, are much deeper and more defined after the etch. The SD in surface height is 3.8 nm, with an RMS value of 4.3 nm, indicating an increase in roughness from typical values of < 1 nm. The ISA is calculated to be 1.3% of the planar area of 25 μm^2.

Figure 5.27 is a 50×50 μm topographic scan of an O-terminated wafer that was partially etched in the 1:99 ml HCl solution. To the left of the image is the etched region, whereas to the right is a section that was masked using PTFE tape and therefore remained relatively untouched. As with *Fig. 5.26*, the etched portion demonstrates deeper scratch marks and it can be seen that many of these features continue, faintly, into the unetched region. This suggests that the 'unetched' region was actually etched

mildly as a result of acid travelling under the mask via capillary action along the scratches. *Figure 5.28* is a 3D projection of a section of *Fig. 5.27*, showing small areas of both the etched and unetched regions of the surface. The non-uniform etching leads to increased depth of existing features or the creation of pits but one does not observe a definite 'step' between etched and unetched regions using the HCl solutions as described.

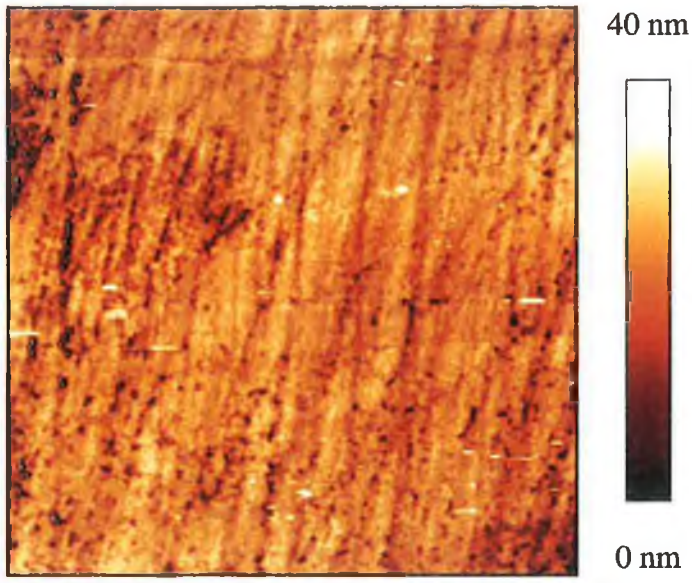

Figure 5.26: *5×5 μm AFM image of an O-terminated surface after etching with the weaker 1:99 ml HCl solution. The acid has a tendency to deepen the small grooves that originally had heights equivalent to a few bi-layers, and a large number of small etch pits are observed (seen as black 'spots').*

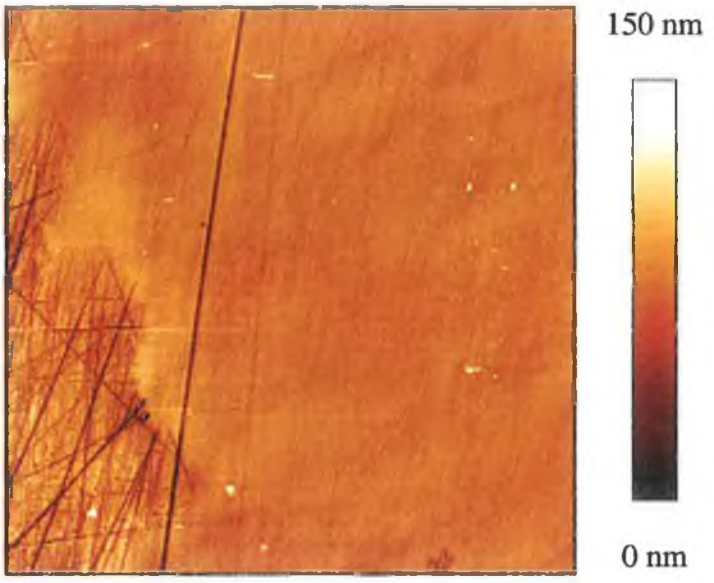

Figure 5.27: *50×50 μm scan of an O-terminated surface where the right portion of the surface was masked from the 1:99 ml HCl solution using PTFE tape. As with Fig. 5.26, the etched section (left) demonstrates an increase in the depth of features. Note that 'scratch' marks also appear, faintly, in the unetched region (right) and can be traced through to the etched portion.*

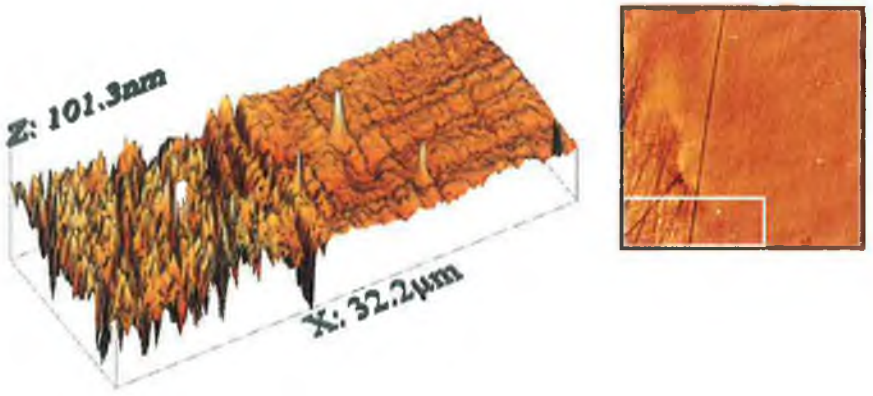

Figure 5.28: *3D projection of a section of Fig. 5.27 (shown right) of etched and unetched O-terminated surface. The etch is non-uniform as a result of the slight variations in surface topography present in the as-received material, and one does not observe a 'step' between etched and unetched regions. Since the depth of features in the etched region is typically 40 nm, and no step is seen one can conclude that the vertical etch rate is ~ 40 nm in 6 seconds. The lateral etch rate is clearly much lower than this, since scratch marks appearing in the etched region are not noticeably wider than in the unetched region (Fig. 5.27).*

In *Section 5.2* the difficulty in determining etch rates was alluded to and it has been demonstrated that the surface topography before the etch greatly influences the morphology during the etching process. Although the lateral-to-vertical rates cannot be directly measured, one can estimate that the vertical rate could be six times the lateral rate for the 1:36 ml HCl solution. One presumes that a similar ratio exists in the case of the 1:99 ml solution since 'scratch' depths are increased in *Fig. 5.27* but their widths in etched and unetched sections appear roughly similar. *Fig. 5.28* also suggests that the etching duration is not sufficient for the creation of a noticeable 'step' between etched and masked regions, and based on the AFM data of the depth of etch pits, the vertical etch rate is approximately 150 nm and 40 nm in six seconds for the 1:36 ml and 1:99 ml HCl solutions respectively. Despite these difficulties, the data is certainly at odds with, and much lower than the etch rate reported by *Vellekoop et al.* for 1% HCl solutions (10 μm per minute).

Having examined the effects of HCl solutions on the O-terminated surface, the impact on Zn-terminated faces is now considered. *Figure 5.29(a)* shows a model of the hexagonal structure of ZnO looking down on the [Zn] surface (i.e. parallel to the *c*-axis along the $(000\bar{1})$ direction), where red and yellow spheres represent Zn and O atoms respectively. *Figure 5.29(b)* illustrates the crystal structure viewed perpendicular to the *c*-axis. Each O atom is tetrahedrally bonded to three Zn atoms in the bi-layer and to one Zn atom in the layer beneath. The Zn atoms terminating at the surface have no dangling electrons, and acid etching of the Zn terminated face is therefore dominated by the interaction between H^+ ions from the acid and O ions with dangling bonds at step edges. In other words, one would expect to observe an equivalent lateral etch rate but a much smaller vertical etch rate for Zn-terminated faces compared to O-terminated faces.

Figures 5.30 and *5.31* are 5×5 μm topographic scans of [Zn] surfaces after etching with the 1:99 ml and 1:36 ml HCl solutions respectively. In both cases there is a broadening of the polish-induced scratches due to the lateral etching of their edges and, while scratches in *Fig. 5.30* appear similar to the unetched Zn-terminated face despite

exposure to the 1:99 ml solution, they appear less defined in *Fig. 5.31* due to the greater lateral etching of the stronger 1:36 ml solution. This observation is supported by the, albeit slight, roughness differences between the images. The SD in height is 6.6 nm for *Fig. 5.30*, with an RMS roughness of 6.7 nm and an ISA ratio of 2.5%. In comparison the SD is 5.4 nm, the RMS is 6.1 nm and the ISA is 2.1% larger than the planar area for *Fig. 5.31*. Although these roughness values are within the range observed for Zn-terminated material before etching, they are at the lower end of the expected values (5 – 10 nm RMS and SD, and ISA ratios of 2.5 to 7%). Thus, the [Zn] faces appear slightly smoother after etching with the more acidic solution.

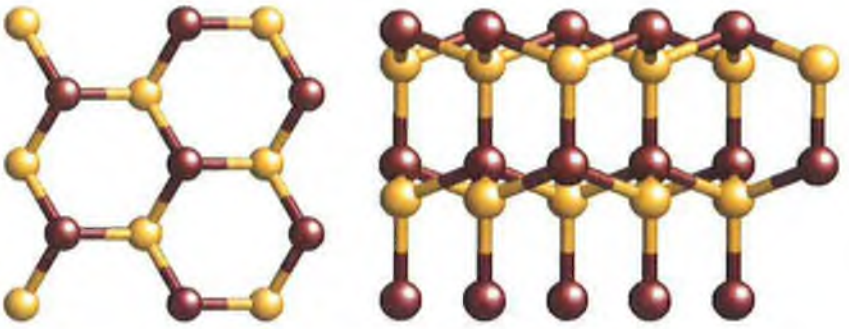

(a) ***(b)***

Figure 5.29: *Illustration of the hexagonal wurtzite structure of ZnO, where Zn and O atoms are represented by red and yellow spheres respectively. Figure (a) shows the (0001) surface (i.e. looking down at the Zn-terminated face from above, parallel to the c-axis) showing that each O-atom is bonded in the bi-layer to three Zn atoms. Figure (b) is a diagram of the structure looking perpendicular to the c-axis, and shows two Zn-O bi-layers. From this perspective it can be seen that each O atom in the surface bi-layer is also bonded to a Zn atom in the bi-layer below. The O-atoms are tetrahedrally bonded to Zn, and since the Zn atoms terminating at the surface have no dangling electrons, the vertical etching of the [Zn] face is substantially reduced compared to the O-terminated face. The lateral etch, however, can occur because O atoms at step/scratch edges will have dangling electrons.*

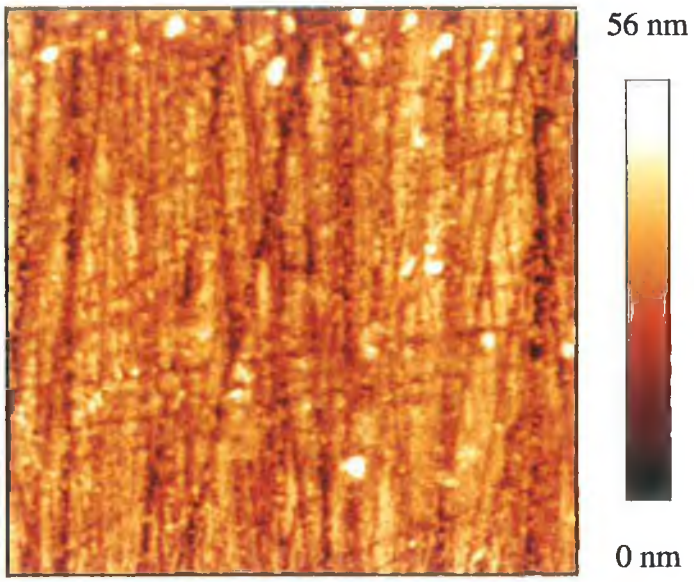

Figure 5.30: *5×5 μm AFM image of the Zn-terminated surface after etching with the 1:99 ml HCl solution. H^+ cations from the acid can bind to O ions present at the edges of the polish-induced scratches and the etching proceeds laterally. This widens the scratches themselves and hence reduces surface roughness.*

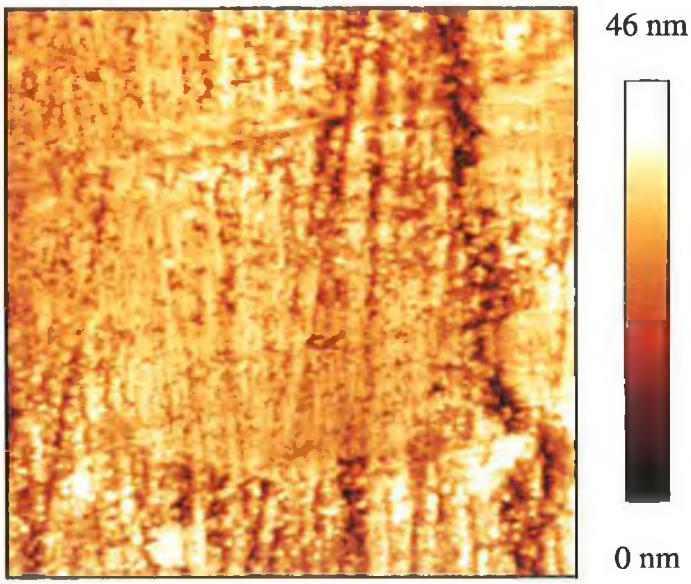

Figure 5.31: *5×5 μm AFM image of the Zn-terminated surface after etching with the more acidic 1:36 ml HCl solution. The scratch marks are less defined than in Fig. 5.33 as a result of the greater lateral etching.*

One can conclude then that HCl will etch Zn-terminated surfaces predominantly laterally and has a tendency to widen the polish scratches, which reduces the surface roughness. *Figures 5.32* and *5.33* show reflectance spectra at 25 K of the Zn-terminated surfaces after etching with the 1:99 ml and 1:36 ml HCl solutions respectively. Although there is an increase in the overall intensity of light reflected from the faces as a result of the reduction in surface roughness, the *B* free-exciton resonance feature also improves. The increase in oscillator strength is more pronounced in *Fig. 3.33* than in *Fig. 3.32*, suggesting that the greater lateral etching and subsequent reduction in surface roughness is responsible. In order to further confirm this, Zn-terminated wafers were etched in 1:99 ml solutions for a total duration of 30 seconds or one minute, after which reflectance spectra were obtained (*Figure 3.34*). Although the acquired data was not normalised to the reference sample and a percentage reflectivity was not obtained, the spectra indicate that the observed improvement in the *B* excitonic feature is related to the strength of acid/duration of etching and hence the degree to which the lateral etch removes polish scratches. In terms of photoluminescence results, there is no observable green band after etching and no change in the bound-exciton region.

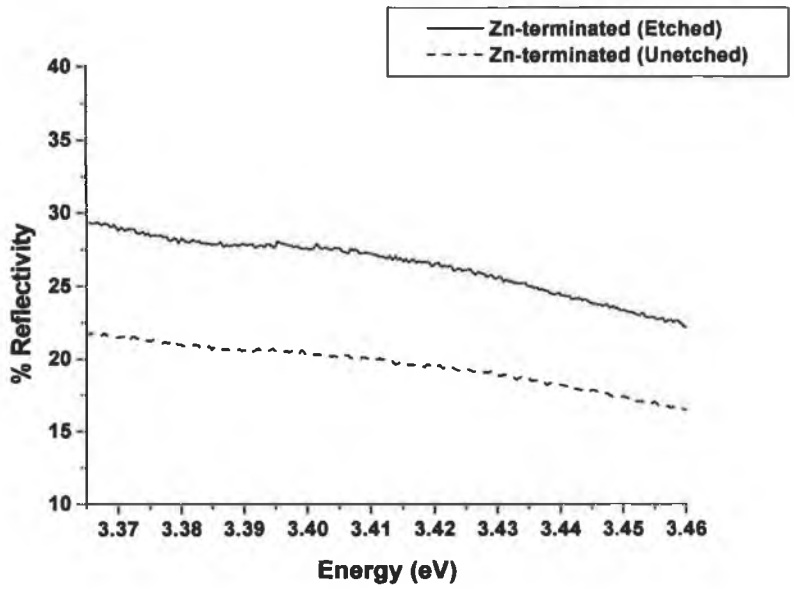

Figure 5.32: *Reflectance spectrum of Zn-terminated surface (25 K) before and after etching with the 1:99 ml HCl solution. One observes a slight increase in the intensity of reflected signal as a result of the smoothing of polish scratches and an increased strength of the B free-exciton resonance.*

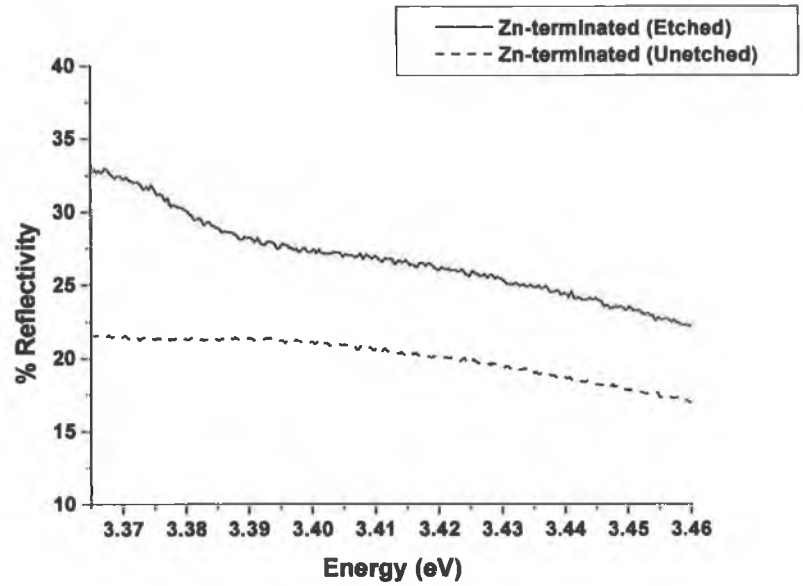

Figure 5.33: *Reflectance spectrum of the Zn-terminated surface (25 K) after etching with the more concentrated 1:36 ml HCl solution. If compared to the figure above (Fig. 5.35), it is apparent that the strength of the B free-exciton resonance is improved as a result of the greater lateral etching of this solution.*

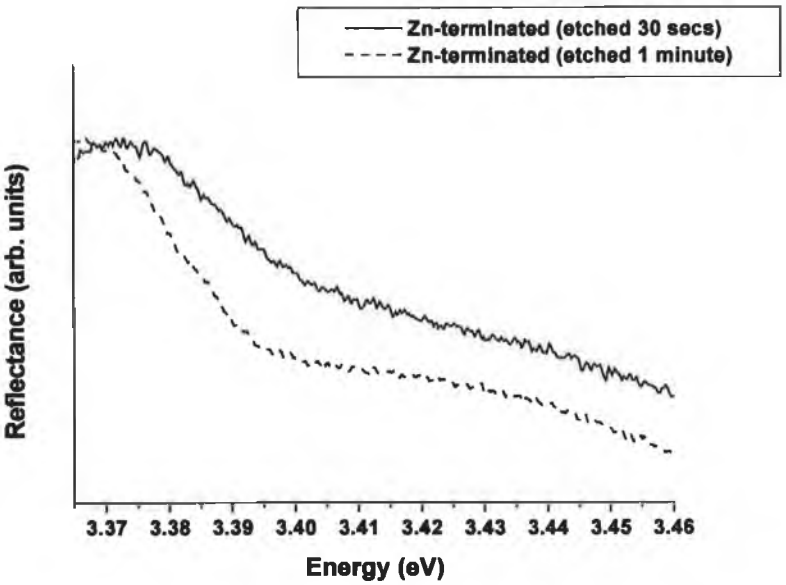

Figure 5.34: *Reflectance spectrum of Zn-terminated surfaces (25 K) after etching with 1:99 ml HCl solutions for 30 seconds and 1 minute. As the etch duration is increased, one observes an gradual improvement in the strength of the B free-exciton feature.*

In contrast, although O-terminated surfaces are also laterally etched, the rapid vertical etching of the polar face dramatically increases the roughness. *Figure 5.35* shows reflectance spectra (25 K) before and after etching with the 1:99 ml solution and demonstrates that overall reflected intensity and free-exciton resonances are substantially reduced, while *Figure 5.36* is a PL spectrum showing a reduction in intensity of bound-exciton features after etching. However, in this case the presence of PL after etching (albeit reduced, due perhaps to deep defects related to oxygen deficiency because of the nature of the etch mechanism), and the dramatic change in reflectance imply that the main effect on reflectance is due to surface roughness. The hypothesis of oxygen vacancy creation during HCl etching is supported by the increase in unstructured green band, seen in *Figure 5.37* below.

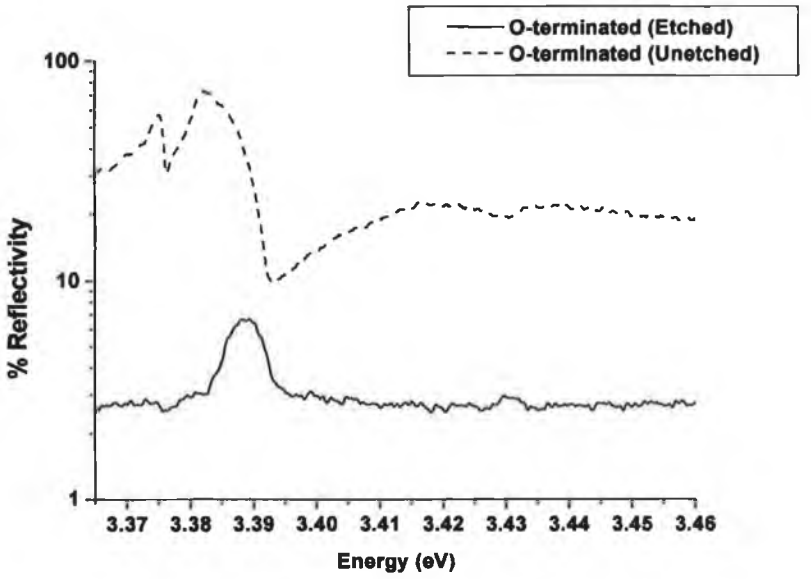

Figure 5.35: *Reflectance spectra of O-terminated surface (25 K) before and after etching with the 1:99 ml HCl solution. Note the logarithmic scale of the y-axis. The overall reflectivity of the sample drops dramatically as a result of the increase in surface roughness, and excitonic resonances are substantially reduced in strength.*

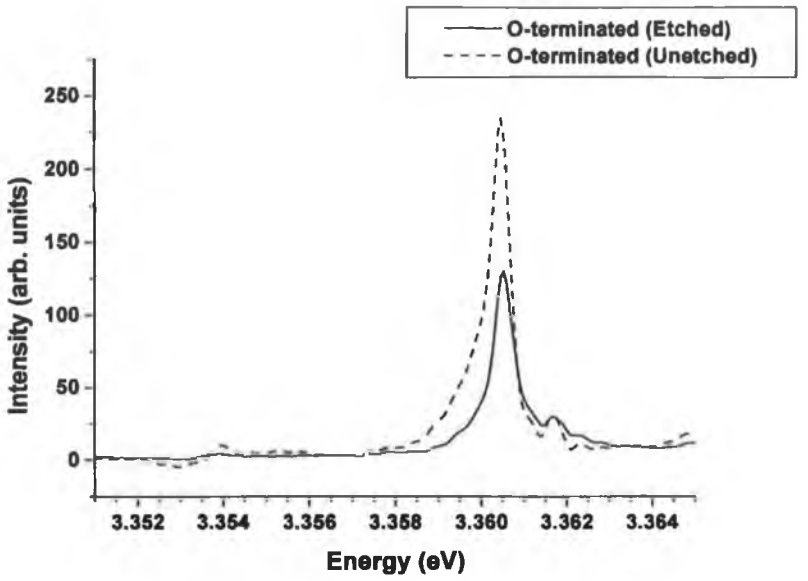

Figure 5.36: *PL spectra of the O-terminated surface (25 K) before and after etching with the 1:99 ml HCl solution, showing the reduction in intensity of bound-exciton peaks. In comparison, there is no detectable luminescence after etching with stronger 1:36 ml solution.*

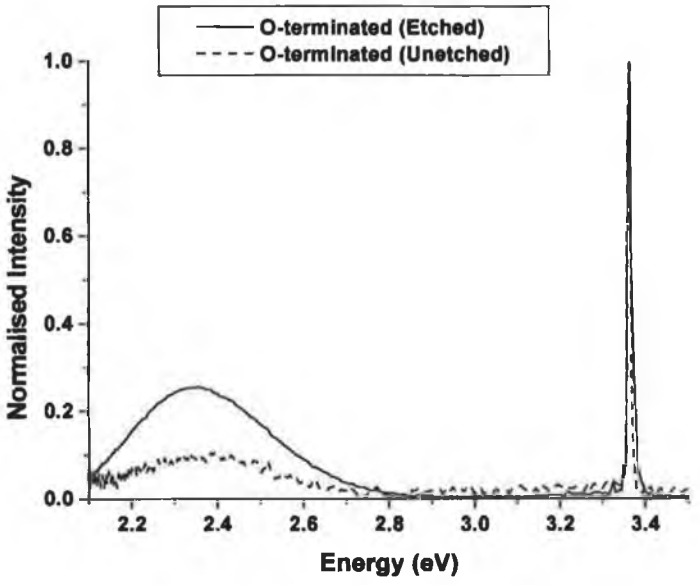

Figure 5.37: *PL spectra of the O-terminated surface before and after etching with the 1:99 ml HCl solution, showing green band luminescence. The spectra have been normalised so that the BE emission peak (~ 3.4 eV) appears to have the same intensity. The unstructured green band is observed to increase, relative to the BE emission, after etching.*

5.5 *Phosphoric/Acetic Acid Etching*

Two separate solutions containing phosphoric and acetic acid were used for etching, as given in *Table 5.1*. *Figure 5.38* is a 10×10 μm AFM image of the [O] face after a wash with the 1:100:100 ml phosphoric acid: acetic acid: water solution for 75 seconds. The SD and RMS roughness values are approximately 32 and 39 nm respectively, with an ISA increase of 1.4% over the expected planar surface area. These figures are similar to those of the O-terminated surface after etching with the 1:36 ml HCl: water solution (*Fig. 5.21*) and one observes similar etch pits, the largest of which have depths of ~ 160 nm and widths of 2 to 3 μm. Since the pits formed after etching with HCl have maximum diameters of 1 μm and roughly equivalent etch depths (~ 150 nm), one can conclude that the lateral-to-vertical etch ratio is greater for the phosphoric/acetic acid solution than for the HCl solution.

Figure 5.39 is a 5×5 μm image of the [O] plane after a 40 second etch with the 1:1:10 ml phosphoric acid: acetic acid: water solution. This concentration produces a more random etch profile, indicating that the etching is more severe despite efforts to match depths based on the reported rates [2]. The SD and RMS surface roughness in this case are 28 and 31 nm respectively, and the ISA increase is 11.7%.

Figure 5.40 shows a 50×50 μm AFM scan of the [Zn] face after an etch with the weaker 1:100:100 ml solution, revealing pits that begin to form along the polish-induced scratches (enlarged in *Figure 5.41*). The roughness figures are 36 nm (SD) and 41 nm (RMS), and the ISA increase is 1.1% for *Figure 5.40*. Similarly, for the enlarged region shown in *Figure 5.41* the SD in height is ~ 28 nm, the RMS roughness is ~ 36 nm, and the ISA increases by 2.6%. The pits formed have maximum widths of ~ 1 μm and depths of ~ 100 nm. After etching with the stronger 1:1:10 ml solution, these pits appear to broaden and merge into one another, having depths of ~ 100 nm and maximum widths of 3 μm (*Figure 5.42*). This image has a SD in height of 20 nm, an RMS roughness of 23 nm, and an ISA increase of 0.7%. Taken together, these images

are strong proof of the etch mechanism, where the broad nature of pits is due to a rapid lateral etch, relative to the [Zn] planar surface, caused by the reaction between H from the acids and dangling O ions on the scratch-edges.

In summary, the morphology as a result of etching with phosphoric/acetic acid solutions appears generally similar to that of the HCl etches discussed above. O-terminated surfaces become rougher as a result of the rapid vertical etching and one observes the formation of etch pits after etching with the 1:100:100 (pH of 1.4 for 75 seconds) phosphoric/acetic acid solution. These pits are similar in dimension to those found after etching with the 1:36 ml HCl solution (pH of 0.9 for 6 seconds), with similar roughness values obtained in each case. The stronger (pH of 0.8 for 40 seconds) 1:1:10 phosphoric/acetic acid solution produces a much more random etch profile, which is to be expected considering that the maximum etch duration with HCl was 6 seconds, and the most concentrated solution used had a pH of 0.9.

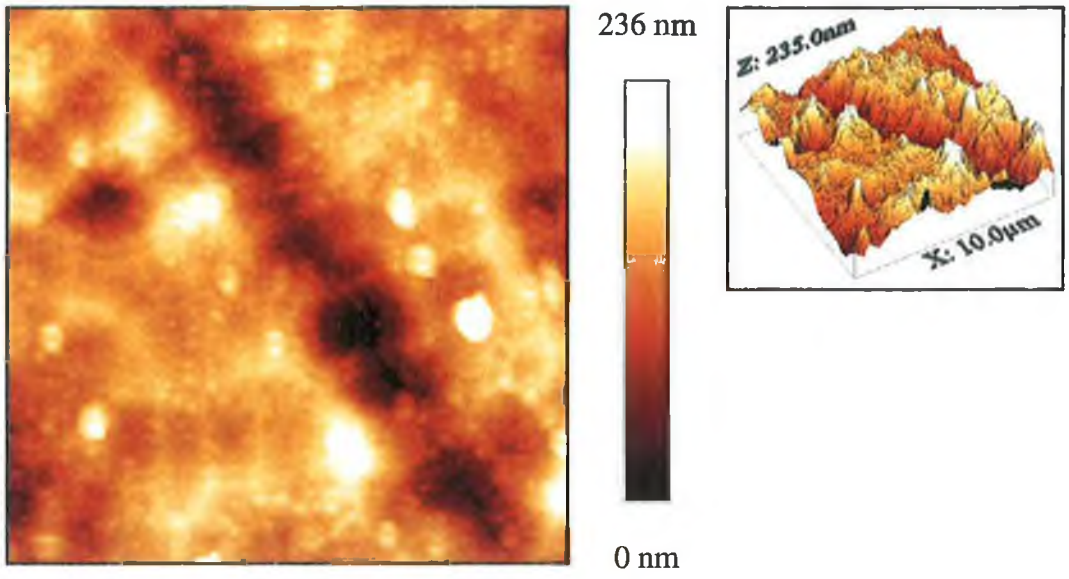

Figure 5.38: *10×10 µm AFM topographic image of the O-terminated surface after etching with the 1:100:100 phosphoric acid: acetic acid: water solution. As with HCl, one observes the formation of etch pits on this polar face*

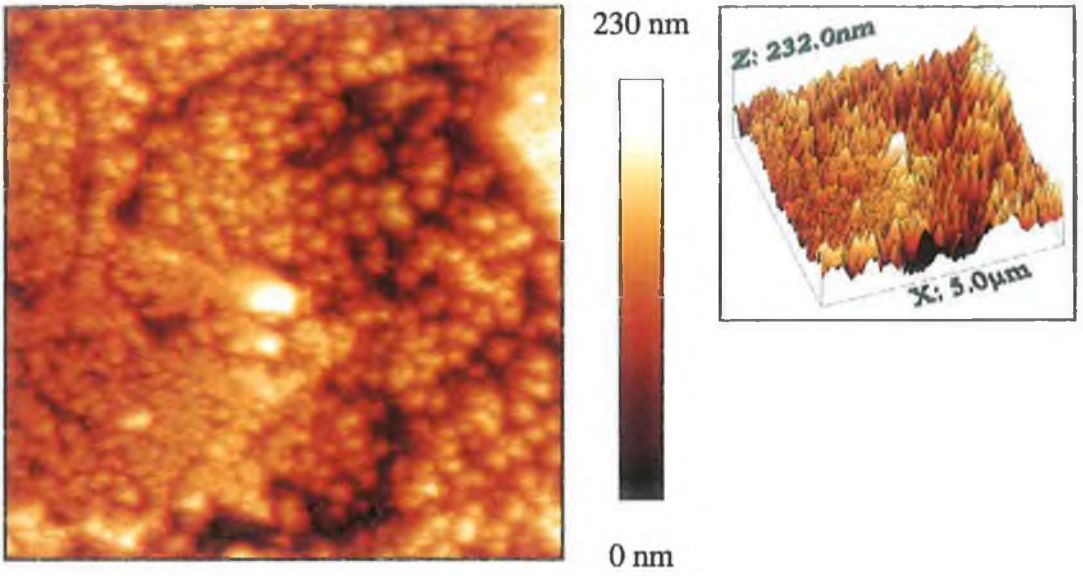

Figure 5.39: *5×5 µm AFM scan of O-terminated surface after etching with the 1:1:10 phosphoric acid: acetic acid: water solution. The etch profile is much more random than for Fig. 5.38 above, although the etch depth appears similar in both cases. This suggests that varying the ratio of acetic to phosphoric acid affects the lateral etch rate.*

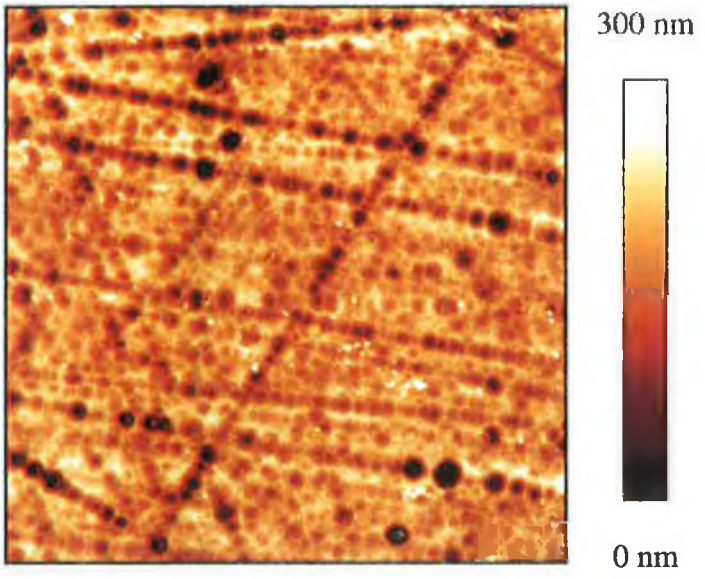

Figure 5.40: *50×50 µm AFM topographic image of the Zn-terminated surface after etching with the 1:100:100 phosphoric acid: acetic acid: water solution. Etch pits form on this face due to a relatively rapid lateral etch and, hence, the image shows that these pits have a tendency to line up along the polish scratches due to O atoms at step/scratch edges with dangling electrons.*

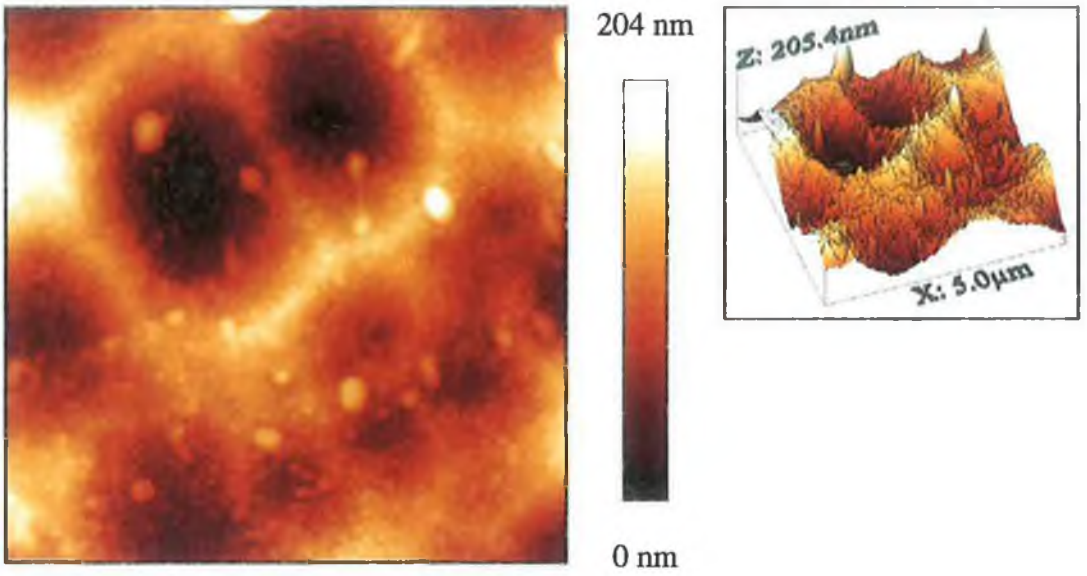

Figure 5.41: *5×5 µm AFM enlargement of a section of Fig. 5.40, showing pits that form on the Zn-terminated face after etching with the 1:100:100 solution. The pits themselves have maximum widths of ~ 1 µm and depths of ~ 100 nm.*

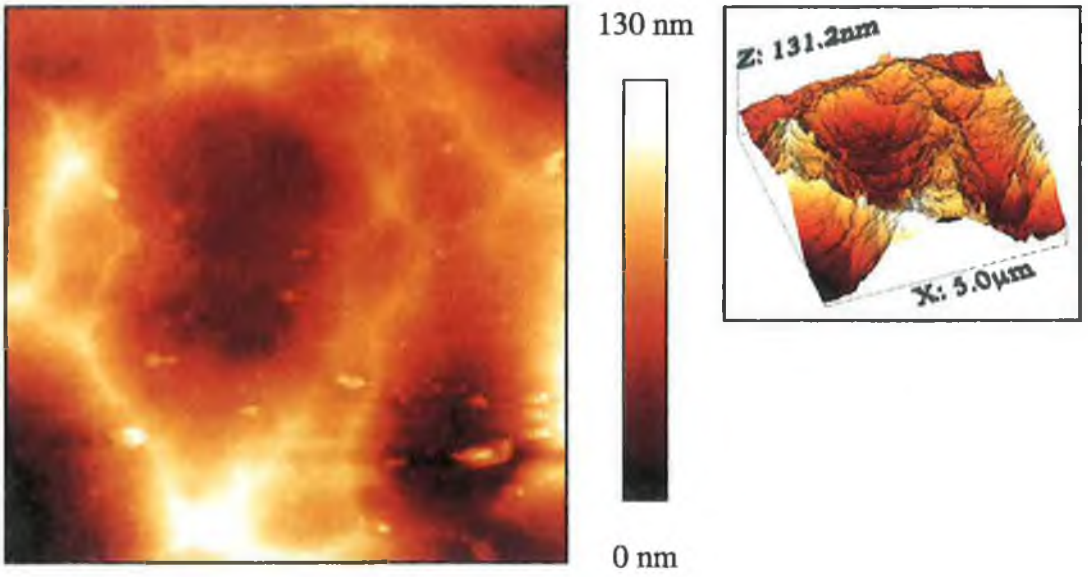

Figure 5.42: *5×5 µm AFM image showing pits that form on the Zn-terminated face after etching with the 1:1:10 solution. These pits have maximum widths of ~ 3 µm and depths of ~ 100 nm and appear to form as a result of the merging together of smaller pits, such as those shown in Fig. 5.41 above.*

One might suspect that the PL and reflectance data for O-terminated samples etched with the phosphoric/acetic solutions should appear similar to those etched with HCl. This is indeed the case, as shown in *Figure 5.43*, and overall reflectivity drops to around 1% with significant distortion and weakening of the free-exciton resonances. PL data, however, reveals that the BE luminescence is more intense for [O] surfaces etched with the stronger 1:1:10 solution than for the 1:100:100 solution (*Figure 5.44*) despite what appears to be the more random etch profile of the former etchant. It should be noted that this result was replicated – two O-terminated samples were etched with each solution and compared. Therefore one must conclude that some form of passivation of the surface occurs on etching with the 1:1:10 solution. Conversely, the green band is more intense (relative to the BE features) for the 1:100:100 solution (*Figure 5.45*). The origin of this effect remains unclear.

Reflectance data for etched Zn-terminated surfaces is presented in *Figure 5.46*. As with the HCl solution, lateral etching reduces the surface roughness and scattering of light from the sample. Although the phosphoric/acetic acid solutions create etch pits along the polish scratches, these are very broad in nature. The overall reflectivity drops slightly but one observes a substantial increase in the strength of the free-exciton resonances. There is no detectable green band luminescence from the [Zn] faces after etching. However, a number of Zn-terminated samples etched with the stronger 1:1:10 solution revealed a weak luminescence feature in the near band-edge region (*Figure 5.47*).

It has been suggested that H can incorporate in high concentrations into ZnO and that it can act as a shallow donor [13]. Simulations have also shown that H can penetrate into MgO (100) by dissociative adsorption of water [14], and *Ohashi et al.* have demonstrated that hydrogenation of ZnO can increase the efficiency of band edge emission [15]. The weak feature observed on etched Zn-terminated faces may therefore be due to hydrogen incorporation into the crystal from the acid and passivation of other

defects. The peak energy of the luminescence line is ~ 3.362 eV (25 K), which is close to the energy of the I_4 line (3.3621 eV at 1.2 K) [16].

As discussed in *Chapter 3* in relation to the Eagle-Picher bulk wafers, the I_4 line has been attributed to recombination of an exciton bound to a H donor. The relative increase in intensity of this BE line after etching is therefore consistent with H incorporation into ZnO surface layers as a result of etching with low pH acids. This mechanism may also be linked to the luminescence of the O-terminated surface (*Fig. 5.44*), discussed above, where the surfaces etched with the lower pH solutions show stronger BE emission.

One other possibility is that the observed line in Zn-terminated material could be due to the 'surface-exciton' reported by *Travnikov et al.* [17], particularly given the feature's broad nature and the known damage to the crystal face after etching.

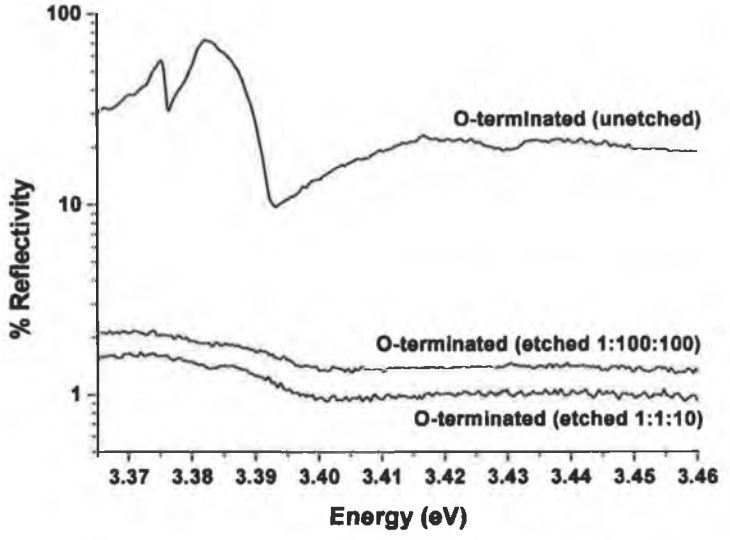

Figure 5.43: *Reflectance spectra (25 K) of O-terminated surfaces before and after etching with either the 1:1:10 or 1:100:100 phosphoric acid: acetic acid: water solutions. The reflectivity drops significantly as a result of the damage to the surfaces and increased scattering of light, and free-exciton resonances are substantially reduced in strength.*

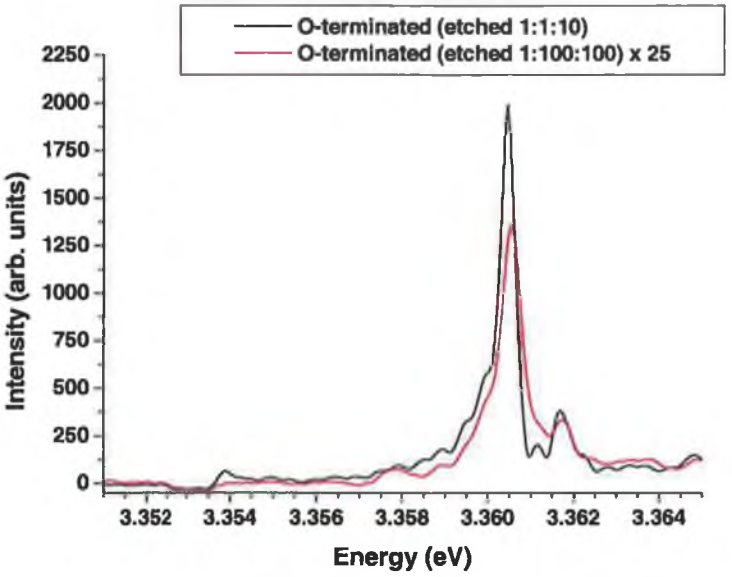

Figure 5.44: *PL spectra (25 K) of O-terminated surface after etching with the 1:1:10 and 1:100:100 solutions. In both cases the intensity of BE emission is reduced compared to the unetched material. Although the 1:1:10 solution produces a more random etch profile, surfaces exhibit much stronger emission than for faces etched with the 1:100:100 solution.*

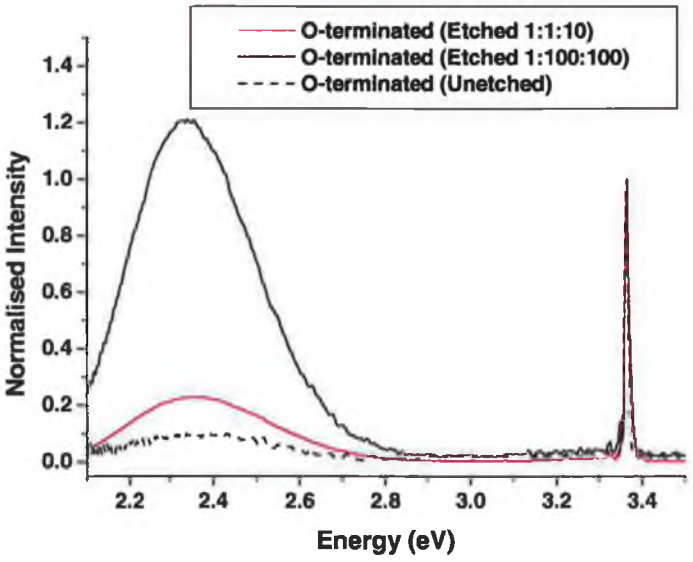

Figure 5.45: *PL spectra (25 K) of green band luminescence from the O-terminated surface before and after etching with the 1:10:10 and 1:100:100 solutions. The spectra have been normalised so that the BE line appears the same intensity in all cases. As with the HCl etchant, one observes an increase in green band intensity compared to the band edge luminescence. However, contrary to the BE phenomena (Fig. 5.47 above) the intensity of the band is greater for the 1:100:100 solution.*

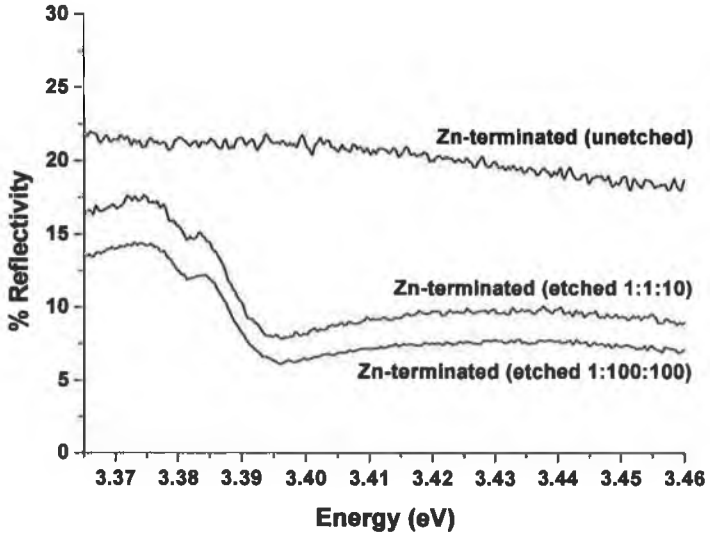

Figure 5.46: *Reflectance spectra (25 K) of the Zn-terminated surface before and after etching with the 1:1:10 and 1:100:100 solutions. Although a slight decrease in overall reflectivity is observed, free-exciton resonances are substantially improved as a result of the 'smoothing' of the face as a result of the lateral etching at scratch edges and the formation of broad pits.*

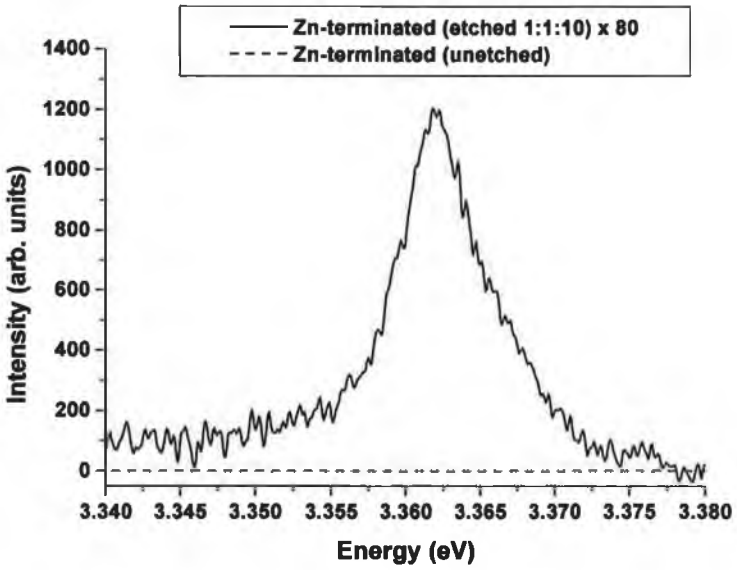

Figure 5.47: *PL spectra (25 K) of the Zn-terminated face before and after etching with the 1:1:10 solution. A weak, but broad line is observed for some samples, with peak energy roughly corresponding to the energy of the I_4 H-related BE line. The presence of the emission feature may indicate hydrogen incorporation into the crystal as a result of the use of low pH acids. Alternatively, the line may be due to the reported surface-exciton.*

5.6 Ammonium Hydroxide/Ammonium Chloride Etching

O- and Zn-terminated samples were etched for periods of two minutes in a 6 g: 4 ml: 30 ml NH_4Cl: NH_4OH: H_2O solution. This etchant is strongly alkaline, with a pH of 9.7 (*Table 5.1*), and it is immediately clear that a different etch mechanism operates compared to the acidic solutions discussed above. The ammonia-based solution does not appear to etch the O-terminated surfaces, and topography and surface roughness are not affected to any degree beyond the typical variations in unetched surfaces one observes from sample to sample. Bound-exciton luminescence and free-exciton resonances are not affected by exposure to the solution, and there is no change in the structure or intensity of the green band.

The [Zn] surface, however, is mildly etched by the NH_4Cl: NH_4OH: H_2O solution. *Figure 5.48* is a 5×5 μm AFM scan of a Zn-terminated face after an etch of four minutes, rather than the two minute duration quoted in *Table 5.1*. Although etching is also observed after two minutes, the effect of the alkaline solution on surface topography is clearer for the longer duration. The determined roughness values are ~ 14 nm (SD) and ~ 16 nm (RMS), and the ISA increase over the planar surface area is 5.5%. If compared to the figure for the as-received wafers (RMS and SD values of 5 – 10 nm, and ISA increases of 2.5% - 7%), it appears that the etch proceeds predominantly in a vertical direction, hence increasing the RMS and SD values, but not altering the surface area significantly. Thus it appears that alkali solutions etch the Zn polar faces in a similar manner to the way acid solutions etch the O-terminated surfaces (i.e. a higher vertical to lateral rate), but the etch rates are substantially lower for Zn-terminated faces. The induced changes in topography have little bearing on the reflectance spectra, which show no improvement in the oscillator strengths of free-exciton and only a slight reduction in intensity overall, and there is no change in BE or green band luminescence.

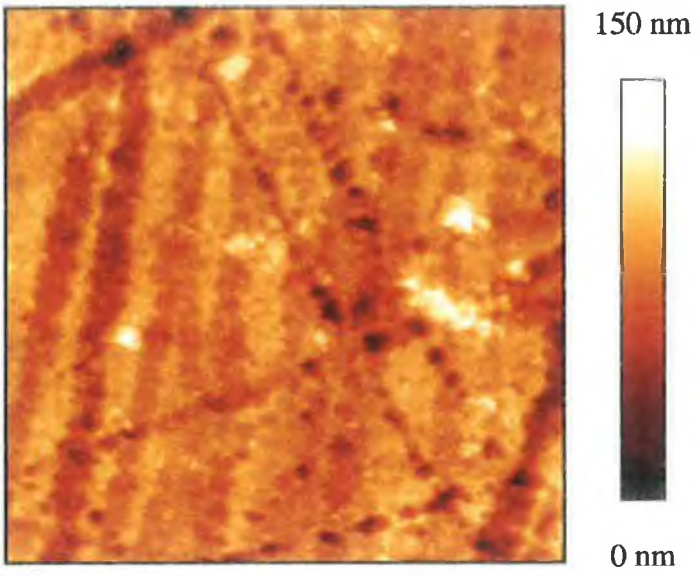

Figure 5.48: *5×5 μm AFM image of a Zn-terminated surface after etching with a 6 g: 4 ml: 30 ml NH_4Cl: NH_4OH: H_2O solution for four minutes.*

5.7 *Etching of Annealed Surfaces*

Finally, the effects of the above etchant solutions on the surface topography and optical properties of annealed wafers shall be examined It has been already demonstrated that annealing O-terminated surfaces creates thermal etch pits and steps across the face, with a corresponding increase in surface roughness values and a decrease in both reflected light intensity and excitonic oscillator strengths. Luminescence of bound-exciton features is quenched and green band intensity is not significantly affected by the anneal, although it does appear more structured. Etching annealed O-terminated faces simply increases the damage to the face and, therefore, this section shall largely concentrate on the etching behaviour of annealed Zn-terminated surfaces.

Figure 5.49 shows 50×50 μm AFM scans of annealed [Zn] faces after etching with *(a)* the 1:36 ml HCl: water solution, *(b)* the 1:1:10 ml and *(c)* 1:100:100 ml phosphoric acid: acetic acid: water solutions, and *(d)* the 6 g: 4 ml: 30 ml NH_4Cl: NH_4OH: water solution. In the case of the acidic solutions *(a)*, *(b)* and *(c)* the morphology is largely similar to that of the unannealed surfaces discussed above, where the changes are the result of a lateral etch. The acids have a tendency to etch the mixed-terminated scratch edges, broadening them and creating pits along their lengths. The lateral etch also attacks the edges of the irregular-shaped plateaus (as shown in *Fig. 5.14*, above) leading to the appearance of circular patterns across the surface. A comparison between *Figs. 5.49(b)* and *(c)* suggests that the lateral etch rate is higher for the 1:1:10 ml phosphoric acid: acetic acid: water solution than for the 1:100:100 ml solution. It should also be noted that for unannealed Zn-terminated surfaces etched with these acids, the etch pits have widths of 3 μm for the 1:1:10 ml solution compared to 1 μm for the 1:100:100 ml solution (*Figs. 5.42* and *5.41* respectively). *Table 5.3* gives RMS and ISA values for each surface shown in *Fig. 5.49*.

Etching the annealed Zn-terminated surface with the alkaline ammonium chloride: ammonium hydroxide: water solution produces a radically different topography (*Fig. 5.49(d)*) with the appearance of large ridges. Such structures were not isolated to an individual surface, and *Fig. 5.50* is a 50×50 μm image of a different Zn-terminated wafer etched similarly. The presence of these ridges may be explained by a mechanism similar to that reported by *Maki et al.* (see *Fig. 5.23*). Ridges on annealed O-terminated surfaces were observed as a result of the anisotropy in the HCl etching which preferentially etches O-terminated terraces downwards compared to lateral etching of the side walls of thermal pits. It is proposed that an analogous situation occurs using an alkaline solution to etch Zn-terminated faces. Annealing the face creates Zn-terminated terraces that are preferentially etched compared to the polish scratches, leaving ridges as observed.

Optically, the annealed and etched Zn-terminated faces demonstrate no bound-exciton luminescence and, in the case of the acidic solutions, no green band luminescence either. However, samples etched with the ammonia-based solution reveal very weak green band luminescence (*Figure 5.51*). Reflected light intensity generally decreases as a result of the etching in all cases, but free-exciton resonances improve slightly on etching with the phosphoric: acetic acids and HCl (*Figure 5.52*).

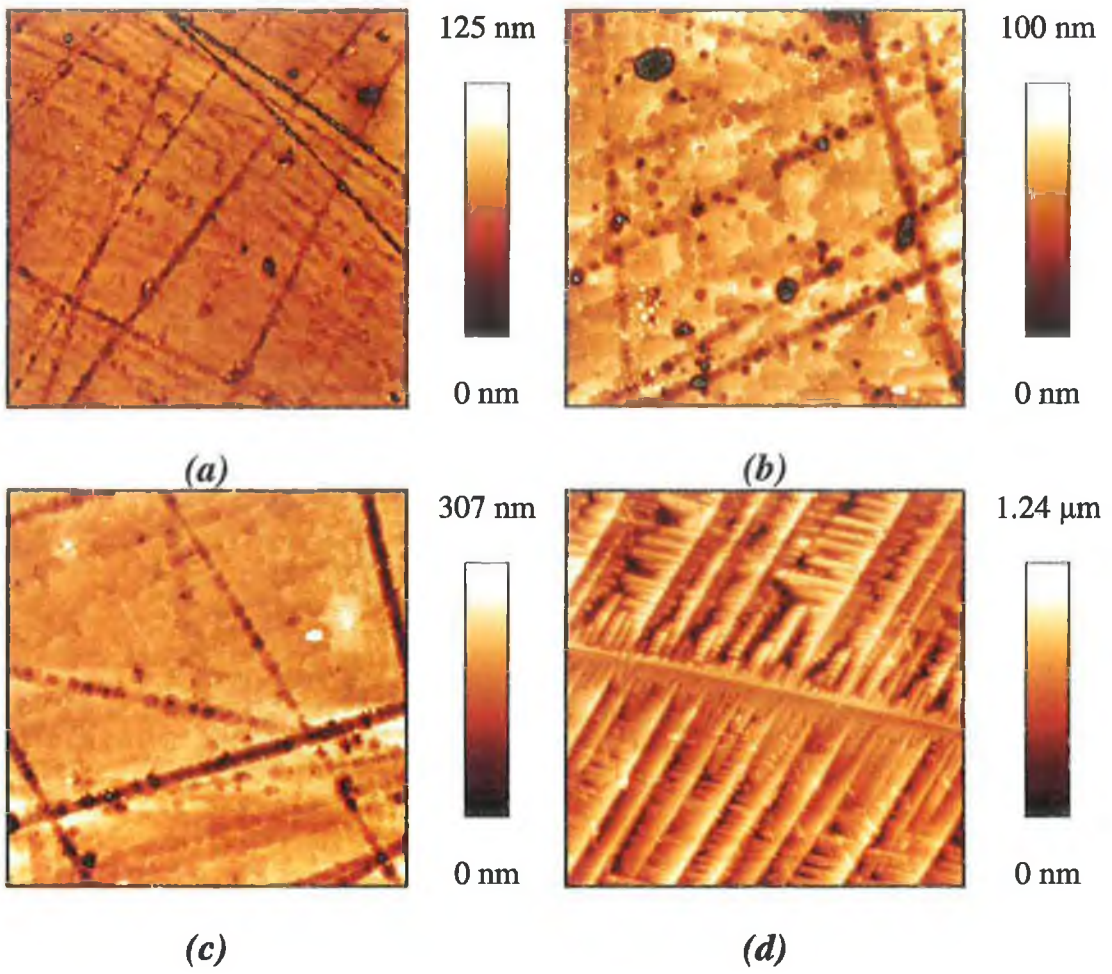

Figure 5.49: *50×50 µm AFM scans of annealed Zn-terminated surfaces (1000 °C for 24 hours in a 0.5 bar O_2 atmosphere) after etching with (a) 1:36 ml HCl: water solution for 6 seconds, (b) 1:1:10 ml phosphoric acid: acetic acid: water solution for 40 seconds, (c) 1:100:100 ml phosphoric acid: acetic acid: water solution for 75 seconds, and (d) 6 g: 4 ml: 30 ml NH_4Cl: NH_4OH: water solution for two minutes. The acidic solutions (a), (b) and (c) laterally etch the surface, creating pits along scratch marks, and attack the edges of the irregular-shaped plateaus (particularly evident in (b) and observed as curved patterns across the face). The difference in the extent of the etching of plateaus in images (b) and (c) suggests the lateral etch rate is faster for the 1:1:10 solution, and thus explains the broad nature of pits observed on unannealed, etched, Zn-terminated faces. The alkali solution creates a radically different morphology (d).*

Table 5.3:

Figure	*Etchant*	*RMS*	*ISA increase*
(a)	1:36 ml HCl: water	14.6 nm	0.21 %
(b)	1:1:10 ml H_3PO_4: $C_2H_4O_2$: H_2O	29.6 nm	0.36 %
(c)	1:100:100 ml H_3PO_4: $C_2H_4O_2$: H_2O	29.4 nm	0.34 %
(d)	4 g: 6 ml: 30 ml NH_4Cl: NH_4OH: H_2O	183.7 nm	9.97%

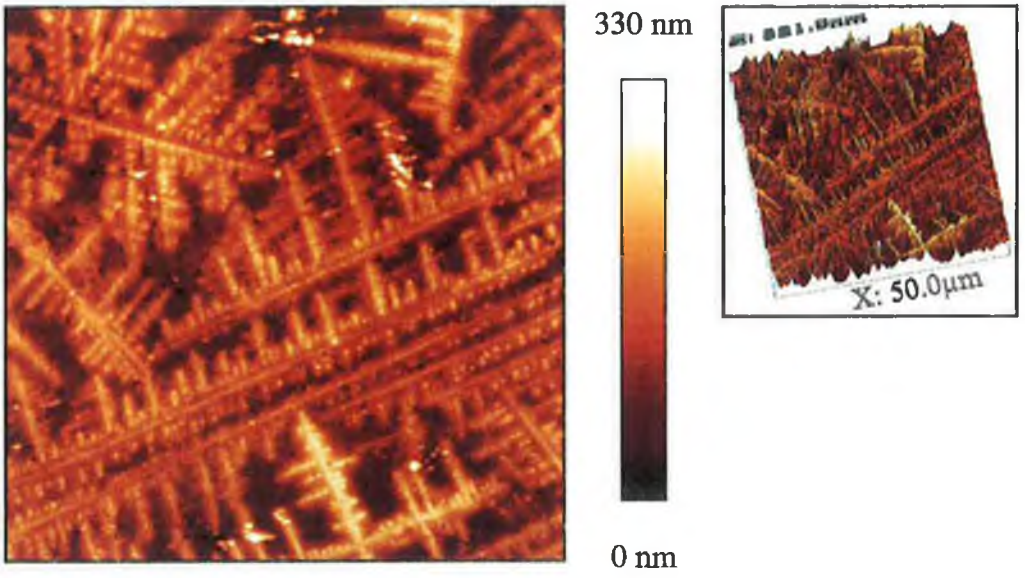

Figure 5.50: *50×50 µm AFM image of annealed Zn-terminated surface after etching with the 4 g: 6 ml: 30 ml NH_4Cl: NH_4OH: H_2O solution, showing ridges. These are believed to form as a result of an anisotropy in etching behaviour, with the solution etching the Zn-terminated terraces faster than the polish scratch edges, leaving the observed ridges.*

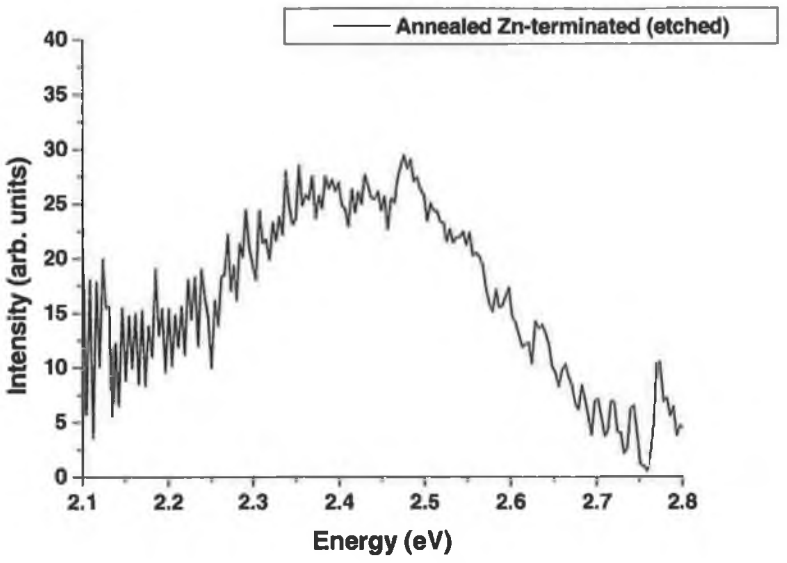

Figure 5.51: *Green band luminescence (25 K) from the annealed Zn-terminated face after etching with the NH_4Cl: NH_4OH: water solution.*

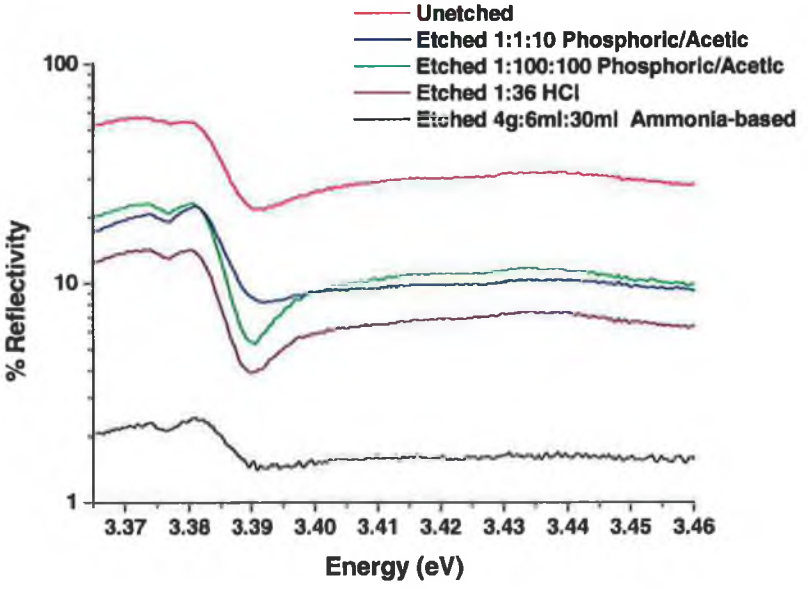

Figure 5.52: *Reflectance spectra of Zn-terminated surfaces (25 K) after etching with each of the solutions.*

5.8 Conclusions

In this chapter it has been shown that the O- and Zn-terminated polar faces of ZnO react differently to both acidic and alkaline solutions. The results of *Chapter 4* indicate that the O-terminated face is strongly hydrophilic and hence rapidly etched by acidic solutions containing high concentrations of H^+ cations. One finds that there is an anisotropy in the etching behaviour of O-terminated faces, whether annealed or unannealed, with relatively high vertical-to-lateral etch rates as a result of differences in binding between O atoms lying at the surface (each having two dangling electrons) and those involved in mixed O-Zn bonding in lateral directions. For HCl solutions, the vertical-to-lateral rate appears relatively fixed and changes in the concentration of the solution merely alter the durations required to achieve particular depths/widths. This is not the case for solutions containing both phosphoric and acetic acid, where the relative ratio of the constituents appears to affect the vertical-to-lateral etch ratio. An immediate application of this result is that by tailoring the phosphoric/acetic acid ratio one might achieve a reasonable degree of control over the etching behaviour.

One observes that O-terminated surfaces which, it has been proposed, stabilise through adsorption of H ions (*Chapter 4*) are rapidly vertically etched by acidic solutions. Conversely, the Zn-terminated surfaces that stabilise though adsorption of OH groups (*Chapter 4*) are largely laterally etched by these acidic solutions, but vertically etched with the aqueous ammonia-based solution containing OH groups.

Annealing surfaces in O_2 atmospheres appears to quench BE emission but increase the structured green band, and it is concluded that the anneal creates deep level defects that quench the near band-edge signals. Although one cannot rule out the possibility of Cu contamination from quartz ampoules and furnace heating elements, the increase in structured green band is largely in accordance with newer studies suggesting the origin of the band is Zn vacancies. The fact that the unstructured green band does

not appear to change suggests that the O_2 environment prevents the creation of oxygen vacancies by the anneal.

As one might expect, the destruction of a relatively uniform surface by acids drastically alters the optical properties of the O-terminated surface. The overall intensity of reflected light from etched surfaces drops as a result of the increase in scattering from the rougher surfaces, and free-excitons resonances are substantially reduced. One also observes either a substantial or total reduction of bound-exciton luminescence, but generally also an increase in the intensity of the unstructured green band. Based on the known etch mechanism, the increase in green band is consistent with the creation of O vacancies which, it is proposed, quench both FE and BE features.

Zn-terminated surfaces display an almost complete reversal of the effects observed for O-terminated faces. In the case of acidic solutions, the etch rate is generally faster laterally than vertically and the polish-induced scratches on the Zn-terminated face are broadened. As a consequence, one finds that the roughness of faces reduces and the strength of free-exciton resonances can be significantly improved. Since Zn-terminated surfaces are etched to a much lesser extent than O-terminated faces, there is, correspondingly, no detectable increase in unstructured green band emission after etching. These results support the hypothesis put forward in *Chapter 3* – that the relative optical differences between the polar faces of Rubicon wafers, certainly in terms of the reflectance characteristics compared to Eagle-Picher and Crystal material, is partially the result of the effectiveness of the polish applied to each surface.

The alkaline solution containing aqueous ammonia and ammonium chloride does not appreciably effect the O-terminated surface either optically or topographically, at least for relatively short exposure times, although it does appear to etch the Zn-terminated face vertically. This is most dramatically seen for annealed Zn-terminated surfaces which exhibit a radically different morphology to that observed in any other case. The exact cause of the features shown in *Figures 5.49(d)* and *5.50* is not

understood, although the criss-cross pattern of ridges is clearly related to the pattern of scratch marks on samples before etching.

Finally, it is observed that there is an anomalous behaviour of the BE luminescence from both O- and Zn-surfaces after etching with the lowest pH phosphoric/acetic acid solution. In the case of the O-terminated face, one finds that the intensity of luminescence is higher than one might expect based on both the extent of the damage to the surface caused by the etching, and a comparison of the damage to that induced by other solutions. Similarly, etching Zn-terminated surfaces with this combination of acids leads to the appearance of a broad BE peak. It has been proposed that H incorporation into the surface layers (within the ~ 50 nm probe depth of the HeCd 325 nm line) may be the cause of the effects on [Zn]-faces.

5.9 *References*

[1] Rubicon Technology, Inc., 3000 Lakeside Drive, Suite 105N, Bannockburn, IL 60015, USA

[2] M. J. Vellekoop, C .C. G. Visser, P. M. Sarro, and A. Venema, *Sensors and Actuators* **A21-A23** (1990) 1027

[3] D. C. Reynolds, D. C. Look, B. Jogai, C. W. Litton, T. C. Collins, W. Harsch, and G. Cantwell, *Phys. Rev. B* **57** (1998) 12151

[4] H. Alves, D. Pfisterer, A. Zeuner, T. Riemann, J. Christen, D. M. Hofmann, and B.K. Meyer, *Optical Materials* **23** (2003) 33

[5] O. Dulab, L. A. Boatner, and U. Diebold, *Surf. Sci.* **519** (2002) 201

[6] Nanotec Electronica, Centro Empresarial Euronova 3, Ronda de Poniente, 2 Edificio 2 - 1ª Planta - Oficina A, 28760 Tres Cantos, Madrid, Spain

WSxM software (V. 4.0, D. 7.4) downloadable from:
www.nanotec.es/download.htm

[7] Private communication, Ignacio Horcas, Director of Software, Nanotec Electronica S.L., Spain (see Ref. [6])
Email: Ignacio.horcas@nanotec.es

[8] J. Fryar, E. McGlynn, M. O. Henry, A. A. Cafolla, and C. J. Hanson, *Physica B* **340-342** (2003) 210

[9] H. Maki, T. Ikoma, I. Sakaguchi, N. Ohashi, H. Haneda, J. Tanaka, and N. Ichinose, *Thin Solid Films* **411** (2002) 91

[10] J. A. Sans, A. Segura, M. Mollar, and B. Marí, *Thin Solid Films* **453-454** (2004) 251

[11] T. Agne, K. Johnston, D. McCabe and the ISOLDE collaboration (CERN), submitted for publication

[12] A. N. Mariano and R. E. Hanneman, *J. Appl. Phys.* **34** (1963) 384

[13] C. G. Van de Walle, *Phys. Rev. B* **85** (2000) 1012

[14] M. Odelius, *Phys. Rev. Lett.* **82** (1999) 3919

[15] N. Ohashi, T. Ishigaki, N. Okada, T. Sekiguchi, I. Sakaguchi, and H. Haneda, *Appl. Phys. Lett.* **80** (2002) 2869

[16] D. C. Reynolds, C. W. Litton, and T. C. Collins, *Phys. Rev.* **140** (1965) A1726

[17] V. V. Travnikov, A. Freiburg, and S. F. Savikhin, *J. Lumin.* **47** (1990) 107

Chapter 6

Semi-Classical Theory of the Exciton-Polariton Interaction

6.1 Introduction

Previous chapters have utilised reflectance spectra in the analysis of etched and unetched samples, but the experimental configuration was such that the data were not easily amenable to mathematical modelling using the well-known polariton model. In this chapter the exciton-polariton interaction is examined using a semi-classical model and the theory is based on the notion that excitons act as oscillating dipoles with a natural frequency of vibration. Incoming light will couple to the excitons and drive this oscillation as the frequency of EM radiation approaches the natural frequency of oscillators. The subsequent resonance of the excitons contributes to the dielectric constant of the material and hence alters the reflectance of samples, as observed by spectroscopic measurements.

The analysis presented in this chapter is broken into five sections. In the first, Maxwell's equations are manipulated to obtain longitudinal and transverse solutions in terms of the dielectric constant of the material. The second section examines the contribution of the excitons themselves to the polarisability of the crystal. Using these results, the third section combines the longitudinal and transverse solutions with the derived expression for the contribution of excitons to the dielectric constant, and hence examines the dispersion of waves in the material. In the fourth and fifth sections, the classical and additional boundary conditions required to model the reflectance from real samples are discussed.

In the next chapter the actual models used and the results obtained from the mathematical modelling of reflectance spectra from polycrystalline, thin film ZnO and bulk ZnO crystals will be shown. However, this chapter will concentrate on the theory of reflectance spectra in a more general sense and closely follows the treatment given by *Hopfield* and *Thomas* [1], from which much of the formalism is taken.

6.2 *Maxwell's Equations*

The discussion begins with a statement of Maxwell's equations, with Gauss' Law (electric and magnetic), Faraday's Law and the modified form of Ampere's Law;

$$\nabla \cdot \vec{E} = \frac{\rho}{\varepsilon_0}$$

Eqn. 6.1

$$\nabla \cdot \vec{B} = 0$$

Eqn. 6.2

$$\nabla \times \vec{E} = -\frac{\partial \vec{B}}{\partial t}$$

Eqn. 6.3

$$\nabla \times \vec{H} = j + \frac{\partial\left(\varepsilon_0 \vec{E} + \vec{P}\right)}{\partial t}$$

Eqn. 6.4

where $\vec{E}$ is the electric field vector, $\vec{B}$ is the magnetic field vector, ρ is the electric charge density, ε_0 is the electric permittivity of free space, and j is the displacement current density. The above equations have been given in a form for a dielectric medium and therefore include the polarisation vector $\vec{P}$, which is the resultant electric dipole moment per unit volume. Based on this polarisation one may define a new field, known as the displacement $\vec{D}$;

$$\vec{D} = \varepsilon_0 \vec{E} + \vec{P}$$

Eqn. 6.5

In short, the electric field that exists in the dielectric medium is the difference between the field that would exist in the absence of polarisation and the field that arises as a result of the polarisation;

$$\vec{E} = \frac{\vec{D}}{\varepsilon_0} - \frac{\vec{P}}{\varepsilon_0}$$

Eqn. 6.6

For a homogenous, linear, isotropic dielectric the polarisation and electric field are in the same direction and mutually proportional. The displacement for such a medium can be written as;

$$\vec{D} = \varepsilon_r \varepsilon_0 \vec{E}$$

Eqn. 6.7

where ε_r is the relative permittivity, or the dielectric constant.

Analogously, the equations above have introduced a magnetic polarisation (or 'magnetisation' vector) $\vec{M}$ as the magnetic dipole moment per unit volume, and subsequently defined $\vec{H}$ as the magnetic field intensity;

$$\vec{H} = \mu_0^{-1} \vec{B} - \vec{M}$$

Eqn. 6.8

For a homogenous, non-ferromagnetic, isotropic medium $\vec{B}$ and $\vec{H}$ are proportional and parallel;

$$\vec{H} = \mu_r^{-1} \mu_0^{-1} \vec{B}$$

Eqn. 6.9

where μ_r is the relative permeability.

It is necessary to modify Maxwell's equations as expressed above so that each is given in terms of the auxiliary vectors $\vec{D}$ and $\vec{H}$;

$$\nabla \cdot \vec{D} = \varepsilon_r \rho$$

Eqn. 6.10

$$\nabla \cdot \vec{H} = 0$$

Eqn. 6.11

$$\nabla \times \vec{D} = -\varepsilon_r \varepsilon_0 \mu_r \mu_0 \frac{\partial \vec{H}}{\partial t}$$

Eqn. 6.12

$$\nabla \times \vec{H} = j + \frac{\partial \vec{D}}{\partial t}$$

Eqn. 6.13

The next step in the discussion involves obtaining a wave-equation for the displacement vector of the form;

$$\nabla^2 \Psi = \frac{1}{v^2} \frac{\partial^2 \Psi}{\partial t^2}$$

Eqn. 6.14

where v is the phase velocity of the wave. For the purposes of this treatise only the electric field components of the EM wave are considered, although the magnetic field contributions can be derived similarly. Clearly the most obvious place to start is with Faraday's Law (*Eqn. 6.12*) and to take the curl of both sides of the equation;

$$\nabla \times \left(\nabla \times \vec{D} \right) = -\varepsilon_r \varepsilon_0 \mu_r \mu_0 \frac{\partial \left(\nabla \times \vec{H} \right)}{\partial t}$$

Eqn. 6.15

Using Ampere's Law (*Eqn. 6.13*) to substitute for the curl of the magnetic field intensity $\left(\nabla \times \vec{H}\right)$, one obtains;

$$\nabla \times \left(\nabla \times \vec{D}\right) = -\varepsilon_r \varepsilon_0 \mu_r \mu_0 \frac{\partial}{\partial t}\left[j + \frac{\partial \vec{D}}{\partial t} \right]$$

Eqn. 6.16

and, after removing the parentheses;

$$\nabla \times \left(\nabla \times \vec{D}\right) = -\varepsilon_r \varepsilon_0 \mu_r \mu_0 \frac{\partial j}{\partial t} - \varepsilon_r \varepsilon_0 \mu_r \mu_0 \frac{\partial^2 \vec{D}}{\partial t^2}$$

Eqn. 6.17

We now examine the LHS of *Eqn. 6.17* and apply the operator;

$$\nabla \times \left(\nabla \times\right) = \nabla\left(\nabla \cdot\right) - \nabla^2$$

Eqn. 6.18

and can then express *Eqn. 6.17* as;

$$\nabla\left(\nabla \cdot \vec{D}\right) - \nabla^2 \vec{D} = -\varepsilon_r \varepsilon_0 \mu_r \mu_0 \frac{\partial j}{\partial t} - \varepsilon_r \varepsilon_0 \mu_r \mu_0 \frac{\partial^2 \vec{D}}{\partial t^2}$$

Eqn. 6.19

Finally, to obtain a wave-equation, one substitutes Gauss's law (electric) (*Eqn. 6.10*) for $\left(\nabla \cdot \vec{D}\right)$ on the LHS and *Eqn. 6.19* becomes;

$$\nabla^2 \vec{D} - \varepsilon_r \varepsilon_0 \mu_r \mu_0 \frac{\partial j}{\partial t} - \varepsilon_r \varepsilon_0 \mu_r \mu_0 \frac{\partial^2 \vec{D}}{\partial t^2} = \nabla\left(\varepsilon_r \rho\right)$$

Eqn. 6.20

which, for an uncharged and non-conducting medium $\left(\rho = j = 0\right)$, reduces to;

$$\nabla^2 \vec{D} = \varepsilon_r \varepsilon_0 \mu_r \mu_0 \frac{\partial^2 \vec{D}}{\partial t^2}$$

Eqn. 6.21

Before continuing it is worth discussing the physical meaning of the derivation this far. Maxwell's equations predict an electromagnetic wave, although only the electric component of the wave has been examined above. If the wave is travelling through a dielectric medium then one finds that the polar charges in the medium have a tendency to follow the electric field vector, resulting in a net dipole moment. The above discussion has taken this interaction into account through the polarisation vector $\vec{P}$, and subsequently the displacement vector $\vec{D}$. The contribution of the medium itself to the electric field is related through the dielectric constant ε_r (*Eqn. 6.7*). A comparison of *Eqn. 6.21* to the wave-equation (*Eqn. 6.14*) reveals that the phase velocity of the wave in the medium is also related to this constant and is given by;

$$v = \frac{1}{\sqrt{\varepsilon_r \varepsilon_0 \mu_r \mu_0}} = \frac{1}{\sqrt{\varepsilon \mu}}$$

Eqn. 6.22

where ε and μ are the electric permittivity and magnetic permeability of the medium respectively.

This forms the theoretical basis for the nature of reflectance spectra in optical/near UV regions. The presence of excitons interacting with the electric field of incident light contributes to the polarisation and dielectric constant of the material, and hence to the refractive index (which is related to the velocity of the wave in the medium). Since the reflectance of a material can be expressed in terms of its refractive index through the Fresnel equations (*Section 6.5*), one can subsequently explain the observed reflectance spectra. Before the excitonic contributions to the dielectric constant can be examined though, it is necessary to obtain expressions for the wave-vector and frequency of the EM wave in terms of the dielectric constant.

From the perspective of modelling the reflectance spectra, the most interesting aspect of the above derivation is *Eqn. 6.17*;

$$\nabla\times\left(\nabla\times\vec{D}\right)=-\varepsilon_r\varepsilon_0\mu_r\mu_0\frac{\partial j}{\partial t}-\varepsilon_r\varepsilon_0\mu_r\mu_0\frac{\partial^2\vec{D}}{\partial t^2}$$

It shall be assumed that the medium is non-conducting, and hence one obtains the expression;

$$\nabla\times\left(\nabla\times\vec{D}\right)=-\varepsilon_r\varepsilon_0\mu_r\mu_0\frac{\partial^2\vec{D}}{\partial t^2}$$

Eqn. 6.23

which, as has been demonstrated above, is a wave-equation.

We consider an electromagnetic wave moving through the dielectric medium, where the electric field (as well as the electric displacement and magnetic field intensity vectors) are varying with respect to both spatial position in the medium and time. For the following analysis it is necessary to examine the dependence of these on the wave-vector *k* and hence we consider harmonic waves of the form;

$$\vec{E}=E_0e^{i(\vec{k}.\vec{r}-\omega t)}$$

Eqn. 6.24

If one replaces the displacement vector in *Eqn. 6.23* with the electric field vector, evaluates the double-derivative on the RHS of the equation, and makes use of the operator given in *Eqn. 6.18* to determine the cross-product on the LHS, *Eqn. 6.23* can be expressed as;

$$\vec{k}^2\vec{E}-\vec{k}\left(\vec{E}\cdot\vec{k}\right)=\omega^2\varepsilon_r\varepsilon_0\mu_r\mu_0\vec{E}$$

Eqn. 6.25

Equation 6.25, above, is of the form;

$$A\vec{E} - B = C\vec{E}$$

and has two solutions – either B is zero or some multiple of $\vec{E}$. Since B corresponds to $\vec{k}\left(\vec{E}\cdot\vec{k}\right)$ in *Eqn. 6.25*, these two possibilities can be achieved through the dot-product if the electric field and wave-vector of the EM wave are perpendicular or parallel to one another respectively.

In the first case, if $\vec{E} \perp \vec{k}$, then the dot-product is zero and;

$$\vec{k}^2\vec{E} = \omega^2\varepsilon_r\varepsilon_0\mu_r\mu_0\vec{E}$$

Eqn. 6.26

Since the phase velocity of the wave in a vacuum is given by *Eqn. 6.22*;

$$c = \frac{1}{\sqrt{\varepsilon_0\mu_0}}$$

the expression can be rearranged to give;

$$\boxed{\frac{\vec{k}^2c^2}{\omega^2} = \varepsilon_r\mu_r}$$

Eqn. 6.27

This is known as the *transverse* solution. The second case, when $\vec{E} \parallel \vec{k}$ and known as the *longitudinal* solution, gives;

$$\boxed{\frac{\omega^2}{c^2}\varepsilon_r\mu_r\vec{E} = 0}$$

Eqn. 6.28

Now that both longitudinal and transverse solutions have been derived, we shall temporarily leave this discussion and examine the effect of the excitons on the polarisability and dielectric constant of the medium.

6.3 *Contribution of Excitons to Polarisability*

From the previous discussion of Maxwell's equations two expressions (*Eqns. 6.5* and *6.7*) describing the relationship between electric field, displacement and polarisation have been used;

$$\vec{D} = \varepsilon_0 \vec{E} + \vec{P}$$

and;

$$\vec{D} = \varepsilon_r \varepsilon_0 \vec{E}$$

where ε_0 is the permittivity of free space and ε_r is the dielectric constant or relative permittivity of the medium. Combining these two equations gives;

$$\varepsilon_r \varepsilon_0 \vec{E} = \varepsilon_0 \vec{E} + \vec{P}$$

Eqn. 6.29

which, after cancelling and rearranging, is;

$$\varepsilon_r = 1 + \frac{1}{\varepsilon_0}\left[\frac{\vec{P}}{\vec{E}}\right]$$

Eqn. 6.30

Thus, one obtains an expression that relates the dielectric constant of the medium to the polarisation, or dipole moment per unit volume, that results from the application of an electric field. Although a vector notation has been used, it is important to note that we are assuming both the polarisation and electric field are waves, i.e.;

$$\vec{P} = P_0 e^{i(\vec{k}.\vec{r}-\omega t)}$$

$$\vec{E} = E_0 e^{i(\vec{k}.\vec{r}-\omega t)}$$

Eqn. 6.31

and for the remainder of this section shall adopt a more general notation. *Equation 6.30* becomes;

$$\varepsilon_r(k,\omega) = 1 + \frac{1}{\varepsilon_0}\left[\frac{P(k,\omega)}{E(k,\omega)}\right]$$

Eqn. 6.32

where the polarisation, electric field and dielectric constant are clearly dependent on both wave-vector and frequency. Subsequently, one can define the polarisability as;

$$\alpha(k,\omega) = \frac{P(k,\omega)}{E(k,\omega)}$$

Eqn. 6.33

The polarisability relates the polarisation of the medium to the applied electric field and is both frequency and wave-vector dependent. For a given wave-vector k one can express *Eqn. 6.33* as;

$$P_k(\omega) = \alpha(k,\omega)E_k(\omega)$$

Eqn. 6.34

The direction the theory takes, at this point, becomes quite clear. In the previous section the transverse and longitudinal solutions of Maxwell's equations were given in terms of the dielectric constant of the medium. In this section it has been shown that the dielectric constant depends on the polarisability of the medium. It is therefore necessary to derive an equation that describes how the presence of excitons affects the polarisability and then relate this back, firstly to the dielectric constant, and then to the solutions of Maxwell's equations.

To obtain such an expression we imagine the presence of dipoles in the medium having a natural frequency of $\omega_j(k)$. The derivation starts with an examination of the behaviour of these dipoles in a static electric field, where the intensity varies as a

function of spatial position in the medium but not of time. Mathematically, the polarisation that results for a static field of given wave-vector can be expressed as;

$$P_k(0) = \alpha(k,0) E_k(0)$$

Eqn. 6.35

Upon application of a static field of wave-vector k, one induces a polarisation field of wave-vector k with amplitude defined by *Eqn. 6.35*. Since the electric field and polarisation are not varying with respect to time in this static case, it follows that;

$$\frac{d^2 P_k(0)}{dt^2} = 0$$

Eqn. 6.36

Assuming the dipoles behave as driven harmonic oscillators of the form;

$$\frac{d^2 x}{dt^2} + \omega_0{}^2 x = A_0 \cos(\omega t)$$

Eqn. 6.37

one can describe the relationship between polarisation and electric field as;

$$\frac{d^2 P_k(0)}{dt^2} + \omega_j{}^2(k) P_k(0) \propto E_k(0)$$

Eqn. 6.38

where $\omega_j{}^2(k) P_k(0)$ is the restoring term and $E_k(0)$ is the driving term. The double derivative on the LHS of the expression is zero (*Eqn. 6.36*), and the equation becomes;

$$\omega_j{}^2(k) P_k(0) = C E_k(0)$$

Eqn. 6.39

where the 'force-like' parameter C has been introduced, which relates to the harmonic restoring force. From *Eqn. 6.39* one obtains;

$$C = \omega_j{}^2(k) \frac{P_k(0)}{E_k(0)}$$

Eqn. 6.40

and, by replacing the ratio of polarisation to electric field by the polarisability (*Eqn. 6.33*);

$$C = \alpha(k,0)\omega_j^{\,2}(k)$$

Eqn. 6.41

where the term $\alpha(k,0)$ is the polarisability as a result of an electric field periodic in space but not time.

It is now necessary to generalise the discussion to examine the polarisability when the electric field is also varying with respect to time and one can write;

$$\frac{d^2P_k(\omega)}{dt^2} + \omega_j^{\,2}(k)P_k(\omega) \propto E_k(\omega)$$

Eqn. 6.42

from the driven harmonic oscillator equation (*Eqn. 6.37*), and the polarisation and electric field are now frequency-dependent.

The assumption is made that the proportionality tensor is also given by C in this case – in effect, we are stating that this relationship is independent of frequency and the parameter C acts as the 'spring-constant' of the system. Introducing both C (*Eqn. 6.41*) and a damping term (which shall not be made dependent on wave-vector), *Eqn. 6.42* becomes;

$$\frac{d^2P_k(\omega)}{dt^2} = \underbrace{-\omega_j^{\,2}(k)P_k(\omega)}_{\text{restoring term}} + \underbrace{\alpha(k,0)\omega_j^{\,2}(k)E_k(\omega)}_{\text{driving term}} - \underbrace{\Gamma\frac{dP_k(\omega)}{dt}}_{\text{damping term}}$$

Eqn. 6.43

Since the polarisation varies with respect to time ($P_k(\omega) = P_0 e^{i(kr-\omega t)}$), then;

$$\frac{d^2 P_k(\omega)}{dt^2} = -\omega^2 P_k(\omega)$$

Eqn. 6.44

and;

$$\frac{dP_k(\omega)}{dt} = -i\omega P_k(\omega)$$

Eqn. 6.45

When *Eqns. 6.44* and *6.45* are substituted into *Eqn. 6.43*, it yields;

$$-\omega^2 P_k(\omega) = -\omega_j^{\,2}(k) P_k(\omega) + \alpha(k,0)\omega_j^{\,2}(k) E_k(\omega) + i\omega\Gamma P_k(\omega)$$

Eqn. 6.46

which becomes;

$$-\omega^2 = -\omega_j^{\,2}(k) + \alpha(k,0)\omega_j^{\,2}(k)\frac{E_k(\omega)}{P_k(\omega)} + i\omega\Gamma$$

Eqn. 6.47

after dividing by $P_k(\omega)$.

Using the relationship (from *Eqn. 6.33*);

$$\frac{1}{\alpha(k,\omega)} = \frac{E_k(\omega)}{P_k(\omega)}$$

Eqn. 6.48

and rearranging *Eqn. 6.47*, the expression for the polarisability as a function of both wave-vector and frequency is;

$$\boxed{\alpha(k,\omega) = \frac{\alpha(k,0)\omega_j^{\,2}(k)}{\omega_j^{\,2}(k) - \omega^2 - i\omega\Gamma}}$$

Eqn. 6.49

In the above derivation we have made no reference to the actual physical source of the polarisation in the medium. Generally the total polarisability can be separated into three parts – electronic, ionic and dipolar [2]. The electronic contribution arises, for example, from the displacement of the electron shells relative to the atomic nuclei, whereas the ionic contribution is the result of the displacement of a charged ion with respect to other ions. The dipolar polarisability comes from a change in orientation of molecules with a permanent electric dipole moment due to the application of the electric field. Typically the dipolar polarisability is dominant at radio/microwave frequencies and the ionic contribution (which is effectively the result of lattice vibrations) largely confined to the infra-red. Therefore it is the electronic polarisability that is of any relevance in the high-frequency optical and near-UV regions of the reflectance spectra examined herein. As well as the displacement of the electron shells, other 'electronic' excitations may affect the polarisability. Excitons, for example, are neutral composite particles with a Coulombic attractive force between the electron and hole (i.e. a dipole). If one were to apply an electric field to a medium, excitons may also contribute to the polarisability. To include the j possible contributing mechanisms to $\alpha(k,\omega)$ we must modify *Eqn. 6.49* to be;

$$\alpha(k,\omega)=\sum_{j}\frac{\alpha_j(k,0)\omega_j{}^2(k)}{\omega_j{}^2(k)-\omega^2-i\omega\Gamma}$$

Eqn. 6.50

Put simply, one considers that all contributions to the polarisability can be expressed in a form identical to that of *Eqn. 6.49* and therefore, to obtain the total polarisability, one must simply sum all of these contributions. Obviously each mechanism could have a different natural frequency, hence the reason this was expressed throughout the discussion as $\omega_j(k)$. The j notation was included at an earlier

stage in order to avoid confusion with ω, which is the driving frequency of the electric field.

Evaluating the sum in *Eqn. 6.50* is complicated due to the presence of resonance and prevents $\alpha(k,\omega)$ being usefully expanded in powers of *k*. Instead, the numerator and denominator of each term must be expanded. To simplify this problem *Hopfield* and *Thomas* [1] chose frequencies near a particular resonance and lumped the sum over all other oscillations into a frequency and wave-vector independent background dielectric constant ε_∞. They also, as has already been mentioned, ignored the wave-vector dependence of the damping term, and chose a direction of *k* such that the polarisability has one principle axis parallel to *k* and the others perpendicular to *k* in directions independent of the magnitude of *k*. Finally, the authors only considered the zero and second-order terms in the expansion. The first order terms vanish for a crystal having inversion symmetry, and are small in other cases. The result of the summation (in S.I. units) is;

$$\alpha(k,\omega)=\varepsilon_0(\varepsilon_\infty-1)+\frac{(\alpha_0+\alpha_2k^2)\omega_0^{\,2}}{\omega_0^{\,2}+\beta k^2-\omega^2-i\omega\Gamma}$$

Eqn. 6.51

Although *Eqn. 6.51* is a general expression, it is now in a form that can be used to discuss the excitonic contribution to the polarisability and hence the dielectric constant. We consider an electromagnetic wave of optical frequency passing through a crystal. The presence of the electric field in the material produces a polarisation field as a result of the induced dipole moment, of which excitonic resonance is one of many contributing mechanisms. The polarisability that relates this polarisation field to the electric field is given by *Eqn. 6.51*. In this case, we decide that the resonance to examine

will be the one due to excitons since this the one revealed by reflectance spectroscopy in the near-UV region. Any resonance not due to the excitons is taken into account through the background dielectric constant ε_∞, while the polarisability of the excitons themselves is given by the α_0 and α_2 terms.

The $\omega_j^2(k)$ term has been expanded to $\omega_0^2 + \beta k^2$, which can readily be interpreted for excitons. The energy of a free-exciton is;

$$E(k) = E_0 + \frac{p^2}{2m^*}$$

Eqn. 6.52

where E_0 is the energy at $k = 0$ and the $\frac{p^2}{2m^*}$ term is the kinetic energy of the free-exciton. Here, m^* is the effective mass of the exciton and p is its momentum. Since $p = \frac{h}{\lambda} = \hbar k$ and $E = \hbar f = \hbar\omega$, one can express *Eqn. 6.52* as;

$$\hbar\omega(k) = \hbar\omega_0 + \frac{\hbar^2 k^2}{2m^*}$$

Eqn. 6.53

and, dividing by $\hbar$, the equation becomes;

$$\omega(k) = \omega_0 + \frac{\hbar k^2}{2m^*}$$

Eqn. 6.54

If one now squares both sides of *Eqn. 6.54* the result is;

$$\omega^2(k) = \omega_0^2 + \omega_0 \frac{\hbar k^2}{m^*} + \cancel{\frac{\hbar^2 k^4}{(2m^*)^2}}$$

Eqn. 6.55

where the last term is considered small and shall be ignored. We can therefore assume that, for the derivation discussed above;

$$\omega_j^{\,2}(k) \approx \omega_0^{\,2} + \omega_0 \frac{\hbar k^2}{m^*}$$

Eqn. 6.56

Comparing this expression to the expansion of $\omega_j^{\,2}(k)$ to $\omega_0^{\,2} + \beta k^2$ it follows that the value of β, in the case of a resonance due to excitons, is given by;

$$\boxed{\beta = \frac{\hbar \omega_0}{m^*}}$$

Eqn. 6.57

6.4 *Exciton Contribution to Dielectric Constant and Dispersion*

Having now obtained an expression that describes the contribution of exciton resonance to the polarisability of the dielectric medium, we now turn our attention to combining this result with the longitudinal and transverse solutions of Maxwell's equations derived in *Section 6.2*. Given that the polarisability with a single oscillator model is (*Eqn. 6.51*);

$$\alpha(k,\omega)=\varepsilon_0(\varepsilon_\infty-1)+\frac{(\alpha_0+\alpha_2k^2)\omega_0^{\,2}}{\omega_0^{\,2}+\beta k^2-\omega^2-i\omega\Gamma}$$

and that the dielectric constant of the crystal can be expressed as (*Eqns. 6.32* and *6.33*);

$$\varepsilon_r(k,\omega)=1+\frac{1}{\varepsilon_0}[\alpha(k,\omega)]$$

the dielectric constant, or relative permittivity, of the medium in frequency regions near an excitonic resonance is;

$$\boxed{\varepsilon_r(k,\omega)=\varepsilon_\infty+\frac{1}{\varepsilon_0}\left(\frac{(\alpha_0+\alpha_2k^2)\omega_0^{\,2}}{\omega_0^{\,2}+\beta k^2-\omega^2-i\omega\Gamma}\right)}$$

Eqn. 6.58

The transverse solution of Maxwell's equations is (*Eqn. 6.27*);

$$\frac{k^2c^2}{\omega^2}=\varepsilon_r\mu_r$$

where the vector notation has been dropped to match the tensor notation of the above discussion. Substituting *Eqn. 6.58* for the dielectric constant and assuming that the magnetic permeability of the crystal is roughly equivalent to that of free space (i.e. the relative permeability $\mu_r=1$) the transverse solution becomes;

$$\frac{k^2c^2}{\omega^2} = \varepsilon_\infty + \frac{1}{\varepsilon_0}\left(\frac{\left(\alpha_0 + \alpha_2 k^2\right)\omega_0{}^2}{\omega_0{}^2 + \beta k^2 - \omega^2 - i\omega\Gamma}\right)$$

Eqn. 6.59

The longitudinal solution, from *Section 6.2* is (*Eqn. 6.28*);

$$\frac{\omega^2}{c^2}\varepsilon_r\mu_r\vec{E} = 0$$

but since clearly the frequency, velocity in free space, and electric field intensity of the EM wave are non-zero, one can conclude that;

$$\varepsilon_r = \frac{\varepsilon}{\varepsilon_0} = 0$$

Eqn. 6.60

Substituting *Eqn. 6.58* for ε_r, the longitudinal solution becomes;

$$\varepsilon_\infty + \frac{1}{\varepsilon_0}\left(\frac{\left(\alpha_0 + \alpha_2 k^2\right)\omega_0{}^2}{\omega_0{}^2 + \beta k^2 - \omega^2 - i\omega\Gamma}\right) = 0$$

Eqn. 6.61

The physical interpretation of these expressions is not immediately obvious, and we shall firstly examine the 'classical' case, where $\alpha_2 = \beta = 0$. The damping term shall also be dropped for simplicity. The transverse and longitudinal solutions, respectively, simplify to;

$$k^2 = \frac{\omega^2}{c^2}\left[\varepsilon_\infty + \frac{1}{\varepsilon_0}\left(\frac{\alpha_0\omega_0{}^2}{\omega_0{}^2 - \omega^2}\right)\right]$$

Eqn. 6.62

and;

$$\varepsilon_\infty + \frac{1}{\varepsilon_0}\left(\frac{\alpha_0\omega_0{}^2}{\omega_0{}^2 - \omega^2}\right) = 0$$

Eqn. 6.63

If the longitudinal solution for this classical case (*Eqn. 6.63*) is rearranged, one obtains;

$$\varepsilon_\infty \varepsilon_0 \left(\omega^2 - \omega_0^{\,2}\right) = \alpha_0 \omega_0^{\,2}$$

Eqn. 6.64

which becomes;

$$\varepsilon_\infty \varepsilon_0 \omega^2 = \alpha_0 \omega_0^{\,2} + \varepsilon_\infty \varepsilon_0 \omega_0^{\,2}$$

Eqn. 6.65

after removing the brackets and collecting ω_0 terms on the RHS of the equation. Dividing by $\varepsilon_\infty \varepsilon_0$, *Eqn. 6.65* gives;

$$\omega^2 = \omega_0^{\,2}\left(1 + \frac{\alpha_0}{\varepsilon_\infty \varepsilon_0}\right)$$

Eqn. 6.66

The driving frequency ω for which *Eqn. 6.66* is satisfied is known as the longitudinal frequency ω_L and can be expressed then as;

$$\boxed{\omega_L = \omega_0 \sqrt{1 + \frac{\alpha_0}{\varepsilon_\infty \varepsilon_0}}}$$

Eqn. 6.67

Figure 6.1 is a plot, using arbitrary values for α_0, ω_0 and ε_∞, of frequency versus the real part of the wave-vector for both transverse (*Eqn. 6.62*) and longitudinal (*Eqn. 6.67*) waves and it can be seen that there are three distinct frequency regions in which the transverse equation operates. In the first case, when $\omega > \omega_L$, one finds that $k^2 > 0$ and hence wave-vectors k have real components and propagate. In the second case, when $\omega_0 < \omega < \omega_L$, the wave-vector is purely imaginary $\left(k^2 < 0\right)$ and therefore the

wave decays. Finally, in the frequency region $\omega < \omega_0$ the wave-vector is also propagating $\left(k^2 > 0\right)$.

As a result of these imaginary, non-propagating solutions for k^2 between ω_0 and ω_L, one finds that the transverse wave divides around these frequencies into upper and lower branches. The lower transverse branch is found to be asymptotic to ω_0 for increasing wave-vector, and we shall therefore refer to ω_0 as the *transverse frequency* of the excitons rather than the 'natural frequency' of oscillators. Subsequently a quantity known as the *longitudinal-transverse (LT) splitting* can be defined as being equal to the difference in frequency between ω_L and ω_0. One may view the process as a 'mixing' of polarisation and bare photon modes to produce mixed modes which are the correct eigenstates of the combined system.

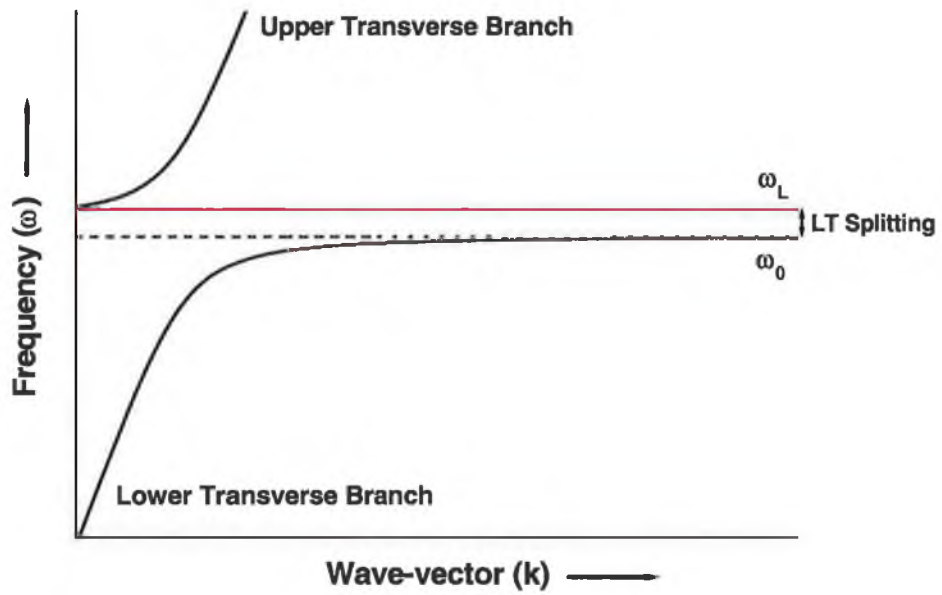

Figure 6.1: *Plot of frequency versus the real part of the wave-vector for both longitudinal and transverse waves in the classical case. The longitudinal wave has a frequency ω_L that is independent of wave-vector and is slightly higher than the transverse frequency ω_0. The transverse wave has both upper and lower branches around these frequencies and the LT splitting is defined as the difference in frequency between ω_0 and ω_L.*

Fig. 6.1 is known as a *dispersion curve*, since it relates the frequency of an EM wave to its wave-vector. It is important to note that the transverse equation (*Eqn. 6.62*) is quadratic in k and at any given frequency ω there will be two waves with the same wavelength but travelling in opposite directions (i.e. they will have opposite wave-vectors). *Fig. 6.1* only shows the set of real positive solutions and it must be borne in mind that there are equivalent negative solutions that lie symmetrically around $k = 0$, and imaginary components that are not shown. Although mathematically these symmetric solutions around $k = 0$ exist, experimental considerations impose a directionality of propagating waves and one need not necessarily consider both solutions as physically relevant. This shall be discussed further in relation to the application of boundary conditions.

The physical interpretation of the transverse equation in this classical case becomes somewhat clearer if *Eqn. 6.62* is expressed as in *Eqn. 6.59*;

$$\frac{k^2c^2}{\omega^2} = \varepsilon_\infty + \frac{1}{\varepsilon_0}\left(\frac{\alpha_0\omega_0{}^2}{\omega_0{}^2 - \omega^2}\right)$$

Eqn. 6.68

where $k = \frac{2\pi}{\lambda}$ and $\omega = 2\pi f$. The expression can subsequently be re-written as;

$$\frac{c^2}{f^2\lambda^2} = \varepsilon_\infty + \frac{1}{\varepsilon_0}\left(\frac{\alpha_0\omega_0{}^2}{\omega_0{}^2 - \omega^2}\right)$$

Eqn. 6.69

and since the velocity of the wave in the dielectric medium is $v = f\lambda$, it becomes;

$$\frac{c^2}{v^2} = \varepsilon_\infty + \frac{1}{\varepsilon_0}\left(\frac{\alpha_0\omega_0{}^2}{\omega_0{}^2 - \omega^2}\right)$$

Eqn. 6.70

or;

$$n^2 = \varepsilon_\infty + \frac{1}{\varepsilon_0}\left(\frac{\alpha_0 \omega_0^{\,2}}{\omega_0^{\,2} - \omega^2}\right)$$

Eqn. 6.71

where n is the refractive index of the medium for the transverse wave.

Figure 6.2 shows a plot of n^2 versus frequency ω, in a frequency region around the transverse frequency ω_0, and demonstrates that the dispersion curve of *Fig. 6.1* actually describes the phase velocity of the transverse wave in the medium. In the region between ω_0 and ω_L wave-vectors are imaginary and so the refractive index is also imaginary $\left(n^2 < 0\right)$ and waves are therefore evanescent.

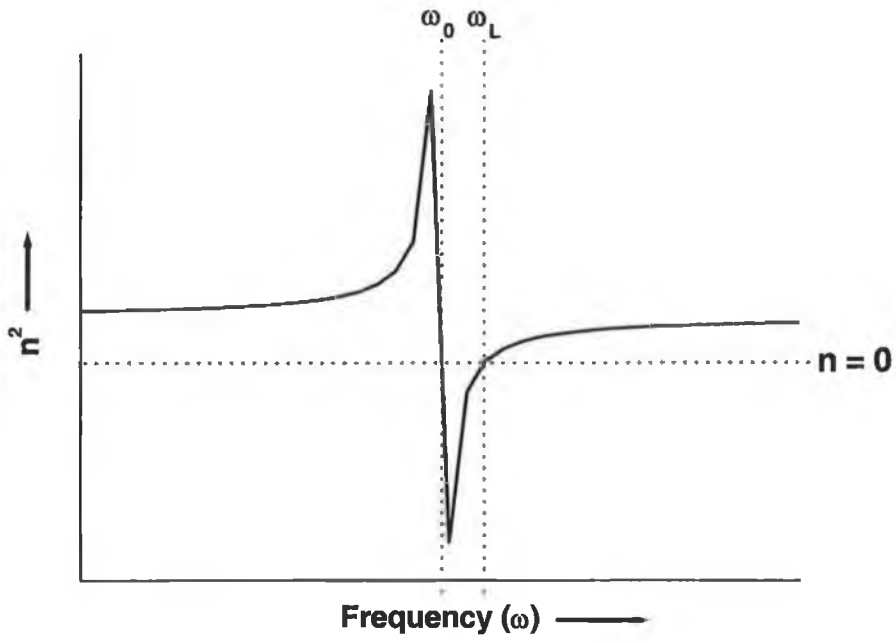

Figure 6.2: *Plot of n^2 versus frequency of EM wave in dielectric medium for the transverse wave, where the frequency region shown is close to ω_0. The presence of both an upper and lower branch in the dispersion curve (Fig. 6.1) manifests as this 'resonance' of the refractive index around the transverse and longitudinal frequencies.*

We now consider the 'non-classical' single oscillator situation, applicable to excitons associated with a single band, where $\alpha_2 = 0$ but $\beta \neq 0$, and the transverse solution (*Eqn. 6.59*) in this case is;

$$\frac{k^2c^2}{\omega^2} = \varepsilon_\infty + \frac{1}{\varepsilon_0}\left(\frac{\alpha_0\omega_0{}^2}{\omega_0{}^2 + \beta k^2 - \omega^2 - i\omega\Gamma}\right)$$

Eqn. 6.72

where the damping term has also been included. After multiplying both sides by the denominator $\omega_0{}^2 + \beta k^2 - \omega^2 - i\omega\Gamma$, *Eqn. 6.72* becomes;

$$\frac{k^2c^2}{\omega^2}\left(\omega_0{}^2 - \omega^2 + \beta k^2 - i\omega\Gamma\right) = \varepsilon_\infty\left(\omega_0{}^2 - \omega^2 + \beta k^2 - i\omega\Gamma\right) + \frac{\alpha_0\omega_0{}^2}{\varepsilon_0}$$

Eqn. 6.73

and subsequently;

$$k^2\left(\frac{c^2\omega_0{}^2}{\omega^2}\right) - k^2c^2 + k^4\left(\frac{\beta c^2}{\omega^2}\right) - ik^2\left(\frac{c^2\Gamma}{\omega}\right) = \varepsilon_\infty\left(\omega_0{}^2 - \omega^2\right) + \varepsilon_\infty\beta k^2 - i\varepsilon_\infty\omega\Gamma + \frac{\alpha_0\omega_0{}^2}{\varepsilon_0}$$

Eqn. 6.74

Unlike the classical case discussed above, the relationship between frequency and wave-vector is quadratic in k^2 rather than in *k*. If we let;

$$x = k^2$$

then *Eqn. 6.74* can be rearranged to give;

$$\boxed{\left(\frac{\beta c^2}{\omega^2}\right)x^2 + \left(\frac{c^2\omega_0{}^2}{\omega^2} - c^2 - i\frac{c^2\Gamma}{\omega} - \varepsilon_\infty\beta\right)x + \left(\varepsilon_\infty\omega^2 - \varepsilon_\infty\omega_0{}^2 + i\varepsilon_\infty\omega\Gamma - \frac{\alpha_0\omega_0{}^2}{\varepsilon_0}\right) = 0}$$

Eqn. 6.75

which can be expressed as the quadratic equation;

$$\boxed{Ax^2 + Bx + C = 0}$$

Eqn. 6.76

where;

$$A = \frac{\beta c^2}{\omega^2}$$

Eqn. 6.77

$$B = \frac{c^2 \omega_0^{\,2}}{\omega^2} - c^2 - i\frac{c^2 \Gamma}{\omega} - \varepsilon_\infty \beta$$

Eqn. 6.78

and;

$$C = \varepsilon_\infty \omega^2 - \varepsilon_\infty \omega_0^{\,2} + i\varepsilon_\infty \omega \Gamma - \frac{\alpha_0 \omega_0^{\,2}}{\varepsilon_0}$$

Eqn. 6.79

Through the introduction of the β parameter, which is related to the transverse frequency of the excitons and their effective mass (*Eqn. 6.57*), it can be seen that the quadratic expression in k^2 for transverse solutions means that for each frequency ω, there are four solutions for k. This differs from the classical case where there were two solutions. For the excitonic resonances, therefore, two transverse waves (either for $k > 0$ or $k < 0$) can exist in the dielectric medium with the same frequency but different wave-vectors – a phenomena known as *spatial dispersion* (*Figure 6.3*).

Following a similar derivation to that of *Eqns. 6.63 – 6.67*, the longitudinal solution in this non-classical case becomes (with zero damping);

$$\omega_L^{\,2} = \omega_0^{\,2}\left(1 + \frac{\alpha_0}{\varepsilon_\infty \varepsilon_0}\right) + \beta k^2$$

Eqn. 6.80

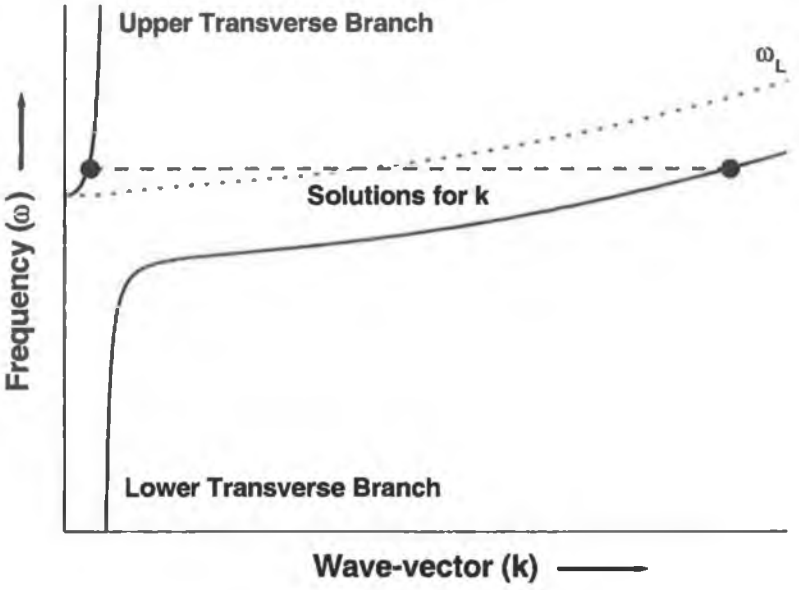

Figure 6.3: *Plot of frequency versus the positive real part of the wave-vector for both longitudinal and transverse waves in the non-classical case. The longitudinal wave has a frequency ω_L that is now dependent on wave-vector through the introduction of the βk^2 term. The transverse wave has both upper and lower branches, as in Fig. 6.1, but spatial dispersion allows two solutions for k, where k >0, for each frequency ω. There are also two negative solutions (i.e. for k <0) which are not shown in the plot, but since these simply refer to waves travelling in the opposite direction, they are equivalent to the positive case shown above. In frequency regions where there appears to be only a single solution for k (for example, at low frequencies) the other solution will be purely imaginary.*

The $\alpha_2 k^2$ term has been ignored in this derivation by setting the polarisability α_2 to zero, although the inclusion of this value in the classical case does not significantly alter the final expression and one finds that *Eqn. 6.62* remains linear in k^2. Since the non-classical case differs from the classical case largely as a result of the β term, the α_2 polarisability also results in no profound change in the transverse equation.

The quadratic equation above describes the transverse waves that propagate through the dielectric medium and can be solved, provided one can obtain values for the effective mass of the excitons (m^*), the transverse frequency (ω_0) and polarisability (α_0), the background dielectric constant (ε_∞), and the damping parameter (Γ). Modelling the reflectance spectra therefore involves comparing a theoretical reflectance spectrum to experimental data, and modifying the above parameters until a reasonable fit is obtained.

To achieve this it is necessary to solve boundary-condition problems, where one considers running waves across the various interfaces of the material under examination. In the next sections we shall examine these boundary conditions in a general sense. In the following chapter these conditions are applied in order to model the reflectance spectra of two samples – a bulk ZnO wafer and a polycrystalline ZnO thin film, grown by a Pulsed Laser Deposition method on a sapphire substrate. Each interface (for example air, followed by ZnO, then followed by sapphire) must be included in the model.

6.5 *Classical Boundary Conditions*

In this section we examine the classical boundary conditions of Maxwell's Equations in a general sense for non-normal incidence, then look at the special case of light incident normally on the surface. A good description of the boundary conditions and their derivation can be found in [3].

6.5.1 $\vec{E}$ *perpendicular to the plane-of-incidence*

In this geometry, the electric field of the incident light is perpendicular to the plane-of-incidence and the magnetic field is parallel to this plane, with the direction of the wave-vector, electric, and magnetic fields obeying the right-hand rule. We assume that the light incident from one medium (refractive index n_i) is both transmitted through the interface into the second medium (refractive index n_t), and also reflected from the interface. *Figure 6.4* is a diagram showing the geometric relationship between the wave-vector (k), electric (E) and magnetic (B) fields, where the subscript notation of i, r, and t refer to the incident, reflected and transmitted waves respectively.

It is assumed, for the moment, that the electric fields of transmitted and reflected light do not undergo phases shifts with respect to the incident light and, in this case, the direction of the E-field remains constant (i.e. towards the reader in *Fig. 6.4*). The x-direction is defined as positive running left to right and the y origin is taken at the interface itself. This choice of y origin ensures that one need not consider any additional phase as a result of waves travelling through the incident medium. However, it is necessary to ensure that the phase of waves encountering multiple interfaces are matched across the boundaries and this requirement shall be discussed in the next

chapter in relation to the boundary conditions used to model the ZnO samples. The angles of incidence, reflection and transmission are given by θ_i, θ_r and θ_t respectively.

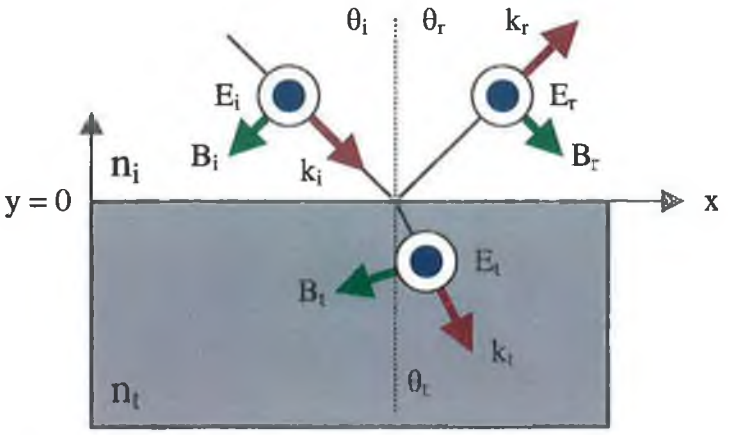

Figure 6.4: *Illustration of the geometry for an electric field perpendicular to the plane-of-incidence between two media. The incident and reflected rays travel in a medium with refractive index n_i, while the transmitted ray passes into a medium with refractive index n_t. It is assumed that the electric fields of transmitted and reflected rays do not undergo a phase shift with respect to the incident light and, in this case, the electric field vector remains perpendicular to the plane-of-incidence and pointing towards the reader. With this assumption, the direction of the B-field is determined by the right-hand rule.*

Clearly with this geometry the tangential component of the E-fields (i.e. that component of the E-fields lying parallel to the surface of the medium n_t) are given simply by E_i, E_r and E_t. The magnitude of these fields is entirely independent of the angles θ_i, θ_r and θ_t. The first boundary condition is that these tangential components are continuous across the boundary and therefore;

$$E_i + E_r = E_t$$

Eqn. 6.81

It should be noted that although the tangential components of the E-fields are continuous across the boundary, the normal components are not. In fact, it is the normal

component of the product εE that is continuous, where ε is the permittivity (or dielectric constant) of the medium.

Due to the perpendicular nature of the E- and B-fields one finds that the exact opposite is the case for the magnetic fields - the normal component of the B-field is continuous across the boundary but it is the tangential component of the product $\mu^{-1}B$ that is continuous. An examination of *Fig. 6.4* reveals that the tangential component of the B-fields must be dependent on angle. The boundary condition for the continuity of the tangential magnetic field is therefore;

$$-\frac{B_i}{\mu_i}\cos\theta_i + \frac{B_r}{\mu_r}\cos\theta_r = -\frac{B_t}{\mu_t}\cos\theta_t$$

Eqn. 6.82

where μ is the magnetic permeability (or relative magnetic permeability) of the medium. One must also consider the direction of the field relative to our defined *x*-axis, hence the negative signs for the incident and transmitted fields. Making use of the fact that the electric and magnetic fields are related by the phase velocity *v* of the wave;

$$B = \frac{E}{v}$$

Eqn. 6.83

the magnetic field boundary condition can be expressed as;

$$\frac{E_i}{\mu_i v_i}\cos\theta_i - \frac{E_r}{\mu_r v_r}\cos\theta_r = \frac{E_t}{\mu_t v_t}\cos\theta_t$$

Eqn. 6.84

If one now multiplies both sides of *Eqn. 6.84* by the velocity of light in vacuum *c*, and replaces the ratio of *c/v* with the refractive index of the medium *n*, the boundary condition becomes;

$$n_i E_i \cos\theta_i - n_i E_r \cos\theta_i = n_t E_t \cos\theta_t$$

Eqn. 6.85

where we have used the fact that the velocity of the incident and reflected wave are the same since they exist in the same medium, that the angle of reflection is the same as the incident angle, and have assumed that $\mu_i = \mu_r = \mu_t$.

From the electric field boundary condition (*Eqn. 6.81*) one obtains the relation;

$$\frac{E_t}{E_i} = \left(1 + \frac{E_r}{E_i}\right)$$

Eqn. 6.86

and by taking the magnetic field boundary condition (*Eqn. 6.85*) and dividing by the incident electric field E_i, this condition becomes;

$$\left(\frac{E_i}{E_i}\right)(n_i \cos\theta_i) - \left(\frac{E_r}{E_i}\right)(n_i \cos\theta_i) = \left(\frac{E_t}{E_i}\right)(n_t \cos\theta_t)$$

Eqn. 6.87

By combining *Eqns. 6.86* and *6.87*, and therefore substituting for $\frac{E_t}{E_i}$, the result is;

$$\left(\frac{E_i}{E_i}\right)(n_i \cos\theta_i) - \left(\frac{E_r}{E_i}\right)(n_i \cos\theta_i) = \left(1 + \frac{E_r}{E_i}\right)(n_t \cos\theta_t)$$

Eqn. 6.88

Finally, bringing the $\frac{E_r}{E_i}$ terms together, the equation describing the ratio of reflected electric field intensity to incident field intensity is;

$$\left(\frac{E_r}{E_i}\right)_\perp = \frac{n_i \cos\theta_i - n_t \cos\theta_t}{n_i \cos\theta_i + n_t \cos\theta_t} = r_\perp$$

Eqn. 6.89

Equation 6.89 is one of the Fresnel equations, and $r_{\perp}$ is known as the *amplitude reflection coefficient* for EM radiation with electric field perpendicular to the plane-of-incidence.

6.5.2 $\vec{E}$ parallel to the plane-of-incidence

The geometry in the case of the E-field lying parallel to the plane-of-incidence is shown in *Figure 6.5* where, similar to the above case, the assumption is that the B-field does not undergo a phase shift as a result of reflection or transmission.

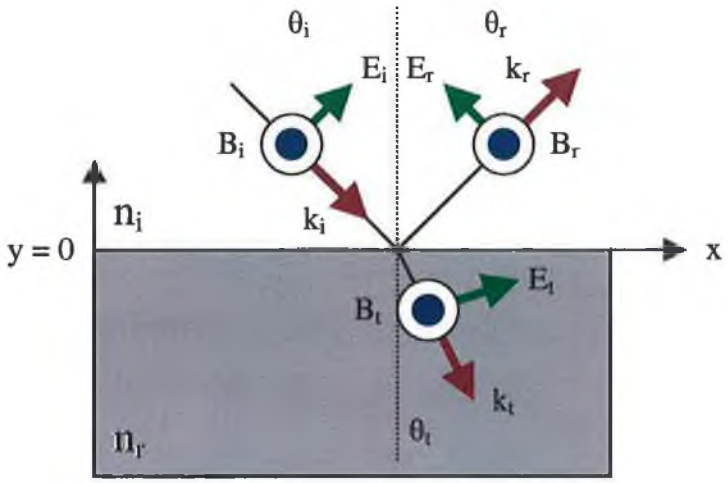

Figure 6.5: *Illustration of the geometry for an electric field parallel to the plane-of-incidence between two media. It is assumed that the magnetic fields of transmitted and reflected rays do not undergo a phase shift with respect to the incident light and, in this case, the magnetic field vector remains perpendicular to the plane-of-incidence and pointing towards the reader. With this assumption, the direction of the E-field is determined by the right-hand rule.*

The continuity of the tangential components of the E-field leads to the boundary condition;

$$E_i \cos\theta_i - E_r \cos\theta_i = E_t \cos\theta_t$$

Eqn. 6.90

and, in much the same way as before, the requirement for the continuity of the tangential components of the B-field yields;

$$n_i E_i + n_i E_r = n_t E_t$$

Eqn. 6.91

Hence in a manner similar to that in the perpendicular case above, the amplitude reflection coefficient $r_{\|}$ is found to be;

$$r_{\|} = \left(\frac{E_r}{E_i}\right)_{\|} = \frac{n_t \cos\theta_i - n_i \cos\theta_t}{n_i \cos\theta_t + n_t \cos\theta_i}$$

Eqn. 6.92

6.5.3 Normal incidence

For light at non-normal incidence one can generally break the E-field into components lying either perpendicular or parallel to the plane-of-incidence and solve the above boundary conditions. At normal incidence, however, these distinctions disappear since the plane-of-incidence becomes undefined and the E- and B-fields will always be tangential to the interface. The requirement for the continuity of electric fields across the interface for normally incident light is therefore just;

$$E_i + E_r = E_t$$

Eqn. 6.93

where we have assumed that the incident, reflected and transmitted E-fields all point in the same direction. At normal incidence the incident and transmitted waves will have wave-vectors that point in the same direction, but the reflected wave will have a wave-vector in the opposite direction. Therefore, the magnetic field of the reflected wave must point in the opposite direction to that of the other waves if the E-field lies in the same direction for all three. The boundary condition for the B-fields is;

$$n_i E_i - n_i E_r = n_t E_t$$

Eqn. 6.94

The amplitude reflection coefficient for normally incident light, determined as above, is;

$$r = \left(\frac{E_r}{E_i} \right) = \frac{n_i - n_t}{n_t + n_t}$$

Eqn. 6.95

and it can be seen that if $n_i < n_t$ then the coefficient r will be negative. This negative value is a direct consequence of the assumptions made regarding the relative direction of E-fields. If, for example, one had chosen the directions such that the reflected E-field actually points in the opposite direction to that of the incident and transmitted waves (i.e. that there is π radian phase shift on reflection), the boundary conditions would have become;

$$E_i - E_r = E_t$$

Eqn. 6.96

$$n_i E_i + n_i E_r = n_t E_t$$

Eqn. 6.97

and the amplitude reflection coefficient in this case is;

$$r = \left(\frac{E_r}{E_i} \right) = \frac{n_i - n_t}{n_i + n_t}$$

Eqn. 6.98

which is positive for $n_i < n_t$.

The aim of applying boundary conditions is to form a series of simultaneous equations that can be solved for the reflected and transmitted E-fields, since one can generally determine the magnitude of the incident E-field experimentally. At non-normal incident angles one finds there are four boundary conditions - two for the case of the E-field perpendicular to the plane-of-incidence, and two for the case of the E-field parallel to the plane-of-incidence. The simultaneous equation set for non-normal incidence is therefore two-dimensional since perpendicular and parallel directions need to be accounted for.

For a normal angle of incidence, the equation set reduces to a one-dimensional problem involving scalars and although it is necessary to make assumptions about the relative phase of the waves and the relative magnitudes of the refractive indices, these assumptions merely alter the sign (either positive or negative) of the fields described by the boundary conditions and the reflection coefficients. No profound change to the form of the boundary conditions occurs.

In the case of the electromagnetic boundary conditions for normal incidence, making no assumptions about the relative magnitude of refractive indices or resultant phase shifts, it does not matter whether one uses the expressions;

$$E_i - E_r = E_t$$

$$n_i E_i + n_i E_r = n_t E_t$$

or;

$$E_i + E_r = E_t$$

$$n_i E_i - n_i E_r = n_t E_t$$

since the fields will be determined to be either positive or negative on solving the equations as a consequence of the scalar nature of the parameters.

We can put this notion on a more solid mathematical foundation by examining the reflectance R rather than the amplitude reflection coefficients. The power per unit area crossing a surface whose normal is parallel to $\vec{S}$, the Poynting vector of the EM wave, is given by the Poynting vector itself;

$$\vec{S} = v^2 \varepsilon \vec{E} \times \vec{B}$$

Eqn. 6.99

where v is the velocity of the wave in a medium having permittivity/dielectric constant ε. The radiant flux density is determined by taking the time-average of the Poynting vector;

$$I = \langle S \rangle_T = \frac{v\varepsilon}{2} E_0^2$$

Eqn. 6.100

which is the average energy per unit time crossing a unit area normal to $\vec{S}$. If we let I_i, I_r and I_t be the incident, reflected and transmitted flux densities respectively, then the powers arriving on, reflected from and transmitted through the interface are;

Incident: $I_i A$

Reflected: $I_r A$

Transmitted: $I_t A$

Eqns. 6.101

where A is the cross-sectional area of each beam. The reflectance R is defined as the ratio of the reflected power to the incident power;

$$R = \frac{I_r A}{I_i A} = \frac{I_r}{I_i}$$

Eqn. 6.102

where the A terms cancel because at normal incidence the cross-sectional area of incident and reflected light will be the same. The quotient $\frac{I_r}{I_i}$ is, according to *Eqn. 6.100*;

$$\frac{I_r}{I_i} = \frac{\frac{v_r \varepsilon_r E_r^2}{2}}{\frac{v_i \varepsilon_i E_i^2}{2}}$$

Eqn. 6.103

and since the incident and reflected rays are in the same medium one obtains;

$$R = \frac{I_r}{I_i} = \left(\frac{E_r}{E_i}\right)^2 = r^2$$

Eqn. 6.104

Thus, one finds that the reflectance R is simply the square of the amplitude reflection coefficient r. If we now examine the square of the amplitude reflectance coefficients for the two cases examined at a normal angles of incidence (i.e. discounting and including a π radian phase shift of reflected light) one obtains;

$$r^2 = \left(\frac{n_i - n_t}{n_i + n_t}\right)^2 = \frac{n_i^2 + n_t^2 - 2n_i n_t}{n_i^2 + n_t^2 + 2n_i n_t}$$

Eqn. 6.105

if we exclude the phase shift (*Eqn. 6.95*) and the identical equation;

$$r^2 = \left(\frac{n_t - n_i}{n_i + n_t}\right)^2 = \frac{n_i^2 + n_t^2 - 2n_i n_t}{n_i^2 + n_t^2 + 2n_i n_t}$$

Eqn. 6.106

if the phase shift is included (*Eqn. 6.98*). It can therefore be seen that for normal incidence the reflectance is;

$$\boxed{R = \left(\frac{n_t - n_i}{n_i + n_t}\right)^2 = r^2}$$

Eqn. 6.107

The Classical Boundary Conditions used here for the modelling of excitonic resonances at normal incidence are;

$$\boxed{E_i + E_r = E_t}$$

for the continuity of tangential electric fields and;

$$\boxed{n_i E_i - n_i E_r = n_t E_t}$$

for the continuity of tangential magnetic fields, where no assumptions are made regarding the relative magnitudes of the refractive indices or the phase shifts that result from reflection or transmission of the incident wave.

6.6 *Additional Boundary Conditions*

Implicit in previous sections is that there is single propagating mode, and hence three fields; E_i, E_r and E_t. It has also been demonstrated that at normal incidence only transverse modes will propagate. In *Section 6.4*, above, the non-classical solution for the transverse wave was derived and it was shown that the inclusion of the β parameter (related to the natural frequency of the exciton and its effective mass) induces spatial dispersion. As shown above in *Fig. 6.3*, spatial dispersion allows two propagating waves for each frequency ω in any given direction in the crystal. Therefore, in the non-classical case, there are four fields to consider; E_i, E_r, E_{TUPB} and E_{TLPB}, where E_{TUPB} is the transverse upper polariton branch and E_{TLPB} is the transverse lower polariton branch.

The spatial dispersion constitutes an additional energy transfer mechanism through the dielectric material and one finds that the classical boundary conditions discussed in *Section 6.5* are not sufficient to solve for the reflectance. One therefore needs additional boundary conditions (ABCs). The simplest ABC is based on the fact that the excitons contributing to the reflectance resonance must be confined to the crystal - an exciton incident on the surface from the crystal-side of the interface must be reflected back into the crystal, i.e. there can be no excitonic polarisation outside the crystal. The cause of this reflection in terms of classical electrodynamics will be examined below, but for now, if we assume the excitons are reflected from the surface it immediately follows that the polarisation due to the presence of excitons must be zero at the interface boundary (known as Pekar's ABC [4]);

$$\boxed{P_{Total} = 0 = P_{UPB}(\omega) + P_{LPB}(\omega)}$$

Eqn. 6.108

We now turn our attention to the classical explanation for the reflection of the exciton from the surface of the crystal by considering the effect of an induced surface charge on an exciton using the theory of image charges [5]. The exciton is considered to consist of a positive and negative charge, separated by a distance *B* which is twice the effective Bohr radius, and located a distance *d* from the interface between media ε_1 and ε_2. The exciton exists in medium ε_1 for which $(z > 0)$ and the interface itself is at $(z = 0)$. To simplify the problem the exciton is set to lie along the *z*-axis and the solutions are therefore one-dimensional (*Figure 6.6*).

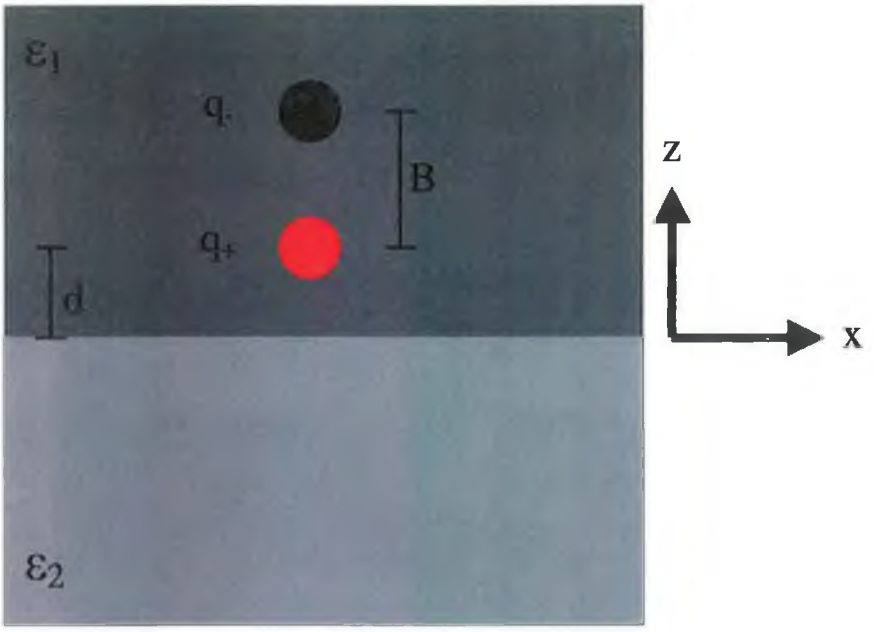

Figure 6.6: *Illustration of an exciton in medium ε_1 where the positive charge is a distance d from the interface with medium ε_2. The interface occurs at $(z = 0)$ and the arrangement of the positive and negative charge is one dimensional for simplicity. The separation between the positive and negative charge is B, equal to twice the Bohr radius of the exciton.*

The presence of the exciton creates an electric field that induces a charge on the interface, or more specifically, the crystal surface. Using the theory of image charges, we can obtain an expression for the force experienced by the exciton from the surface and hence the potential of the exciton at any point within the crystal. The image charge construction is shown in *Figure 6.7.*

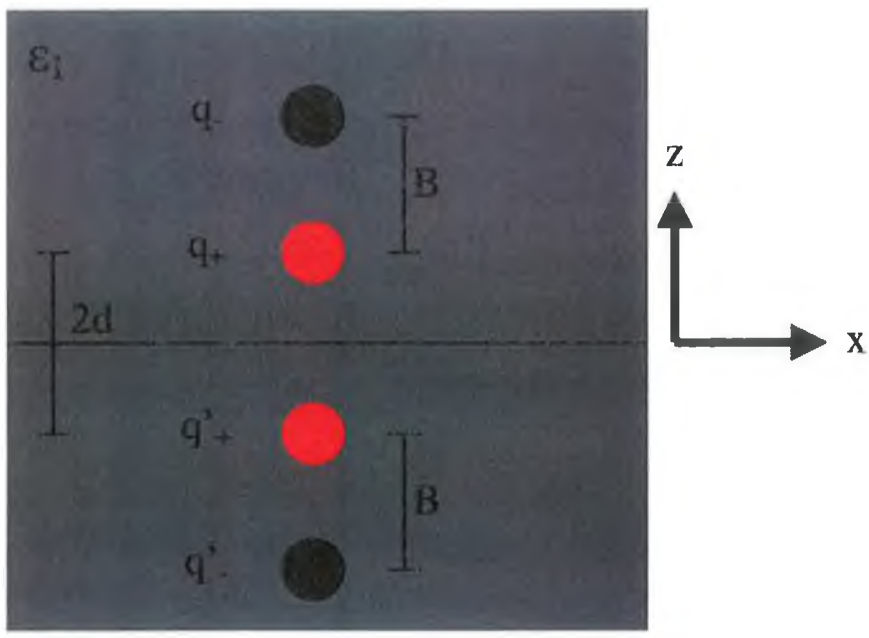

Figure 6.7: *Illustration of the image charge as a result of the interaction of the exciton electric field with the crystal surface. We imagine that the force experienced by the exciton as a result of the surface is equivalent to that force exerted by image charges q'_+ and q'_- located at an equal distance but on the negative side, with respect to the z-axis, of the interface.*

For the moment it will be assumed that each image charge has the *same* sign as the corresponding real charge, but this shall be proven to be the case below. It is now possible to determine the forces on the exciton as a result of the image charges. The relationship between image charge and real charge is;

$$q' = -\left(\frac{\varepsilon_2 - \varepsilon_1}{\varepsilon_2 + \varepsilon_1}\right) q$$

Eqn. 6.109

and this result is given in Ref. [6]. For the moment we shall express this relationship as;

$$q' = Aq$$

Eqn. 6.110

for clarity in the following mathematical derivation.

The repulsive force between the positive real and image charge is given by Coulomb's Law;

$$Rp_+ = \frac{Aq^2}{4\pi\varepsilon_1 (2d)^2}$$

Eqn. 6.111

and for the negative real and image charges is given by;

$$Rp_- = \frac{Aq^2}{4\pi\varepsilon_1 \left[2(d+B)\right]^2}$$

Eqn. 6.112

Consequently, the total repulsive force is obtained;

$$Rp_T = Rp_+ + Rp_- = \frac{Aq^2}{4\pi\varepsilon_1 (2d)^2}\left[1 + \frac{1}{\left(1 + B/d\right)^2}\right]$$

Eqn. 6.113

It is necessary to expand the denominator $\left(1 + B/d\right)^2$ and hence the total repulsive force experienced by the exciton can be re-written as;

$$Rp_T \approx \frac{Aq^2}{4\pi\varepsilon_1 (2d)^2}\left[2 - \frac{2B}{d} + \frac{3B^2}{d^2}\right]$$

Eqn. 6.114

where only the first three terms in the expansion have been taken.

One performs a similar analysis of the attractive forces experienced by the exciton. The magnitude of the attractive force between the positive real and negative image charges is given by;

$$|At_{+}| = \frac{Aq^2}{4\pi\varepsilon_1 (2d+B)^2}$$

Eqn. 6.115

and the magnitude of the attractive force between the negative real and positive image charges is;

$$|At_{-}| = \frac{Aq^2}{4\pi\varepsilon_1 (2d+B)^2}$$

Eqn. 6.116

Hence, the magnitude of the total attractive force is the summation;

$$|At_T| = |At_{+}| + |At_{-}| = \frac{Aq^2}{4\pi\varepsilon_1 (2d)^2}\left[\frac{2}{\left(1+B/2d\right)^2}\right]$$

Eqn. 6.117

As with the repulsive forces it is necessary to expand the denominator and we take the first three terms in the expansion as before;

$$|At_T| \approx \frac{Aq^2}{4\pi\varepsilon_1 (2d)^2}\left[2 - \frac{2B}{d} + \frac{6B^2}{(2d)^2}\right]$$

Eqn. 6.118

The total force on the exciton is then just the summation of the total repulsive force in the positive *z*-direction and the total attractive force in the negative *z*-direction;

$$F_T = Rp_T + \left(-At_T\right) = \frac{Aq^2}{4\pi\varepsilon_1 (2d)^2}\left[\left(2 - \frac{2B}{d} + \frac{3B^2}{d^2}\right) - \left(2 - \frac{2B}{d} + \frac{6B^2}{(2d)^2}\right)\right]$$

Eqn. 6.119

which can be reduced to just;

$$F_T = \frac{3Aq^2B^2}{32\pi\varepsilon_1}\left[\frac{1}{d^4}\right]$$

Eqn. 6.120

Having obtained an expression for the force exerted on the exciton, it is a simple matter to calculate the energy of the exciton as a result of the induced surface charge, at a given distance z from the crystal surface. This energy is, by definition, equivalent to the work done in moving the exciton from an infinite distance to the finite distance z from the surface;

$$W = -\int_{\infty}^{z} F_T \, dd = -\frac{3Aq^2B^2}{32\pi\varepsilon_1}\int_{\infty}^{z} \frac{dd}{d^4}$$

Eqn. 6.121

and result of the integration yields;

$$W = \frac{Aq^2B^2}{32\pi\varepsilon_1}\left(\frac{1}{z^3}\right)$$

Eqn. 6.122

Substituting A with *Eqn. 6.109*, and using the fact that B is twice the effective Bohr radius (R_B) the energy is;

$$W = -\frac{1}{8\pi}\left(\frac{\varepsilon_2 - \varepsilon_1}{\varepsilon_2 + \varepsilon_1}\right)\left[\frac{q^2}{\varepsilon_1 R_B}\right]\left(\frac{R_B}{z}\right)^3$$

Eqn. 6.123

Since the charge q is equivalent to the charge of an electron e, and the Bohr radius (for the ground state) can be expressed as;

$$R_B = \frac{\varepsilon_1 \hbar^2}{m^* e^2}$$

Eqn 6.124

the substitution of *Eqn. 6.124* for R_B enables the parameters in square brackets (*Eqn. 6.123*) to be re-written as;

$$\left[\frac{q^2}{\varepsilon_1 R_B}\right] = \left[\frac{e^2}{\varepsilon_1}\right]\left[\frac{m^* e^2}{\varepsilon_1 \hbar^2}\right] = \frac{m^* e^4}{\varepsilon_1^2 \hbar^2}$$

Eqn. 6.125

where m^* is the effective mass of the exciton. The Rydberg equation gives the exciton binding energy E_B (for the ground state) as;

$$E_B = \frac{m^* e^4}{2\varepsilon_1^2 \hbar^2}$$

Eqn. 6.126

and comparing this equation to *Eqn. 6.125*, the energy of the exciton is therefore;

$$W = -\frac{1}{8\pi}\left(\frac{\varepsilon_2 - \varepsilon_1}{\varepsilon_2 + \varepsilon_1}\right)[2E_B]\left(\frac{R_B}{z}\right)^3$$

Eqn. 6.127

It should be noted that the energy is negative as a consequence of the relationship between charge and image charge (*Eqn. 6.109*);

$$q' = -\left(\frac{\varepsilon_2 - \varepsilon_1}{\varepsilon_2 + \varepsilon_1}\right)q$$

In the case studied herein, we can consider that the medium ε_2 is air (or vacuum) and therefore;

$$q' = -\left(\frac{\varepsilon_0 - \varepsilon_1}{\varepsilon_0 + \varepsilon_1}\right) q$$

Eqn. 6.128

Replacing each permittivity with the relative permittivity, or dielectric constant gives;

$$q' = -\left(\frac{\varepsilon_0 - \varepsilon_1}{\varepsilon_0 + \varepsilon_1}\right)\left(\frac{\varepsilon_0^{-1}}{\varepsilon_0^{-1}}\right) q = -\left(\frac{1 - \varepsilon_r}{1 + \varepsilon_r}\right) q$$

Eqn. 6.129

where ε_r is the dielectric constant of the crystal. It is immediately obvious that if $\varepsilon_r > 1$, which invariably will be true for a semiconductor compared to free space or air, the fraction in parenthesis will be negative due to the numerator. In this case one obtains the expression;

$$q' = \left(\frac{\varepsilon_r - 1}{\varepsilon_r + 1}\right) q$$

Eqn. 6.130

and it can be seen that in this case the image charge has the same sign as the real charge, as assumed above. Finally, using this relationship between charge and image charge, the energy of the exciton at a distance *z* from the crystal surface is given by;

$$\boxed{W = \frac{1}{4\pi}\left(\frac{\varepsilon_r - 1}{\varepsilon_r + 1}\right)[E_B]\left(\frac{R_B}{z}\right)^3}$$

Eqn. 6.131

Thus one finds that as $z \to 0$ the energy $W \to \infty$ and the exciton not only experiences a repulsive force as it approaches the crystal surface, but can never actually reach the surface itself! The classical turning point for the reflection should therefore occur at a finite distance within the crystal and one can consider that the polarisation due to the excitons becomes zero at this particular distance, rather than simply at the

surface itself as assumed for *Eqn. 6.108* above. The approximation made by *Hopfield* and *Thomas* [1] is that there exists an infinite potential barrier a distance L_0 from the surface through which the excitons are unable to penetrate and are reflected from. These concepts are illustrated in *Figure 6.8*.

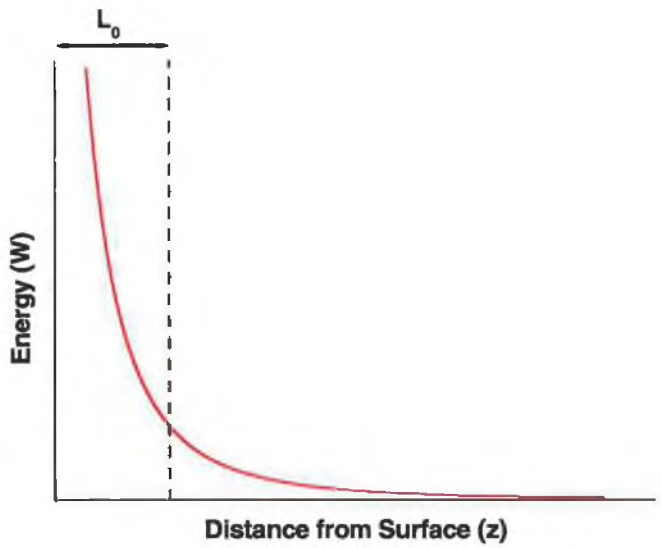

Figure 6.8: *Plot of exciton energy versus distance from the surface. The red line is a plot of Eqn. 6.131 and it can be seen that an infinite amount of energy is required to move an exciton to the surface. Correspondingly, the exciton will be reflected at a finite distance inside the crystal as a result of the repulsive force from the surface. To model this behaviour, one can consider that there exists an infinite potential barrier at a finite distance L_0 from the crystal surface (dashed line). The region $(0 < z < L_0)$ is known as the exciton 'dead-layer' since excitons cannot penetrate into this region and the boundary conditions one applies at the interface between dead-layer and air $(z = 0)$ are classical. At the interface between dead-layer and crystal $(z = L_0)$ one applies classical boundary conditions and the additional condition that the polarisation must be zero at this point.*

From the perspective of modelling one can consider a simplistic model in which the additional boundary condition is just;

$$\boxed{P_{Total} = P_{UPB}(\omega) + P_{LPB}(\omega) = 0}, \qquad (z = 0)$$

Eqn. 6.132

and that the polarisation is zero at the crystal surface. In other words, one applies this boundary condition at the interface between air and the crystal. Alternatively, based on *Eqn. 6.131* and the infinite-barrier approximation of *Hopfield* and *Thomas*, a more accurate modelling would require that the polarisation reaches zero at some finite distance L_0 inside the crystal and that an exciton 'dead-layer' exists in the region $(0 < z < L_0)$. With the inclusion of a dead-layer, classical boundary conditions will apply for the interface between air and the dead-layer at $(z = 0)$, and classical conditions and the additional requirement that the polarisation be zero will apply at the interface between dead-layer and crystal $(z = L_0)$. Classically, since the exciton can be considered to have a diameter of twice the effective Bohr radius, a reasonable assumption is that L_0 should also be equal to about twice the effective Bohr radius and this provides an order of magnitude check on the fitted solution. The additional boundary condition used is one of the simplest of a wide range in common use. The differences between various ABCs is slight in most cases, and our choice has the benefit of immediate physical plausibility.

6.7 *References*

[1] J. J. Hopfield and D. G. Thomas, *Phys. Rev.* **132** (1963) 563

[2] C. Kittel in *Introduction to Solid State Physics*, 7th edn. (John Wiley & Sons, Inc., 1996), chapter 13, p. 391

[3] E. Hecht in *Optics*, 4th edn. (Addison Wesley, 2002), chapter 4, p. 113

[4] S. I. Pekar, Zh. Eksp. Teor. Fiz. **33** (1957) 1022 [Sov. Phys.-JETP **6** (1958) 785] S.I. Pekar, J. Phys. Chem. Solids **5** (1958) 11

[5] D. J. Griffiths in *Introduction to Electrodynamics*, 3rd edn. (Prentice-Hall, 1981), chapter 3, p. 121

[6] J. D. Jackson in *Classical Electrodynamics*, 3rd edn. (John Wiley and Sons, 1998), chapter 4, p. 154

Chapter 7

Modelling of Reflectance Spectra

7.1 Introduction

Having examined the theory of the contribution of excitonic resonances to the dielectric constant of a material, and the resultant expressions describing the longitudinal and transverse solutions of Maxwell's equations, we now turn our attention to the use of this theory to model reflectance spectra from both bulk and thin film ZnO samples.

Before the modelling can proceed it is necessary to examine the structure of these samples and experimentally obtain reflectance spectra at normal incidence. The boundary conditions that will be applied must take this structure into account, and the samples themselves are discussed in *Section 7.2* along with the experimental set-up required for normal incidence.

In *Section 7.3* the equations of *Chapter 6* are modified slightly to allow dispersion curves including both *A* and *B* free-exciton resonances to be calculated. On the basis of these curves, the boundary conditions are applied across each interface and the amplitude reflection coefficient (and hence the reflectivity) can be determined (*Sections 7.4* and *7.5*).

A comparison between the reflectance spectra produced by the models and the experimentally obtained data is given in *Section 7.6*, along with the values for the fitting parameters.

7.2 *Experimental Details and the Nature of Samples*

It has been shown in *Chapter 6* that the exciton resonance causes upper and lower transverse branches, and the modelling will concentrate on obtaining parameters for the non-classical transverse solution of Maxwell's equations. At non-normal angles of incidence the boundary conditions required are considerably more complicated and the observed reflectance spectra are the result of a mixing of longitudinal and transverse modes. To simplify the analysis, reflectance spectra presented in this chapter were experimentally obtained at near-normal incidence. Under this condition only transverse modes are present in the crystal and the boundary conditions reduce to a one-dimensional scalar system of simultaneous equations.

With regard to experimentally obtaining reflectance spectra that can be accurately modelled, it is necessary to ensure that there are a minimum number of additional optical components between the sample and the spectrometer. This eliminates possible phase shifts that may distort the reflectance characteristics as a result of light travelling through focusing optics. Since it is the overall structure of the resonance features that are of interest, a higher resolution scan is also required compared to the data presented in previous chapters, despite the fact that the intensity of light will actually drop as a result of the removal of focusing lenses. For the experimental spectra presented in this chapter the FT spectrometer took the average of 1200 scans of each sample at a resolution of ~ 0.1 meV, compared to ~ 400 – 800 scans at a ~ 0.5 meV resolution for the previous data.

Figure 7.1 is an illustration of the experimental arrangement for obtaining reflectance spectra at near-normal incidence. Based on measurements of the positions of

the mirror used to bring white light onto the sample, the sample within the cryostat, and the parabolic mirror that brings light into the spectrometer, simple trigonometric calculations indicate that the angle of incidence used was less than 7°. As with the reflectance spectra shown in previous chapters, a reference sample was used to normalise the intensity.

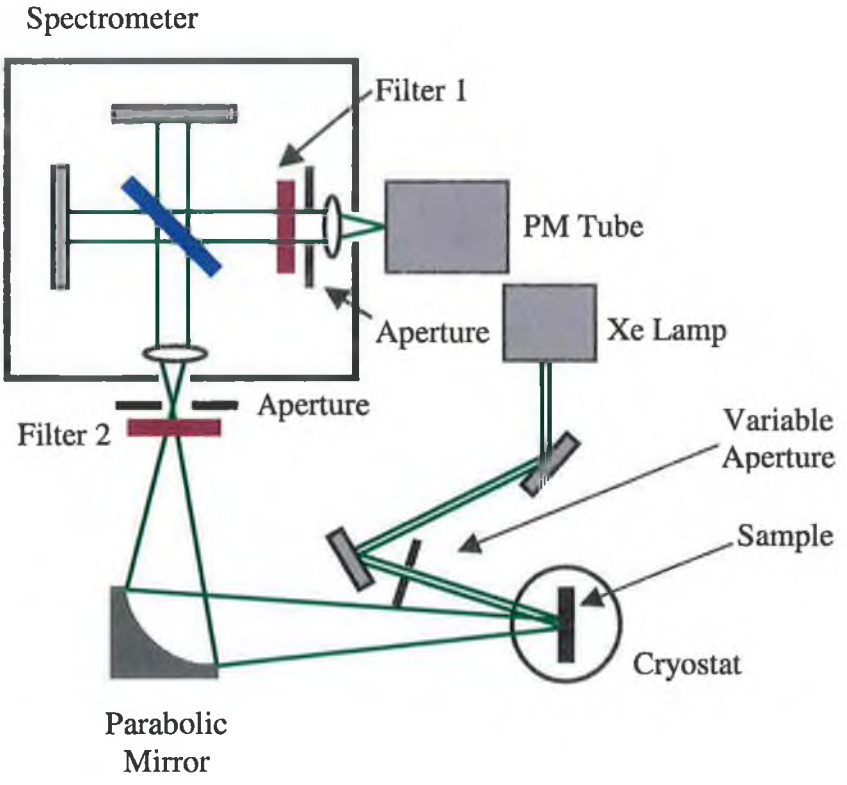

Figure 7.1: *Illustration of the experimental arrangement used to obtain reflectance spectra at near-normal angles of incidence. The actual angle of incidence was calculated to be < 7° based on distances from reflecting optics to the centre of the cryostat. The filters used in this arrangement are identical to those described in Chapter 2 for reflectance at a ~ 45° angle of incidence, with two BG25 Schott-glass short-pass filters placed at the spectrometer entrance aperture and before the PM tube. The short focal-length lens used in non-normal incidence is removed in this arrangement to prevent the possibility of introducing phase shifts in light passing through the optical component. Although this reduces the intensity of light falling on the detector, one partly compensates by increasing the number of scans.*

The reflectance spectrum obtained from each of two samples was modelled – ZnO thin film layers grown on a sapphire substrate using the Pulsed Laser Deposition (PLD) technique, and a bulk Eagle-Picher wafer grown using the seeded physical-vapour transport (SVPT) method. For the PLD samples a ceramic polycrystalline ZnO target (99.99% purity) was ablated using a KrF excimer laser (λ = 248 nm) with an energy density of 1.7 J/cm^2 at a pulse repetition rate of 10 Hz and pulse width of 26 ns. The target to substrate distance was ~ 4 cm and the ZnO films were deposited on (0001) sapphire substrates at an oxygen (99.99% purity) pressure of 0.3 mbar (225 mTorr). During the growth process the substrate temperature was maintained at 400°C, and the films were subsequently annealed in the chamber at temperatures of 400 or 500°C (*Table 7.1*) immediately after deposition. The annealing also took place in the O_2 environment (0.3 mbar). The PLD material was grown by *J. G. Lunney*, *D. O'Mahony* and *E. dePodesta* at the Physics Department of Trinity College, Dublin (Ireland).

Table 7.1: *Annealing parameters of polycrystalline samples grown using PLD*

Sample	***Annealing Temperature (°C)***	***Annealing Duration (mins)***
(a)	No anneal	0
(b)	400	10
(c)	500	15

These polycrystalline ZnO films have been extensively studied, although the exact nature of these experiments are beyond the scope of this dissertation. However, the film thickness has been measured to be in the 150-200 nm region for all samples and the grain structure is columnar with *c*-axis orientation [1]. It should be noted that the veracity of the modelling technique presented herein is partially demonstrated by its success in determining this film thickness. Raman and AFM measurements have shown

that the unannealed sample has the smallest grain size and the largest surface roughness (a standard deviation of ~ 10 nm), and that the grain size increases and surface roughness decreases (to ~ 3 nm) with increasing annealing temperature/duration.

Figure 7.2 shows the experimental reflectance spectra from each polycrystalline sample at a temperature of 17 K. The reflectance characteristics improve in terms of both the intensity of light and strength of excitonic resonances with increasing grain size, due to a reduction in both surface roughness and the electric fields caused by charge trapping at grain boundaries. For the purposes of modelling, only *Sample (c)* shall be examined (annealed for 15 minutes at 500°C) since the spectrum of this material provides the greatest signal-to-noise ratio.

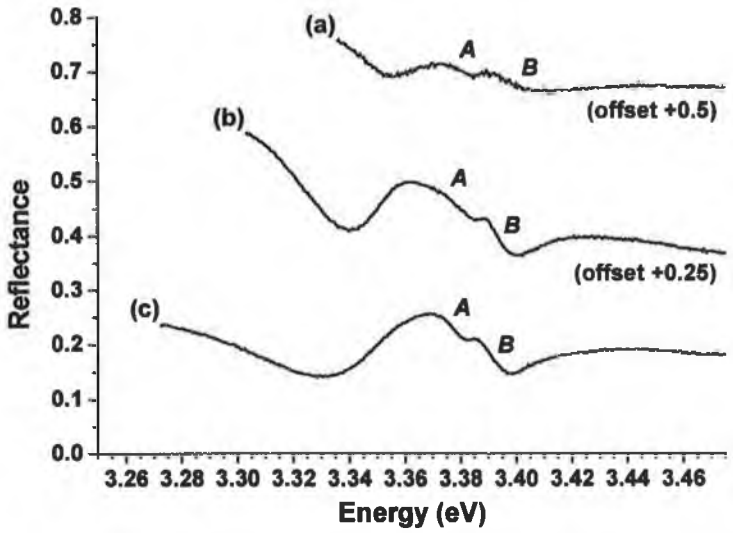

Figure 7.2: *Reflectance spectra (17 K) of (a) unannealed; (b) annealed 400°C, 10 minutes; (c) annealed 500°C, 15 minutes PLD polycrystalline thin-film ZnO samples. In each case one observes both A and B free-exciton resonances which improve in strength with increasing annealing temperature/duration.*

The reflectance from the Eagle-Picher bulk (0001)-oriented wafer is shown in *Figure 7.3*, again at a temperature of 17 K. This data shall also be modelled and used as a reference for the polycrystalline material. Thus, one observes resonances corresponding to the *A* and *B* free-exciton bands in both the PLD *Sample (c)* and in the bulk Eagle-Picher wafer. One must slightly alter the equations of *Chapter 6* in order to take account of both these resonant mechanisms and, in the next section, we shall look at how these changes are accomplished along with the method of determining rough estimates of various fitting parameters.

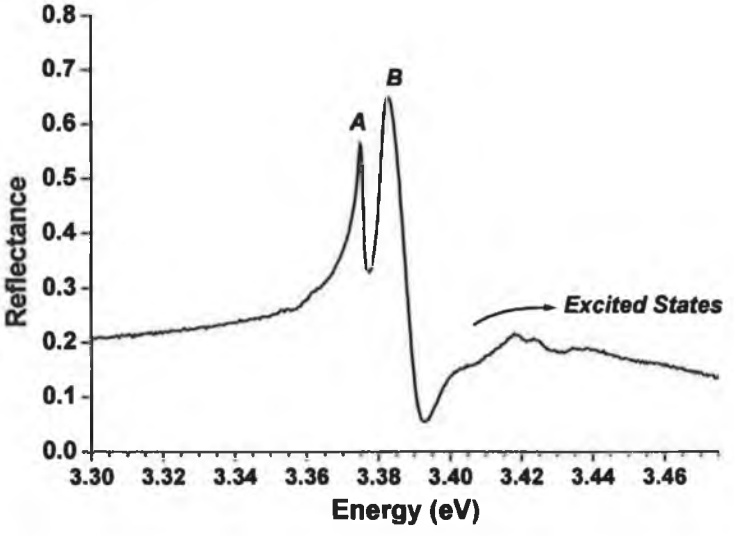

Figure 7.3: *Reflectance spectrum at near-normal incidence (17 K) of the bulk Eagle-Picher SVPT ZnO wafer (O-terminated surface). As with the PLD material one observes clear evidence of both A and B free-exciton resonances. The slight oscillations between ~ 3.40 and 3.44 eV are the excited states of the A and B free-excitons.*

7.3 *Modelling Reflectance Spectra – Obtaining the Dispersion Curve*

The previous discussion has shown that the reflectance spectra of ZnO material generally exhibits two resonances, corresponding to excitons where the electron has been excited from either the *A* or *B* valence bands. In the derivation of *Chapter 6* an expression for the transverse solution of Maxwell's equations in terms of the polarisability due to excitons was obtained. This mathematical relationship for the non-classical case above is;

$$\frac{k^2c^2}{\omega^2} = \varepsilon_\infty + \frac{1}{\varepsilon_0}\left(\frac{\alpha_0\omega_0{}^2}{\omega_0{}^2 + \beta k^2 - \omega^2 - i\omega\Gamma}\right)$$

and clearly only describes the contribution of a single resonant mechanism to the polarisability/dielectric constant of the material, where the background dielectric constant ε_∞ was introduced to represent the contributions from other oscillations. To include both *A* and *B* excitonic resonators, one can simply sum their polarisabilities;

$$\frac{k^2c^2}{\omega^2} = \varepsilon_\infty + \frac{\alpha_{A0}}{\varepsilon_0}\left(\frac{\omega_{AT}{}^2}{\omega_{AT}{}^2 + \beta_A k^2 - \omega^2 - i\omega\Gamma_A}\right) + \frac{\alpha_{B0}}{\varepsilon_0}\left(\frac{\omega_{BT}{}^2}{\omega_{BT}{}^2 + \beta_B k^2 - \omega^2 - i\omega\Gamma_B}\right)$$

Eqn. 7.1

by virtue of *Eqn. 6.50*;

$$\alpha(k,\omega) = \sum_j \frac{\alpha(k,0)\omega_j{}^2(k)}{\omega_j{}^2(k) - \omega^2 - i\omega\Gamma}, \qquad \text{with } j = A, B$$

Regarding *Eqn. 7.1*, α_{A0} is the static polarisability for the *A* exciton, α_{B0} is the static polarisability for the *B* exciton, ω_{AT} and ω_{BT} are the transverse frequencies of the *A* and *B* excitons respectively, and Γ_A and Γ_B are the damping coefficients. In each case the parameters refer to the transverse modes since only these propagate at normal angles of incidence. The value of the β parameter will be different for *A* and *B* excitons

because this is related to both the transverse frequency and effective mass of the exciton.

To simplify the following discussion and reduce the notation, *Eqn. 7.1* shall be expressed as;

$$Ak^2 = \varepsilon_\infty + \frac{B}{C + \beta_A k^2} + \frac{D}{E + \beta_B k^2}$$

Eqn. 7.2

where we have set;

$$A = \frac{c^2}{\omega^2}$$

$$B = \frac{\alpha_{A0}}{\varepsilon_0}\omega_{AT}{}^2$$

$$C = \frac{\varepsilon_0 B}{\alpha_{A0}} - \omega^2 - i\omega\Gamma_A$$

$$D = \frac{\alpha_{B0}}{\varepsilon_0}\omega_{BT}{}^2$$

$$E = \frac{\varepsilon_0 D}{\alpha_{B0}} - \omega^2 - i\omega\Gamma_B$$

Eqns. 7.3

Multiplying by the denominators on the RHS, *Eqn. 7.2* becomes;

$$Ak^2\left(C + \beta_A k^2\right)\left(E + \beta_B k^2\right) = \varepsilon_\infty\left(C + \beta_A k^2\right)\left(E + \beta_B k^2\right) + B\left(E + \beta_B k^2\right) + D\left(C + \beta_A k^2\right)$$

Eqn. 7.4

and, after multiplying out the bracketed parameters and collecting terms, one obtains the expression;

$$\left(A\beta_A\beta_B\right)k^6 + \left(AC\beta_B + AE\beta_A - \varepsilon_\infty\beta_A\beta_B\right)k^4 + \left(ACE - \varepsilon_\infty C\beta_B - \varepsilon_\infty E\beta_A - B\beta - D\beta\right)k^2 - \left(\varepsilon_\infty CE + BE + DC\right) = 0$$

Eqn. 7.5

To summarise the progression then, in the classical case discussed in the previous chapter, where the β term and hence spatial dispersion were ignored, the solution of the transverse equation is quadratic in k for a single oscillator. When spatial dispersion is included, one obtains the non-classical transverse equation which is quadratic in k^2. In the above discussion, where we have now included two coupled oscillators, the transverse equation becomes cubic in k^2, as in *Eqn. 7.5*.

Figure 7.4 is a plot of *Eqn. 7.5* for the real, positive wave-vectors k as a function of frequency ω, where arbitrary values of each parameter (*Eqns. 7.3*) have been chosen. Since the expression is cubic in k^2 one finds that for each frequency there are six possible wave-vectors but, similar to the classical and non-classical cases involving a single resonant mechanism, this total of six actually corresponds to just two sets of three solutions that are symmetric, positive and negative, around $k = 0$. At frequencies in *Fig. 7.4* where there appears to be only a single solution for positive wave-vectors, the other solutions are imaginary (i.e. evanescent solutions) and hence are not shown in this graph, though they must be included in reflectance calculations.

Although the two sets of symmetric solutions are mathematically equivalent, since they correspond to identical waves moving in opposite directions, physically one would not expect both sets of waves to propagate in the crystal due to the directionality imposed by the reflectance set-up. Experimentally, one shines light at a near-normal incidence onto the sample surface and the transmitted waves will propagate in the same direction as the incident light (i.e. the wave-vectors of incident and transmitted radiation will point in the same direction). *Therefore to model the reflectance spectra one need consider only the three propagating modes in this given direction, rather than the complete set of six that are mathematical solutions of Eqn. 7.5.*

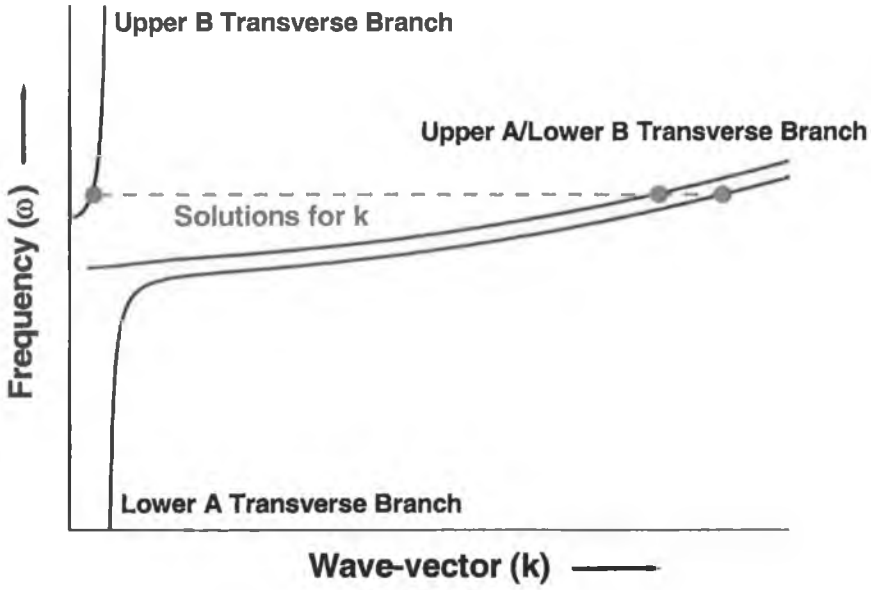

Figure 7.4: *Dispersion curve for positive, real wave-vectors including both A and B free-exciton oscillators (Eqn. 7.5). At each frequency ω there exists six wave-vectors although for each positive wave-vector there exists a symmetric negative wave-vector. Since these negative wave-vectors simply refer to waves travelling in the opposite direction they are equivalent to the positive case. Although at some frequencies there appears to be only a single solution for positive wave-vectors (for example, at low frequencies) the other two solutions will be imaginary. Since the A and B oscillators are coupled, one observes a mixing of the upper A and lower B transverse branches.*

The first step in the actual modelling of reflectance spectra is to obtain the complex dispersion curve, by solving *Eqn. 7.5*, which will appear similar to *Fig. 7.4* for real wave-vectors. From an experimentally obtained reflectance spectrum one can quickly determine the frequency region in which the *A* and *B* free-exciton resonances occur. Values are chosen for ε_∞, α_{A0}, α_{B0}, ω_{AT}, ω_{BT}, β_A, β_B, Γ_A and Γ_B in *Eqn. 7.1*/*7.5* and, taking upper and lower limits for the frequency based on the experimental data, this cubic equation is solved for k^2 at each frequency ω within these limits.

Though there are a total of nine unknown parameters one may deduce rough initial values for the majority of these. The background dielectric constant ε_∞ is calculated by looking at the experimental reflectance at frequency regions far removed from the excitonic resonances. In such frequency regimes the transverse solution to Maxwell's equations reduces to;

$$\frac{k^2c^2}{\omega^2} = \varepsilon_\infty$$

Eqn. 7.6

or, using the refractive index *n*;

$$n = \sqrt{\varepsilon_\infty}$$

Eqn. 7.7

The reflectance *R* is given by (*Eqn. 6.105*);

$$R = \left(\frac{n - n_i}{n + n_i}\right)^2$$

Eqn. 7.8

and since the refractive index n_i of the incident medium (presumed to be air/vacuum) is equal to one, the refractive index and hence the background dielectric constant can be determined by;

$$n = \sqrt{\varepsilon_\infty} = -\left(\frac{1+\sqrt{R}}{1-\sqrt{R}}\right)$$

Eqn. 7.9

If one examines the classical dispersion curve for a single oscillator (where the damping term was ignored and $\beta = 0$, as shown in *Fig. 6.1*) it is clear that the transverse frequency ω_0 lies at a lower frequency, and hence energy, than the longitudinal frequency ω_L. It is therefore possible to make a good estimate of the

transverse frequencies ω_{AT} and ω_{BT}, and the longitudinal frequencies ω_{AL} and ω_{BL} of the *A* and *B* free-excitons from the experimental reflectance spectrum. *Figure 7.5* is an enlargement of *Fig. 7.3* showing both *A* and *B* resonances for the bulk wafer, which manifest as a sudden increase in reflectance at low energy followed by a decrease at higher energy. The transverse energy for the excitons must therefore occur somewhere near the respective low-energy reflectance maxima of the resonances and similarly, the longitudinal energies lie close to the minima. Although the energy and hence frequency can not be determined directly from the experimental data, one can certainly impose limits for these parameters.

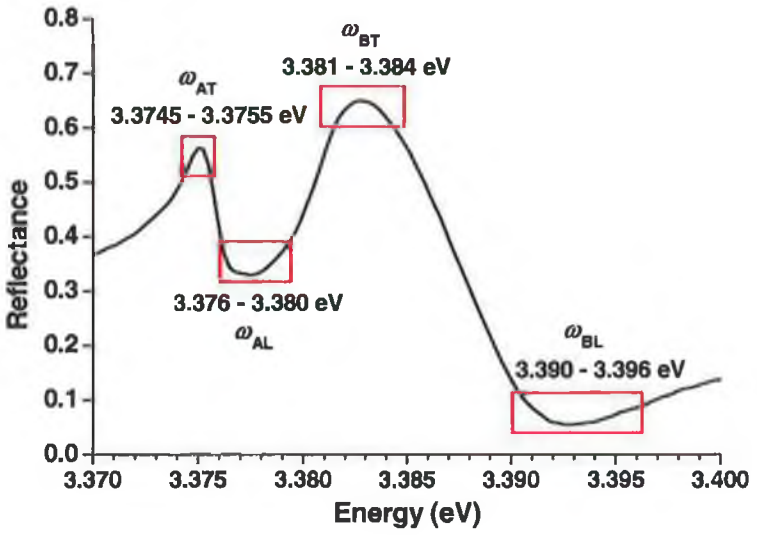

Figure 7.5: *Enlargement of an energy region of the reflectance spectrum obtained from the Eagle-Picher bulk wafer (Fig. 7.3). Since the dispersion curve (Fig. 6.1) indicates that the transverse natural frequency is slightly lower than the longitudinal frequency, one can conclude that the reflectance maxima (which are located at lower energy with respect to the minima of the resonance and indicated by the boxes) must roughly correspond with the transverse exciton energies. This allows an estimate of the transverse natural frequency of both A and B free-excitons and therefore initial values for the fitting parameters* ω_{AT} *and* ω_{BT}. *Similarly, the minima allow a rough estimate of the longitudinal frequencies* ω_{AL} *and* ω_{BL}.

From *Eqn. 6.61*, the longitudinal solution to Maxwell's equations is;

$$\varepsilon_\infty + \frac{1}{\varepsilon_0}\left(\frac{\alpha_{A0}\omega_{AT}{}^2}{\omega_{AT}{}^2 + \beta_A k^2 - \omega^2 - i\omega\Gamma_A}\right) + \frac{1}{\varepsilon_0}\left(\frac{\alpha_{B0}\omega_{BT}{}^2}{\omega_0{}^2 + \beta_B k^2 - \omega^2 - i\omega\Gamma_B}\right) = 0$$

Eqn. 7.10

where both *A* and *B* excitonic resonators have been included, as with the transverse solution above. At this stage it is worth recalling the derivation of *Chapter 6* where it was shown that, since the frequency, velocity in free space, and electric field intensity are non-zero, the dielectric constant must be zero to satisfy the longitudinal equation (*Eqn. 6.60*), hence the value of zero on the RHS of *Eqn. 7.10*. The frequency ω which satisfied this condition for a single mechanism was subsequently defined as the longitudinal frequency.

In *Eqn. 7.10*, which includes the coupled *A* and *B* excitons, one finds that there are two frequencies at which the dielectric constant becomes zero corresponding to the longitudinal frequencies of both *A* and *B* excitons, ω_{AL} and ω_{BL} respectively. In other words ω_{AL} and ω_{BL} are the solutions for ω that satisfy *Eqn. 7.10*, and this expression can be re-written as [2];

$$\varepsilon_\infty\left(1 + \frac{\omega_{BL}{}^2 - \omega_{AT}{}^2}{\omega_{BT}{}^2 - \omega_{AT}{}^2}\,\frac{\omega_{AL}{}^2 - \omega_{AT}{}^2}{\omega_{AT}{}^2 - \omega^2 + \beta_A k^2 - i\omega\Gamma_A} + \frac{\omega_{AL}{}^2 - \omega_{BT}{}^2}{\omega_{AT}{}^2 - \omega_{BT}{}^2}\,\frac{\omega_{BL}{}^2 - \omega_{BT}{}^2}{\omega_{BT}{}^2 - \omega^2 + \beta_B k^2 - i\omega\Gamma_B}\right) = \varepsilon(\omega, k)$$

Eqn. 7.11

where $\varepsilon(\omega,k) = 0$ when $\omega = \omega_{AL}$ or $\omega = \omega_{BL}$. Comparing *Eqns. 7.10* and *7.11* it follows that;

$$\alpha_{A0} = \varepsilon_\infty\left(\frac{\varepsilon_0}{\omega_{AT}{}^2}\right)\left(\omega_{BL}{}^2 - \omega_{AT}{}^2\right)\left(\frac{\omega_{AL}{}^2 - \omega_{AT}{}^2}{\omega_{BT}{}^2 - \omega_{AT}{}^2}\right)$$

Eqn. 7.12

and;

$$\alpha_{B0} = \varepsilon_{\infty}\left(\frac{\varepsilon_0}{\omega_{BT}^{\ 2}}\right)\left(\omega_{AL}^{\ 2} - \omega_{BT}^{\ 2}\right)\left(\frac{\omega_{BL}^{\ 2} - \omega_{BT}^{\ 2}}{\omega_{AT}^{\ 2} - \omega_{BT}^{\ 2}}\right)$$

Eqn. 7.13

Since the longitudinal and transverse frequencies can be estimated from the experimental reflectance spectra, the static polarisabilities can subsequently be determined.

Using initial values for each of the fitting parameters, one must calculate the reflectance for each frequency between the limits imposed through examination of the experimental spectra. The reflectance can be determined by applying appropriate boundary conditions and solving the resultant set of simultaneous equations at each frequency. However, before examining the boundary conditions themselves in the next sections, we must calculate values for a number of additional variables.

The dispersion curve implies that for any given direction in the crystal one has three propagating waves each with a different wave-vector. These vectors shall be labelled k_1, k_2 and k_3 at any given frequency. The refractive index of the crystal for each wave, at frequency ω, will therefore be;

$$n_1 = \frac{k_1 c}{\omega}$$

$$n_2 = \frac{k_2 c}{\omega}$$

$$n_3 = \frac{k_3 c}{\omega}$$

Eqns. 7.14

In applying the boundary conditions one must therefore take the different refractive indices for each propagating wave, at each frequency, into account. The additional boundary condition states that the polarisation drops to zero at some boundary (either at the dead-layer or crystal surface depending on the model used). It is also necessary to calculate the polarisability at each frequency ω of the *A* and *B* free-excitons using the equation (*Eqn. 6.51*);

$$\alpha(k,\omega)=\varepsilon_0(\varepsilon_\infty-1)+\frac{\alpha_0{\omega_0}^2}{{\omega_0}^2+\beta k^2-\omega^2-i\omega\Gamma}$$

Since there are three waves, with wave-vectors k_{1-3}, the polarisabilities of the *A* exciton for each of the wave-vectors at a given frequency are;

$$\alpha_A(k_1,\omega)=\varepsilon_0(\varepsilon_\infty-1)+\frac{\alpha_{0A}{\omega_{AT}}^2}{{\omega_{AT}}^2+\beta{k_1}^2-\omega^2-i\omega\Gamma}$$

$$\alpha_A(k_2,\omega)=\varepsilon_0(\varepsilon_\infty-1)+\frac{\alpha_{0A}{\omega_{AT}}^2}{{\omega_{AT}}^2+\beta{k_2}^2-\omega^2-i\omega\Gamma}$$

$$\alpha_A(k_3,\omega)=\varepsilon_0(\varepsilon_\infty-1)+\frac{\alpha_{0A}{\omega_{AT}}^2}{{\omega_{AT}}^2+\beta{k_3}^2-\omega^2-i\omega\Gamma}$$

Eqns. 7.15

and;

$$\alpha_B(k_1,\omega)=\varepsilon_0(\varepsilon_\infty-1)+\frac{\alpha_{0B}{\omega_{BT}}^2}{{\omega_{BT}}^2+\beta{k_1}^2-\omega^2-i\omega\Gamma}$$

$$\alpha_B(k_2,\omega)=\varepsilon_0(\varepsilon_\infty-1)+\frac{\alpha_{0B}{\omega_{BT}}^2}{{\omega_{BT}}^2+\beta{k_2}^2-\omega^2-i\omega\Gamma}$$

$$\alpha_B(k_3,\omega)=\varepsilon_0(\varepsilon_\infty-1)+\frac{\alpha_{0B}{\omega_{BT}}^2}{{\omega_{BT}}^2+\beta{k_3}^2-\omega^2-i\omega\Gamma}$$

Eqns. 7.16

for the *B* excitons.

To conclude this section, the following is a procedural list of each step in the modelling process. The program was written in MATLAB [3] and is reproduced in *Appendix II.* Although the program presented is a version used to model the thin film PLD ZnO sample, the only difference between this and the other programs used are the boundary conditions, which appear as a matrix in the software.

7.3.1 Procedural List for Modelling Reflectance

1. Pick initial values for parameters in *Eqn. 7.5*
2. Set frequency limits for modelling between ω_{START} and ω_{END}
3. Set $\omega = \omega_{START}$
4. Solve *Eqn. 7.5* for k at frequency ω
5. Determine refractive indices and polarisabilities at frequency ω
6. Solve boundary conditions and obtain the reflectance at frequency ω
7. Increase frequency ω and loop back to Step 4 until $\omega = \omega_{END}$
8. Convert modelled reflectance data from frequency to energy
9. Compare modelled reflectance and experimental reflectance residuals
10. Adjust fitting parameters and loop back to Step 2 until residuals close to 1

7.4 *Models of the PLD Sample without Exciton Dead-Layer*

7.4.1 *Model 1 - PLD Sample including the Thin Film nature*

Figure 7.6 is an illustration of the first model used to examine excitonic resonances in the thin film PLD *Sample (c)*. In this case one assumes no dead-layer and the material consists therefore of only air-ZnO and ZnO-sapphire interfaces. We consider the incident (E_I) and reflected (E_R) electric fields on the air-ZnO boundary, and assign the air a refractive index of (n_0). The electric field transmitted into the ZnO thin film can be broken into three components (E_1), (E_2) and (E_3) representing each solution for $k>0$ of the two-band oscillator model described in *Section 7.3*. Since spatial dispersion occurs, the refractive index of the ZnO layer is not equivalent for each wave and hence one introduces the refractive indices (n_1), (n_2) and (n_3) for (E_1), (E_2) and (E_3) respectively.

At the ZnO-sapphire interface, one assumes that each of the waves (E_1), (E_2) and (E_3) will be reflected. Thus (E_4) is the reflected component of (E_1), (E_5) the reflected component of (E_2), and (E_6) the reflected component of (E_3). The refractive indices for waves (E_4), (E_5) and (E_6) will also be (n_1), (n_2) and (n_3) respectively. Finally, (E_T) is the transmitted wave into sapphire where the refractive index is (n_S) and we neglect reflection from the rough, rear sapphire surface. One now applies both the classical and non-classical boundary conditions, where the thickness of the ZnO thin-film layer is *L*. In *Fig. 7.6*, below, it should be noted that the black arrows represent

the direction of propagation of each wave or, in other words, the direction of the wave-vector and not the presumed direction of the electric fields.

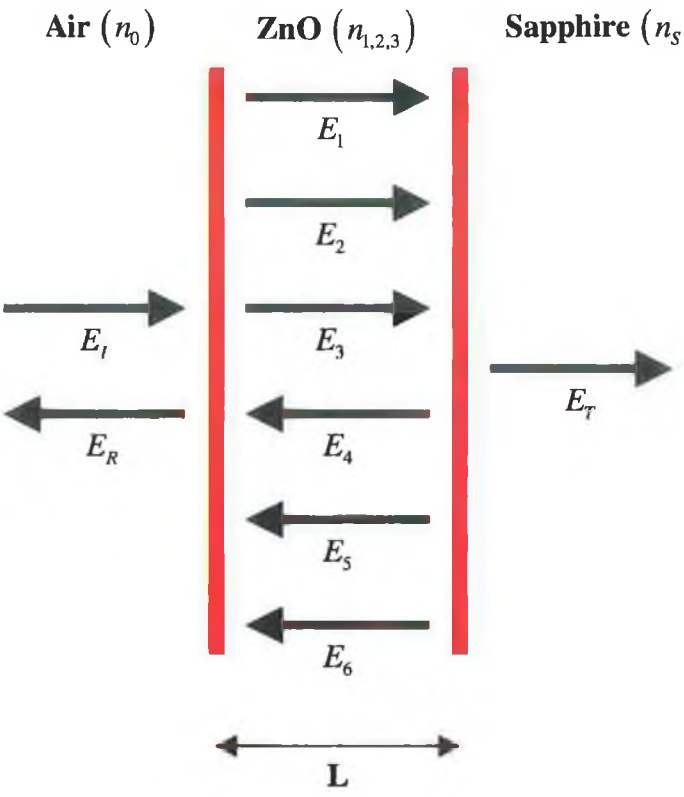

Figure 7.6: *Illustration of the first model used to examine reflectance from the thin film PLD sample. Ignoring the effects of the exciton dead-layer, one need consider only the air-ZnO and ZnO-sapphire interfaces. The three waves in ZnO travelling left-to-right represent the three solutions of the two-band oscillator model incorporating resonances from the A and B free-excitons. It should be noted that the direction of each arrow represents the direction of the wave-vector of the wave, not the direction of the electric field.*

7.4.2 Model 1 - Classical Boundary Conditions At Air-ZnO Interface

From the previous chapter, the classical boundary conditions used for normal incidence are;

$$E_i + E_r = E_t$$

for the electric fields across the boundary, and;

$$n_i E_i - n_i E_r = n_t E_t$$

for the magnetic fields across the boundary where the subscript *i*, *r* and *t* notation refers to the incidence, reflected and transmitted waves. Based on the sign convention of the above conditions, one applies these to the PLD model shown in *Fig. 7.6*. The sum of the electric fields on the air-side of the air-ZnO interface must be equal to the sum of the electric fields on the ZnO-side;

$$E_I + E_R = E_1 + E_2 + E_3 + E_4 + E_5 + E_6$$

Eqn. 7.17

where the positive value for each is due to the assumption that the electric field of each wave points in the same direction regardless of the actual direction of the wave (i.e. that the electric field direction is independent of the wave-vector *k*). Although the waves (E_4), (E_5) and (E_6) are reflected waves from the ZnO-sapphire interface, we will also assume that they can travel through the crystal to the air-ZnO boundary.

If each electric field is considered to point in the same direction, then it is immediately obvious that the direction of the magnetic fields depends on the wave-vector. This leads to the boundary condition;

$$n_0 E_I - n_0 E_R = n_1 E_1 + n_2 E_2 + n_3 E_3 - n_1 E_4 - n_2 E_5 - n_3 E_6$$

Eqn. 7.18

for the magnetic fields at the air-ZnO interface, where the magnetic fields of (E_I), (E_1), (E_2) and (E_3) (with wave-vectors pointing left-to-right in *Fig. 7.6*) are deemed to lie in the opposite direction to the magnetic fields of (E_R), (E_4), (E_5) and (E_6) (with wave-vectors pointing right-to-left).

7.4.3 Model 1 - Classical Boundary Conditions At ZnO-Sapphire Interface

In taking the boundary conditions at the air-ZnO interface it will be noticed that the expressions have not included any reference to possible phase shifts. For the waves (E_I), (E_R) and (E_T) one need not consider their phase explicitly since they encounter only a single interface. This does *not* imply that they are necessarily in phase with one another since the solutions for (E_I), (E_R) or (E_T) will, in general, be complex. Waves (E_{1-6}), on the other hand, encounter two interfaces – the air-ZnO boundary and the ZnO-sapphire boundary.

Thus, in obtaining the simultaneous equation set we find that for the air-ZnO interface one obtains classical boundary conditions that include (E_I) and (E_R), but *not* (E_T). Conversely, for the ZnO-sapphire interface it will be shown that one obtains boundary conditions that include (E_T), but *not* (E_I) and (E_R). The waves (E_{1-6}) will appear in the boundary condition equations at *both* interfaces. Therefore, for waves (E_{1-6}), one must explicitly include the difference in phase from one interface to the other if the equation set is to be consistent.

It will be assumed that the waves travelling left-to-right in the ZnO layer will have an additional *positive* phase on reaching the ZnO-sapphire boundary. It follows that the waves (E_4), (E_5) and (E_6) must then have an additional *negative* phase, relative to the air-ZnO interface, since they travel right-to-left. This phase ϕ of waves reaching the ZnO-sapphire interface, where the thickness of the ZnO layer is L, can simply be expressed as;

$$\phi = \frac{2\pi L}{\lambda} = kL$$

Eqn. 7.19

Since the wave-vector k is related to the frequency ω and phase-velocity v of the wave by;

$$k = \frac{\omega}{v}$$

the additional phase as a result of travelling through the ZnO thin film can be expressed as;

$$\phi = \frac{\omega L}{v}$$

Eqn. 7.20

The phase-velocity of the wave is related to the refractive index n;

$$v = \frac{c}{n}$$

and so, the phase becomes;

$$\phi = \frac{n\omega L}{c}$$

Eqn. 7.21

We can now apply the boundary condition for electric fields across the ZnO-sapphire interface;

$$E_{T'} = E_1 e^{i(n_1\omega L/c)} + E_2 e^{i(n_2\omega L/c)} + E_3 e^{i(n_3\omega L/c)} + E_4 e^{-i(n_1\omega L/c)} + E_5 e^{-i(n_2\omega L/c)} + E_6 e^{-i(n_3\omega L/c)}$$

Eqn. 7.22

where the phase for (E_1), (E_2) and (E_3) is considered positive, and negative for (E_4), (E_5) and (E_6). Similarly, the boundary condition for the magnetic fields is;

$$n_S E_T = n_1 E_1 e^{i(n_1\omega l/c)} + n_2 E_2 e^{i(n_2\omega l/c)} + n_3 E_3 e^{i(n_3\omega l/c)} - n_1 E_4 e^{-i(n_1\omega l/c)} - n_2 E_5 e^{-i(n_2\omega l/c)} - n_3 E_6 e^{-i(n_3\omega l/c)}$$

Eqn. 7.23

7.4.4 Model 1 - Additional Boundary Conditions

It is clear that with just the four classical conditions one has an insufficient number of equations to solve the expressions simultaneously. We therefore apply the additional boundary conditions at each interface, which state that the polarisation due to excitons must be zero at the air-ZnO and ZnO-sapphire interfaces, in the absence of taking account an exciton dead-layer. Since there are two resonances, corresponding to the *A* and *B* free-excitons, one obtains;

$$\alpha_{0A}(k_1,\omega)[E_1 + E_4] + \alpha_{0A}(k_2,\omega)[E_2 + E_5] + \alpha_{0A}(k_3,\omega)[E_3 + E_6] = 0$$

Eqn. 7.24

for the *A* free-exciton polarisation at the air-ZnO interface, and;

$$\alpha_{0B}(k_1,\omega)[E_1 + E_4] + \alpha_{0B}(k_2,\omega)[E_2 + E_5] + \alpha_{0B}(k_3,\omega)[E_3 + E_6] = 0$$

Eqn. 7.25

for the *B* free-exciton polarisation. Analogously at the ZnO-sapphire interface the additional boundary conditions are;

$$\alpha_{0A}(k_1,\omega)\left[E_1 e^{i(n_1\omega l/c)} + E_4 e^{-i(n_1\omega l/c)}\right] + \alpha_{0A}(k_2,\omega)\left[E_2 e^{i(n_2\omega l/c)} + E_5 e^{-i(n_2\omega l/c)}\right] + \alpha_{0A}(k_3,\omega)\left[E_3 e^{i(n_3\omega l/c)} + E_6 e^{-i(n_3\omega l/c)}\right] = 0$$

Eqn. 7.26

and;

$$\alpha_{0B}(k_1,\omega)\left[E_1 e^{i\left(n_1\omega l/c\right)}+E_4 e^{-i\left(n_1\omega l/c\right)}\right]+\alpha_{0B}(k_2,\omega)\left[E_2 e^{i\left(n_2\omega l/c\right)}+E_5 e^{-i\left(n_2\omega l/c\right)}\right]+$$
$$\alpha_{0B}(k_3,\omega)\left[E_3 e^{i\left(n_3\omega l/c\right)}+E_6 e^{-i\left(n_3\omega l/c\right)}\right]=0$$

Eqn. 7.27

where the phase difference between the air-ZnO and ZnO-sapphire boundaries has been accounted for.

7.4.5 Model 1 - Solution Of Boundary Conditions

If one takes the first classical boundary condition (*Eqn. 7.17*);

$$E_I + E_R = E_1 + E_2 + E_3 + E_4 + E_5 + E_6$$

and re-arranges the terms, one arrives at the expression;

$$E_R - E_1 - E_2 - E_3 - E_4 - E_5 - E_6 + (0)E_T = -E_I$$

Eqn. 7.28

where all waves in the problem have been included, hence the $(0)E_T$ term for the transmitted wave into the sapphire substrate. Dividing this by (E_R) we get;

$$r - A - B - C - D - E - F + 0G = -1$$

Eqn. 7.29

where the ratio E_R/E_I is the amplitude reflection coefficient *r*, and;

$$A = \frac{E_1}{E_I}$$
$$\vdots \quad \vdots \quad \vdots$$
$$F = \frac{E_6}{E_I}$$
$$G = \frac{E_T}{E_I}$$

Eqns. 7.30

Following an identical procedure, the eight boundary conditions are;

$$r - A - B - C - D - E - F + 0G = -1$$

(Air-ZnO: Electric field)

$$r + n_1 A + n_2 B + n_3 C - n_1 D - n_2 E - n_3 F + 0G = 1$$

(Air-ZnO: Magnetic field)

$$0r + Ae^{an_1} + Be^{an_2} + Ce^{an_3} + De^{-an_1} + Ee^{-an_2} + Fe^{-an_3} - G = 0$$

(ZnO-sapphire: Electric field)

$$0r + n_1 Ae^{an_1} + n_2 Be^{an_2} + n_3 Ce^{an_3} - n_1 De^{-an_1} - n_2 Ee^{-an_2} - n_3 Fe^{-an_3} - n_s G = 0$$

(ZnO-sapphire: Magnetic field)

$$0r + \alpha_{A1} A + \alpha_{A2} B + \alpha_{A3} C + \alpha_{A1} D + \alpha_{A2} E + \alpha_{A3} F + 0G = 0$$

(Air-ZnO: polarisation zero for A free-exciton)

$$0r + \alpha_{B1} A + \alpha_{B2} B + \alpha_{B3} C + \alpha_{B1} D + \alpha_{B2} E + \alpha_{B3} F + 0G = 0$$

(Air-ZnO: polarisation zero for B free-exciton)

$$0r + \alpha_{A1} e^{an_1} A + \alpha_{A2} e^{an_2} B + \alpha_{A3} e^{an_3} C + \alpha_{A1} e^{-an_1} D + \alpha_{A2} e^{-an_2} E + \alpha_{A3} e^{-an_3} F + 0G = 0$$

(ZnO-sapphire: polarisation zero for A free-exciton)

$$0r + \alpha_{B1} e^{an_1} A + \alpha_{B2} e^{an_2} B + \alpha_{B3} e^{an_3} C + \alpha_{B1} e^{-an_1} D + \alpha_{B2} e^{-an_2} E + \alpha_{B3} e^{-an_3} F + 0G = 0$$

(ZnO-sapphire: polarisation zero for B free-exciton)

Eqns. 7.31

where;

$$a = i\omega L/c$$

$$\begin{pmatrix} \alpha_{A1} \\ \alpha_{A2} \\ \alpha_{A3} \end{pmatrix} = \begin{pmatrix} \alpha_{0A}(k_1,\omega) \\ \alpha_{0A}(k_2,\omega) \\ \alpha_{0A}(k_3,\omega) \end{pmatrix}$$

$$\begin{pmatrix} \alpha_{B1} \\ \alpha_{B2} \\ \alpha_{B3} \end{pmatrix} = \begin{pmatrix} \alpha_{0B}(k_1,\omega) \\ \alpha_{0B}(k_2,\omega) \\ \alpha_{0B}(k_3,\omega) \end{pmatrix}$$

Eqns. 7.32

and the refractive index of air (n_0) has been set to one. To solve the simultaneous equation set, one arranges the boundary conditions (*Eqns. 7.31*) in a matrix;

$$\underbrace{\begin{pmatrix} -1 & 1 & 1 & 1 & 1 & 1 & 1 & 0 \\ 1 & n_1 & n_2 & n_3 & -n_1 & -n_2 & -n_3 & 0 \\ 0 & e^{an_1} & e^{an_2} & e^{an_3} & e^{-an_1} & e^{-an_2} & e^{-an_3} & -1 \\ 0 & n_1 e^{an_1} & n_2 e^{an_2} & n_3 e^{an_3} & -n_1 e^{-an_1} & -n_2 e^{-an_2} & -n_3 e^{-an_3} & -n_S \\ 0 & \alpha_{A1} & \alpha_{A2} & \alpha_{A3} & \alpha_{A1} & \alpha_{A2} & \alpha_{A3} & 0 \\ 0 & \alpha_{B1} & \alpha_{B2} & \alpha_{B3} & \alpha_{B1} & \alpha_{B2} & \alpha_{B3} & 0 \\ 0 & \alpha_{A1}e^{an_1} & \alpha_{A2}e^{an_2} & \alpha_{A3}e^{an_3} & \alpha_{A1}e^{-an_1} & \alpha_{A2}e^{-an_2} & \alpha_{A3}e^{-an_3} & 0 \\ 0 & \alpha_{B1}e^{an_1} & \alpha_{B2}e^{an_2} & \alpha_{B3}e^{an_3} & \alpha_{B1}e^{-an_1} & \alpha_{B2}e^{-an_2} & \alpha_{B3}e^{-an_3} & 0 \end{pmatrix}}_{A} \underbrace{\begin{pmatrix} r \\ A \\ B \\ C \\ D \\ E \\ F \\ G \end{pmatrix}}_{b} = \underbrace{\begin{pmatrix} 1 \\ 1 \\ 0 \\ 0 \\ 0 \\ 0 \\ 0 \\ 0 \end{pmatrix}}_{c}$$

Eqn. 7.33

which has the form $Ab=c$. Hence, one can solve the equation for the amplitude reflection coefficient r by taking the inverse of square matrix A;

$$b=A^{-1}c$$

Eqn. 7.34

and examining the first row of the product of $A^{-1}c$. Squaring r then gives the reflectance R.

7.4.6 Model 2 - PLD Sample excluding the Thin Film nature

Although the above model provides a good fit to the experimental data (discussed below in *Section 7.6*) it will also be useful to examine a model which does not include the thin film nature of the sample. Such a model is shown in *Figure 7.7*.

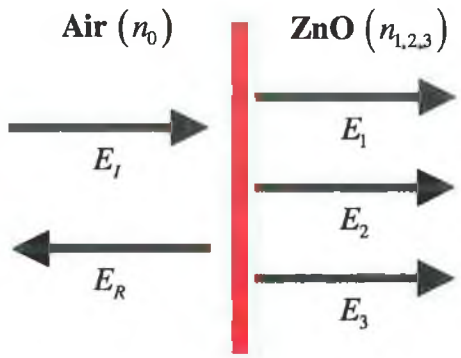

Figure 7.7: *Model of PLD sample where neither the thin film nature nor an exciton dead-layer have been taken into account. In this case the incident and reflected waves are* (E_I) *and* (E_R) *respectively on the air-ZnO interface, and the waves* (E_{1-3}) *are the three transmitted waves (corresponding to the three solutions of the two-band oscillator model in the last section). Note that because we assume an infinite slab of ZnO material, we do not include the reflected waves from the ZnO-sapphire interface or the transmitted wave into the sapphire substrate.*

The boundary conditions in this case are relatively simple since one considers only a single interface. For the electric fields at the air-ZnO boundary;

$$E_I + E_R = E_1 + E_2 + E_3$$

Eqn. 7.35

and for the magnetic fields;

$$n_0 E_I - n_0 E_R = n_1 E_1 + n_2 E_2 + n_3 E_3$$

Eqn. 7.36

The additional boundary conditions are therefore just;

$$\alpha_{0A}(k_1,\omega)E_1+\alpha_{0A}(k_2,\omega)E_2+\alpha_{0A}(k_3,\omega)E_3=0$$

Eqn. 7.37

for the polarisation of the A excitons at the interface and;

$$\alpha_{0B}(k_1,\omega)E_1+\alpha_{0B}(k_2,\omega)E_2+\alpha_{0B}(k_3,\omega)E_3=0$$

Eqn. 7.38

for the B excitons. As before, each equation in the simultaneous set is divided by (E_I) and the four boundary conditions become;

$$\begin{aligned}
r-A-B-C&=-1\\
r+n_1A+n_2B+n_3C&=1\\
0r+\alpha_{A1}A+\alpha_{A2}B+\alpha_{A3}C&=0\\
0r+\alpha_{B1}A+\alpha_{B2}B+\alpha_{B3}C&=0
\end{aligned}$$

Eqns. 7.39

where;

$$r=\frac{E_R}{E_I}$$

$$A=\frac{E_1}{E_I}$$

$$B=\frac{E_2}{E_I}$$

$$C=\frac{E_3}{E_I}$$

$$\begin{pmatrix}\alpha_{A1}\\ \alpha_{A2}\\ \alpha_{A3}\end{pmatrix}=\begin{pmatrix}\alpha_{0A}(k_1,\omega)\\ \alpha_{0A}(k_2,\omega)\\ \alpha_{0A}(k_3,\omega)\end{pmatrix}$$

$$\begin{pmatrix}\alpha_{B1}\\ \alpha_{B2}\\ \alpha_{B3}\end{pmatrix}=\begin{pmatrix}\alpha_{0B}(k_1,\omega)\\ \alpha_{0B}(k_2,\omega)\\ \alpha_{0B}(k_3,\omega)\end{pmatrix}$$

Eqns. 7.40

and the refractive index of air (n_0) has been set to one.

The matrix equation is subsequently;

$$\begin{pmatrix} r \\ A \\ B \\ C \end{pmatrix} = \begin{pmatrix} -1 & 1 & 1 & 1 \\ 1 & n_1 & n_2 & n_3 \\ 0 & \alpha_{A1} & \alpha_{A2} & \alpha_{A3} \\ 0 & \alpha_{B1} & \alpha_{B2} & \alpha_{B3} \end{pmatrix}^{-1} \begin{pmatrix} 1 \\ 1 \\ 0 \\ 0 \end{pmatrix}$$

Eqn. 7.41

which is solved for *r* and hence the reflectance.

7.5 *Model 3 - Bulk Crystal with Exciton Dead-Layer*

To model the reflectance of the Eagle-Picher bulk ZnO wafer one follows a similar procedure to that used for the PLD material, the major difference being the inclusion of an exciton dead-layer in this case. One need consider only two interfaces - the boundary between air and the ZnO dead-layer (in which there is no polarisation due to the excitons), and the boundary between the dead-layer and the ZnO bulk material (in which this polarisation will occur). *Figure 7.8* is a diagram showing the model used to determine the boundary conditions for the bulk wafer, where the thickness of the dead-layer is L_0.

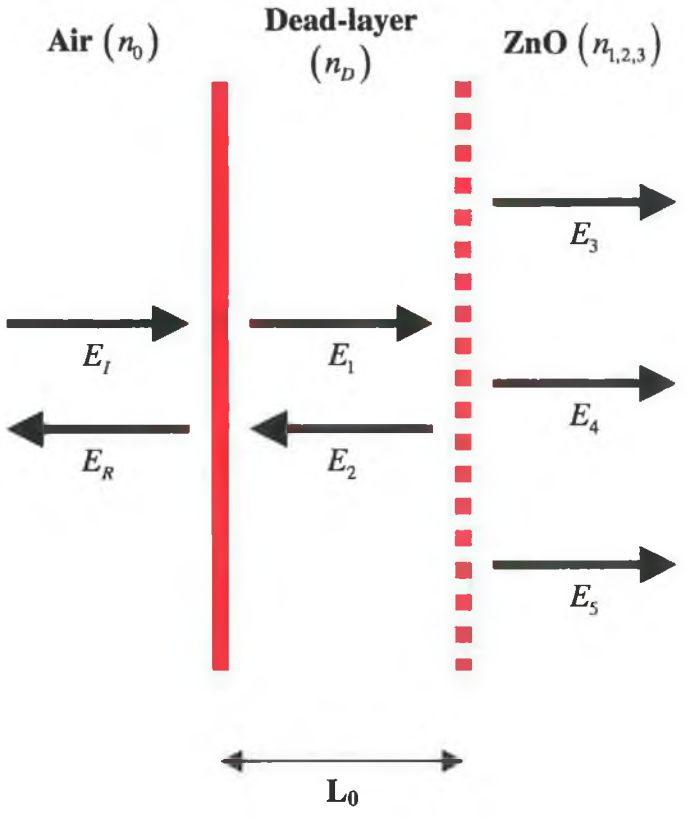

Figure 7.8: *Diagram of the model applied to the Eagle-Picher bulk ZnO wafer. In this case one considers an exciton dead-layer of thickness L_0. The wafer is sufficiently thick (~ 0.5 mm) that one does not need to consider the ZnO/dead-layer or dead-layer/air interfaces on the opposite side of the crystal.*

In *Fig. 7.8*, the waves (E_I) and (E_R) are assigned as the incident and reflected waves respectively from the air/dead-layer interface, where the refractive indices are (n_0) for air and (n_D) for the dead-layer. There will be both a transmitted wave (E_1) into the dead-layer, and a reflected wave (E_2) from the dead-layer/bulk interface. In the bulk ZnO material itself, the three transmitted waves are (E_{3-5}) corresponding to each solution for *k* in *Eqn. 7.5*. We assume that the bulk crystal is sufficiently thick (~ 0.5 mm), compared to the thin film PLD sample (~ 200 nm), that one does not need to consider the bulk/dead-layer or dead-layer/air interfaces on the opposite side of the wafer. As with the PLD material one now applies both classical and additional boundary conditions at each interface.

The classical boundary conditions at the air/dead-layer interface are;

$$E_I + E_R = E_1 + E_2$$

Eqn. 7.42

for the electric fields, and;

$$n_0 E_I - n_0 E_R = n_D E_1 - n_D E_2$$

Eqn. 7.43

for the magnetic fields. Similarly, at the dead-layer/bulk interface the boundary conditions are;

$$E_1 e^{i\left(n_D \omega l_D / c\right)} + E_2 e^{-i\left(n_D \omega l_D / c\right)} = E_3 + E_4 + E_5$$

Eqn. 7.44

and;

$$n_D E_1 e^{i\left(n_D \omega l_D / c\right)} - n_D E_2 e^{-i\left(n_D \omega l_D / c\right)} = n_1 E_3 + n_2 E_4 + n_3 E_5$$

Eqn. 7.45

for the electric and magnetic fields respectively. Only the waves (E_1) and (E_2) encounter two interfaces and hence, only these waves appear in both sets of equations obtained at each boundary. Therefore, for the equation set to be consistent, the relative phase difference of these waves between the air/dead-layer and dead-layer/bulk interfaces has been explicitly included in an analogous manner to the phase difference included in the PLD model where the thin film nature was examined.

The additional boundary conditions, applied at the dead-layer/bulk interface are;

$$\alpha_{A0}(k_1,\omega)E_3+\alpha_{A0}(k_2,\omega)E_4+\alpha_{A0}(k_3,\omega)E_5=0$$

Eqn. 7.46

for the polarisation of the *A* exciton and;

$$\alpha_{B0}(k_1,\omega)E_3+\alpha_{B0}(k_2,\omega)E_4+\alpha_{B0}(k_3,\omega)E_5=0$$

Eqn. 7.47

for the polarisation of the *B* exciton.

If one now divides each boundary condition by (E_1), as before, they become;

$$-r+A+B+0C+0D+0E=1$$

$$r+n_D A-n_D B+0C+0D+0E=1$$

$$0r+Ae^{i\left(n_D\omega l_0/c\right)}+Be^{-i\left(n_D\omega l_0/c\right)}-C-D-E=0$$

$$0r+n_D Ae^{i\left(n_D\omega l_0/c\right)}-n_D Be^{-i\left(n_D\omega l_0/c\right)}-n_1C-n_2D-n_3E=0$$

$$0r+0A+0B+\alpha_{A0}(k_1,\omega)C+\alpha_{A0}(k_2,\omega)D+\alpha_{A0}(k_3,\omega)E=0$$

$$0r+0A+0B+\alpha_{B0}(k_1,\omega)C+\alpha_{B0}(k_2,\omega)D+\alpha_{B0}(k_3,\omega)E=0$$

Eqns. 7.48

where;

$$r = \frac{E_R}{E_I}$$
$$A = \frac{E_1}{E_I}$$
$$\vdots \quad \vdots \quad \vdots$$
$$E = \frac{E_5}{E_I}$$

Eqns. 7.49

and the refractive index of air (n_0) is one. The refractive index of the dead-layer is given by *Eqn. 7.7*;

$$n_D = \sqrt{\varepsilon_\infty}$$

One obtains the matrix equation;

$$\begin{pmatrix} -1 & 1 & 1 & 0 & 0 & 0 \\ 1 & n_D & -n_D & 0 & 0 & 0 \\ 0 & e^{i\phi} & e^{-i\phi} & -1 & -1 & -1 \\ 0 & n_D e^{i\phi} & -n_D e^{-i\phi} & -n_1 & -n_2 & -n_3 \\ 0 & 0 & 0 & \alpha_{A1} & \alpha_{A2} & \alpha_{A3} \\ 0 & 0 & 0 & \alpha_{B1} & \alpha_{B2} & \alpha_{B3} \end{pmatrix} \begin{pmatrix} r \\ A \\ B \\ C \\ D \\ E \end{pmatrix} = \begin{pmatrix} 1 \\ 1 \\ 0 \\ 0 \\ 0 \\ 0 \end{pmatrix}$$

Eqn. 7.50

which is solved as before, where;

$$\phi = n_D \omega \, L_0 / c$$

$$\begin{pmatrix} \alpha_{A1} \\ \alpha_{A2} \\ \alpha_{A3} \end{pmatrix} = \begin{pmatrix} \alpha_{0A}(k_1, \omega) \\ \alpha_{0A}(k_2, \omega) \\ \alpha_{0A}(k_3, \omega) \end{pmatrix}$$

$$\begin{pmatrix} \alpha_{B1} \\ \alpha_{B2} \\ \alpha_{B3} \end{pmatrix} = \begin{pmatrix} \alpha_{0B}(k_1, \omega) \\ \alpha_{0B}(k_2, \omega) \\ \alpha_{0B}(k_3, \omega) \end{pmatrix}$$

Eqns. 7.51

7.6 *Results and Discussion*

Figure 7.9 shows the experimentally obtained reflectance spectra for both the bulk crystal and PLD *Sample (c)*. The spectra have been divided into three energy regions – region II contains the actual resonances due to the excitons, and I and III correspond to regions at lower and higher energy respectively. Although the PLD sample exhibits substantially reduced excitonic features with respect to the bulk wafer (which is due, as shall be described below, to large differences in the damping parameters), it can be seen that there is also a dissimilarity in the structure of region I (~ 3.26 – 3.33 eV). At these lower energies the bulk crystal reflectance appears to smoothly return to a value that is ultimately determined by the background dielectric constant ε_∞, while the PLD sample demonstrates an oscillatory structure and a dramatic increase in the reflectance with respect to the excitonic resonances. There is also evidence of these differences in structure in region III between ~ 3.45 and 3.48 eV.

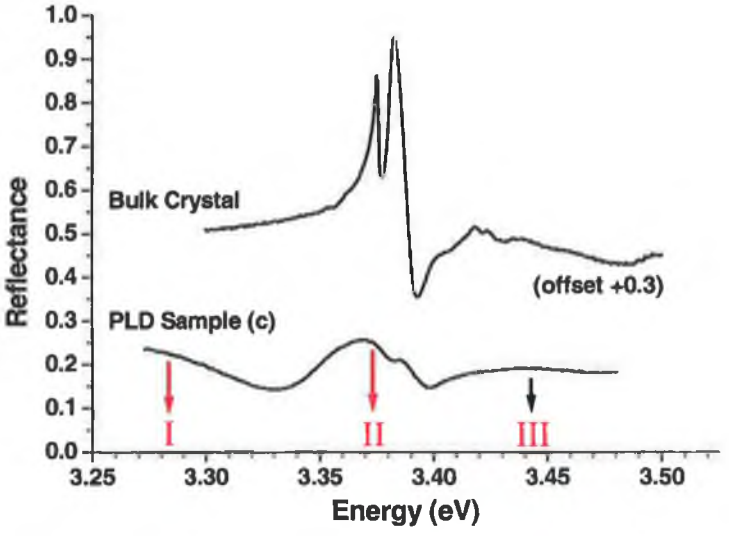

Figure 7.9: *Experimental reflectance spectra of both the bulk and polycrystalline thin film ZnO material. Note the differences in the structure in regions I and III for each sample.*

We can begin to understand the reason for this behaviour by examining both models of the PLD material discussed in previous sections. *Figure 7.10* shows the experimental reflectance data from *Sample (c)*, along with the best fit produced by both models of the PLD material. For '*Model 1*' the thin film nature of the sample was taken into account when applying the boundary conditions and assumed the presence of reflected waves from the ZnO/sapphire interface. The values of the fitting parameters used in this model, which included the film thickness, are shown in *Table 7.2*. Using identical values for the fitting, '*Model 2*' considered only an air/ZnO interface and assumed the ZnO layer was semi-infinite.

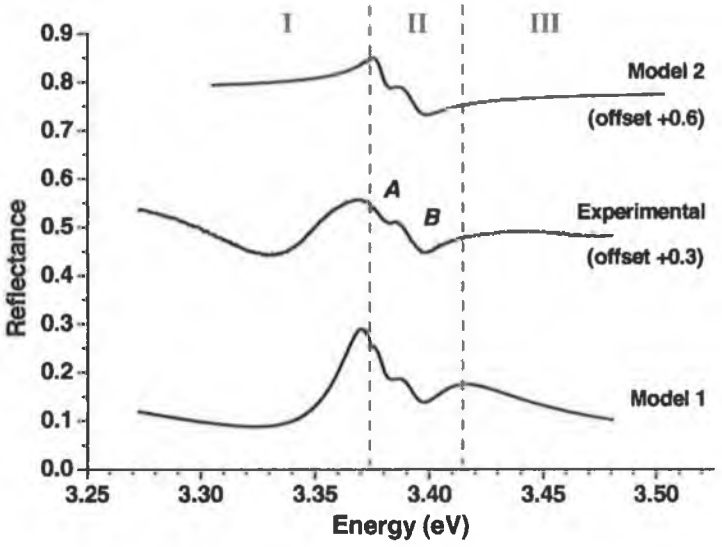

Figure 7.10: *Comparison of experimental reflectance spectra with computed reflectance spectra for PLD Sample (c). For Model 1 the boundary conditions included the effects of reflections from the ZnO/sapphire interface, and for Model 2 these reflections were ignored. Although both models provide a good qualitative fit to the excitonic resonances in region II, one finds that Model 1 provides a better fit of the spectrum in regions I and III suggesting that Fabry-Perot oscillations in the thin film are responsible for the structure in these energy regions.*

Table 7.2: *Fitting parameters used for modelling the PLD and bulk crystal*

Parameter	***Bulk Crystal***	***PLD sample***	***Literature value [2,4]***
$\hbar\varpi_{AT}$ *(transverse A exciton energy, eV)*	3.3753	3.3781	3.3758
$\hbar\varpi_{BT}$ *(transverse B exciton energy, eV)*	3.3813	3.3904	3.3810
$\hbar\varpi_{AT} - \hbar\varpi_{BT}$ *(A-B splitting, meV)*	6	12.3	5.2
Δ_{LT}^{A} *(A exciton LT splitting, meV)*	2	1.9	1.8
Δ_{LT}^{B} *(B exciton LT splitting, meV)*	11.9	3.6	10.2
$\hbar\Gamma_{A}$ *(A exciton damping, meV)*	0.7	6.8	0.7
$\hbar\Gamma_{B}$ *(B exciton damping, meV)*	0.7	13.7	0.7
M *(multiples of electron mass)*	0.87	0.5	0.87
Dead-layer thickness (nm)	4	N/A	4
Film thickness (nm)	N/A	215 nm	200 nm (***Ref. [1]***)

One finds that both models provide a reasonable fit to the excitonic resonances in region II but that the oscillations in regions I and III are not reproduced by the model in which the thin film reflections were ignored (*Model 2*). *Model 1*, however, which included reflections from the ZnO/sapphire interface (refractive index of sapphire is ~ 1.8) is found to provide a better qualitative fit at these energies. The reflectance minimum at ~ 3.327 eV and the reflectance increase at lower energies are reproduced, as is the oscillatory behaviour in the 3.4 – 3.45 eV range. The ZnO layer thickness was used as a fitting parameter in this model and was determined to be 215 nm, in excellent agreement with the known values measured by AFM. We can conclude, therefore, that the structure in regions I and III is due to Fabry-Perot (FP) oscillations in the thin film.

The origin of this behaviour, where FP oscillations are seen at energies below and above the exciton-photon interaction region, while the central excitonic region is well described by a model neglecting the thin film nature of the sample, may be understood as follows. *Figure. 7.11* shows the calculated dispersion of the exciton-polaritons in ZnO and indicates regions I, II and III. FP oscillations will only be observed if the spatial damping of the propagating modes is sufficiently small that the modes can make at least two passes through the film to cause FP interference. This condition is quantified by requiring that the sample thickness L is significantly less than γ, where;

$$\gamma = \frac{1}{n_i k_0}$$

Eqn. 7.52

and n_i in this case is the imaginary part of the mode refractive index, and k_0 the free space wave-vector [5]. The γ values of the photon-like branches in regions I and III, where mixing with the highly damped exciton is minimal, are ~ 120,000 nm and ~ 40,000 nm respectively and γ >> 200 nm. Thus one would expect to see oscillatory structure in the reflectance. In region II γ for all modes is < 400 nm due to the large damping of the exciton and the strong exciton-photon mixing. Therefore no oscillations would be expected in region II, in agreement with observation. FP oscillations of this sort have been reported previously for single excitonic resonances in CdSe platelets [6].

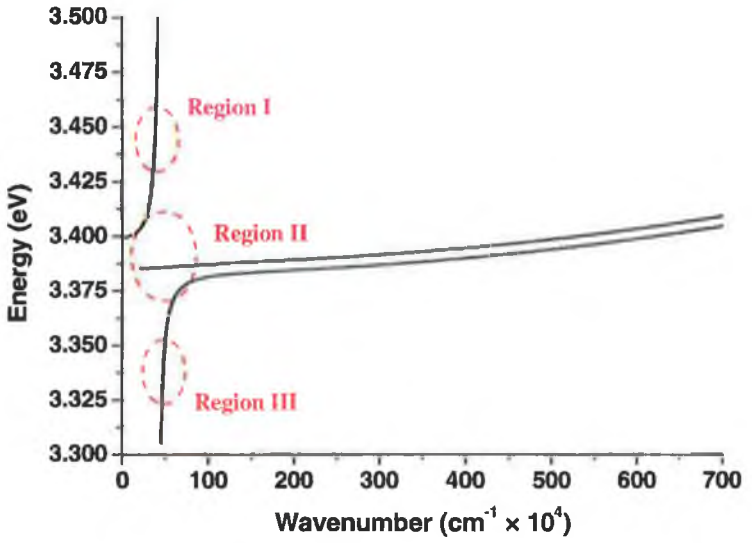

Figure 7.11: *Computed exciton-polariton dispersion curve for PLD sample showing regions I, II and III. In regions I and III the waves are photon-like and the value of γ is much larger than the film thickness. In this case the waves can make two passes through the film with the result that Fabry-Perot interference effects are observed at lower and higher energies than the exciton resonances. In region II the value of γ is < 400 nm, implying that the waves are damped due to exciton-photon mixing and are unable to make two passes through the film.*

Figure 7.12 shows a comparison between the experimental reflectance data from the bulk crystal and the theoretical reflectance using *Model 3*, which considered a semi-infinite slab of ZnO and included the effects of an exciton dead-layer. One may compare the parameters for the PLD sample with those found for the bulk sample in *Table 7.2*. There is a substantial change in the transverse *A-B* splitting, due to both biaxial strain arising from lattice mismatch with the substrate and grain boundary electric fields [1,7]. The LT splitting of the *B*-exciton in the PLD sample is also substantially different to the value in the bulk crystal. The physical origin of such a dramatic difference is not clear, but may also be due to the combination of strain and electric fields in these samples. In particular, it is clearly seen that the exciton damping factors for the *A*- and *B*-excitons in the PLD sample are much larger than the values in

the bulk sample as expected on the basis of the significantly poorer crystal quality of the PLD material and the small grain sizes. The exciton dead-layer thickness in the fit for the PLD sample is zero, while the exciton effective mass is 0.5 times the electron mass. While both these values are different to those found for the bulk sample, the fit is largely insensitive to these parameters given the rather large damping. Visually identical spectra are computed with the bulk values of these quantities.

The exciton dead-layer, in the case of the bulk crystal, has been calculated to be ~ 4 nm and, as mentioned in the previous chapter, is used as an 'order of magnitude' check of the fit. According to the classical description shown in *Chapter 6*, where we considered repulsion of free-excitons from the surface of the crystal due to image charge effects, one would expect the thickness of the dead-layer to be roughly twice the effective Bohr radius (i.e. the minimum physical distance from the surface at which the exciton can exist within the crystal, according to classical electrodynamics). *Y. S. Park et al.* have given the effective Bohr radius as 2.2 nm [8] in ZnO, in good agreement with the thickness of the dead-layer determined by the reflectance model.

In the above discussion, relatively simply models for the PLD sample were described which did not take into account an exciton dead-layer. A more complicated model for this sample was also used, which includes exciton dead-layers between the air-ZnO and ZnO-sapphire boundaries and also takes account of the thin film nature of the sample. The model, boundary conditions and derived matrix are shown in *Appendix III*. Despite the additional complexity, however, the reflectance fits produced were no better than those obtained using *Model 1* above.

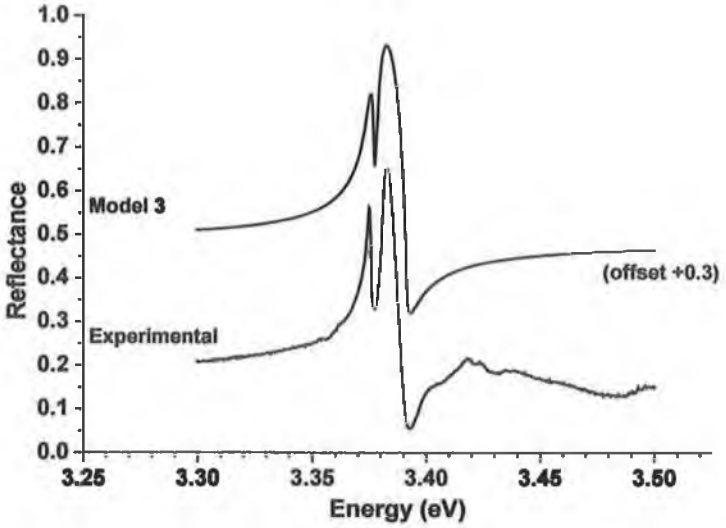

Figure 7.12: *Comparison of experimental reflectance spectra with computed reflectance spectra for bulk crystal. For Model 3 the boundary conditions included the effects of an exciton dead-layer and assumed a semi-infinite slab of ZnO material.*

7.7 Conclusions

In this chapter, the reflectance from both bulk and polycrystalline ZnO samples has been modelled using a two-band dielectric response function. This semi-classical model provides good qualitative fitting to the observed experimental spectra. In the case of the PLD polycrystalline sample the experimental data is adequately described by a model based on the interaction of strongly damped excitons with a photon mode. Fabry-Perot oscillations are observed both above and below the strong interaction regime, where the photon-like mode is weakly damped. In the strong interaction regime, where all propagating modes are strongly damped due to mixing, no oscillations are seen. It is therefore important to consider the full polariton picture in interpreting the reflectance spectra of polycrystalline ZnO material. More complicated models, which included dead-layers on each side of the thin film failed to improve upon the fits of the simpler models discussed in this chapter due to the large damping and the subsequent insensitivity of the model to certain other parameter values.

7.8 References

[1] C. Roy, S. Byrne, E. McGlynn, J.-P. Mosnier, E. de Posada, D. O'Mahony, J. G. Lunney, M. O. Henry, B. Ryan, and A. A. Cafolla, *Thin Solid Films* **436** (2003) 273

[2] J. Lagois, *Phys. Rev. B* **16** (1977) 1699

[3] MATLAB, Version 5.3
Published by The Mathworks, 3 Apple Hill Drive, Natick, MA 01760-2098, USA
Website: www.mathworks.com

[4] J. Lagois, *Phys. Rev. B* **23** (1981) 5511

[5] E.L. Ivchenko in *Excitons*, edited by E.I. Rashba and M.D. Sturge (North-Holland, Amsterdam, 1982), p. 141

[6] V. A. Kiselev, B. S. Razbirin, and I. N. Uraltsev, *Phys. Stat Sol. (b)* **72** (1975) 161

[7] G. Tobin, J. Fryar, E. McGlynn, J.-P. Mosnier, M. O. Henry, E. de Posada, D. O'Mahony, and J. Lunney in *Physics of Semiconductors 2002*, Institute of Physics Conference Series Number 171, edited by A.R. Long and J.H. Davies (IOPP, Bristol, 2002), paper number H26

[8] Y. S. Park, C. W. Litton, T. C. Collins, and D. C. Reynolds, *Phys. Rev.* **143** (1966) 512

Chapter 8

Conclusions and Further Work

8.1 Conclusions and Further Work

To summarise the experiments described in this thesis, the O- and Zn-terminated polar surfaces of bulk ZnO crystals have been studied using both optical spectroscopy techniques and surface probe microscopy methods. ZnO wafers, grown by three different companies, reveal substantial optical (in terms of luminescence features and free-exciton reflectance resonances) and topographical differences when compared to one another. An analysis of AFM force-displacement plots, and of results obtained by lateral force microscopy, has been performed in order to determine whether adsorbed fluid layers are present on the polar surfaces in ambient conditions. The resultant surface morphology after wet chemical etching has also been examined and an attempt has been made to correlate the topographic properties with optical characteristics. Finally, we have used a two-band dielectric response function to model the reflectance resonances observed for both thin film polycrystalline and bulk ZnO samples.

The conclusions drawn from these experiments have largely been given at the end of the pertinent chapters, although here, some of the more important conclusions shall be recapitulated. The study of as-received ZnO wafers suggests that the Zn-terminated surface of the Eagle-Picher material demonstrates unusually intense bound-exciton luminescence and strong free-exciton reflectance resonances when compared to the other crystals. It has been speculated that this behaviour may be due to chemo-mechanical nature of the polish applied, or some other unknown additional processing of the surface (for example, exposure of the face to H plasmas). It is suggested that the diminished optical properties of the Zn-terminated face of Rubicon wafers, in comparison to the O-terminated face, is partially due to the differences in topography and effectiveness of the epi-polish applied to each polar surface, and these conclusion are supported by the results of the acid etching described below.

In relation to the observed stability of polar faces, a number of authors have proposed mechanisms involving H and OH adsorption on O- and Zn-terminated

surfaces respectively, and have speculated that water layers of considerable thickness may be stable in ambient conditions. The results of *Chapter 4* support this assertion, and one finds that fluid layers are approximately twice as thick on the hydrophilic O-terminated surface than on the Zn-face. It has been shown that the presence of these fluid layers can influence the efficacy of cleaning procedures and may also help explain discrepancies in the literature as to which polar face is optimal for epitaxial growth.

The hydrophilic nature of the O-terminated surface plays an important role in the interaction of the face with acidic solutions. High vertical-to-lateral etch rates are observed on this particular polar face due to the interaction of O atoms at the surface with H cations present in the acids. Conversely, the etching of Zn-terminated surfaces proceeds predominantly laterally due to the presence of O atoms along polish-induced scratches. This anisotropy results in a smoothing of Zn-terminated faces and corresponding increases in the oscillator strengths of free-excitons observed by reflectance spectroscopy. Etching Zn-terminated surfaces with low pH solutions increases bound-exciton emission from this polar face, and it is proposed that passivation as a result of H incorporation into the surface layers is responsible. This mechanism may account for the intensity of luminescence from the Eagle-Picher Zn-terminated surface after chemo-mechanical polishing. It is found that, after etching with acidic solutions, the unstructured green band generally increases in intensity. Since the etch mechanism is expected to be due to the removal of O from the material, this growth is in keeping with studies that suggest this band is due to oxygen vacancies.

The semi-classical exciton-polariton theory of *Hopfield* and *Thomas*, in conjunction with the relatively simple additional boundary condition of *Pekar*, has been successfully used to model the reflectance of bulk and polycrystalline ZnO material. The model of the PLD-grown ZnO that includes the thin-film nature of the sample not only provides good fits to the excitonic resonances, but also predicts the presence of Fabry-Perot oscillations in the reflectance spectra and provides an accurate determination of the film thickness.

More generally, this thesis has attempted to combine results obtained by scanning probe microscopy measurements and optical spectroscopy as a means to elucidate material behaviour. In this regard, reflectance spectroscopy has been found to be a particularly useful technique since the overall intensity of reflected light has been shown, in relation to the etching of polar faces, to be related to the induced surface topography. Furthermore, examination of the excitonic resonances provides valuable additional information regarding surfaces and this is most strikingly seen in the modelling of the PLD material.

Finally there are several outstanding questions that this research has not been able to answer, and a number of avenues for future work. Although image charge theory suggests that the fluid layers should, at most, be approximately 30% thicker on O-terminated surfaces than on Zn-faces (assuming metallization of the O-face occurs), it is difficult to explain the relative scale of the fluid thicknesses observed. Clearly a theoretical analysis of the formation of water slabs on the polar faces is required in order to shed light on the possible mechanisms that would account for this, and experimentally it would be of benefit to examine how the fluid thickness changes as a function of ambient humidity. One aspect that has not been investigated here is the effect of different cleaning procedures on the fluid layer thicknesses, and STM studies of the hydrogen coverage after these procedures could help in the understanding of the formation of fluid layers.

The lateral force microscopy results indicate that the frictional forces experienced by the AFM cantilever are generally higher for Zn-terminated faces than for O-terminated surfaces, in contrast to the force curve data obtained in water, and the reason for this is not understood at present. With calibrated AFM cantilevers it should be possible to examine the slopes of the load-portion of force-curves and hence examine the elastic deformation of each polar face as a function of applied normal force. This may provide additional information regarding the interaction of tips with the surfaces. The reduced frictional forces of O-terminated surfaces may somehow be related to the

presence of thicker fluid layers on this surface, and a study of the change in lateral deflections as a function of scan rate may also be of benefit.

With regard to the acidic etching of the polar faces, examining x-ray rocking curve widths from etched Zn-terminated surfaces would be of interest. This would enable a study of how the sub-surface strain is affected by the etch and, if used in combination with normal-incidence reflectance studies and the exciton-polariton modelling discussed above, may provide a deeper understanding of the mechanism by which one observes increases in oscillator strengths and slight changes in the energies of resonance features. Similar studies of PLD material may also help to quantify the effects of in-situ annealing of these samples.

Finally, random lasing action has been demonstrated by a number of other authors from PLD material, where scattering among the columnar grains generates 'random' cavities. Disordering bulk O-terminated faces through the application of acidic solutions may produce topographically similar structures and these may behave similarly under optical excitations. This would be an interesting application of some of the results of this thesis.

Appendices

Appendix I Transmission of Filters

BG25 Filter

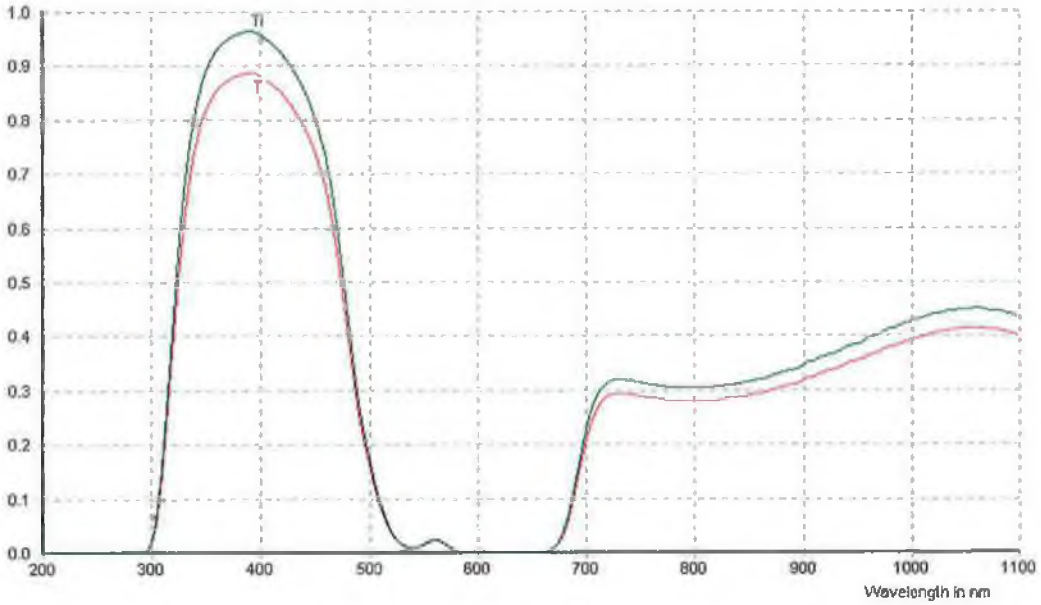

C3C21 Filter

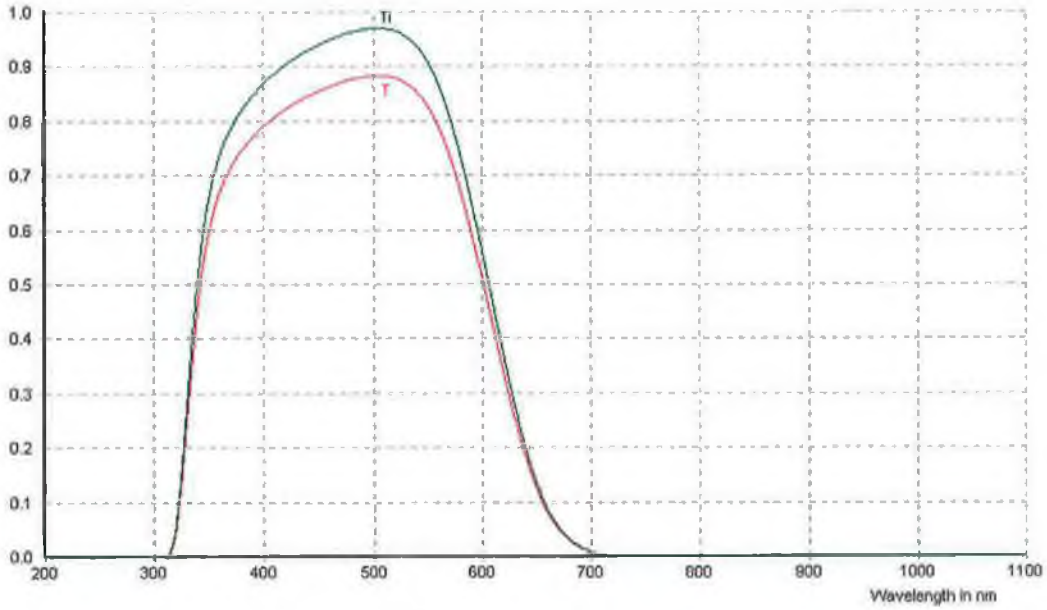

Appendix II MATLAB Program for Modelling Reflectance (Model 1)

```
function [error]=ref_disp_tfi(param,w_l_a,w_l_b,x_data,y_data)
%x_data=[3.30:0.0001:3.50];
warning off;
spec_range=length(x_data);

h_bar=(6.63e-34/(2*3.1415));
m_elec=9.1e-31;
e_vac=8.85e-12;
c=2.998e8;

del_a=param(1);
del_b=param(2);
gam_a=abs(param(3));
gam_b=abs(param(4));
d=abs(param(5));
m_star=abs(param(6));
e_rel_inf=6.2;
n_s=1.8;

w_o_a=w_l_a-(del_a^2);
w_o_b=w_l_b-(del_b^2);

m_eff=m_star*m_elec;
beta_a=h_bar*w_o_a/m_eff;
beta_b=h_bar*w_o_b/m_eff;
alpha_a=e_rel_inf*(e_vac/(w_o_a^2))*((w_l_b^2)-(w_o_a^2))*((w_l_a^2)-(w_o_a^2))/((w_o_b^2)-(w_o_a^2));
alpha_b=e_rel_inf*(e_vac/(w_o_b^2))*((w_l_a^2)-(w_o_b^2))*((w_l_b^2)-(w_o_b^2))/((w_o_a^2)-(w_o_b^2));
```

```
n_inf=sqrt(e_rel_inf);

y1=zeros(spec_range,1);
y2=zeros(spec_range,1);
y3=zeros(spec_range,1);

ref=zeros(spec_range,1);

sum=0;

for count=1:spec_range

        w=(x_data(count)*1.6e-19)/h_bar;

        term1=(w_o_a^2)-(w^2)-(i*w*gam_a);
        term2=(w_o_b^2)-(w^2)-(i*w*gam_b);

        coeff=[beta_b*beta_a*(c^2)/(w^2);
        -(e_rel_inf*beta_b*beta_a)+(term2*beta_a*(c^2)/(w^2))+(term1*beta_b*(c^2)/(w^2));
        (term1*term2*(c^2)/(w^2))-(beta_b*e_rel_inf*term1)-(beta_a*e_rel_inf*term2)-(alpha_a*(w_o_a^2)*beta_b/e_vac)-
        (alpha_b*(w_o_b^2)*beta_a/e_vac);
        -(e_rel_inf*term1*term2)-(alpha_a*(w_o_a^2)*term2/e_vac)-(alpha_b*(w_o_b^2)*term1/e_vac)];

        k_values=sqrt(roots(coeff));

        if imag(k_values(1))>0
                k_values(1)=-k_values(1);
        else
        end
```

```
if imag(k_values(2))>0
        k_values(2)=-k_values(2);
else
end

if imag(k_values(3))>0
        k_values(3)=-k_values(3);
else
end

n_a=k_values(1)*c/w;
n_b=k_values(2)*c/w;
n_c=k_values(3)*c/w;

d_a=exp(i*n_a*w*d/c);
d_b=exp(i*n_b*w*d/c);
d_c=exp(i*n_c*w*d/c);
d_a_1=exp(-i*n_a*w*d/c);
d_b_1=exp(-i*n_b*w*d/c);
d_c_1=exp(-i*n_c*w*d/c);

a_a=(alpha_a*(w_o_a^2)/e_vac)/((w_o_a^2)-(w^2)-(i*w*gam_a)+(beta_a*(w^2)*(n_a^2)/(c^2)));
a_b=(alpha_a*(w_o_a^2)/e_vac)/((w_o_a^2)-(w^2)-(i*w*gam_a)+(beta_a*(w^2)*(n_b^2)/(c^2)));
a_c=(alpha_a*(w_o_a^2)/e_vac)/((w_o_a^2)-(w^2)-(i*w*gam_a)+(beta_a*(w^2)*(n_c^2)/(c^2)));

b_a=(alpha_b*(w_o_b^2)/e_vac)/((w_o_b^2)-(w^2)-(i*w*gam_b)+(beta_b*(w^2)*(n_a^2)/(c^2)));
b_b=(alpha_b*(w_o_b^2)/e_vac)/((w_o_b^2)-(w^2)-(i*w*gam_b)+(beta_b*(w^2)*(n_b^2)/(c^2)));
b_c=(alpha_b*(w_o_b^2)/e_vac)/((w_o_b^2)-(w^2)-(i*w*gam_b)+(beta_b*(w^2)*(n_c^2)/(c^2)));
```

```
        mat=[-1,1,1,1,1,1,1,0;
        1,n_a,n_b,n_c,-n_a,-n_b,-n_c,0;
        0,d_a,d_b,d_c,d_a_1,d_b_1,d_c_1,-1;
        0,n_a*d_a,n_b*d_b,n_c*d_c,-n_a*d_a_1,-n_b*d_b_1,-n_c*d_c_1,-n_s;
        0,a_a,a_b,a_c,a_a,a_b,a_c,0;
        0,b_a,b_b,b_c,b_a,b_b,b_c,0;
        0,d_a*a_a,d_b*a_b,d_c*a_c,d_a_1*a_a,d_b_1*a_b,d_c_1*a_c,0;
        0,d_a*b_a,d_b*b_b,d_c*b_c,d_a_1*b_a,d_b_1*b_b,d_c_1*b_c,0];

        v=[1;1;0;0;0;0;0;0];

        inmat=inv(mat);

        v1=inmat*v;
        x_data(count);

        r1=v1(1);

        ref(count)=((abs(r1))^2)+0.4;

        diff=(ref(count)-y_data(count))^2;
        sum=sum+diff;

        end

error=sum/spec_range;

plot(x_data,ref,x_data,y_data);
```

Appendix III *Model of PLD Sample Including Dead-Layers*

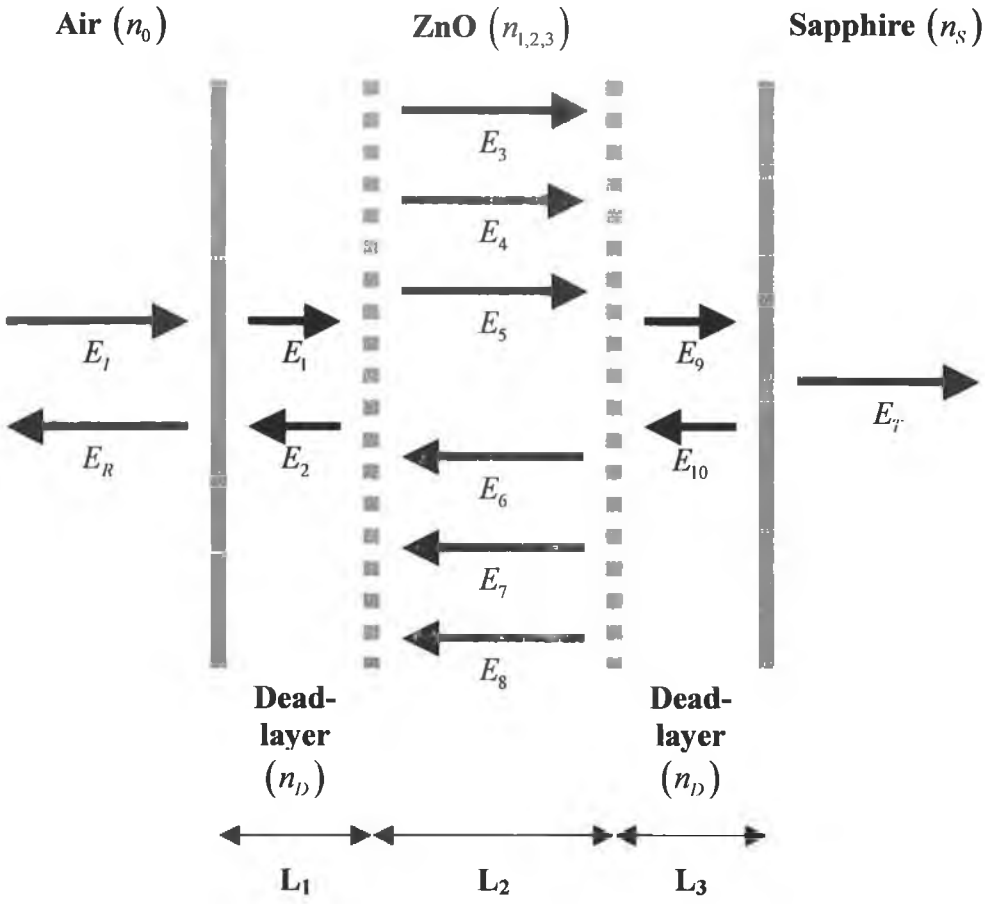

Figure III.1: *Model of PLD sample including an exciton dead-layer between the air-ZnO and ZnO-Sapphire interfaces. The thin film is also taken into account an the model allows for Fabry-Perot oscillations.*

Classical Boundary Conditions

$$E_I + E_R = E_1 + E_2$$

Air/Dead-layer 1 (electric field)

$$n_0 E_I - n_0 E_R = n_D E_1 - n_D E_2$$

Air/Dead-layer 1 (magnetic field)

$$E_1 e^{i\left(n_D \omega l_1 / c\right)} + E_2 e^{-i\left(n_D \omega l_1 / c\right)} = E_3 + E_4 + E_5 + E_6 + E_7 + E_8$$

Dead-layer 1/ZnO (electric field)

$$n_D E_1 e^{i\left(n_D \omega l_1 / c\right)} - n_D E_2 e^{-i\left(n_D \omega l_1 / c\right)} = n_1 E_3 + n_2 E_4 + n_3 E_5 - n_1 E_6 - n_2 E_7 - n_3 E_8$$

Dead-layer 1/ZnO (magnetic field)

$$E_3 e^{i\left(n_1 \omega l_2 / c\right)} + E_4 e^{i\left(n_2 \omega l_2 / c\right)} + E_5 e^{i\left(n_3 \omega l_2 / c\right)} + E_6 e^{-i\left(n_1 \omega l_2 / c\right)} + E_7 e^{-i\left(n_2 \omega l_2 / c\right)} + E_8 e^{-i\left(n_3 \omega l_2 / c\right)} = E_9 + E_{10}$$

ZnO/Dead-layer 2 (electric field)

$$n_1 E_3 e^{i\left(n_1 \omega l_2 / c\right)} + n_2 E_4 e^{i\left(n_2 \omega l_2 / c\right)} + n_3 E_5 e^{i\left(n_3 \omega l_2 / c\right)} - n_1 E_6 e^{-i\left(n_1 \omega l_2 / c\right)} - n_2 E_7 e^{-i\left(n_2 \omega l_2 / c\right)} - n_3 E_8 e^{-i\left(n_3 \omega l_2 / c\right)} = n_D E_9 - n_D E_3$$

ZnO/Dead-layer 2 (magnetic field)

$$E_9 e^{i\left(n_D \omega l_3 / c\right)} + E_{10} e^{-i\left(n_D \omega l_3 / c\right)} = E_T$$

Dead-layer 2/Sapphire (electric field)

$$n_D E_9 e^{i\left(n_D \omega l_3 / c\right)} - n_D E_{10} e^{-i\left(n_D \omega l_3 / c\right)} = n_S E_T$$

Dead-layer 2/Sapphire (magnetic field)

Additional Boundary Conditions

$$\alpha_{A0}(k_1,\omega)[E_3+E_6]+\alpha_{A0}(k_2,\omega)[E_4+E_7]+\alpha_{A0}(k_3,\omega)[E_5+E_8]=0$$

Dead-layer 1: A exciton polarisation

$$\alpha_{B0}(k_1,\omega)[E_3+E_6]+\alpha_{B0}(k_2,\omega)[E_4+E_7]+\alpha_{B0}(k_3,\omega)[E_5+E_8]=0$$

Dead-layer 1: B exciton polarisation

$$\alpha_{A0}(k_1,\omega)\left[E_3e^{i\left(n_1\omega l_2/c\right)}+E_6e^{-i\left(n_1\omega l_2/c\right)}\right]+\alpha_{A0}(k_2,\omega)\left[E_4e^{i\left(n_2\omega l_2/c\right)}+E_7e^{-i\left(n_2\omega l_2/c\right)}\right]$$
$$+\alpha_{A0}(k_3,\omega)\left[E_5e^{i\left(n_3\omega l_2/c\right)}+E_8e^{-i\left(n_3\omega l_2/c\right)}\right]=0$$

Dead-layer 2: A exciton polarisation

$$\alpha_{B0}(k_1,\omega)\left[E_3e^{i\left(n_1\omega l_2/c\right)}+E_6e^{-i\left(n_1\omega l_2/c\right)}\right]+\alpha_{B0}(k_2,\omega)\left[E_4e^{i\left(n_2\omega l_2/c\right)}+E_7e^{-i\left(n_2\omega l_2/c\right)}\right]$$
$$+\alpha_{B0}(k_3,\omega)\left[E_5e^{i\left(n_3\omega l_2/c\right)}+E_8e^{-i\left(n_3\omega l_2/c\right)}\right]=0$$

Dead-layer 2: B exciton polarisation

Matrix

$$
\begin{pmatrix}
-1 & 1 & 1 & 0 & 0 & 0 \\
1 & n_D & -n_D & 0 & 0 & 0 \\
0 & -e^{i\left(n_D\omega\frac{L_1}{c}\right)} & -e^{-i\left(n_D\omega\frac{L_1}{c}\right)} & 1 & 1 & 1 \\
0 & -n_D e^{i\left(n_D\omega\frac{L_1}{c}\right)} & n_D e^{-i\left(n_D\omega\frac{L_1}{c}\right)} & n_1 & n_2 & n_3 \\
0 & 0 & 0 & e^{i\left(n_1\omega\frac{L_2}{c}\right)} & e^{i\left(n_2\omega\frac{L_2}{c}\right)} & e^{i\left(n_3\omega\frac{L_2}{c}\right)} \\
0 & 0 & 0 & n_1 e^{i\left(n_1\omega\frac{L_2}{c}\right)} & n_2 e^{i\left(n_2\omega\frac{L_2}{c}\right)} & n_3 e^{i\left(n_3\omega\frac{L_2}{c}\right)} \\
0 & 0 & 0 & 0 & 0 & 0 \\
0 & 0 & 0 & 0 & 0 & 0 \\
0 & 0 & 0 & \alpha_{A0}(k_1,\omega) & \alpha_{A0}(k_2,\omega) & \alpha_{A0}(k_3,\omega) \\
0 & 0 & 0 & \alpha_{B0}(k_1,\omega) & \alpha_{B0}(k_2,\omega) & \alpha_{B0}(k_3,\omega) \\
0 & 0 & 0 & \alpha_{A0}(k_1,\omega)e^{i\left(n_1\omega\frac{L_2}{c}\right)} & \alpha_{A0}(k_2,\omega)e^{i\left(n_2\omega\frac{L_2}{c}\right)} & \alpha_{A0}(k_3,\omega)e^{i\left(n_3\omega\frac{L_2}{c}\right)} \\
0 & 0 & 0 & \alpha_{B0}(k_1,\omega)e^{i\left(n_1\omega\frac{L_2}{c}\right)} & \alpha_{B0}(k_2,\omega)e^{i\left(n_2\omega\frac{L_2}{c}\right)} & \alpha_{B0}(k_3,\omega)e^{i\left(n_3\omega\frac{L_2}{c}\right)}
\end{pmatrix}
$$

$$
\begin{pmatrix}
0 & 0 & 0 & 0 & 0 & 0 \\
0 & 0 & 0 & 0 & 0 & 0 \\
1 & 1 & 1 & 0 & 0 & 0 \\
-n_1 & -n_2 & -n_3 & 0 & 0 & 0 \\
e^{-i\left(n_1\omega\frac{L_2}{c}\right)} & e^{-i\left(n_2\omega\frac{L_2}{c}\right)} & e^{-i\left(n_3\omega\frac{L_2}{c}\right)} & -1 & -1 & 0 \\
-n_1 e^{-i\left(n_1\omega\frac{L_2}{c}\right)} & -n_2 e^{-i\left(n_2\omega\frac{L_2}{c}\right)} & -n_3 e^{-i\left(n_3\omega\frac{L_2}{c}\right)} & -n_D & n_D & 0 \\
0 & 0 & 0 & e^{i\left(n_D\omega\frac{L_3}{c}\right)} & e^{-i\left(n_D\omega\frac{L_3}{c}\right)} & -1 \\
0 & 0 & 0 & n_D e^{i\left(n_D\omega\frac{L_3}{c}\right)} & -n_D e^{-i\left(n_D\omega\frac{L_3}{c}\right)} & -n_S \\
\alpha_{A0}(k_1,\omega) & \alpha_{A0}(k_2,\omega) & \alpha_{A0}(k_3,\omega) & 0 & 0 & 0 \\
\alpha_{B0}(k_1,\omega) & \alpha_{B0}(k_2,\omega) & \alpha_{B0}(k_3,\omega) & 0 & 0 & 0 \\
\alpha_{A0}(k_1,\omega)e^{-i\left(n_1\omega\frac{L_2}{c}\right)} & \alpha_{A0}(k_2,\omega)e^{-i\left(n_2\omega\frac{L_2}{c}\right)} & \alpha_{A0}(k_3,\omega)e^{-i\left(n_3\omega\frac{L_2}{c}\right)} & 0 & 0 & 0 \\
\alpha_{B0}(k_1,\omega)e^{-i\left(n_1\omega\frac{L_2}{c}\right)} & \alpha_{B0}(k_2,\omega)e^{-i\left(n_2\omega\frac{L_2}{c}\right)} & \alpha_{B0}(k_3,\omega)e^{-i\left(n_3\omega\frac{L_2}{c}\right)} & 0 & 0 & 0
\end{pmatrix}
\begin{pmatrix} r \\ A \\ B \\ C \\ D \\ E \\ F \\ G \\ H \\ I \\ J \\ K \end{pmatrix}
=
\begin{pmatrix} 1 \\ 1 \\ 0 \\ 0 \\ 0 \\ 0 \\ 0 \\ 0 \\ 0 \\ 0 \\ 0 \\ 0 \end{pmatrix}
$$

III.4